Durham University

Durham E-Theses

Models of stress at mid-ocean ridges and their offsets

Maria C. Neves

How to cite:

Neves, Maria C. (2000) Models of stress at mid-ocean ridges and their offsets. Doctoral thesis, Durham University.

Use policy

The full-text may be used and/or reproduced, and given to third parties in any format or medium, without prior permission or charge, for personal research or study, educational, or not-for-profit purposes provided that:

- a full bibliographic reference is made to the original source
- a https://etheses.durham.ac.uk/id/eprint/4408/ is made to the metadata record in Durham E-Theses
- the full-text is not changed in any way

The full-text must not be sold in any format or medium without the formal permission of the copyright holders.

Please consult the full Durham E-Theses policy for further details.

Academic Support Office, The Palatine Centre, Durham University, Stockton Road, Durham, DH1 3LE
e-mail: e-theses.admin@durham.ac.uk Tel: +44 0191 334 6107
https://etheses.durham.ac.uk

Models of stress at mid-ocean ridges and their offsets

The copyright of this thesis rests with the author. No quotation from it should be published in any form, including Electronic and the Internet, without the author's prior written consent. All information derived from this thesis must be acknowledged appropriately.

by

Maria C. Neves

A Thesis submitted for the degree of

Doctor of Philosophy

at the University of Durham

Department of Geological Sciences

June 2000

19 JUN 2001

To Artur and David

Models of stress at mid-ocean ridges and their offsets

Maria C. Neves

ABSTRACT

This thesis aims to investigate the stresses at mid-ocean ridge offsets, and particularly at the particular class of offsets represented by oceanic microplates. Among these, the Easter microplate is one of the best surveyed. This thesis first studies the stress field associated with mid-ocean ridges and simple types of ridge offsets, and then uses the stress field observed at Easter to constrain the driving mechanism of microplates. Two-dimensional finite element modelling is used to predict the lithospheric stress indicators, which are then compared with observations.

Extensional structures at high angles ($> 35°$) to ridge trends are often observed at ridge-transform intersections and non-tranform offsets, but remained unexplained until now. This study proposes that the topographic loading created by the elevation of mid-ocean ridges relative to old seafloor is a source of ridge parallel tensile stresses, and shows they can be explained by the rotation of ridge parallel tensile stresses at locked offsets.

The elasto-plastic rheology is used to investigate the evolution of normal faults near mid-ocean ridges. It is shown that variations in the lithospheric strength, caused entirely by variations in the brittle layer thickness, can account for the observed variations in fault character with spreading rate and along-axis position. Plasticity is shown to prevent the achievement of large fault throws in thin brittle layers. Consequently, it may be important at fast spreading ridges.

A new dynamic model is proposed for Easter microplate. It mainly consists of: 1) driving forces along the East and West Rifts, resulting from the combination of a regional tensile stress with an increasing ridge strength towards rift tips, 2) mantle basal drag resisting the microplate rotation, and contributing with less than 20% to the total resisting torque, and 3) resisting forces along the northern and southern boundaries. To explain both the earthquake focal mechanism evidence and the existence of compressional ridges in the Nazca plate, the boundary conditions along the northern boundary are required to change with time, from completely locked to locked in the normal direction only.

This study does not invalidate the microplate kinematic model proposed by Schouten et al. (1993), but shows that normal resisting forces along the northern and southern boundaries of Easter microplate must exist in order to explain the stress observations. Also, it suggests that ridge strength variations play an important role in the dyamics of mid-ocean ridge overlap regions.

Acknowledgements

First I wish to thank my two supervisors, Prof. Roger Searle and Prof. Martin Bott. Their guidance and encouragement literally kept me going during this project. Roger first suggested the work on the dynamics of microplates, and only with his help and patience did I finally come to grips with it. Martin kindly introduced me to his finite element program, guided me through the field of lithospheric stress, and provided invaluable suggestions and comments. I am grateful to both for their prompt and thorough reviews of earlier drafts of this thesis.

I also wish to thank the staff of the Department of Geological Sciences, particularly David Stevenson for computer support, and Dave Asbery and Carole Blair for assistance on many occasions.

Thanks to Prof. Mendes Victor and Dr. João Fonseca for having supported and encouraged my decision of starting a Ph.D. at Durham.

Thanks also to Teresa, Afonso, Hulda, Arnar, and especially John and Elaine, for their friendship and hospitality.

Last but not least thanks to Rui, for his love and encouragement. Our parents, Inácia, Alberto, Amélia, and António, also provided great support, and baby-sitting.

This Ph.D. was funded by the Calouste Gulbenkian Foundation and by the Marie Curie fellowship scheme.

Declaration

I declare that this dissertation describes my own work, except where acknowledgement is made in the text, and is not substantially the same as any work that has been or is being submitted to this and any other university for any degree, diploma or other qualification.

Maria C. Neves

June 2000

Contents

1 Introduction **1**

1.1 Context of this study 1

1.2 Mid-ocean ridges 2

1.3 Faulting observations at Mid-Ocean Ridges 8

1.4 Previous models of faulting at Mid-Ocean Ridges 11

1.5 Mid-ocean ridge segmentation 14

1.6 Previous models of stress at mid-ocean ridge offsets 16

1.7 Microplates 20

1.8 The roller-bearing kinematic model 23

1.9 The Pacific plate in the region of Easter microplate 26

1.10 Previous work on the asymmetric subsidence of the East Pacific Rise near 20°S 28

1.11 Aims and structure of this dissertation 31

2 Lithospheric stress **33**

2.1 Introduction 33

2.2 Definitions of stress 34

2.3 Relation between stress and faulting 38

2.4 Stress indicators in the lithosphere 39

2.5 Plate boundary forces at oceanic plates 40

2.5.1 The basal drag force 41

2.5.2 The ridge push force 43

2.5.3 The ridge resistance 46

2.5.4 The transform resistance 48

2.6 Other sources of tectonic stress 50

2.7 The state of stress from mid-ocean ridges to intraplate regions 51

2.8 Stress indicators at transform and non-transform offsets 53

2.9 Observations at Easter microplate 57

2.10 Stress indicators at Easter microplate 62

3 Stress and the finite element method 69

3.1 Introduction 69

3.2 Elastic stress analysis 70

3.3 Derivation of the element equations for elastic stress analysis 72

3.4 Viscoelastic analysis 78

3.5 Elasto-viscoplastic analysis 79

3.6 The dual node technique for fault modelling 81

4 The anomalous subsidence of the East Pacific Rise 83

4.1 Introduction 83

4.2 Grid and rheology 84

4.3 Modelling principles 89

4.4 The density structure in normal plate cooling models 90

4.5 The density structure in anomalous subsidence models 91

4.6 The density structure at the ridge axis 93

4.7 Boundary conditions 94

4.8 Presentation of the models 94

4.9 General description of the results 95

4.10 Changing the strength of the ridge 98

4.11 Anomalous versus normal subsidence 103

4.12 Estimate of neglected factors 106

4.13 Discussion 107

5 Elasto-plastic models of normal faulting in the oceanic lithosphere 111

5.1 Introduction 111

5.2 Rheology 112

5.3 Strength envelope 113

5.4 Model length and thickness 117

5.5 Fault parameters 118

5.6 Grid 120

5.7 Application of extension 121

5.8 Infill loading 122

5.9 Presentation of the models 123

5.10 General description of the results 137

5.11 The effect of changing the brittle layer thickness 141

5.12 The effect of changing the fault dip angle 143

5.13 The effect of loading by infill 144

5.14 Comparison between elastic and elasto-plastic models 146

5.15 Discussion 147

5.15.1 Comparison with observations 147

5.15.2 Tectonic strain 148

5.15.3 Fault longevity 149

6 Models of stress at mid-ocean ridge offsets 151

6.1 Introduction 151

6.2 Modelling assumptions and procedure 152

6.2.1 Rheology 152

6.2.2 Grid geometry and boundary conditions 153

6.2.3 Application of the topographic loading 155

6.3 Models of stress from mid-ocean ridges to intraplate regions 159

6.3.1 Elastic model (slow spreading ridge) 159

6.3.2 Elasto-plastic model (slow spreading ridge) 160

6.3.3 Fast versus slow spreading ridges 168

6.4 Models of stress at transform faults 170

6.4.1 Locked versus unlocked faults 170

6.4.2 The effect of topography 174

6.4.3 The effect of ridge strength 174

6.4.4 Transform as finite width weak zones 177

6.5 Comparison of the results with observations at transform faults . . . 181

6.6 Models of stress at non-transform offsets 183

6.7 Discussion 185

7 Easter microplate dynamics **187**

7.1 Introduction 187

7.2 Modelling assumptions and procedure 189

7.3 The strength of the microplate 191

7.4 Estimating the basal drag force 193

7.5 Estimating possible driving forces 198

7.5.1 The Schouten et al. hypothesis 198

7.5.2 The rift driven hypothesis 201

7.6 Expanding the rift driven hypothesis 205

7.7 Comparison with observations at Easter microplate 211

7.8 A new dynamic model for Easter 213

7.9 Comparison with strength estimates 220

7.10 Discussion 224

8 Summary and conclusions **226**

8.1 Summary 226

8.1.1 Stress on the EPR flanks 226

8.1.2 Normal faulting at mid-ocean ridges 228

8.1.3 Ridge transform and non-transform offsets 229

8.1.4 Dynamics of Easter microplate 230

8.2 The strength of the lithosphere 232

8.3 The origin of Easter microplate 234

8.4 Further work 235

8.4.1 The dynamics of other microplates 235

8.4.2 The origin of microplates 238

8.5 Conclusions 238

References 241

Chapter 1

Introduction

1.1 Context of this study

Much attention has been focused on the evolution of rapidly spinning oceanic microplates (e.g. Hey et al., 1985; Engeln et al., 1988; Searle et al., 1989; Larson et al., 1992; Schouten et al., 1993; Rusby and Searle, 1995). Nevertheless, the dynamics of these large dual spreading systems has never been investigated. The principal motivation of this dissertation is to explore the driving mechanism of oceanic microplates. This is done by modelling the observed patterns of lithospheric stress, using the finite element method.

In recent years, great improvements in the definition of mass heterogeneities in the mantle have lead to global models of mantle circulation capable of predicting plate tectonic velocities and geoid anomalies (e.g. Hager et al., 1985; Ricard et al., 1989; Van der Hilst et al., 1997). Despite this progress, earth models of mantle circulation coupled with moving surface plates have not yet been able to predict the observed global patterns of stress in the lithosphere (e.g. Wuming et al., 1992). In the absence of a model which successfully relates the lithospheric stress and the mantle dynamics, the alternative has been to isolate the lithosphere and consider that tectonic plates are stressed by plate boundary forces (e.g. Forsyth and Uyeda, 1975) and/or intra-lithospheric mass heterogeneities (e.g. Fleitout and Froidevaux, 1982).

This study follows the approach that microplates are driven by plate boundary forces. But microplates are a complex type of mid-ocean ridge offset, so mid- ocean ridges and simpler types of ridge offsets are the first targets of this work. Investigated are the East Pacific Rise in the region of Easter microplate, normal faults in the vicinity of mid-ocean ridges, and ridge transform and non-transform offsets. This prepares the ground for the analysis of the dynamics of Easter microplate, a representative example of microplates. The remainder of chapter 1 constitutes an introduction to these subjects. It presents the observations and previous modelling efforts relevant to the questions that will be addressed.

1.2 Mid-ocean ridges

Mid-ocean ridges are diverging plate boundaries where magma and depleted mantle upwells giving rise to new oceanic lithosphere. Early observations at mid-ocean ridges revealed that the gross morphology of spreading centres varies with the spreading rate (Fig. 1.1). Slow spreading ridges (10-50 mm/yr full rate) such as the Mid-Atlantic Ridge (MAR) show median valleys, whereas fast spreading ridges (90-180 mm/yr full rate) such as the East Pacific Rise (EPR) show axial highs. Intermediate spreading ridges (50-90 mm/yr full rate) show a transition between the Atlantic and the Pacific type of axial topography (e.g. Macdonald, 1982).

Although median valleys are typical of slow spreading ridges and axial highs typical of fast spreading ridges, exceptions to this pattern exist, proving that the spreading rate is not the only factor controlling the axial morphology. One such exception occurs at the slow spreading (20 mm/yr full rate) Reykjanes ridge, which shows an axial high north of 59°N (e.g. Appelgate and Shor, 1994). In this case the source of the anomalous topography is believed to be the Iceland hotspot and associated anomalously high subsurface temperatures. Temperature controls the strength and thickness of the lithosphere and these are, according to current mechanical models, the factors that determine the axial morphology (e.g. Lachenbruch, 1973; Tapponnier and Francheteau, 1978; Phipps Morgan et al., 1987; Chen and Morgan, 1990; Eberle and Forsyth, 1998).

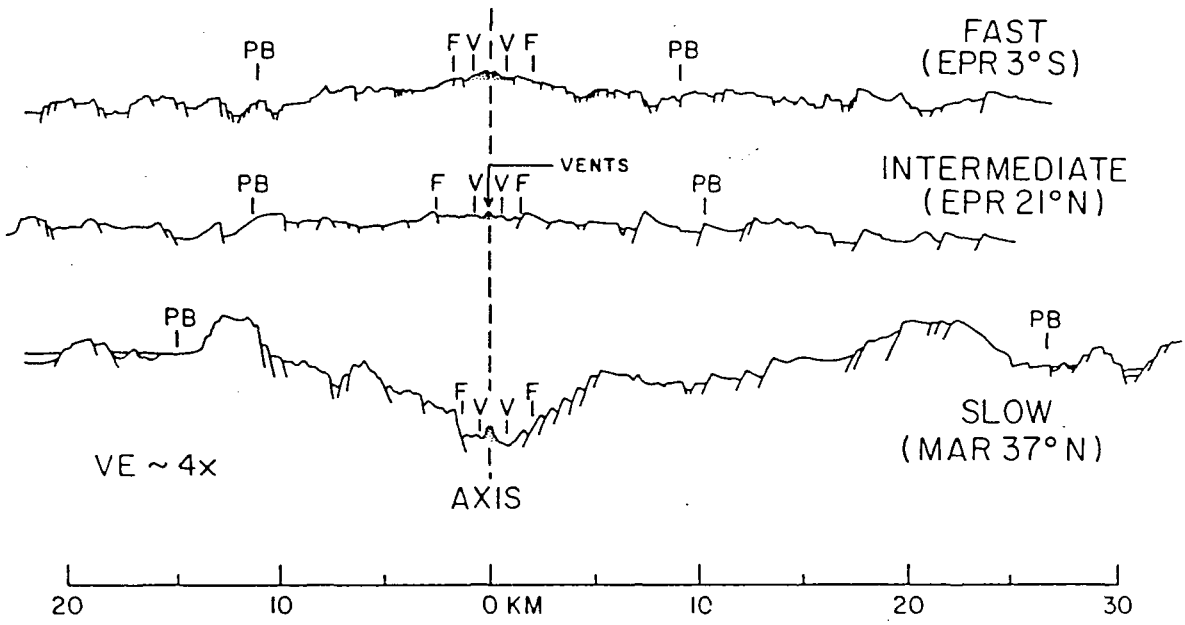

Fig. 1.1 Bathymetric profiles of mid-ocean ridges at fast, intermediate and slow rates. Neovolcanic zone is indicated by Vs, zone of fissuring by Fs, and plate boundary zone (width of active faulting) by PBs. Median valleys at slow spreading ridges are typically 1-3 km deep and have an inner floor 5-15 km wide. Axial highs at fast spreading ridges are typically 200-400 m high and 5-15 km wide (after Macdonald, 1982).

Mid-ocean ridges are formed by segments bounded by transform faults and non-transform offsets. Both at slow and fast spreading ridges it has been found that ridge segment centres are associated with mantle Bouguer anomaly lows while segment ends are associated with mantle Bouguer anomaly highs (Fig. 1.2)(e.g. Kuo and Forsyth, 1988). The mantle Bouguer anomaly lows at segment centres reflect a mass deficiency arising from an increase in crustal thickness and/or anomalous low densities in the upper mantle. The argument that crustal thickening and anomalous low densities is the result of enhanced mantle upwelling, lead to the the proposal of a model of mantle upwelling focussed towards the centre of segments (Kuo and Forsyth, 1988; Lin et al., 1990). Magmas are believed to rise from a zone of high-melt content below the ridge, maybe as the result of gravitational instabilities (Whitehead et al., 1984), filling magma chambers along the ridge axis, and erupting to the surface more or less frequently depending on the spreading rate. Indirect observations, such as the thickness of the extrusive layer and the extent of the axial volcanoes, suggest that the interval between eruptions is about 50 years at fast spreading ridges, and about 10000 years at slow spreading ridges (Macdonald, 1982).

The hypothesis of focussed mantle upwelling constitutes the basis of one of the main models of ridge segmentation (Fig. 1.3). According to it the mid-ocean ridge is divided into stable spreading cells and ridge discontinuities occur at the distal ends of magmatic pulses (e.g. Macdonald et al., 1991).

Along-axis variations in the mantle Bouguer anomaly are several times larger on the MAR than on the EPR. To explain this, it has been suggested that mantle upwelling at slow spreading ridges has a 3D structure, forming discrete diapirs of partial melt beneath segment centres, whereas at fast spreading ridges the mantle flow is more 2D or sheet-like (Parmentier and Phipps Morgan, 1990; Lin and Phipps Morgan, 1992). Gravity modelling at the southern EPR showed that a 3D focused model of mantle upwelling may be applicable even at fast spreading ridges, provided there is a shallow and efficient mechanism of along-axis magma transport (Wang and Cochran, 1993; Cormier et al., 1995).

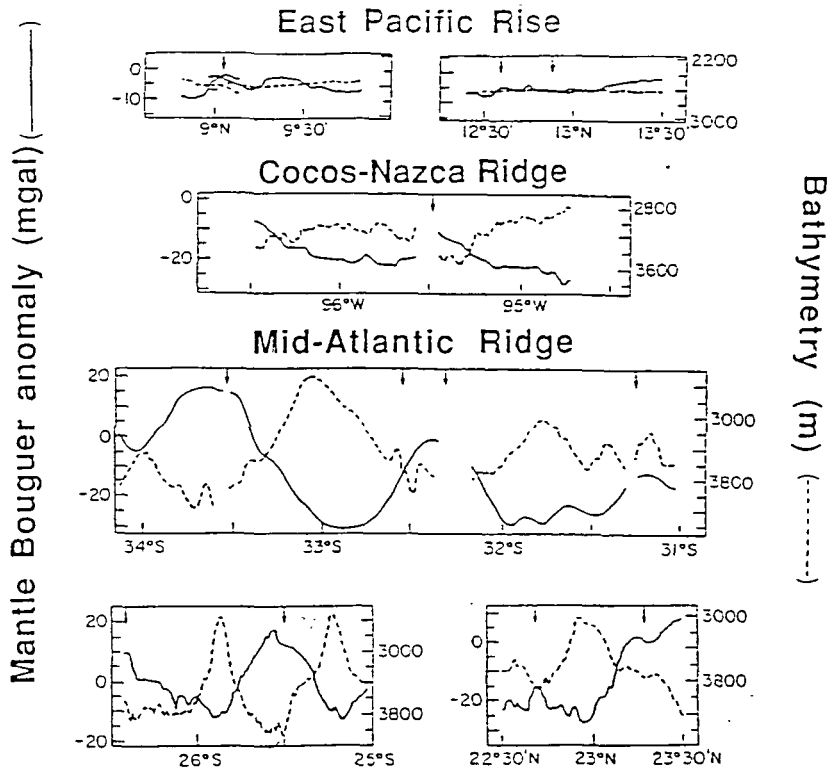

Fig. 1.2 Along-axis profiles of seafloor depth (dashed lines) and Mantle Bouguer Anomaly (solid lines) at fast, intermediate and slow spreading ridges. Arrows mark first and second order discontinuities (after Lin and Phipps Morgan, 1992).

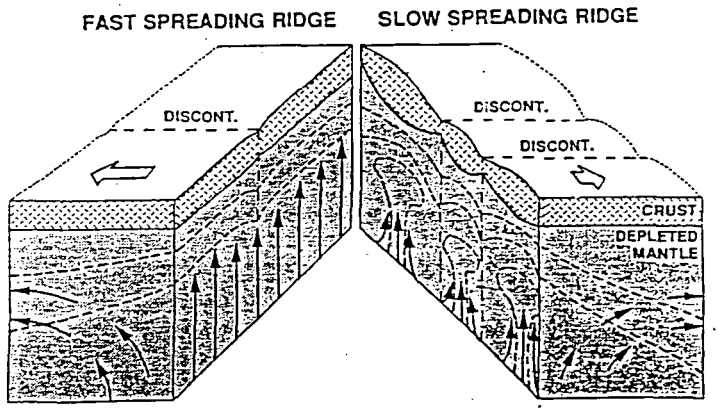

Fig. 1.3 The model of crustal accretion and mantle upwelling proposed to explain the along-axis bathymetry and gravity observations in Fig. 1.2. Solid arrows show mantle flow directions, and open arrows show plate motion vectors (after Lin and Phipps Morgan, 1992).

The residual mantle Bouguer anomaly (RMBA) is obtained by subtracting from the mantle Bouguer anomaly the gravity signal associated with lithosphere cooling. At the Mid-Atlantic Ridge, crust at inside corners of mid-ocean ridge offsets (which occur between the ridge axis and the active discontinuity) has consistently higher values of RMBA than crust formed at outside corners (which occur on the opposite side of the ridge, adjacent to the inactive trace of the offset) (e.g. Tucholke and Lin, 1994). Based on this RMBA asymmetry, Tucholke and Lin (1994) estimated that the inside corner crust at the MAR near the Atlantis fracture zone is 2-3 km thinner than the outside corner crust. Apart from that the inside corner crust is shallower, has more widely spaced and larger throw normal faults, and fewer volcanic features than the outside corner. Moreover, mafic and ultramafic rocks are commonly found at the inside corners but not at the outside corners. All these observations support the hypothesis of thin or missing crust at inside corners and have lead to an alternative model of ridge segmentation at slow spreading ridges. According to it, slow spreading ridge segmentation is controlled by the presence of low angle detachment faults (Mutter and Karson, 1992) or by some combination of detachment faulting and focussed mantle upwelling (Tucholke and Lin, 1994; Tucholke et al., 1997).

Seismic observations in general agree with the hypothesis that ridge segmentation is due to focused magmatic accretion at segment centres and/or increased tectonic extension at segment ends.

At the EPR a shallow reflector, lying 1-2 km below the ridge axes and presumed to mark the top of a narrow (1-4 km wide) and thin (tens to hundreds of meters thick) lens of melt, is identified whenever the axial depth and the ridge cross sectional area point to strong magmatic activity (e.g. Detrick et al., 1987; Mutter et al., 1995). This reflector lies on top of a much broader seismic low velocity zone, interpreted to be a largely solidified plutonic body containing only a small fraction of melt. A magma chamber, having similar characteristics (dimensions and depth) to those observed at fast and intermediate spreading ridges, has been reported at the slow spreading Reykjanes ridge (Navin et al., 1998). This similarity in the process of

accretion despite the different spreading rate, is consistent with the uniformity of the mature oceanic crust observed throughout the world oceans.

Mid-ocean ridge earthquake data are extremely important to constrain thermal and mechanical models of spreading centres, because they provide an estimate of the depth extent of faulting and thus of the depth of the brittle-ductile transition in the axial region. Earthquake data sets at mid-ocean ridges fall into two categories: (1) in situ recorded microearthquakes, and (2) large earthquakes ($m > 5$) whose parameters are obtained from inversion of long period P and SH waves. This last category is however limited to full spreading rates less than 40-45 mm/yr because earthquakes generated at faster spreading ridges are not large enough to be recorded at teleseismic distances.

Among the microearthquake surveys at the MAR two were particularly important in placing limits on the amount of brittle lithosphere thinning at segment centres. The first was performed at 23° N and revealed that hypocenters had focal depths of 4-8 km beneath the median valley seafloor (Toomey et al., 1988). The second took place at 26° N and revealed hypocenters with focal depths ranging from 2 to 8 km beneath the ridge axis. The shallower earthquakes, with hypocentral depths less than 4 km, were concentrated below the along-axis high in the middle section of the ridge segment (Kong et al., 1992).

At several ridges with full spreading rates less than 45 mm/yr, Huang and Solomon (1988) found that the centroid depths of teleseismically recorded earthquakes ranged from 2 to 6 km below the seafloor. Arguing that centroid depths mark the mean depth of fault slip, they proposed that earthquake faulting, and thus the brittle domain, extend to a depth of 2-10 km beneath slow spreading ridges. They also verified that the maximum centroid depths decreased with increasing spreading rate.

Purdy et al. (1992) further investigated the relation between spreading rate and seismic structure at mid-ocean ridges. They compiled and compared depths to the top of the low-velocity-zone below 6 different ridges, with full spreading rates ranging from 20 to 150 mm/yr. Their conclusion was that as full spreading rate

decreased from 150 to 20 mm/yr the depth below the seafloor to the top of the low velocity zone increased approximately from 1 to 4 km.

1.3 Faulting observations at Mid-Ocean Ridges

The character of faulting at mid-ocean ridges depends primarily on the spreading rate and secondly on the location along the ridge segment. Although along-axis variations in fault characteristics occur at fast spreading ridges (Carbotte and Macdonald, 1994), they are much more important at slow spreading ridges. For that reason, fault parameters at slow spreading ridges are described at segment centres and at segment ends. At segment ends of slow spreading ridges there is also an across-axis change in fault occurrence, in that faulting at outside corners differs from faulting at inside corners. In fact, it has been noted that the variation in fault characteristics observed along segments arises mainly from variations occurring between the segment centre and the inside corner at the segment end (e.g. Tucholke and Lin, 1994; Escartin et al., 1999).

- *Fault heave and throw.* Fault heave and throw diminish with increasing spreading rate. At fast spreading ridges fault vertical offsets do not usually exceed tens of meters. For example, at the East Pacific Rise near 9°N, the mean fault throw is 40 m (Fig. 1.4)(Carbotte and Macdonald, 1994). In contrast, at the Mid-Atlantic Ridge near 29°, Shaw (1992) reports vertical offsets of faults ranging from 200-600 m at segment centres to 800- 1200 m at segment ends. At the same location on the MAR, Escartin et al. (1999) report an apparent average fault heave at the segment centre of 150 m or 250 m depending on the ridge flank, of 400 m on the inside corner and of only 100 m on the outside corner (Fig. 1.5).
- *Fault spacing.* Fault spacing also diminishes with increasing spreading rate. At the East Pacific Rise (at 8°30′N-10°N) the mean fault spacing is 1.5 km (Carbotte and Macdonald, 1994). At the MAR (at 28°-30°N) the mean fault spacing is approximately 0.2-2 km at the segment centre and up to 4-8 km at the segment ends (Shaw, 1992).

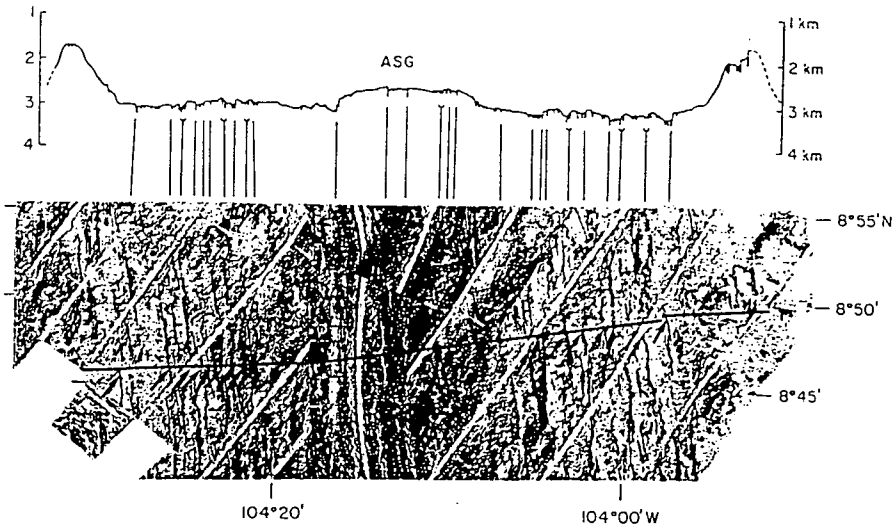

Fig. 1.4 Faults scarps across the East Pacific Rise at 8°50′N. Location of the Deeptow bathymetric profile (at the top) is delineated on the seaMARC II side scan data (at the bottom) with a solid line. Identified fault scarps are indicated by thin lines below Deeptow profile and by arrows on seaMARC II data (after Carbotte and Macdonald, 1994).

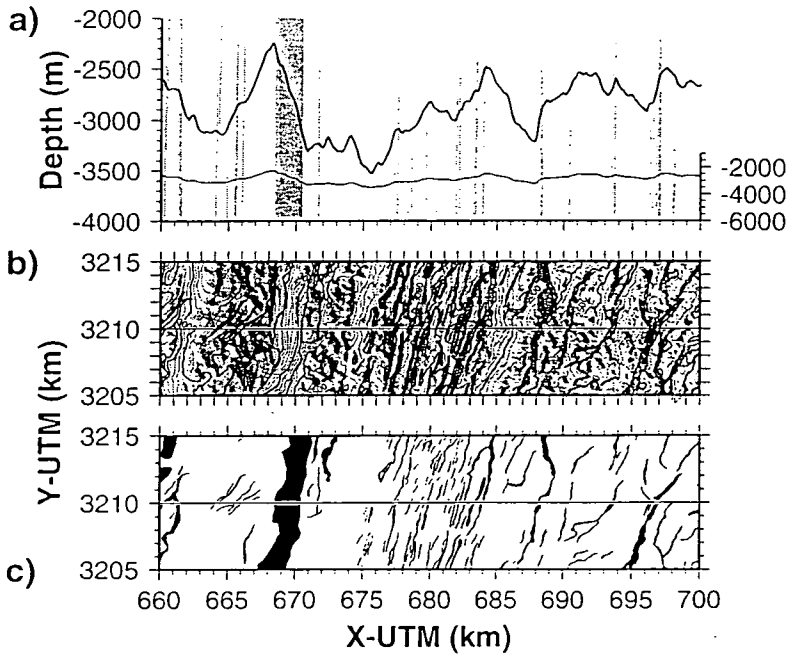

Fig. 1.5 Fault scarps across the MAR at 29°N (segment centre). The bathymetric profile is shown with (8x) and no vertical exaggeration (thick and thin lines, respectively). (a) Comparison of the interpreted fault scarps (grey bars) from the backscatter data with multibeam bathymetric data. (b) Location of the bathymetric profile on a relief map of the area (100 m contours). (c) Faults interpreted from digital-side scan sonar mosaics (after Escartin et al., 1999).

- *Fault length and strike.* The number of short faults is observed to increase with the spreading rate. At the East Pacific Rise (at 8°30′-10°N) the mean fault length is 7.5 km (Carbotte and Macdonald, 1994). At the MAR segment studied by Shaw (1992) faults up to 40 km long exist at the segment centre, while at the segment ends faults are continuous for only 5-10 km.

- *Range of activity.* Although some faults may remain active beyond distances of 20 km off axis, there is a general consensus that at all spreading rates most active faulting lies within 5-10 km of the ridge axis. Using plots of cumulative fault throw with distance from the ridge axis, Bicknell et al. (1987) concluded that at the East Pacific Rise at 19°30′S, active faulting occurs within 5-8 km of the rise axis. Based on the character of sonar data Escartin et al. (1999) concluded that faults at the MAR at 29°N nucleate 1-2 km from the ridge axis and cease to be active within 10-20 km of the axis. At the same MAR latitude the across-axis distribution of microearthquakes also suggest that the active fault zone lies within 10 km of the ridge axis (Wolfe et al., 1995).

- *Fault dip angle.* Information on the dip angle of MOR faults comes mainly from fault plane solutions of microearthquakes and fine scale morphology surveys. At fast spreading ridges such information is not available and fault dip angles are usually assumed to be the same as observed on slow spreading ridges. From inversion of teleseismically recorded earthquakes, Huang and Solomon (1988) inferred that fault planes at slow spreading ridges are characterised by predominantly normal faulting, on planes that dip at 45°. The same result was obtained by Wolfe et al. (1995) from the source mechanisms of microearthquakes recorded at the MAR at 29°N. Also at the MAR, and based on submersible observations and bottom photographs, Karson and Dick (1983) report across-axis differences at segment ends: at outside corners steep faults (70°-90°) group to form fault zones of moderate average slope (30°), while at inside corners two groups of faults are observed, one dipping at 20°-60° and the other dipping at 70°-90°.

- *Fault facing direction.* Inward facing faults dip towards the ridge axis and outward facing faults dip in the opposite direction. Both inward and outward facing faults occur at all spreading rates. However, at slow spreading ridges, inward facing faults largely outnumber outward facing faults, while at the fastest spreading rates they occur in approximately equal numbers (Carbotte and Macdonald, 1994, Escartin et al., 1999).

1.4 Previous models of faulting at Mid-Ocean Ridges

Faulted lithosphere responds to tectonic extension by slip along faults, accompanied by flexure (Fig. 1.6).

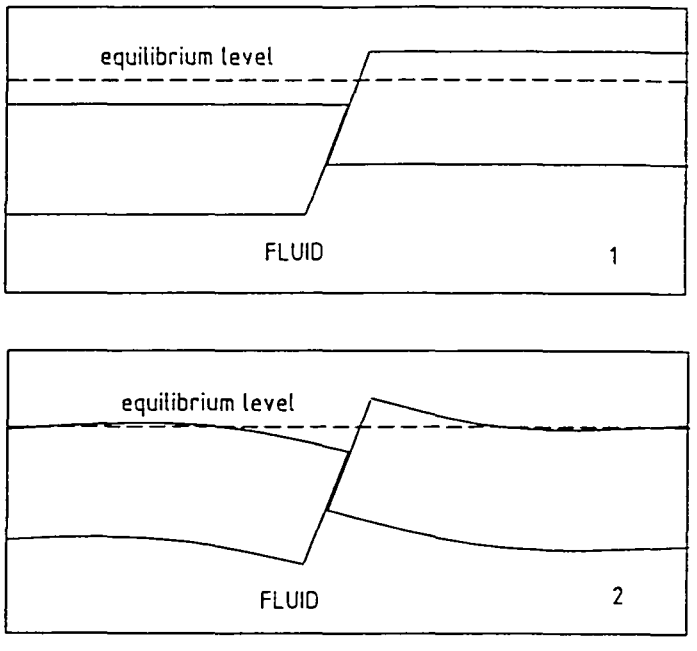

Fig. 1.6 The displacement along the fault is the response to tectonic extension. The extension causes opposite edge forces to act along the fault planes due to their inability to withstand shearing stress. In 1 the footwall is displaced above the initial isostatic equilibrium level and the hanging wall is displaced below the equilibrium level. In 2 the plate bends in response to the topographical load caused by the offset. The two processes oppose each other and occur simultaneously.

If faults at mid-ocean ridges are only active while in the close proximity of the ridge axis, as seem to happen at all spreading rates, then part of the flexural response to faulting must occur between the fault and the ridge axis. The question arises as to whether the lithosphere at mid-ocean ridges can withstand elastic strain and flexure, that is whether flexural models of faulting are relevant at mid-ocean ridges. Models of ridge axis morphology provide a possible answer to this question. Bathymetric and gravity data are well matched by models that explain the axial high at fast spreading ridges and the elevation of rift flanks at slow spreading ridges by flexure of an elastic plate (Madsen et al., 1984; Weissel and Karner, 1989, Wang and Cochran, 1993). Moreover, the wavelengths of the flexural response predicted by such models are based on values of the elastic plate thickness consistent with estimates of the brittle layer thickness derived from seismicity studies at mid- ocean ridges.

The most specific models of faulting at mid-ocean ridges presented to date were developed by Shaw and Lin (1996) and Escartin et al. (1997). These models attempt to explain the dependence of the fault style on the spreading rate and on the along-axis position at slow spreading ridges.

Shaw and Lin (1996) investigated the development of normal faults at mid-ocean ridges using the flexural fault model of Forsyth (1992). According to Forsyth's model the stress necessary to produce continued slip along a fault is the sum of the stress necessary to overcome friction plus the stress necessary to overcome the uplift-induced stresses caused by previous slip. The stresses needed to overcome the uplift-induced stresses depend on the elastic thickness of the plate and on the amount of uplift (Forsyth, 1992).

It has been proposed that fluctuations in magma reservoir pressure create alternating tectonic and magmatic phases, with plate separation being mainly accommodated by seafloor accretion during the magmatic phase and extension being mainly accommodated by the growth of closely spaced faults during the tectonic phase (e.g. Thatcher and Hill, 1995). During the tectonic or amagamatic phase it is still uncertain if more than one fault can be active at the same time. In Shaw and

Lin's (1996) most successful model only one fault is active at a time, and it occurs on planes that minimise the resistance to cohesive, frictional and flexural forces. An active fault grows while moving away from the ridge axis as long as the total stress needed to continue slip, as derived by Forsyth (1992), is less than the total stress needed to initiate a new fault. When this condition is no longer true the fault reaches its maximum throw and fault activity jumps inward to a new nucleation site where the next active fault begins to grow.

Shaw and Lin (1996) applied their 2D cyclic faulting model to across-axis sections of rheology and temperature. The rheological structure they used was based on the model proposed by Chen and Morgan (1990) in which the lower crust may be weaker than the mantle below. Along-axis gradients in temperature would be responsible for the existence of isolated weak zones decoupling the brittle upper crust from the brittle upper mantle, particularly at the centre of slow spreading segments. The existence of these weak zones at slow spreading ridges would generate large along-axis variations in the thickness of the brittle layer, which in turn would generate the observed large scale along axis variations in fault throw and spacing. At fast spreading and hotspot affected ridge segments, the brittle mantle and the brittle upper crust would be decoupled along the whole segment, except possibly in the vicinity of a major offset, and this would result in small along-axis variations in fault styles.

The layered rheological model of Chen and Morgan (1990) was contested by Hirth et al. (1998) who presented evidence against the existence of a weak and ductile lower oceanic crust at mid-ocean ridges. Following this view, Escartin et al. (1997) argued against Shaw and Lin's (1996) results and proposed an alternative explanation for the variation in fault style along the axis of slow spreading segments. According to them the increase in fault spacing and throw towards the end of ridge segments is primarily due to changes in the coefficient of friction, and only secondly caused by thermally induced changes in the brittle layer thickness. They attributed the along-axis change in the coefficient of friction of faults to the distribution of serpentinites, which seem to be more abundant at the segment ends. Since serpen-

tinites are believed to strongly reduce the strength of faults by enhancing strain localisation, substantial weakening at the segment ends would result in larger fault spacing and throws (Escartin et al., 1997).

The fault modelling results presented by Shaw and Lin (1996) depend fundamentally on the brittle layer thickness, and can not be disregarded because of the rheological structure assumed. Their sequential model was successful in predicting the main fault observations, but it should be stressed that it was based on Forsyth's (1992) flexural fault model. Forsyth's (1992) flexural fault model is an idealisation in the sense that the plate remains perfectly elastic as extension proceeds, and that there is no erosion or sedimentation. In the vicinity of mid-ocean ridges sedimentation may occur in the form of extrusive volcanism and eroding fault wall debris. Also, elastic plate models are an oversimplification, producing anomalous low values of the effective elastic thickness, and plate curvatures broader than observed. Elasto-plastic models, which take into account strength envelopes, have been successful in sharpening the flexural bending at subduction zones (e.g. McAdoo et al., 1978; Goetze and Evans, 1979) and in attributing the low estimates of the effective elastic thickness to plastic yielding (Buck, 1988; Kusznir et al., 1991; Bott, 1997). One would therefore like to investigate the evolution of normal faults in the oceanic lithosphere, and their dependence on the brittle layer thickness, while considering the effects of both plastic yielding and sedimentation. This is the aim of chapter 5.

1.5 Mid-ocean ridge segmentation

The finding that the ridge axis is interrupted by many small offsets, which unlike transform faults do not have a clearly defined strike-slip fault connecting the ridge segment ends, dates only from the early eighties, when multibeam swath mapping tools started to be used. Since then the characteristics of ridge offsets have been systematised and a hierarchy of ridge discontinuities has been proposed based on their size, geometry and behaviour (Macdonald et al., 1988). According to this hierarchy a ridge segment between transform faults is broken into smaller segments

by second to fourth order discontinuities (Fig. 1.7), which become increasingly unstable and mobile as the ridge offset diminishes.

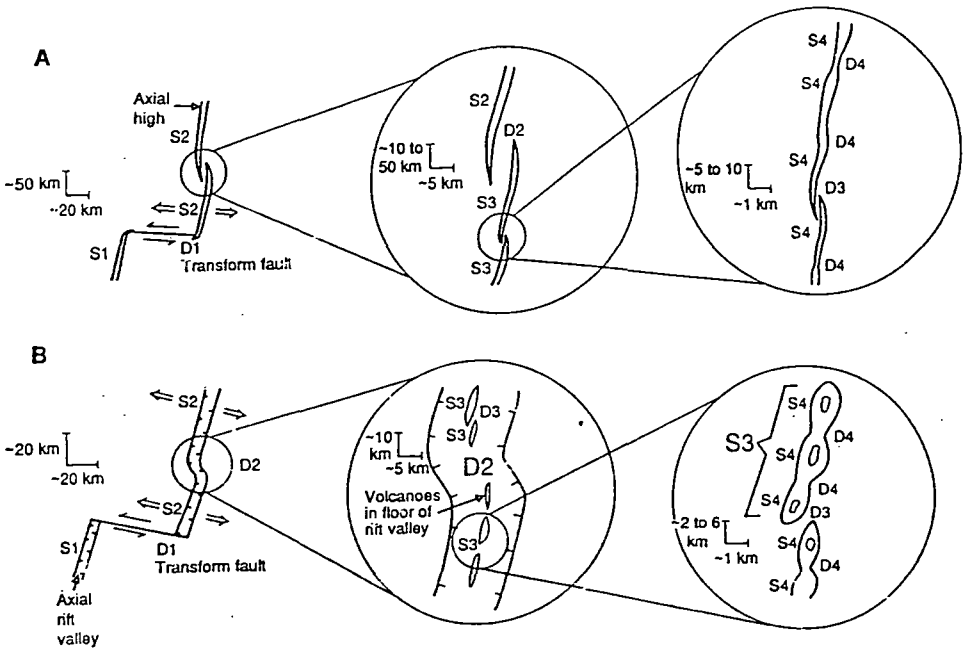

Fig. 1.7 A hierarchy of ridge segmentation for **A**-fast and **B**-slow spreading ridges (after Macdonald et al., 1991). First order discontinuities offset the ridge by more than 30 km and are transform faults at both fast and slow spreading ridges. Second order discontinuities offset the ridge by 2-30 km, and can be either Overlapping Spreading Centres at fast spreading rates or oblique shear zones and rift valley jogs at slow spreading rates. Third order segmentation has a characteristic offset of 0.5-2 km, occurring in the form of small Overlapping Spreading Centres or in the form of intervolcano gaps. Fourth order discontinuities are deviations from axial linearity resulting in slight bends or lateral offsets of less than 1 km.

Whatever the discontinuity order there is a strong correlation between the spacing of discontinuities and the spreading rate. Fast spreading ridges have on average longer and smoother segments than slow spreading ones. Also, ridge discontinuities generally constitute local maxima along the ridge axis depth profile. The magnitude of the deepening at segment ends is, like the segment length, strongly correlated with the spreading rate. For instance, the spacing between transform faults ranges from less than 200 km on the slowest spreading ridges, to 600-900 km on intermediate and

fast spreading ridges. At transform faults of slow spreading ridges depth anomalies range from 500 to 2000 m, while at fast spreading ridges they range from 300 to 600 m (Macdonald et al., 1991). The depth anomalies decrease with the order of the discontinuities, being non-existent or less than a few tens of meters at fourth order discontinuities.

1.6 Previous models of stress at mid-ocean ridge offsets

Early estimates of stress at ridges and transforms aimed to explain the observed ridge-transform orthogonal pattern. Lachenbruch and Thompson (1972) were the first to propose that " it is more difficult for diverging plates to spread a kilometre of ridge than to slip a kilometre of transform". By stating that the most stable configuration is the one that offers the least resistance to plate separation, they concluded that the resistance to spreading must be greater than the resistance to slipping because the observed orthogonal pattern minimises the length of the opening ridges. They interpreted the resistance to plate motion at transforms as a frictional or viscous resistance to shearing displacement, and the resistance to plate separation at ridges as a tectonic tension or tensile resistance resulting from a deficiency in stress in the spreading direction relative to the lithostatic state.

Based on laboratory experiments with wax, Oldenburg and Brune (1972; 1975) investigated the necessary conditions for the maintenance of the ridge-transform orthogonal pattern. They concluded that the resistive stresses acting on the transform must be smaller than the shear strength of the surrounding lithosphere. Their most relevant observations are: (1) the upwelling of the material at the ridge axis is passive, resulting only from hydrostatic forces in the fluid caused by the separation of the plates, (2) symmetric spreading occurs under conditions of no tensile strength across the ridge and (3) the stability of transforms is a consequence of their lack of strength.

More quantitative estimates of the ratio between the ridge resistance to spreading and the transform resistance to slip were later presented by Phipps Morgan and

and Parmentier (1984). They used a finite element model to investigate if the ridge resistance and the transform resistance forces could account for the observed stress field at ridge transform intersections. Their modelling showed that: (a) to maintain a narrow zone of strike-slip deformation along transforms the ratio of the ridge normal stress to the transform shear stress should be in the range of 3 to 5, and (b) with these relative magnitudes, the ridge resistance force and the transform resistance force could alone explain the curvature of the ridge axis and adjacent normal faults at ridge-transform intersections (the observed stress field at ridge-transform intersections is described in more detail in section 2.8).

Following a similar approach, Grindlay and Fox (1993) studied the stress field associated with non-transform offsets of slow spreading ridges. In addition to changes in the ratio of the ridge normal tensile stress to the transform shear stress, they considered the effect of varying the length of the offset. The aim of their modelling was to compare the structural patterns predicted from the calculated stress field with the morphological and tectonic structures observed at non-transform offsets.

The morphology of non-transform offsets of slow spreading ridges is variable, but seems to be partly controlled by the length of the offset (Sempere et al., 1993). Along the MAR three characteristic types of non-transform discontinuities have been recognised (Fig 1.8): (**A**) en-echelon jogs of the ridge axis, with slightly overlapping ridge tips, (**B**) en-echelon jogs of the ridge axis, with a ridge parallel basin, and (**C**) oblique shear zones consisting of a large extensional basin, oriented approximately at 45° relative to the strike of the ridge axis (Grindlay et al., 1991). These non-transform offsets appear to accommodate shear stresses over a broad area by both strike-slip and extensional tectonics.

Grindlay and Fox (1993) successfully modelled the structural geometries of non-transform offsets of types (**A**) and (**B**). They concluded that the predicted and observed tectonic structures were compatible for a range of offset lengths from 5 to 40 km, provided that the ridge normal tensile stress was 3 to 5 times greater than the offset shear strength. Their modelling also suggested that at fast spreading ridges a weaker ratio of ridge-normal stress to discontinuity shear stress must exist.

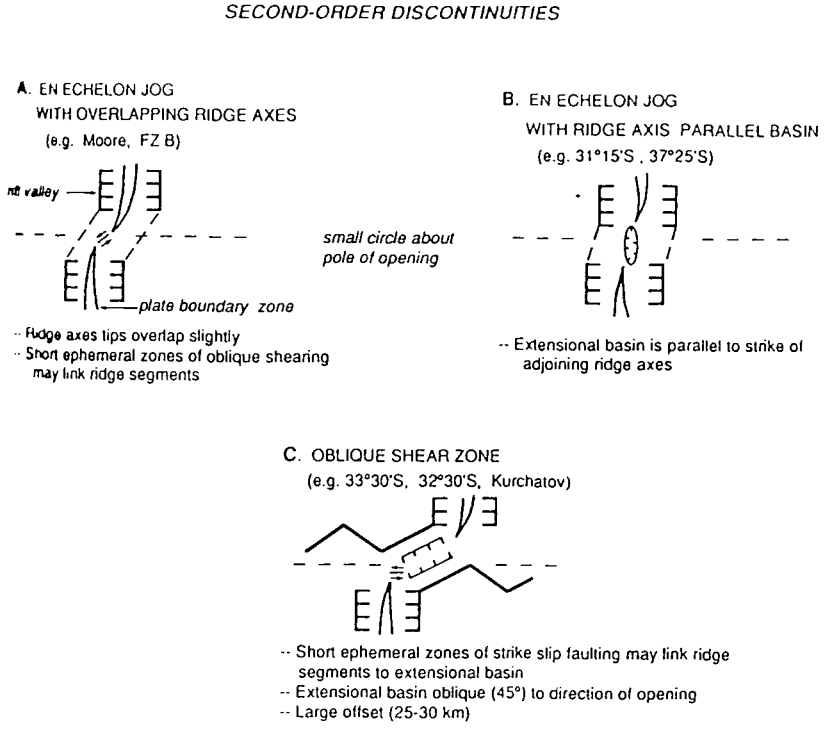

Fig. 1.8 Schematic structural geometries of second-order discontinuities seen along the southern Mid-Atlantic Ridge (after Grindlay et al., 1991).

Another approach considers the effect of regional stresses upon ridge-transform systems. Using a finite element model, Fujita and Sleep (1978) found that when regional stresses are applied at an oblique angle to the transform, high concentrations of stresses, also oblique to the transform, extend to the interior corners of the ridge-transform intersections. As a result ridges reorient to remain perpendicular to the stress field in such a way that the connecting transform fault is shortened. Assuming that ridges can jump (or propagate) to locations of maximum deviatoric stress, the modelling of collinear transform faults showed that oblique regional stresses may be at the origin of ridge jumps. Sources of regional stress at finite angles to transforms may occur for example on subducting plates due to the plate boundary forces associated with oceanic trenches (Fujita and Sleep, 1978).

Some transform faults contain structural elements indicating extension across them. One such transform showing, besides strike-slip faults, normal faults and dikes parallel to the transform, is exposed on land in North Iceland (Gudmundsson, 1995). To explain the extensional structures observed, Gudmundsson (1995) proposed that in addition to a ridge-perpendicular tensile stress, transform faults

are at least occasionally subjected to a ridge-parallel tensile stress. He tested this hypothesis using boundary element models, and found: (a) the ridge normal tensile stress tends to lock the transform, producing shear stresses responsible for the strike-slip faulting and associated earthquakes along the transform fault; (b) a ridge parallel tensile loading is required to explain the transform parallel normal faults, tensile fractures, dikes and intra-transform spreading centres; and (c) the combination of ridge parallel and ridge perpendicular tensile loading unlocks and makes slip easier on the transform. Moreover, this combination produces stresses compatible with the oblique faulting observed at transforms, particularly at ridge-transform intersections.

The origin of ridge parallel tensile stresses at transform faults is unclear. Gudmundsson (1995) argued that thermoelastic stresses cannot account for the shallow transform-parallel tension fractures and normal faults observed at fracture zones, because model calculations show thermal stresses are zero at the surface, reaching a maximum at 4 kilometres depth (Turcotte, 1974). Alternatively, he suggested that the source of ridge parallel tensile stresses is the ridge perimeter increase resulting from the migration and expansion of ridges after continental break-up. The migration of ridges in a radial direction away from the region of their origin would also account for the general fanning of oceanic transform faults. However, the increase in the ridge perimeter may not necessarily produce significant ridge parallel tensile stresses, because it can be accommodated by the lengthening of the ridge segments, and by the development of lower order ridge discontinuities.

An alternative source of ridge parallel tensile stresses is proposed in this study. The topographic loading created by the subsidence of the seafloor away from ridges has never been included in models of stress at ridge transform and non-transform offsets. Such topographic loading may produce significant ridge parallel tensile stresses, and may explain the non-transform offsets of type (C) in Fig. 1.8, i.e. shear zones oblique at 45° relative to the strike of the ridge axis. These possibilities are analysed in chapter 6.

1.7 Microplates

Oceanic microplates are a type of ridge offset particularly of fast spreading systems. They are sites where two spreading ridge arms are separated by a tectonically independent region, hundreds of kilometres wide, showing evidence of independent motion from the surrounding major tectonic plates. Their formation is linked to rift propagation through thin lithosphere. A propagating rift occurs when one segment of a spreading centre at a ridge offset grows at the expense of the other (Hey et al., 1980). The failing rift is expected to take some time to cease spreading, during which an overlap region is formed between a dual spreading system. Microplates have been regarded as large scale overlap regions, arising because of the long time necessary for one spreading centre to slow and eventually fail, while the other propagates and gradually takes up all the spreading (Hey et al., 1985).

Many active microplates and palaeoplates (abandoned microplates) have been identified or proposed. Some examples are the Rivera microplate in the Gulf of California (McKenzie and Morgan, 1969), a continental microplate in the region of the Afar Triple Junction (Courtillot et al., 1980), the Galapagos microplate (Lonsdale, 1988), the Juan Fernandez microplate (Francheteau et al., 1987), the Bauer palaeoplate (Mammerickx et al., 1980), the Mathematician palaeoplate (Mammerickx et al., 1988), etc. The existence of palaeoplates suggests that microplates are a transient phenomenon. When one of the spreading segments fails the microplate is welded to one of the major plates, becoming a palaeoplate. Rift propagation and the formation of overlap systems, including microplates, provide therefore a mechanism of seafloor transfer from one plate to another, and are a process by which plate boundaries reorganise.

Among the active microplates, Easter and Juan Fernandez are some of the best studied (e.g. Hey et al., 1985, Searle et al., 1989, Larson et al., 1992, Rusby and Searle, 1995). They are remarkably similar (Fig. 1.9).

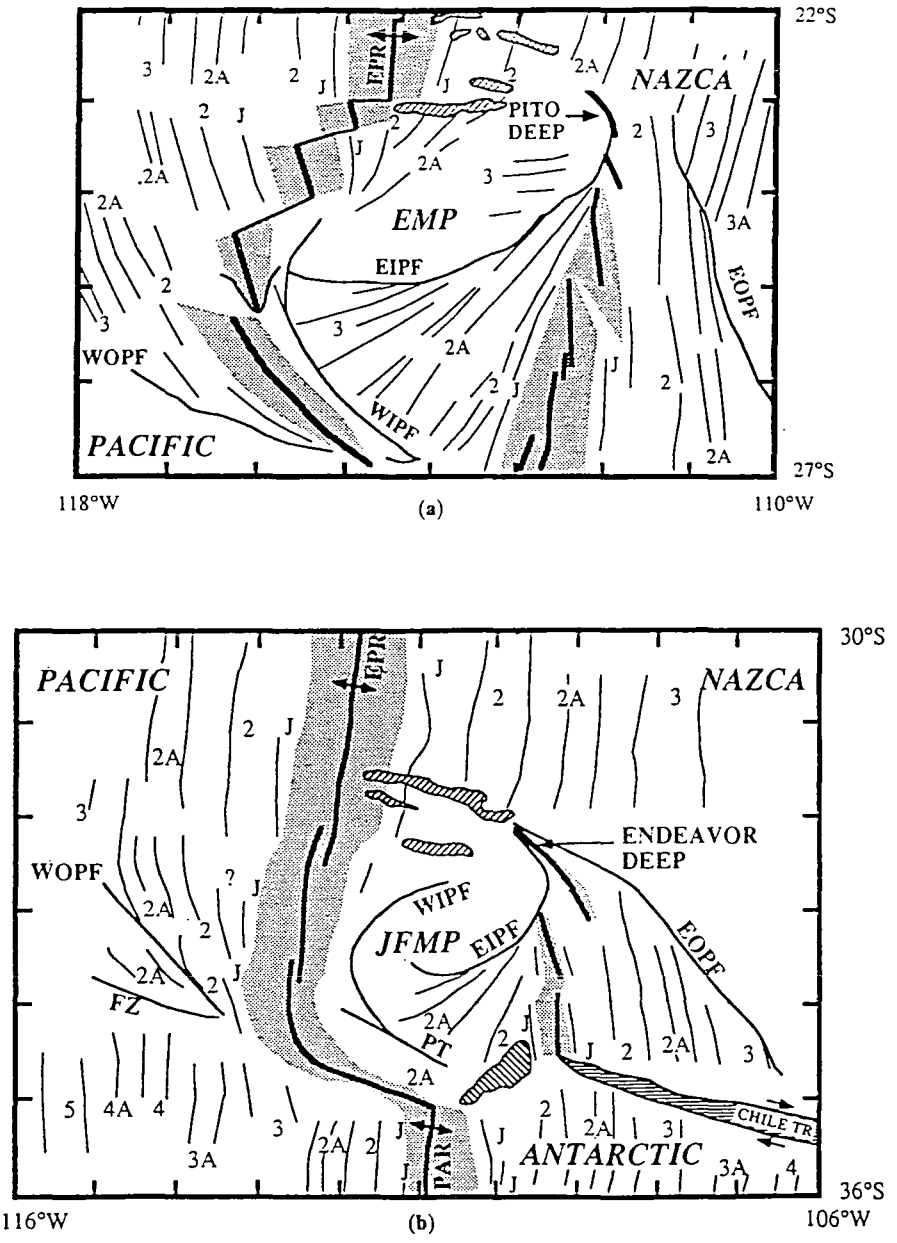

Fig. 1.9 Structures and isochrons of (**a**) Easter microplate (EMP) and (**b**) Juan Fernandez microplate (JFMP). Heavy lines indicate the spreading centres and medium lines are the pseudofaults (WOPF, WIPF, EOPF, EIPF are the western outer and inner and eastern outer and inner pseudofaults, respectively). Light lines and lettering are the magnetic isochrons. The stippled region represents the extent of the Brunhes anomaly. Diagonally hatched areas are the compressional ridges at the northern boundaries of the microplates, and complex structures of the JFMP-Antarctic boundary. Horizontal hatching is the Chile Transform. FZ indicates the inactive western limb of the Chile transform and PT is the part of Chile transform that has been inactivated by the growth of the Juan Fernandez microplate. EPR and PAR are the East Pacific Rise and Pacific-Antarctic Rise, respectively (after Searle et al., 1993).

As well as a correspondence in age and size the resemblance between Easter and Juan Fernandez microplates includes the existence in their interiors of fanned magnetic lineation patterns, a history of northwards propagation of the eastern ridge and southwards propagation of the western ridge, compressional ridges at the northern boundary and curved inner pseudofaults (which are traces of disrupted seafloor resulting from the propagation of rifting, and indicate the locus of past positions of the rift tip).

These similarities suggest that a general principle of evolution of microplates exists. According to it, microplates grow by rift propagation, and undergo two main stages of evolution. Initially they are deformed by internal shearing, perhaps by bookshelf faulting, and after reaching a critical size ($\sim$ 100 km) start to rotate rigidly (Searle et al., 1993). A model of rigid rotation is supported by most of Easter structural data (Engeln et al., 1988) and by the tectonic reconstruction of the history of the microplate, based on the interpretation of magnetic, bathymetric and GLORIA data (Rusby and Searle, 1995).

The dynamics of rift propagation has been investigated by Phipps Morgan and Parmentier (1985). They proposed a mechanical model in which the shallower of two ridge segments tends to propagate, in response to gravitational stresses concentrated at the rift tip. Their model can explain why most propagating rifts of the East Pacific Rise are migrating away from shallow sections of the ridge axis, but it is not consistent with the spawning of new spreading centres near overlapping spreading centres or within transform faults (e.g. Fornari et al., 1989; Bird and Naar, 1994). Other mechanisms for rift propagation have been proposed, but none can fully account for the migration of ridge discontinuities observed at the EPR (Cormier et al., 1996).

Although rift propagation is involved in the formation of microplates, its role on their dynamics has been underestimated. A kinematic model that predicts the rotation of microplates, known as the 'roller-bearing' model, has been successfully applied to the Galapagos, Easter and Juan Fernandez microplates (Schouten et al., 1993; Searle et al., 1993). However, this model ignores the contribution of rift

propagation to the driving mechanism of microplates, and has never been tested from a dynamic point of view. In chapter 7 Easter microplate is used as a 'type' example of microplate behaviour to analyse the dynamic implications of the 'roller-bearing' model.

1.8 The roller-bearing kinematic model

Schouten et al. (1993) presented a kinematic model, known as the roller-bearing model, that describes Easter microplate rotation (Fig. 1.10). According to this model the microplate rotates as a rigid block between plates moving in opposite directions. If the coupling between the microplate and the two bounding plates is perfect, two points at the boundaries, which are the instantaneous poles of rotation of the microplate relative to the main plates, are instantaneously fixed to the main plates. The basic postulate of this model is that the microplate is driven at the instantaneous points of contact by the drag of the main plates.

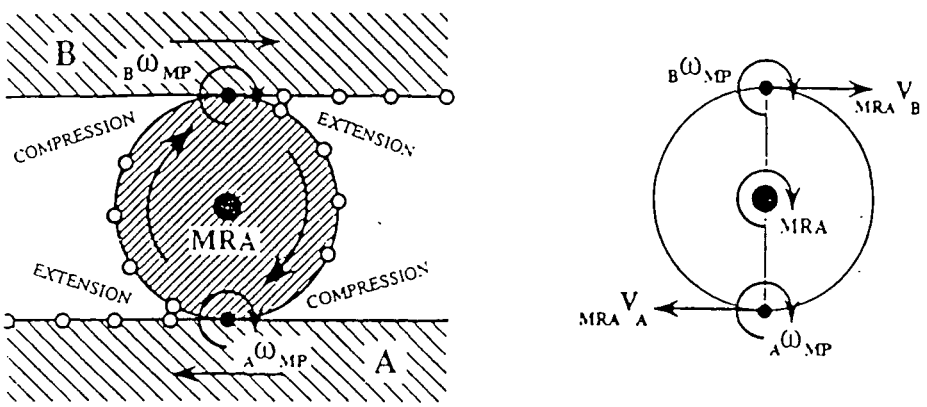

Fig. 1.10 The edge-driven kinematic model. A circular microplate resembling a circular gear rotates between two moving plates A and B. The microplate rotates with constant angular velocity (ω) about the microplate's rotation axis (MRA). The instantaneous relative rotation axes $_A\omega_{MP}$ and $_B\omega_{MP}$ (which describe the motion of the microplate relative to plates A and B) lie on the points of contact between the microplate and the driving plates. Relative to plates A and B these axes move with constant velocities $_{MRA}V_A$ and $_{MRA}V_B$. The traces (small circles in the diagrams) of the propagation of extension (pseudofaults) provide the trajectories of the instantaneous relative rotation axes (after Schouten et al., 1993).

The main difference between the roller-bearing model and previous edge-driven block models (e.g. McKenzie and Jackson, 1983) is that the points that pin the microplate to the major plates are not fixed but move along the microplate's margins. The pivots (or the instantaneous relative rotation poles) move with the tips of the propagating rifts. As a consequence the pseudofaults associated with the propagating rifts provide the trajectories of the microplate's instantaneous rotation axes relative to the bounding major plates.

If the coupling between the microplate and the major plates is not perfect then there is some slip along the boundaries of the microplate. In this case the instantaneous poles of rotation of the microplate relative to the main plates are not located along the microplate boundaries. As the amount of slip increases, the distance d between the Euler poles also increases, and as a consequence the rotation rate of the microplate, given by v/d where v is the spreading rate between the major plates, decreases (Fig. 1.11).

A more elaborate version of the roller-bearing model is that of an expanding gear where the distance between the propagating rift tips grows with time, implying the decreasing of the rotation rate with the growth of the microplate (Schouten et al., 1993). The rift propagation at large angles to the spreading direction produces inner pseudofaults that are not concentric to a common axis, but whose curvature increases with age, reflecting the decreasing rotation rate (e.g. EIPF, Fig. 1.9a).

The main aspects of the roller-bearing model apply to Easter (Searle et al., 1993). The present distance between the Euler poles (about 610 km) and the present rotation rate of $15° - 18°$/Ma, derived from the magnetic anomaly data (Naar and Hey, 1991; Rusby and Searle, 1995), is in excellent agreement with the relation derived in Fig. 1.11 (considering that the Pacific- Nazca spreading rate is about 160 mm/yr). The reasonable fit between the pseudofaults geometry and the model predictions constitutes another argument in favour of this kinematic model.

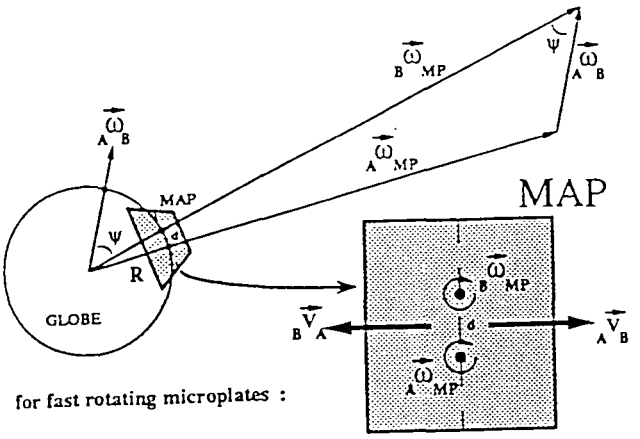

for fast rotating microplates :

$$ {}_A\vec{\omega}_{MP} = {}_B\vec{\omega}_{MP} >> {}_A\vec{\omega}_B \ , \quad d << R $$

$$ \frac{d}{R} \approx \frac{|\,{}_A\vec{\omega}_B\,| \sin\psi}{|\,{}_B\vec{\omega}_{MP}\,|} $$

$$ d \approx \frac{|\,{}_A\vec{\omega}_B\,| R \sin\psi}{|\,{}_B\vec{\omega}_{MP}\,|} \approx \frac{|\,{}_A\vec{V}_B\,|}{|\,{}_B\vec{\omega}_{MP}\,|} \approx \frac{|\,{}_A\vec{V}_B\,|}{|\,{}_A\vec{\omega}_{MP}\,|} $$

Fig. 1.11. Schematic diagram showing the relationship between the rotation rate of the microplate and the distance between the Euler poles. The angular velocity vectors ${}_A\omega_B$, ${}_A\omega_{MP}$, and ${}_B\omega_{MP}$ describe the motion of plate B relative to A, and of microplate MP relative to plates A and B, respectively. The length of these vectors is proportional to the angular velocity. The three vectors pierce the globe along the same great circle (dashed line on map projection). Because of the high angular velocity of microplate rotation, the microplate vectors ${}_A\omega_{MP}$ and ${}_B\omega_{MP}$ are almost the same length, and pierce the globe close together at a distance d. The major plates velocities ${}_AV_B$ and ${}_BV_A$ can be considered uniform across the map, because of the small dimensions of the microplate, and proximity of the microplate motion vectors (after Schouten et al., 1993).

Nevertheless, not all the features of the edge-driven model are supported by observations. For instance, the present instantaneous poles of Pacific-Easter and Nazca-Easter motion derived by Rusby and Searle (1995) lie 50 km away from the microplate boundaries and not actually on them. This implies there is some degree of decoupling between the microplate and the major plates. Also, the plate reconstructions show that the instantaneous poles of rotation have been fixed with respect to the main plates, and thus have not moved with the rift tips through time. This implies that the pseudofaults do not trace the trajectories of the Euler poles, but only the path of the propagating rift tips (Rusby and Searle, 1995).

1.9 The Pacific plate in the region of Easter microplate

The Easter microplate, located on the East Pacific Rise near 25°S, 114°W, limits a zone of asymmetric subsidence (Fig. 1.12). The microplate itself is at the centre of a broad region of anomalously shallow bathymetry (Mammerickx et al., 1980) and low shear wave velocities in the upper mantle (Woodhouse and Dziewonski, 1984). The shallow bathymetry and the low seismic velocities result from a broad thermal anomaly related to the Easter-Sala y Gomez Hotspot Chain to the east of Easter microplate, and the Tuamoto Hotspot Chain to the west of the microplate. The interaction between the hotspot related thermal anomaly and the mid-ocean ridge system suggests intensive mantle convection and a thin lithosphere in the region of Easter microplate (Hey et al., 1985).

At a larger scale, the whole region between the EPR and 160°W, and between 0°-40°S, is 250-1000 m shallower than predicted by empirical depth-age relations. It comprises a large number of hot-spots and associated island chains, and has been identified as the South Pacific Superswell (McNutt and Fischer, 1987). The origin, geophysical and geochemical characteristics of the South Pacific Superswell have been the subject of numerous studies, and have recently been summarised by McNutt (1998).

Some observations at the Superswell region, such as the low values of the elastic plate thickness and the high vulnerability of the lithosphere to midplate volcanism, led McNutt and Fischer (1987) to initially propose that the Superswell was the result of an anomalously thin lithosphere. But when satellite altimetry data revealed that a strong geoid anomaly low existed over the centre of the Superswell this explanation was regarded as insufficient, because any shallow isostatic compensation of the anomalous uplift should lead to a geoid high instead.

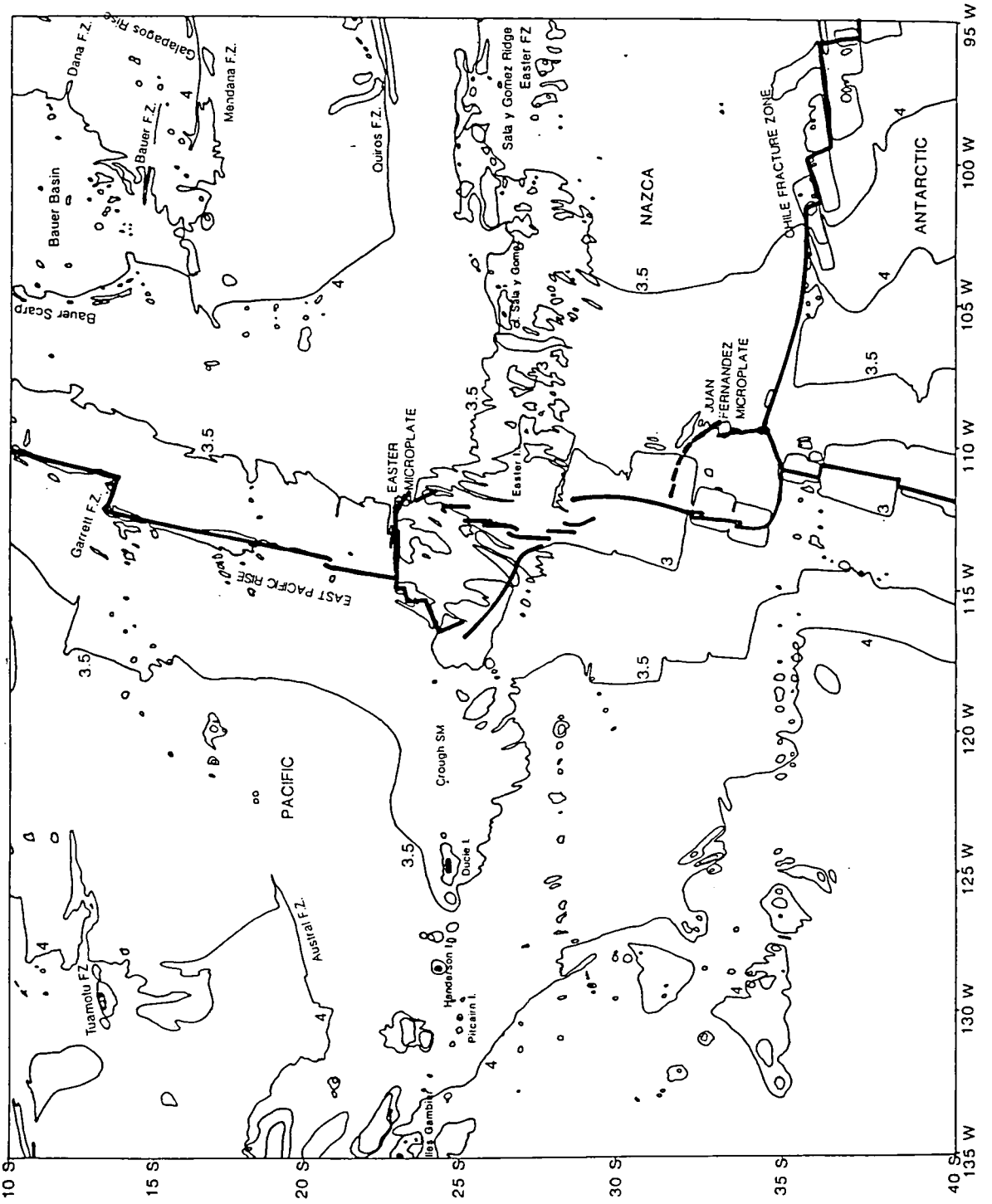

Fig. 1.12 Map of the Easter microplate region, in the southeast Pacific. Heavy lines represent plate boundaries. Bathymetric contours are from GEBCO chart 5.11 and are labelled in km (after Rusby and Searle, 1995). The asymmetric subsidence to the north of Easter microplate is clearly shown by the 3.5 km isobath.

McNutt and Judge (1990) and McNutt (1998) suggested an alternative explanation involving a broad, low density upwelling in the upper mantle compensated by uplift of both the surface and the core-mantle boundary. The positive geoid anomaly arising from the upwarp of the core-mantle boundary should be undetected at the wavelengths corresponding to the size of the Superswell, and therefore the mass deficit resultant from the mantle upwelling should dominate the geoid signal.

A substantial thinning of the lithosphere over the Superswell is also not supported by heat flow measurements, because the average heat flow over the Superswell is similar to that over other Pacific regions (McNutt, 1998). Nevertheless, seismic experiments support the existence of an anomalously hot layer beneath the lithosphere in the Superswell region (Nishimura and Forsyth, 1985; Su et al., 1992 in McNutt, 1998). Slow shear wave velocities are concentrated in the upper mantle, but extend from the surface down to 450 km. Assuming that the shear wave velocity anomalies arise only from temperature variations in the upper mantle, the thermal anomalies beneath the Superswell are estimated to range from −20°C to +40°C (McNutt, 1998).

In contrast with the central region of the Superswell, over the East Pacific Rise the geoid anomaly is strongly positive, specially between 10°S and 20°S. At approximately these latitudes the free air anomaly indicates that the lithosphere within 150 km of the East Pacific Rise is isostatically compensated (e.g. Eberle et al., 1998). This means that the surface mass excess responsible for the geoid anomaly high near the East Pacific Rise overlies a subsurface mass deficit of equal magnitude.

1.10 Previous work on the asymmetric subsidence of the East Pacific Rise near 20°S

The most specific work on the asymmetric subsidence of the EPR, between approximately 9°S and 22°S, has been carried out by Cochran (1986). He restricted his analysis of bathymetric profiles to distances within 300 to 500 km from the ridge

crest, corresponding to lithospheric ages up to 5 Ma, to avoid areas of intraplate volcanism and hot spot swells. He also excluded from his study the region of Easter microplate due to its complex bathymetry, but the determination of the subsidence rates between 30.5°S and 31.5°S lead him to conclude that the anomalous subsidence does not extend south of Easter microplate.

Cochran (1986) calculated the average subsidence rates for latitude intervals and for lithospheric age intervals. Between the Garret fracture zone at 13°S, and the Easter microplate at 22°S, he calculated an average subsidence rate between 0 and 5 Ma of 198 m $Ma^{-1/2}$ on the west of the EPR and 356 m $Ma^{-1/2}$ on the east (Fig. 1.13). Using a limited set of bathymetric profiles between 18°S and 21°S, extending to lithosphere 12 Ma old, he concluded that the asymmetric subsidence rate continues to at least 12 Ma old lithosphere.

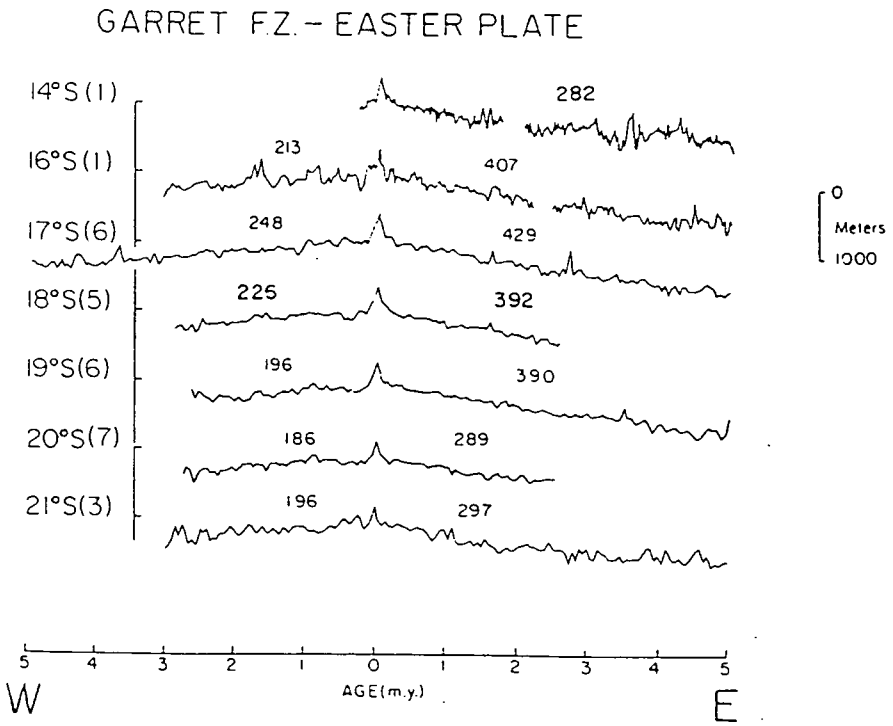

Fig. 1.13 Bathymetric profiles across the East Pacific Rise formed by averaging profiles within 1° latitude bands. Latitude to the left of profile indicates northern end of band and number in parentheses shows the number of profiles combined. Best fitting value of subsidence (in m $Ma^{-1/2}$) is given over each profile. Dashes to the left of each profile show 3000 m depth (after Cochran, 1986).

The asymmetric subsidence near 20°S had already be noted by Rea (1978). He suggested that it could be due to a discrete off-ridge heat source beneath the West flank of the EPR. Cochran (1986) disputed this idea because the asymmetric subsidence begins right at the ridge crest (it is visible in the bathymetric profiles for ages less than 1 Ma), implying that it must be the result of a process extending to the ridge crest, and not of any off-ridge disturbance.

Cochran (1986) proposed that the asymmetric subsidence is due to a lateral gradient in the asthenosphere temperature. That temperature gradient in the asthenosphere has two main effects upon the subsidence rate. One is a thermal effect, due to the expansion of the lithosphere when heated from below. The other is an isostatic effect, due to the density variations in the asthenosphere which result from the temperature variations.

Assuming that the thermal expansion of the lithosphere can be approximated by the thermal expansion of a half-space having a time dependent surface boundary condition, Cochran (1986) estimated that the elevation produced by the thermal effect was only about 6% of the observed subsidence. He concluded that the asymmetric subsidence is mainly an isostatic effect.

The isostatic effect is computed by balancing mass columns between the sea surface and the compensation depth. For an average spreading velocity of 80 mm/yr and a depth of compensation of 150 km, the observed subsidence rate on the western flank of the EPR could be explained by a lateral temperature gradient of 0.1°C/km starting right at the ridge crest. Alternatively the observed subsidence rate could also be explained by a lateral temperature gradient of 0.06°C/km starting at 5 Ma to the east of the EPR, superimposed on a symmetric subsidence rate of 300 $mMa^{-1/2}$ (Cochran, 1986).

Another modelling study in an area of 250 km adjacent to the East Pacific Rise (in the Pacific plate) between 18°S and 21°S indicates upper mantle thermal anomalies of about 65°C (Cormier et al., 1995). In the northern part of that study area, anomalously abundant seamount production, anomalously shallow bathymetry and enhanced axial magmatic budget are correlated with a regional gradient in

the free air gravity residual anomaly. Assuming the existence of mantle thermal anomalies between 20 and 150 km depth, Cormier et al. (1995) found that the gravity gradient could be explained by a mantle temperature gradient of 0.26°C/km. In the southern part of study area, a mantle temperature gradient of 0.14°C/km was inferred.

The above studies suggest that it is reasonable to assume that a temperature gradient in the upper mantle is the cause for the anomalously shallow depths on the western flank of the East Pacific Rise. How the upper mantle thermal anomaly and associated anomalous subsidence are related to the stress in the lithosphere is the question addressed in Chapter 4. Modelling the anomalous subsidence of the East Pacific Rise offers insights into the intraplate stress in the region of Easter microplate, and provides a framework for the local near-ridge phenomena analysed in other chapters.

1.11 Aims and structure of this dissertation

The aim of modelling the lithospheric stress is either to infer the mechanical properties of the geological structures or to determine the forces acting on them. To achieve this objective the modelling results must fit the observations, in particular the stress indicators. Chapter 2 includes the description of the stress indicators at each location of study. It also gives a review of the most important definitions and sources of stress in the lithosphere.

The finite element method is used to model the stress. In this method a geological structure is represented by a numerical grid with specified rheological properties. Boundary and/or body forces are applied to the grid, and the resultant stress field calculated numerically by solving the dynamic equations of equilibrium. Chapter 3 gives an outline of the rheologies and of the finite element techniques that are used in this thesis.

Chapter 4 models the lithospheric stress produced by a mid-ocean ridge on the adjacent plates. Its principal objective is to investigate if the thermal anomaly in

the asthenosphere responsible for the asymmetric subsidence of the East Pacific Rise can explain any of the stress observations in the region of Easter microplate.

The response of normal faults to tectonic extension in the vicinity of mid-ocean ridges is analysed in chapter 5. A realistic (elasto-plastic) rheological model is used to investigate the role of plasticity, brittle plate thickness, fault dip angle, and loading by volcanic infill on the evolution of normal faults at mid-ocean ridges.

Chapter 6 presents a formulation that allows the inclusion of the effect of topography on two-dimensional horizontal models of stress. The chapter focuses on the topographic load created by the subsidence of the seafloor away from mid-ocean ridges, and investigates if this loading can account for the observations at mid-ocean ridge offsets, in particular the well known curvature of normal faults at ridge-transform intersections and non-transform offsets.

The aims of chapter 7 are to examine if the roller-bearing kinematic model for microplate rotation is viable from a dynamic point of view, and to determine what combination of forces best fits the stress indicators at Easter microplate. The relative magnitude of the plate boundary forces governing Easter rotation is estimated by assuming that the microplate is in mechanical equilibrium.

Chapter 8 brings together the results of the previous modelling chapters, suggests further areas of research, and lists the overall conclusions.

Chapter 2

Lithospheric stress

2.1 Introduction

Forsyth and Uyeda (1975) were among the first to define the set of plate boundary forces acting on the lithosphere, and assess their relative importance by balancing the torque of forces acting on each plate. The set of main plate boundary forces includes the ridge push, the slab pull, resisting forces at subduction zones, the trench suction, the continental collisional resistance and the basal drag. Among the large scale plate boundary forces, the more important in the oceanic lithosphere, away from subduction zones, are the ridge push and possibly the basal drag. Because this study focusses on several regions of the young oceanic lithosphere, particular attention is given to the basal drag (section 2.5.1) and the ridge push (section 2.5.2) forces.

The observed correlation between the direction of maximum horizontal stress and the direction of absolute plate motions suggests that the plate boundary forces that govern plate motions are also responsible for the first order pattern of stress (e.g. Zoback, 1992). As a result a number of two-dimensional modelling efforts, including global (e.g. Solomon et al., 1975; Richardson et al., 1979) and single plate studies (e.g. Cloetingh and Wortel, 1986; Richardson and Reding, 1991; Wortel et al., 1991), have made use of the intraplate stress pattern to constrain the tectonic forces.

Like most of these modelling efforts, I use the finite element method to predict the stress pattern and constrain the tectonic forces. My models of stress at mid-ocean ridge offsets (chapter 6) and of Easter microplate dynamics (chapter 7) are also 2D and horizontal, but their scale is substantially smaller than the scale of the global and single plate models mentioned above. At small scales local perturbations to the first order stress pattern become important. Such local perturbations may arise from a variety of sources, such as for instance the ridge resistance (section 2.5.3) and the transform resistance (section 2.5.4). Other local sources of stress are referred to in section 2.6.

In addition to an introduction to the plate boundary forces, this chapter gives a description of the stress indicators in the young oceanic lithosphere, in particular at ridge offsets and at the Easter microplate. It starts with a review of the main definitions of lithospheric stress.

2.2 Definitions of stress

Stress is force per unit area. Stresses that act perpendicular to a surface are normal stresses. Those that act parallel to a surface are shear stresses. The state of stress at any point in a material is defined by the six independent components of stress (e.g. Jaeger, 1969),

$$\sigma_{xx},\ \sigma_{yy},\ \sigma_{zz},\ \tau_{xy} = \tau_{yx},\ \tau_{xz} = \tau_{zx},\ \tau_{yz} = \tau_{zy}. \tag{2.1}$$

Above σ_{xx}, σ_{yy} and σ_{zz} are the normal stresses across three orthogonal planes defined in a Cartesian x,y,z co-ordinate system. τ_{xy}, τ_{xz} and τ_{yz} are the shear stresses acting on those planes. The first index denotes the direction of the normal to the plane and the second index denotes the direction in which the component of stress acts.

Normal stresses can be tensile or compressive. A tensile stress is a surface force per unit area that tends to pull the material on one side of the surface away from that on the other side. A compressive stress tends to press the material on one side

of the surface against that on the other side. Here I use the convention followed in the geological literature in which tensile stresses are negative and compressive stresses are positive.

Three orthogonal axes can always be chosen such that all the shear components of stress are zero. These are the principal axes of stress. The normal stresses acting on planes perpendicular to these axis are called the *principal stresses*, and are usually denoted as σ_1, σ_2 and σ_3. By convention,

$$\sigma_1 \geq \sigma_2 \geq \sigma_3, \tag{2.2}$$

so that σ_1 is the maximum principal stress and σ_3 is the minimum principal stress.

When $\sigma_1 = \sigma_2 = \sigma_3$ the state of stress is *isotropic*. In such case there are no shear stresses in any coordinate system, i.e.

$$\sigma_{xx} = \sigma_{yy} = \sigma_{zz} = \sigma_1 = \sigma_2 = \sigma_3, \tag{2.3}$$

and any set of orthogonal axes is a set of principal axes.

The *pressure* is invariant to the choice of the coordinate system and is defined as the mean normal stress,

$$\begin{aligned} P &= \frac{\sigma_{xx} + \sigma_{yy} + \sigma_{zz}}{3} \\ &= \frac{\sigma_1 + \sigma_2 + \sigma_3}{3}. \end{aligned} \tag{2.4}$$

In geodynamic applications it is useful to express the normal stress as the sum of an isotropic and deviatoric part. The isotropic part is the pressure. The deviatoric part represents the non-hydrostatic part of the stress system. In any coordinate system the *deviatoric stresses* are defined as

$$\begin{aligned} \sigma^D_{xx} &= \sigma_{xx} - P, & \tau^D_{xy} &= \tau_{xy}, \\ \sigma^D_{yy} &= \sigma_{yy} - P, & \tau^D_{xz} &= \tau_{xz}, \\ \sigma^D_{zz} &= \sigma_{zz} - P, & \tau^D_{yz} &= \tau_{yz}. \end{aligned} \tag{2.5}$$

Similarly, in the principal axis coordinate system the *deviatoric principal stresses* are defined as

$$\begin{aligned} \sigma_1^D &= \sigma_1 - P, \\ \sigma_2^D &= \sigma_2 - P, \\ \sigma_3^D &= \sigma_3 - P. \end{aligned} \tag{2.6}$$

Deviatoric stresses may be related to permanent deformation and are important in problems involving yielding and flow (e.g. Ranalli, 1995).

In the earth the normal stress due to the weight of the overlying rock, or overburden, is known as *lithostatic stress.* Choosing a coordinate system in which the z axis is vertical, has origin on the surface and points downwards, the lithostatic stress is

$$\sigma_{zz} = \int_0^z \rho g dz, \tag{2.7}$$

where ρ is the density of the overlying rock, g is the acceleration of gravity and z is the depth beneath the surface. The *lithostatic state of stress* is an idealisation in which the three components of normal stress are all equal to the lithostatic stress, i.e.

$$\sigma_{xx}^L = \sigma_{yy}^L = \sigma_{zz}^L = \sigma_1 = \sigma_2 = \sigma_3 = \int_0^z \rho g dz. \tag{2.8}$$

"The lithostatic state of stress is equivalent to the hydrostatic state of stress in a motionless body of fluid wherein pressure forces are exerted equally in all directions and pressure increases proportionally with depth" (Turcotte and Schubert, 1982).

Like the resolution of stress into isotropic and deviatoric components, it is often useful to consider the actual state of stress in the earth as the sum of a lithostatic and a *non-lithostatic* state of stress. The non-lithostatic state of stress is due to sources of stress in the lithosphere such as the plate boundary forces, and always needs to be referenced to a standard density-depth profile. The non-lithostatic components of stress are represented as $\Delta\sigma_{xx}$, $\Delta\sigma_{yy}$, $\Delta\sigma_{zz}$, $\Delta\tau_{xy}$, $\Delta\tau_{xz}$ and $\Delta\tau_{yz}$.

According to these definitions the *actual state of stress* in the lithosphere is described as

$$\begin{aligned}
\sigma_{xx} &= \sigma_{xx}^{L} + \Delta\sigma_{xx}, \qquad \tau_{xy} = \Delta\tau_{xy}, \\
\sigma_{yy} &= \sigma_{yy}^{L} + \Delta\sigma_{yy}, \qquad \tau_{xz} = \Delta\tau_{xz}, \\
\sigma_{zz} &= \sigma_{zz}^{L} + \Delta\sigma_{zz}, \qquad \tau_{yz} = \Delta\tau_{yz}.
\end{aligned} \tag{2.9}$$

The non-lithostatic stress is sometimes refereed as the *tectonic* stress, although the term tectonic stress is particularly used when the principal stresses are horizontal and vertical. Some authors wrongly use the designation tectonic stress and deviatoric stress without distinction. I always distinguish between the terms tectonic and deviatoric. This is because in my modelling the lithostatic contribution is always ignored, and the non-lithostatic stress is made up of an isotropic and a deviatoric component.

Why do I ignore the lithostatic contribution? My models are two-dimensional and use either the assumptions of plane strain or plane stress. Under the assumption of plane stress the out-of-plane stress is zero. Under the assumption of plane strain the out-of-plane strain is zero and the out-of-plane stress is the sum of the in-plane stresses multiplied by Poisson's ratio. In both cases, to include the lithostatic stress in the modelling gives rise to unrealistic high stress differences between the principal stress components. These high stress differences exceed the strength of most rocks, and make impracticable the use of failure criteria.

The non-lithostatic stress is separated into an isotropic and deviatoric part because the deviatoric component is more directly related to viscous and plastic deformation and to elastic bending. The *deviatoric non-lithostatic stresses* are defined as the actual non- lithostatic stresses less the non-lithostatic pressure,

$$\begin{aligned}
\Delta\sigma_{xx}^{D} &= \Delta\sigma_{xx} - (\Delta\sigma_{xx} + \Delta\sigma_{yy} + \Delta\sigma_{zz})/3, \\
\Delta\sigma_{yy}^{D} &= \Delta\sigma_{yy} - (\Delta\sigma_{xx} + \Delta\sigma_{yy} + \Delta\sigma_{zz})/3, \\
\Delta\sigma_{zz}^{D} &= \Delta\sigma_{zz} - (\Delta\sigma_{xx} + \Delta\sigma_{yy} + \Delta\sigma_{zz})/3,
\end{aligned} \tag{2.10}$$

$$\begin{aligned}\Delta\tau_{xy}^{D} &= \Delta\tau_{xy},\\ \Delta\tau_{xz}^{D} &= \Delta\tau_{xz},\\ \Delta\tau_{yz}^{D} &= \Delta\tau_{yz}.\end{aligned} \tag{2.11}$$

The deviatoric non-lithostatic stresses are equal to the actual deviatoric stresses of Eq. 2.5.

In this study, stresses are referred to the principal axes of stress. The term principal stresses refers to principal non-lithostatic stresses, and deviatoric stresses refer to deviatoric principal non-lithostatic stresses.

2.3 Relation between stress and faulting

Brittle failure gives raise to faulting and earthquakes in the upper lithosphere. Anderson's theory of faulting is used to relate the principal stress directions in the lithosphere, assumed to be approximately horizontal and vertical, with the focal mechanisms of earthquakes and the structural observations. According to this theory the relation between the principal tectonic stresses and the fault regimes are as follows (considering compressional stresses positive),

$$\begin{aligned}\text{Normal faults} &: \quad \sigma_{vertical} > \sigma_{horizontal(1)} > \sigma_{horizontal(2)},\\ \text{Thrust faults} &: \quad \sigma_{horizontal(2)} > \sigma_{horizontal(1)} > \sigma_{vertical},\\ \text{Strike-slip faults} &: \quad \sigma_{horizontal(2)} > \sigma_{vertical} > \sigma_{horizontal(1)}.\end{aligned} \tag{2.12}$$

In each case the intermediate stress lies in the fault plane.

Consider a horizontal plane under the plane stress assumption. In this case the vertical stresses are zero and the relation between the tectonic stresses and the fault regimes is simply: (1) if both horizontal principal tectonic stresses are negative there is a normal fault regime; (2) if both horizontal principal tectonic stresses are positive there is a thrust fault regime and (3) if one of the horizontal principal tectonic stresses is positive and the other one is negative there is a strike-slip fault regime.

Consider a vertical plane under the plane strain assumption. If the out of plane stress is the intermediate stress (horizontal (1) in equation 2.12) then there can only be a normal fault or a thrust fault regime.

2.4 Stress indicators in the lithosphere

The most important indicators of stress in the lithosphere are earthquake focal mechanisms, directions of fault slip, volcanic alignments, well bore breakouts, and in situ stress measurements (hydraulic fracturing and overcoring). These types of stress indicators constitute the database of the World Stress Map Project (WSM), whose first aim is to characterise the state of stress within plates (Zoback, 1992). The stress indicators in the database are classified according to a quality ranking scheme, based on criteria such as the accuracy of measurements, depth interval and volume of rock sampled, number of determinations, and general reliability of the method.

In the oceanic lithosphere, where in situ stress measurements and rock sampling are hard to perform, the most common stress indicators are earthquake focal mechanisms. The type and trend of tectonic structures observed in bathymetric and side-scan sonar maps are also often used as stress indicators.

Earthquake focal mechanisms provide information on the stress regime and relative magnitudes of principal stress. Most are not good stress indicators because the P (maximum compression) and T (minimum compression) axis of individual earthquakes may significantly differ from the actual stress orientations (e.g. McKenzie, 1969). The mean directions of several close earthquakes are better indicators since they agree well with regional stresses inferred from independent data (e.g. Michael, 1987). In the WSM database, larger earthquakes are assigned higher quality ranks, because large earthquakes generally present better constrained focal mechanisms.

Maybe the most important characteristic of the stress field in the lithosphere is that principal stresses lie approximately in vertical and horizontal planes (Anderson,

1951). Fault planes observed in the field or inferred from earthquakes, the attitude of dykes and deep in situ stress measurements are some of the evidence supporting this finding.

When plotted at a global scale, the stress indicators of the WSM database show a first order pattern of stress, mainly characterised by (Zoback, 1992):

- Broad regions (over distances of up to 5000 km) of uniformly oriented horizontal stresses within plate interiors.

  Plate interiors dominated by compression, i.e. by thrust and strike-slip regimes in which the maximum principal stress is horizontal.

- Active extensional tectonics, i.e. normal fault regimes in which the maximum principal stress is vertical, associated with topographically elevated areas.

- A strong correlation between directions of maximum horizontal stress and absolute plate motions.

Local perturbations of the first order pattern of stress happen at a variety of scales and are due to a variety of sources. The sources of the first order stress field and of its local perturbations are analysed in the following sections.

2.5 Plate boundary forces at oceanic plates

The horizontal tectonic force is defined as the stress difference $\sigma_{xx} - \sigma_{zz}$ integrated with respect to the depth, z, across the lithosphere thickness, L, i.e.

$$F_{xx} = \int_0^L (\sigma_{xx} - \sigma_{zz}) dz \tag{2.13}$$

Plate boundaries are zones of weakness, due to the upwelling of hot material at mid-ocean ridges or due to the presence of weak faults at subduction zones and transforms. Zones of weakness cannot withstand large deviatoric stresses, and are

characterised by nearly equal vertical and horizontal normal stresses. Consequently at plate boundaries the tectonic force is zero.

Different depth-density profiles at the edges of oceanic plates arise mainly because of lithospheric plate cooling with age. The actual integrated horizontal pressure (the force per unit length perpendicular to the vertical section) is greater at mid-ocean ridges than at subduction zones, and it is this imbalance in edge forces that drives the oceanic plates.

Plate boundary forces have always to be referenced to a standard depth-density distribution, for the same reason non-lithostatic stress is always referenced to a standard situation without applied loads. Otherwise very high stress values would be attained.

2.5.1 The basal drag force

The motion of the lithosphere with respect to the asthenosphere implies the existence of viscous shear tractions at the base of the lithosphere. The plate boundary force that results from these shear tractions is known as the basal drag. The magnitude of the basal drag depends on the lithospheric plate velocity relative to the base of the asthenosphere and on the asthenosphere viscosity.

There is still no consensus as to whether the basal drag drives or resists the motion of lithospheric plates. If it drives the plates, then the velocity of the mantle flow at the top of the asthenosphere should be aligned with the absolute plate motion directions. The same should happen with the stresses generated within the lithosphere by the basal drag.

Early models of mantle convection including large scale convection cells can hardly account for the movement of small plates, or explain how cells of simple geometry could drive plates with irregular margins. More recent models of large scale mantle convection driven by mass heterogeneities have been used to impart shear stresses at the base of the lithosphere, and subsequently compute the lithospheric stress (e.g. Wuming et al., 1992). To date these models have been inconclusive due

to their poor resolution, so that it is not yet possible to use them to confirm or disregard the hypothesis of a driving basal drag.

Numerical plate stress models provide contrasting answers to this problem. While most models show that a resisting basal drag force improves the fit between the calculated and the observed stresses (e.g. Forsyth and Uyeda, 1975; Richardson et al., 1979; Wortel et al., 1991), others suggest that a driving basal drag force may be important (e.g. Meijer and Wortel, 1992). Still other models indicate that the basal drag is too small to influence plate motions, so that it does not matter if it is a driving or resisting force (e.g. Wang et al., 1997).

Nevertheless, several arguments favour the hypothesis of a resisting basal drag. The low viscosity of the asthenosphere implies a weak effective coupling between the lithosphere and the asthenosphere. Consequently, to propel the plates the asthenosphere would have to move much faster than the plates. Since hotspots are believed to originate from mantle plumes rising from the lower mantle, the existence of large velocities in the asthenosphere is hard to reconcile with the lack of relative motion between the hot-spots around the world. Also, the driving basal drag hypothesis is unlikely from a thermodynamic point of view, because the high strain rates in the asthenosphere imply an amount of viscous dissipation that exceeds the heat transport through the mantle (Bott, 1982). Furthermore, plates with the largest areas of continental lithosphere have the lowest absolute velocities, supporting the idea that the resisting basal drag is larger beneath stable continents (arguably with the deepest 'keels' and greatest coupling to asthenosphere) than beneath oceans.

Richardson et al. (1979) gave one of the first (and to date most used) estimates of the magnitude of the basal drag force. They assumed the basal drag opposed the absolute plate motions, and that its magnitude per unit of area of the plate, F_D, was proportional to a drag coefficient D and to the absolute plate velocity V,

$$F_D = -DV. \tag{2.14}$$

The drag coefficient beneath the continents could be different from that beneath the oceans, and could vary spatially with the age of the plate. Richardson et al (1979)

chose values of D in order to produce basal shear stresses of 0.1 MPa for a plate velocity of 10 mm/yr. Increasing the drag coefficient and the basal shear stresses degraded the fit between the calculated and the observed stresses.

Subsequent numerical models of plate boundary forces also indicate basal shear stress magnitudes of the order of $10^{-1} - 10^{-2}$ MPa (e.g. Richardson and Reding, 1991; Wortel et al., 1991). Relatively higher magnitudes of basal shear stresses, though not over 1 MPa, are predicted in the vicinity of mid-ocean ridges (Bott, 1991).

2.5.2 The ridge push force

The ridge push is probably the main source of intraplate tectonic stress in the oceanic lithosphere. It results from the lateral density variations associated with lithosphere plate cooling.

It has long been recognised that lateral variation in the density distribution, of either thermal or lithological origin, are an important source of lithospheric stress. Artyushkov (1973) was one of the first to show that topography and its compensation at depth can generate stresses capable of influencing the tectonic style. Fleitout and Froidevaux (1982) showed that long-wavelength density heterogeneities within the lithosphere (i.e. density heterogeneities whose lateral extent is large with respect to the thickness of the lithosphere) produce a vertical stress proportional to the first moment of the density anomaly, and are fully compensated by topography. The application of this result to the oceanic lithosphere implies that in the absence of basal drag the horizontal tectonic force (the ridge push force) is proportional to the first moment of the density anomaly (Fleitout and Froidevaux, 1983).

The ridge push has also been derived as the net force resultant from boundary forces applied at the edges of an oceanic plate (Lister, 1975; Parsons and Richter, 1980; Dahlen, 1981). Both approaches are equivalent, and lead to the result that the ridge push force is proportional to the first moment of the anomalous density variation associated with lithospheric plate cooling.

To evaluate the tectonic force in the oceanic lithosphere due to the ridge push, I follow the theory developed by Bott (private communication). The objective is to evaluate the horizontal tectonic force acting on the two dimensional section of the oceanic lithosphere (Fig. 2.1), between R (the ridge) and P (an arbitrary point), and between the depths $z = 0$ (the elevation of the ridge crest) and $z = D$ (the compensation depth).

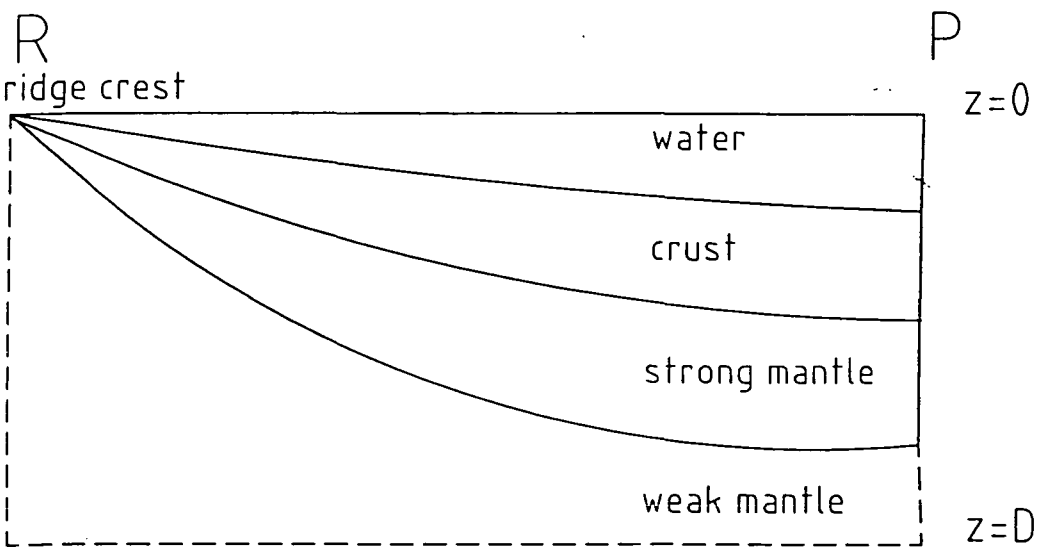

Fig. 2.1 Schematic geometry used to derive the ridge push, showing a vertical section of the lithosphere between the ridge crest (R) and an arbitrary point (P). The density of the lithosphere is $\rho_r(z)$ at the ridge crest, and is $\rho(z)$ at point P. The elevation of the ridge crest corresponds to z=0 and the compensation depth is at z=D.

The following assumptions are made:

- The density is laterally uniform above $z = 0$ and below $z = D$.
- There is simple local isostatic equilibrium, i.e. $\int_0^D g\rho dz = constant$, where ρ is the density, and includes a water layer.

- Beneath the ridge crest we assume that $\sigma_{xx}=\sigma_{zz}$ at all depths, i.e. there are no stress differences as it is weak and no ridge resistance occurs. Thus,

$$\int_0^D \sigma_{xx} dz = \int_0^D \sigma_{zz} dz = \int_0^D \left[\int_0^z g\rho_r dh\right] dz, \tag{2.15}$$

  where $\rho_r(z)$ is the density at the ridge crest and h is a dummy variable. Consequently, at the ridge crest the tectonic force $\int_0^D(\sigma_{xx} - \sigma_{zz})dz = 0$.

- No horizontally acting drag force acts at depth D.

The tectonic force at P is,

$$F_P = \int_0^D (\sigma_{xx} - \sigma_{zz})dz. \tag{2.16}$$

But the condition of equilibrium implies that the horizontal force at P $\left[\int_0^D \sigma_{xx}dz\right]_P$ must equal the horizontal force at the ridge crest $\left[\int_0^D \sigma_{xx}dz\right]_R$. Thus, from Eq. 2.15 we have $\left[\int_0^D \sigma_{xx}dz\right]_P = \int_0^D \left[\int_0^z g\rho_r dh\right] dz$. Hence,

$$F_P = \int_0^D \left[\int_0^z g\rho_r dh\right] dz - \int_0^D \left[\int_0^z g\rho dh\right] dz, \tag{2.17}$$

where $\rho(z)$ is the density at depth z below P. Putting $\Delta\rho = \rho - \rho_r$ in Eq. 2.17 gives,

$$F_P = -\int_0^D \left[\int_0^z g\Delta\rho dh\right] dz. \tag{2.18}$$

Integrating by parts, putting $u = \int_0^z g\Delta\rho dh$ and $v = z$ gives,

$$\begin{aligned} F_P &= -\left[z\int_0^z g\Delta\rho dh\right]_0^D + \int_0^D g\Delta\rho z dz \\ &= -D\int_0^D g\Delta\rho dh + \int_0^D g\Delta\rho z dz. \end{aligned} \tag{2.19}$$

But the condition of isostasy implies that $\int_0^D g\Delta\rho dh = 0$, and therefore,

$$F_P = \int_0^D g\Delta\rho z dz. \tag{2.20}$$

This gives the horizontal tectonic force at P, which is also the force needed to support the push exerted by the ridge, i.e. the ridge push. This derivation incorporates the concentration of tectonic stress in the upper strong parts of the lithosphere, as the water and ductile mantle may not be able to bear stress differences. Kusznir (1991) demonstrated that the tectonic stress produced by the ridge push is concentrated in the shallow competent layers of the lithosphere, decreasing to zero at the lithosphere asthenosphere interface.

The ridge push is usually referenced to the standard depth-density profile of old seafloor (e.g. 70 Ma). In young oceanic lithosphere the ridge push is negligible, even where there is an hotspot close to the ridge axis (Bott, 1991), as happens for instance along the East Pacific rise at the latitude of Easter. The ridge push increases linearly with age at an approximate rate of 3.6×10^{10} N/m per Ma (Parsons and Richter, 1980). For ages greater than 40 Ma different values of the ridge push are predicted by different thermal models. Nevertheless, for lithosphere 80-100 Ma there is good agreement that the ridge push is between 2.0×10^{12} N/m and 3.6×10^{12} N/m (Lister, 1975; Dahlen, 1981; Fleitout and Froidevaux, 1983).

2.5.3 The ridge resistance

The ridge resistance is a local plate boundary force that explains the tectonic extension observed at mid-ocean ridges. It arises from a stress deficiency at the ridge axis relative to the lithostatic state of stress of the nearby lithosphere. It can be viewed as a pressure deficiency in a viscous fluid that rises passively between diverging lithospheric plates (Lachenbruch and Thompson, 1972).

Lachenbruch (1973) proposed a model for oceanic spreading centres that, although an oversimplification, allows one to estimate the magnitude of the ridge resistance force. In the model it is assumed that there is a vertical conduit at the ridge axis where viscous material rises up. The rising is passive in the sense that it results from the difference in density between the material inside the conduit and the material of the surrounding lithosphere. The rising process is assumed to be steady,

implying that the conduit walls accrete at the same rate as the plates spread. These simple boundary conditions allow the discussion of the energetics of the conduit in terms of the mean specific weight of the conduit material (γ), the mean specific weight of the adjacent lithosphere (γ^*) and the conduit height (H) assumed to be equal to the lithospheric thickness.

When there is a deficit in pressure inside the conduit relative to the lithostatic pressure of the adjacent lithosphere, a net tectonic tensile stress develops in the conduit, resisting plate separation. The integrated effect of this tectonic tensile stress at the conduit wall, over the depth of the lithosphere, is the ridge resistance force. The ridge resistance force is therefore proportional to the height of the conduit wall, i.e. proportional to the brittle thickness of the lithosphere at the ridge axis. Lachenbruch (1973) estimated that the mean resistance force in the conduit is,

$$\sigma_R = \frac{1}{2}(\gamma^* - \gamma)H. \tag{2.21}$$

He also derived a relation between the mean viscosity of the fluid (η), the conduit dimensions (half-width a) and the plate's half-spreading velocity (V) by assuming that the material in the conduit was an incompressible Newtonian fluid. In the simple case of a uniform viscosity distribution within the conduit that relation is reduced to,

$$\gamma^* - \gamma = \frac{3\eta V H}{2a^3}. \tag{2.22}$$

Using $\gamma^* = 33000\ N/m^3$, $\gamma = 96\%\gamma^*$ and $H = 50$ km in Eq. 2.21, Lachenbruch (1973) estimated that the maximum tensile stress at the ridge axis is of the order of 33 MPa. Using the same values in Eq. 2.22, he concluded that for a half-spreading velocity $V = 20$ mm/yr there is the following correspondence between the fluid's viscosity and the conduit half-width,

$$\eta \sim 3 \times 10^{19}\ Pas \Rightarrow a \sim 10 \text{ km},$$

$$\eta \sim 3 \times 10^{16}\ Pas \Rightarrow a \sim 1 \text{ km}.$$

Estimates of the maximum ridge resistance stress, or the ridge's strength, were independently made by Sleep and Rosendahl (1979). They used numerical fluid dynamic modelling to study the variation of material properties at the ridge axis as a function of spreading rate. At slow spreading rates a viscoplastic rheology with a yield strength of 20 MPa successfully predicted the median valley axial morphology. At fast spreading ridges only models with a very low viscosity for the magma chamber and intrusion zone gave a reasonable fit to the bathymetry of the ridge axial high. In such models, low stresses of less than 10 MPa prevailed in the axial region and in the adjacent lithosphere.

Observational constraints also confirm that slow spreading ridges are stronger than fast spreading ones. The strength of the lithosphere is mainly controlled by the brittle thickness, increasing with it. Both seismic evidence and thermo-mechanical and gravity modelling proved that the brittle plate thickness at slow spreading ridges is on average 2 to 6 km thicker than at fast spreading ridges (section 1.2). Further evidence that slow spreading ridges have larger brittle strengths than fast spreading ones is provided by their relatively higher levels of seismicity, larger fault throws and general rougher topography.

2.5.4 The transform resistance

The transform resistance force is the frictional resistance to the relative plate displacements that occur at transform faults. The frictional resistance is determined by the magnitude of the shear stresses acting parallel to the fault's surface and by the fault's surface area.

When the two sides of the fault are pressed together by a normal stress σ_n, the criterion for the onset of frictional sliding is that a shear stress of magnitude $\tau \doteq f_s \sigma_n$ must be applied parallel to the fault (e.g. Turcotte and Schubert, 1982). f_s is the coefficient of friction.

The absolute fault strength is the magnitude of the shear stress required to cause slip on the fault. The relative fault strength is the ratio between the absolute fault

strength and the maximum shear stress that can be supported by the surrounding lithosphere. Stress indicators at transform faults, described ahead in section 2.8, indicate that transform faults are weak in both absolute and relative senses. Although the reason for the apparent weakness of transform faults is not exactly known, two main kinds of explanations have been proposed. The first considers that the low shear strength is due to high pore fluid pressures. The second attributes the low shear strength of transforms to low coefficients of friction.

The effect of the pore fluid pressure is to reduce the normal stress across the fault. Possible causes of high pore fluid pressures are the sealing of internally generated fluids (released for instance by dehydration reactions during metamorphism), and continued flow of overpressured fluids (e.g. Hickman, 1991).

Low coefficients of friction at oceanic transform faults are possibly due to the presence of serpentinites. The presence of serpentinites at mid-ocean ridges is inferred from serpentinized peridotite outcrops, and from structural and geochemical observations at ophiolites. The location of the outcrops suggests that serpentinization of the oceanic lithosphere occurs preferentially at ridge discontinuities, namely transform faults (Escartin et al., 1997). The main polytypes of oceanic serpentinized peridotite (lizardite and chrysotile) have coefficients of friction around 0.3, which is considerably lower than that of other rock, around 0.85 (Byerlee, 1978). Therefore, the source of weakness of oceanic transform faults may well be the presence of these minerals.

Attempts to estimate the frictional resistance of transform faults from numerical modelling have followed two approaches. Studies of the dynamics of single plates, like the American plate (Richardson and Reding, 1991) and the Juan de Fuca plate (Wang et al., 1997), indicate that the shear stresses along well developed transform faults are quite low, of the order of 5-10 MPa. Other numerical models investigate the interaction between the ridge and transform stress fields. These models do not provide absolute magnitudes of the transform resistance force, but have suggested that the ratio of the ridge normal stress to the transform shear stress is about 3 to 5 (section 1.6).

2.6 Other sources of tectonic stress

The most important sources of local perturbations to the first order pattern of stress are stresses caused by small topographic loads, bending stresses and thermal stresses.

The main effect of small topographic loads, which are supported by the rigidity of the lithosphere, is to modify the vertical stress, and produce local deviatoric tension or compression depending on whether the load is positive or negative.

Bending stresses are associated with the flexure of the lithosphere. Significant flexure of the oceanic lithosphere occurs as a result of downbending at subduction zones, and as result of topographic loads, such as seamount chains, that are not compensated by underlying density heterogeneities. Thus bending stresses occur as a result of short wavelength surface or subsurface loading when it deviates from simple Airy isostasy.

Thermal stresses are generated by the cooling and contraction of the lithosphere as it moves away from mid-ocean ridges. It can be shown that for an elastic half space confined in the horizontal direction and unconstrained in the vertical direction (a reasonable assumption in the upper crust), the horizontal normal stresses resulting from a temperature change ΔT are (Ranalli, 1995),

$$\sigma_{xx} = \sigma_{yy} = \frac{E}{1-\nu}\alpha\Delta T, \tag{2.23}$$

where α is the linear expansion coefficient in the lithosphere. A decrease in temperature generates a change in volume that induces tensile thermal stresses.

Very large bending and thermal stresses, of up to thousands of MPa, have been estimated for the oceanic lithosphere. Nevertheless, it has also been shown that these stresses are rapidly relieved by brittle and plastic deformation (e.g. Goetze and Evans, 1979). Because of their rapid dissipation with time, thermal and bending stresses have been classified as non-renewable stresses and are not expected to produce large scale tectonic deformation (Bott and Kusznir, 1984). They may, however, produce significant local deformation. For instance, it has been proposed that bending stresses are the origin of the ridge axial morphology (Tapponnier and

Francheteau, 1978; Eberle and Forsyth, 1998), and that thermal stresses are the cause of transform faults (Turcotte, 1974; Collette, 1974).

A thermo-rheological model of thermal stresses for cooling oceanic lithosphere has been developed by Kusznir (1991). He studied the evolution in time and the distribution with depth of the thermal stresses, and found that both brittle and plastic deformation allow the release of the initial tensile thermal stresses in the upper lithosphere, so that when material below cools and contracts it takes the upper lithosphere into compression. His modelling predicts compressive stresses at the surface of lithosphere as young as 1 Ma.

2.7 The state of stress from mid-ocean ridges to intraplate regions

It is well established that mid-ocean ridges are characterised by extension and that plate interiors are characterised by compression. The state of stress in the region between ridges and plate interiors, i.e. in young oceanic lithosphere, is not so well determined.

Evidence of compression at plate interiors consists of the recognition that the few earthquakes recorded in lithosphere older than 35 Ma have thrust or strike-slip mechanisms (e.g. Bergman and Solomon, 1984). Evidence of extension at mid-ocean ridges consists of earthquakes characterised by normal fault plane solutions (e.g. Sykes, 1967) and extensive active normal faulting observed within 5-10 km of the ridge axis (section 1.3).

From a global point of view earthquake focal mechanisms suggest that both compression and extension occur in oceanic lithosphere younger than 35 Ma (Fig. 2.2). Nevertheless, most of the extensional events occur in the Central Indian ocean (Weins and Stein, 1984; Bergman and Solomon, 1984). The high level of seismicity recorded in the Central Indian ocean, indicating extension parallel to nearby ridges, has been explained in terms of the plate geometry and interaction of plate boundary forces (Cloetingh and Wortel, 1986).

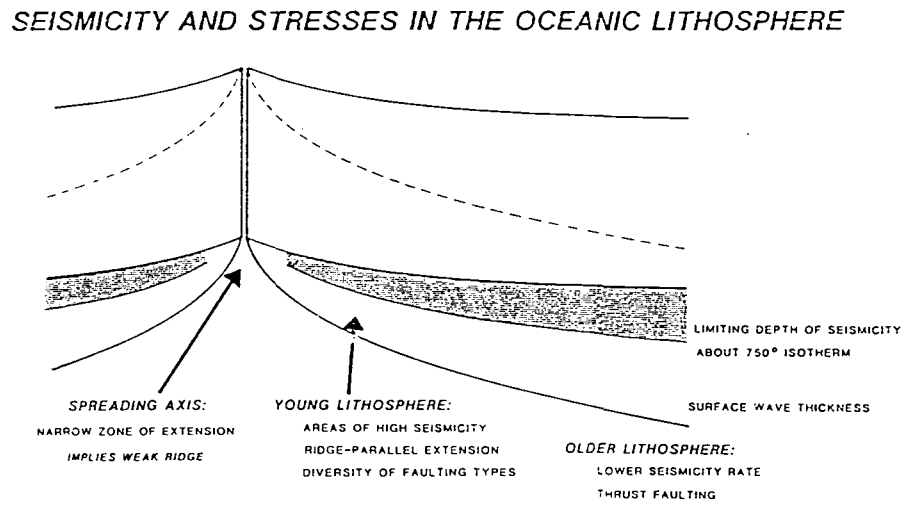

Fig. 2.2 Schematic diagram relating seismicity observations to the tectonics of the oceanic lithosphere (after Stein and Pelayo, 1991).

Other sources of ridge parallel extension often pointed out are thermoelastic stresses resulting from the cooling of the young lithosphere (Turcotte and Oxburgh, 1973). The rate of release of thermoelastic stresses is likely to be proportional to the rate of cooling of the lithosphere, decreasing with lithospheric age in the same way as seismicity (Bergman and Solomon, 1984). Also, the crust and mantle are likely to respond differently to temperature changes. In particular, the product of the coefficient of thermal expansion and Young's modulus may be smaller in the crust than in the mantle, explaining why near ridge seismicity is concentrated below the Moho (Turcotte, 1974). Furthermore, thermoelastic stresses can account for the depth stratification of earthquakes observed in lithosphere younger than 35 Ma, with thrust faulting events showing a tendency to occur at shallower levels than normal faulting events (Stein and Pelayo, 1991; Kusznir, 1991).

Despite the contribution of the thermoelastic stresses to the stress field, intraplate earthquakes observed in young oceanic lithosphere tend to be located in small seismically active regions, suggesting that local processes are the origin of this seismicity (Weins and Stein, 1984). Not taking into account local processes, and possibly a low level 'background' associated with thermoelastic stresses (Stein et al., 1987), it seems that the first order pattern of stress involves a gradual transi-

tion from ridge perpendicular extension to compression as we move away from the ridge axis. This idea has been claimed by some authors for being able to reconcile the earthquake observations with theoretical stress predictions (Fleitout and Froidevaux, 1983), and will be adopted in this thesis.

2.8 Stress indicators at transform and non-transform offsets

Earthquakes at well developed transform faults have mainly strike-slip mechanisms. Most strike-slip events have fault planes parallel to the orientation of the transform, reflecting the displacement along the fault and therefore some frictional resistance to plate motions. Despite the occurrence of earthquakes considerable evidence indicates that the frictional resistance of transform faults is very low. Heat flow measurements in shallow boreholes along what is probably the best surveyed transform fault, the San Andreas fault, indicate low values of generated frictional heat. These measurements imply that the average shear resistance to fault motion is no greater than 20 MPa (e.g. Brune et al., 1969, Lachenbruch and Sass, 1981), although this is at present subject of debate (Scholz, 2000).

Principal stress directions parallel and perpendicular to fault planes minimise the shear stresses acting along those planes, i.e. minimise the fault's frictional resistance. At the San Andreas and the Great Sumatran faults, earthquake focal mechanisms and well bore breakout data indicate that the maximum horizontal principal stress direction is oriented nearly perpendicular to the fault's strike (e.g. Zoback, 1991; Mount and Suppe, 1992).

Observational constraints on the strength of oceanic transform faults are scarce, but available evidence indicates principal stress directions at high angles to the faults, hence a low value of shear strength. Microearthquakes at the Kane transform show normal faulting on planes striking nearly parallel to the main trace of the transform (Wilcock et al., 1990). This implies that the Kane transform has a low

frictional strength, but also means that the tension axis is oriented perpendicular to the trend of the transform.

Another well studied oceanic transform is the Mendocino transform fault. The maximum compressive stress constrained by earthquake focal mechanisms is consistently N-S in the vicinity of the Mendocino transform (e.g. Wang et al., 1997). This has been interpreted as an indication that the Mendocino transform fault, like the Kane transform, is much weaker than the surrounding lithosphere, in spite of the differing stress regimes i.e. fault-normal compression versus fault-normal extension.

Structural observations at ridge-transform intersections are important indicators of stress. Some of the best mapped ridge-transform intersections include the Quebrada (Lonsdale, 1978), Tamayo (Macdonald et al., 1979), Clipperton (Kastens et al., 1986; Gallo et al., 1986; Pockalny, 1997), Siqueiros (Crane, 1976; Fornari et al., 1989), Vema (e.g. Macdonald et al., 1986) and Kane (Karson and Dick, 1983; Tucholke and Schouten, 1988) transforms. At these and other ridge-transform junctions the ridge axis is observed to locally curve towards the transform fault, as does the adjacent tectonic fabric. Examples are presented in Fig. 2.3 and Fig. 2.4 at the Vema and Clipperton transforms respectively.

The curved tectonic fabric at ridge transform intersections often consists of several sets of fractures, but only two or three of these sets are consistently observed. One, the oblique set, makes an angle of $20° - 50°$ to the trend of the ridge axis. The other two sets are parallel to either the ridge axis or the transform fault (e.g. Fox et al., 1986). Focal mechanisms and direct observations suggest that many of these fractures are normal faults (e.g. Whitmarsh and Laughton, 1975, Fox et al., 1986; Macdonald et al., 1986; Kastens et al., 1986).

Because both normal faulting and ridge axis dike emplacement are expected to occur perpendicular to the direction of the least compressive stress, the observed curving of the ridge axis and adjacent tectonic fabric towards the transform implies a change in the orientation of the least compressive stress. In addition to the change in the principal stress direction an increase in the observed seismicity at ridge-transform junctions implies an increase in the stress magnitudes (Rowlett, 1981).

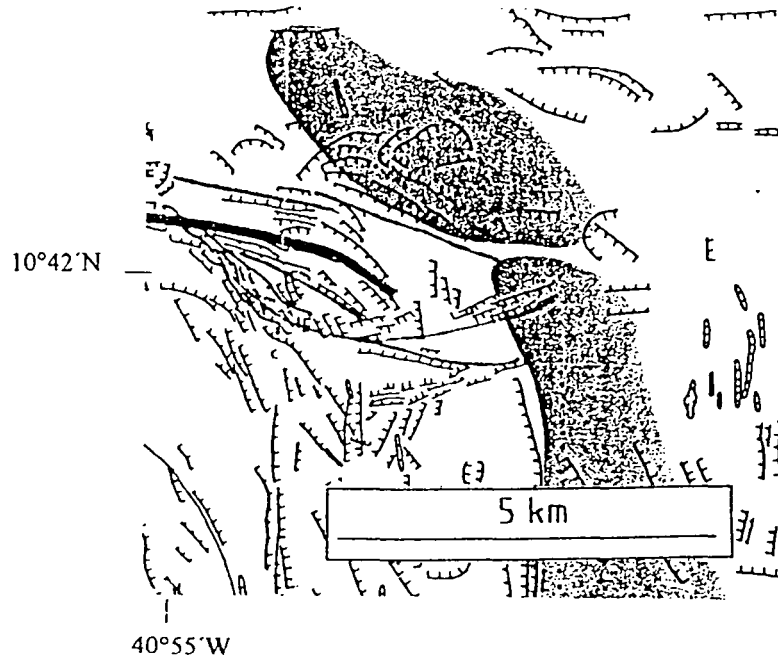

Fig. 2.3 Detail of the tectonic chart of the eastern end of the Vema transform fault and its intersection with the MAR. Note how the neovolcanic zone (stippled area) curves following the trend of the transform (bold line). The fault scarps forming the west wall of the rift valley change from a strike 000° to 340° as the ridge transform intersection is approached (modified from Macdonald et al., 1986).

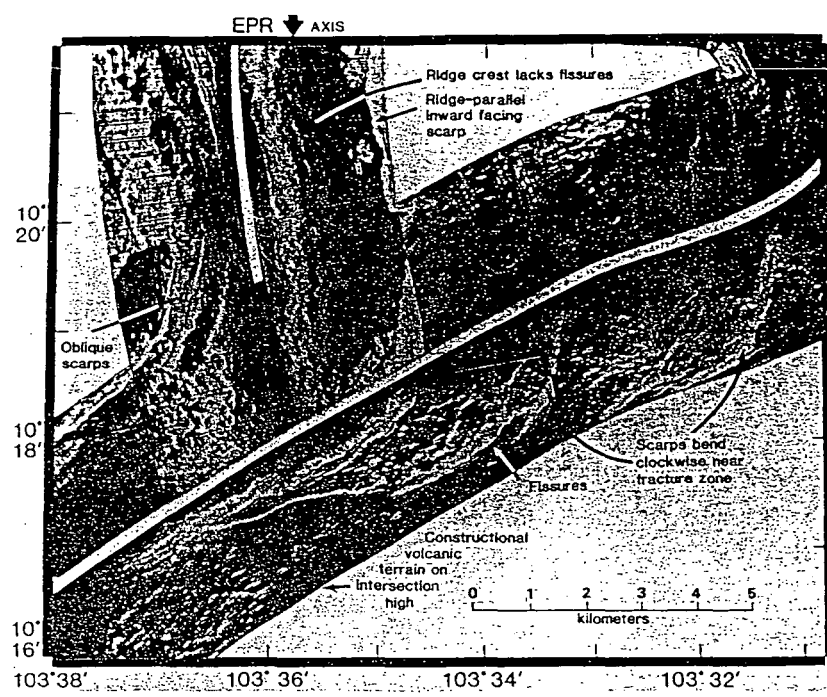

Fig. 2.4 SeaMARC image of the eastern intersection of the Clipperton transform fault with the East Pacific Rise. The degree of rotation (up to 80°) of the ridge-parallel scarps is unusually high at this ridge-transform intersection (after Kastens et al., 1986).

The structural geometry of non-transform offsets of the Mid-Atlantic Ridge has been analysed in great detail in recent years (section 1.6). Fig. 2.5 shows an example of a non-transform offset characterised by an extensional basin oriented at 45° relative to the strike of the ridge axis. This type of structural geometry at non-transform offsets is predicted by the modelling in chapter 6.

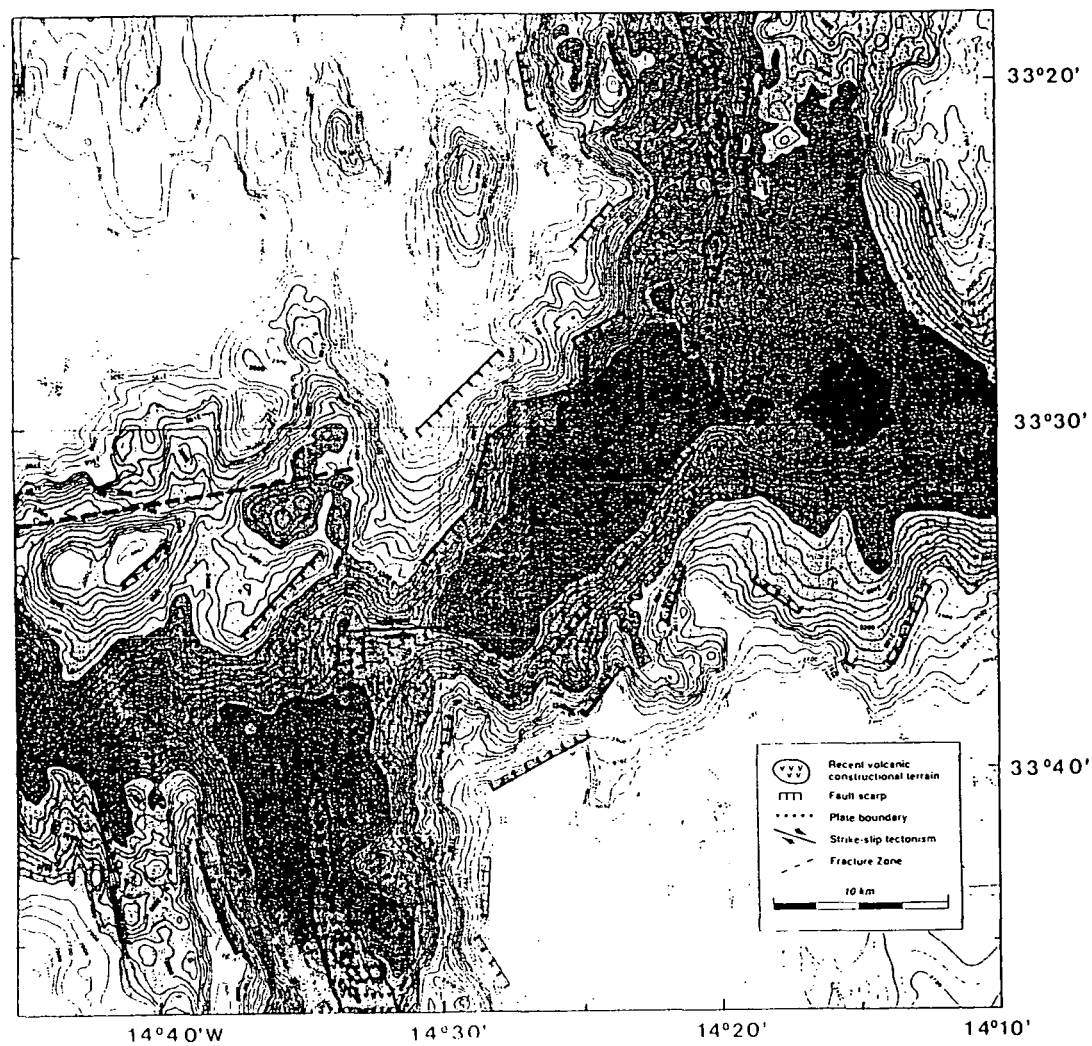

Fig. 2.5 A 50 m-contour interval map with structural interpretation for the Mid-Atantic Ridge offset at 33°35'S. A rectangular basin approximately 20 km x 6 km is outlined by two linear escarpments that create over 1000 m of relief. The escarpments strike approximately 45° oblique to the ridge segments (after Grindlay et al., 1991).

2.9 Observations at Easter microplate

Herron (1972) and Forsyth (1972) were the first to propose the existence of Easter microplate, based on the analysis of magnetic anomaly data and the ring-shaped epicentral distribution. Anderson et al. (1974) were the first to suggest that the existence of the microplate could be connected with Easter hotspot and with the extremely high spreading velocities in the East Pacific Rise. The full spreading rate of the EPR, just north of Easter, is about 160 mm/yr, and south of Easter is even higher, about 170 mm/yr. More recent studies including analysis of earthquake focal mechanisms (Engeln and Stein, 1984), SeaMarcII and GLORIA long- range sidescan data, Sea Beam and magnetic profiling data (Hey et al., 1985; Francheteau et al., 1988; Martinez et al., 1991; Naar and Hey, 1991; Larson et al., 1992; Rusby and Searle, 1995) revealed in detail Easter tectonics and evolution.

Easter microplate is about 550 km in diameter and lies between two parallel arms of the EPR, often called the East and West Rifts (Fig. 2.6). The West Rift consists of four spreading segments, one of which (25° S) is a propagating rift. Three of these spreading segments are connected by three right-lateral transform faults, named Terevaka, Raraku and Anakena after features in Easter island. The East Rift is divided into six segments with offsets less than 50 km. No developed transform faults exist and three of these segments have recently propagated northward to the inside (west) of the axis they replace.

The northern boundary of the microplate follows roughly the 23° S latitude, extending from approximately 112°20′ W to the northern Triple Junction at 114°32′W. Its eastern end is a broad (70-100 km) zone of high relief nested grabens, enclosing the 5980 m deep 'Pito deep' at 23° S, 111°56.5′ W. Between the Pito deep and 113°00′ W there is a series of ENE-WSW trending faults. Francheteau et al. (1988) interpreted a narrow band of these faults as a transform fault with almost pure strike-slip movement, and named it as the Pito fracture zone. Near 112°20′ W the principal shear zone is 4-5 km wide, and lies within a 40-50 km wide domain characterised by ENE-WSW faults. To the West, at 112°35′W, the transform becomes a

2 km wide valley in the middle of a 35 km wide raised massif, with a mean depth of 3500 m. At 113°00′ W what remains of the transform is a small notch at the submit of a 1700 m elevated ridge. That ridge, trending roughly 260° – 265°, continues for more than 120 km, from 113°10′ W to 114°22′ W. It is about 15 km wide and stands 1-2 km above the surrounding seafloor. South of this ridge and parallel to it the seafloor is about 500 m lower than to the North (Fig. 2.7).

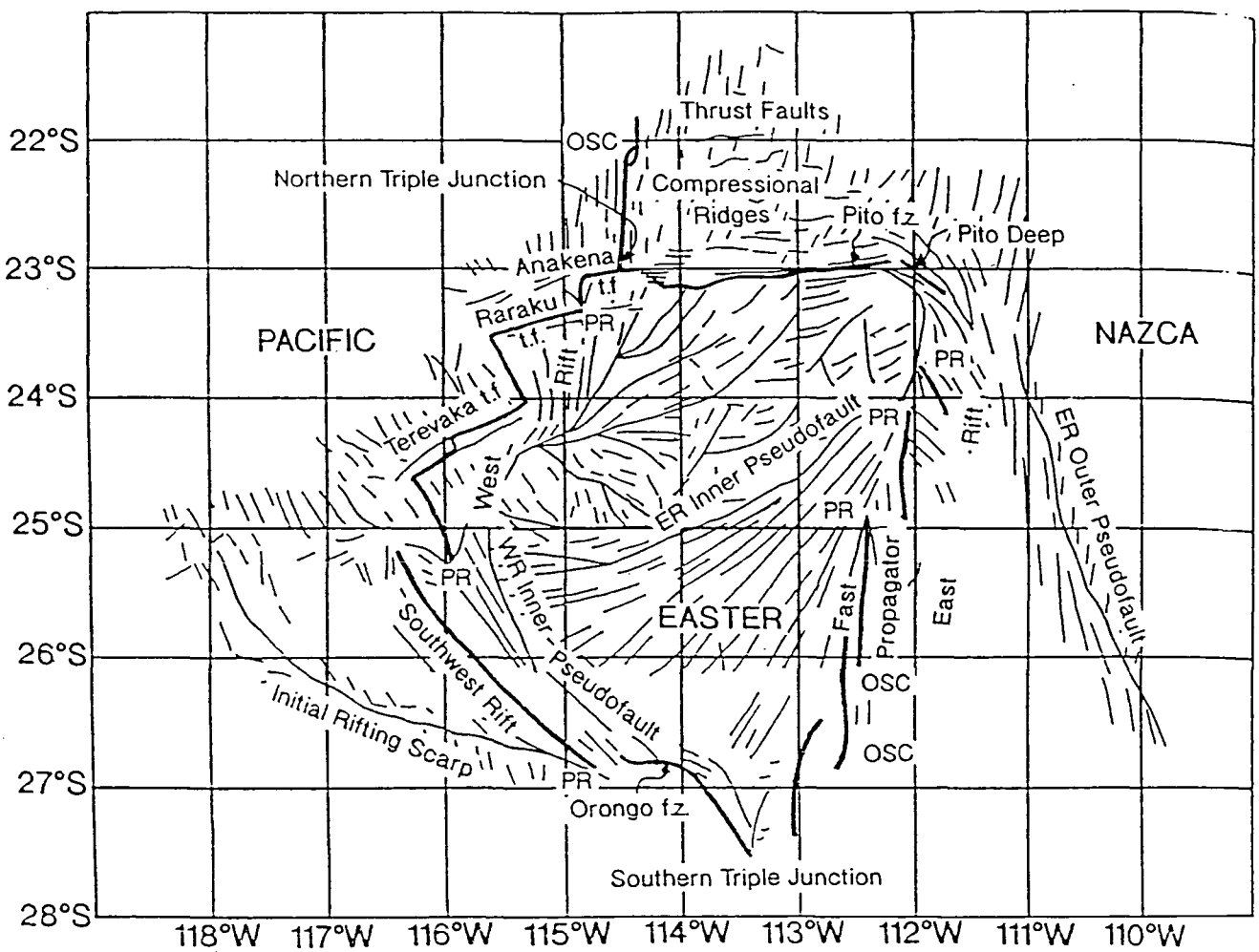

Fig. 2.6 Simplified tectonic interpretation of Easter microplate based on GLORIA sidescan sonar data. Location names are used throughout the text (t.f. indicates active transform fault, f.z. fracture zone, PR propagating rift, OSC Overlapping Spreading Centre, ER East Rift and WR West Rift (after Rusby and Searle, 1995).

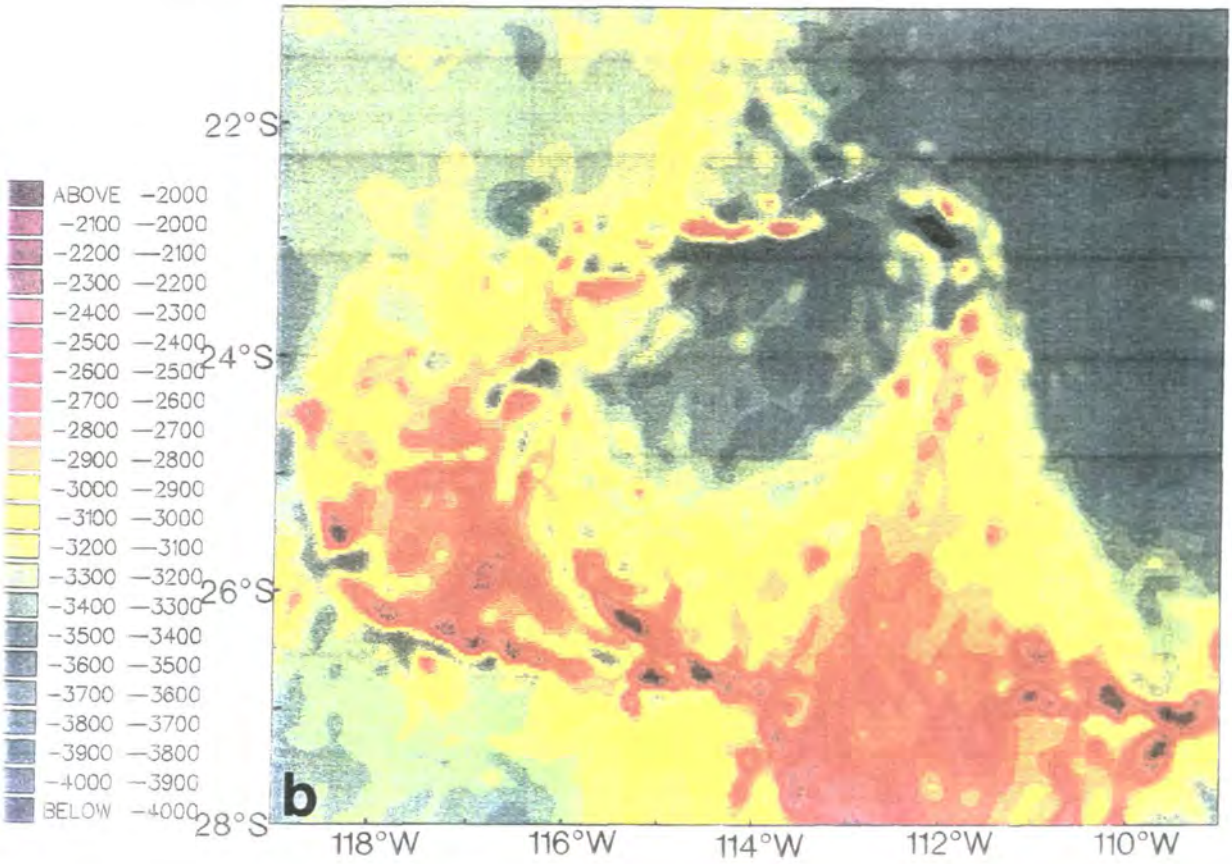

Fig. 2.7 Colour shaded contour map of bathymetric data at Easter microplate (100 m contour interval). Actual maximum and minimum depths are 5980 m at the Pito Rift and 640 m near the Orongo fracture zone (after Rusby, 1992).

The strike and elevation of the northern boundary is consistent with an approximately N-S direction of maximum compression. The estimates of relative plate motions lead to the calculation of the Easter-Nazca rotation pole at about 22.5° S, 112.4°W (Naar and Hey, 1989; Rusby and Searle, 1995; Fig. 2.9). This pole predicts a N-S component of motion along the northern boundary, decreasing towards the east, and an East-West strike-slip component which increases towards the east.

The southern boundary of the microplate is not well defined. Its western end consists of two elevated ridges, composed of en echelon scarps separated by short offsets, that converge eastwards at 26°43′S, 114°13′W. Francheteau et al. (1988) interpreted a 2 km wide valley, that runs into the southern ridge at 26°45.5′S, 114°50′W, as the first expression of a transform fault called the Orongo fracture zone. After the convergence of the two parent ridges, the Orongo fracture zone continues also

as a ridge in a southeasterly direction, decreasing rapidly in relief from over 2000m west of 113°10′W to less than 200m at 113°05′W. Both the two parent ridges and the Orongo fracture zone are extremely shallow, which has been interpreted as a sign of strong N-S compression (Rusby, 1992).

To the east of Orongo fracture zone, the sonar images show a complex tectonic fabric, with ridges and scarps of varying trends, but no evidence of any defined plate boundary. There is also evidence of significant off-axis magmatism, since the whole area around 27° S is scattered with volcanic edifices and lava flows (Rusby, 1992). A broad and shallow NW-SE trending ridge, extending from 26°50′ S, 113°30′ W to 28°02′ S, 113°08′ W, has been recognised as the southern continuation of Orongo fracture zone. The position of the instantaneous Pa-Ea axis of rotation at 27.7° S, 114.0° W predicts a NE-SW compression at the latitude of this ridge, which would explain the shallow depths observed (Rusby and Searle, 1995). Between this ridge and another one continuing to the south, there is an overlap region 60 km in a N-S direction and 30 km wide. The southern triple junction (Ridge-Ridge-Fault) is thought to lie within this overlap, at about 28° S, 113° W (Naar and Hey, 1991, Rusby, 1992).

Handschumacker et al. (1981) identified the southward fanning of the magnetic anomalies about the East Rift, implying faster spreading rates in the south than in the north (Fig. 1.9). From the magnetic anomaly fanning associated with the East rift it was inferred that the microplate grew by the northward propagation of the East Rift at the expense of the West Rift. Rigid rotations of magnetic anomaly and GLORIA data back in time lead Rusby and Searle (1995) to conclude that 2.5 Ma after Easter microplate initiation about 5 Ma ago, the East Rift ceased propagation and the Southwest Rift began to open along the southern boundary of the microplate.

In the Nazca plate to the north of Easter occur some of the most notable features in the whole region: a series of high-relief E-W trending ridges extending from around 22°S, 114°W, close to the EPR, to near the Pito deep area at 23°S, 112°W (Fig. 2.8).

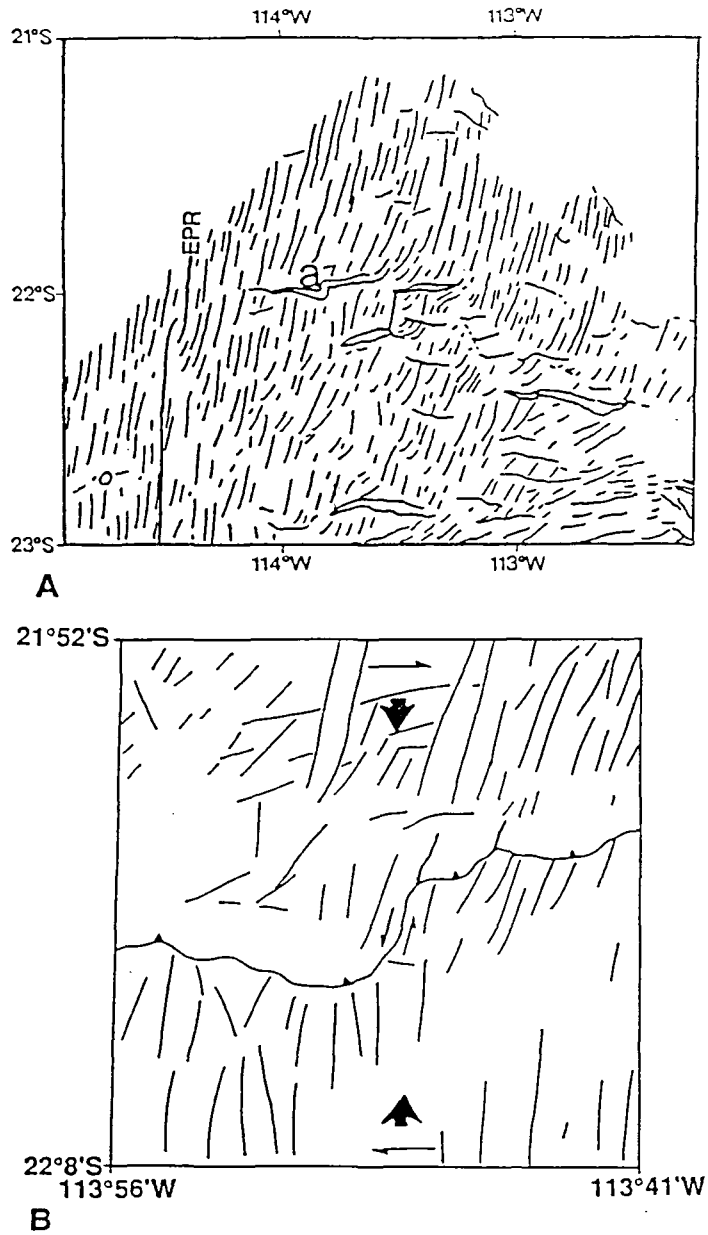

Fig. 2.8 A) Interpretation of GLORIA image of part of Nazca plate north of Easter. Normal fault scarps formed at the EPR are orthogonal to the spreading direction. Large, broad, east-west trending features, cross-cutting the normal faults are asymmetric ridges (confirmed as so by bathymetric data). **B)** close-up of ridge labelled a in the top diagram. The pair of asymmetric ridges appears to be linked by a transfer fault. The abrupt termination of the EPR-parallel spreading fabric against steep, south-facing slopes, as well as the sharp base of those slopes, indicates the ridges have a faulted origin. Arrows indicate dextral transpressive stress (combination of north-south compression and east-west dextral shear) (after Rusby and Searle, 1993).

These ridges vary in length between 20 and 50 km and some stand by more than 1 km above the surrounding seafloor. They show pronounced asymmetry, with steeper slopes ($\sim 30° - 40°$) to the south than to the north ($\sim 7°$), and many are found to truncate the spreading fabric to the south (Rusby and Searle, 1993). The finding of these ridges to the north of Easter suggests that the northern boundary of the microplate is unable to accommodate all the convergence between the Easter and Nazca plates, and that the Nazca plate has been undergoing compressional deformation. The asymmetry and steepness of these ridges led Rusby and Searle (1993) to propose that they were actually thrust faults. The observation that the abyssal-hill fabric in the GLORIA images often terminates abruptly against the ridges has also been interpreted as evidence of the ridge's faulted origin.

The interior of the microplate is characterised by seafloor fanning and age contrasts, due to the varying spreading rates, ridge propagation, and the microplate's rotation. The tectonic fabric consists predominantly of normal fault scarps and abyssal hills formed near and parallel to the ridges (Searle et al., 1989). Several anomalous ridges are observed inside the microplate, such as three ridges trending roughly N-S near 23°30′S, 112°30′W. These ridges are similar to the E-W trending anomalous ridges in the Nazca plate. Considering that the fabric within the microplate has been severely rotated in a clockwise direction, it is possible that the initial trend of the anomalous ridges observed in the microplate was also E-W. Since the age of these ridges is not known, it is not possible to verify this hypothesis.

2.10 Stress indicators at Easter microplate

The indicators of stress directions in Easter microplate fall into two categories: the structural observations described in the previous section, and the earthquake focal mechanism solutions listed in Table 2.1.

Table 2.1 Earthquake focal mechanisms in Easter microplate.

Year	Event	Lat.	Lon.	Mo	Strike	Dip	Slip	Strike	Dip	Slip
1963	3-07	-26.94	-113.49		280	82	188			
1964	6-06	-26.54	-114.42		324	65	270			
1965	11-03	-22.41	-113.94		65	85	165			
1965	11-06	-22.17	-113.86		52	60	166			
1968	8-09	-22.35	-113.15		140	78	182			
1969	4-22	-26.67	-113.96		203	88	170			
1970	7-31	-27.04	-113.14		20	79	12			
1973	5-13	-23.56	-111.82		330	35	90			
1974	6-22	-22.19	-113.36		294	40	90			
1974	12-16	-24.81	-112.07		70	89	360			
1976	9-14	-26.37	-114.73		320	67	270			
1978	78	-26.78	-115.12	1.3	127	26	-98	315	64	-86
1979	177	-24.45	-112.02	1.6	121	58	175	213	85	32
1980	31	-23.13	-114.35	2.7	63	66	9	329	81	156
1980	349	-26.09	-113.09	1.3	175	90	180	265	90	0
1980	456	-23.39	-113.45	2.0	312	90	180	42	90	0
1981	218	-22.66	-113.23	7.8	246	76	-6	338	84	-166

TABLE 2.1 (cont. I)

Year	Event	Lat.	Lon.	Mo.	Strike	Dip	Slip	Strike	Dip	Slip
1981	340	-26.94	-114.31	1.0	340	34	-46	111	67	-115
1984	140	-25.69	-116.07	3.8	123	62	-177	31	88	-28
1985	50	-27.13	-113.40	1.0	110	64	-178	19	88	-26
1985	83	-25.40	112.28	2.7	134	82	-177	43	87	-8
1986	92	-23.98	-114.40	6.4	78	72	-1	168	89	-162
1986	09	-26.97	-114.28	3.8	123	35	-124	343	61	-38
1986	08	-24.11	-112.22	1.8	149	18	-96	335	72	-88
1986	09	-23.81	-112.09	2.2	138	30	-108	338	61	-80
1987	53	-23.34	-114.05	5.9	109	41	79	303	50	99
1988	75	-27.04	-113.52	1.7	200	83	4	109	86	173
1988	28	-21.67	-114.11	6.5	157	90	180	247	90	0
1988	64	-23.47	-111.88	1	111	27	-112	316	65	-79
1988	92	-24.70	-116.19	2.5	146	90	180	236	90	0
1988	160	-26.66	-112.58	1.7	343	78	174	74	84	13
1990	105	-25.84	-116.44	3.5	290	90	-180	20	90	0
1990	113	-27.05	-114.72	0.9	297	45	-90	117	45	-90

TABLE 2.1 (cont. II)

Year	Event	Lat.	Lon.	Mo	Strike	Dip	Slip	Strike	Dip	Slip
1990	114	-27.24	-114.91	1.5	117	36	-108	318	56	-78
1990	65	-25.00	-112.42	2.9	156	90	-180	246	90	0
1990	121	-26.71	-114.16	6.9	274	87	179	4	89	3
1991	55	-26.43	-114.69	1.1	201	68	-4	293	87	-158
1991	58	-24.35	-116.14	2.2	155	80	-177	65	87	-11
1991	75	-22.62	-113.04	1.2	142	90	180	232	90	0
1991	84	-22.95	-112.58	7.3	168	90	-180	258	90	0
1991	168	-21.93	-113.99	2.0	74	79	5	343	85	169
1991	81	-26.41	-115.21	3.0	176	34	-87	353	57	-92
1993	4	-25.12	-112.33	7.1	83	82	-2	173	88	-172
1993	7	-25.21	-112.35	4.0	71	77	-1	161	89	-167
1994	85	-21.82	-113.41	3.8	173	90	-180	263	90	0
1994	107	-21.84	-113.73	6.5	47	84	5	317	38	174
1995	167	-26.89	-112.42	2.6	69	74	14	335	76	163
1995	180	-27.56	-112.85	1.4	124	58	177	215	87	32
1995	112	-24.41	-116.15	1.0	153	90	-180	243	90	0

Most of the listed focal mechanisms are displayed in Fig. 2.9, but some were omitted to avoid superpositions. The earthquakes until 1965 are from Engeln and Stein (1984). The remaining is a compilation of the Centroid Moment Tensor (CMT) solutions published each quarter (Dziewonski and Woodhouse, 1983). The focal mechanisms are located around the microplate, having a more diffuse distribution along the northern boundary than along the southern one. There is a large proportion of high magnitude earthquakes occurring in the Nazca plate.

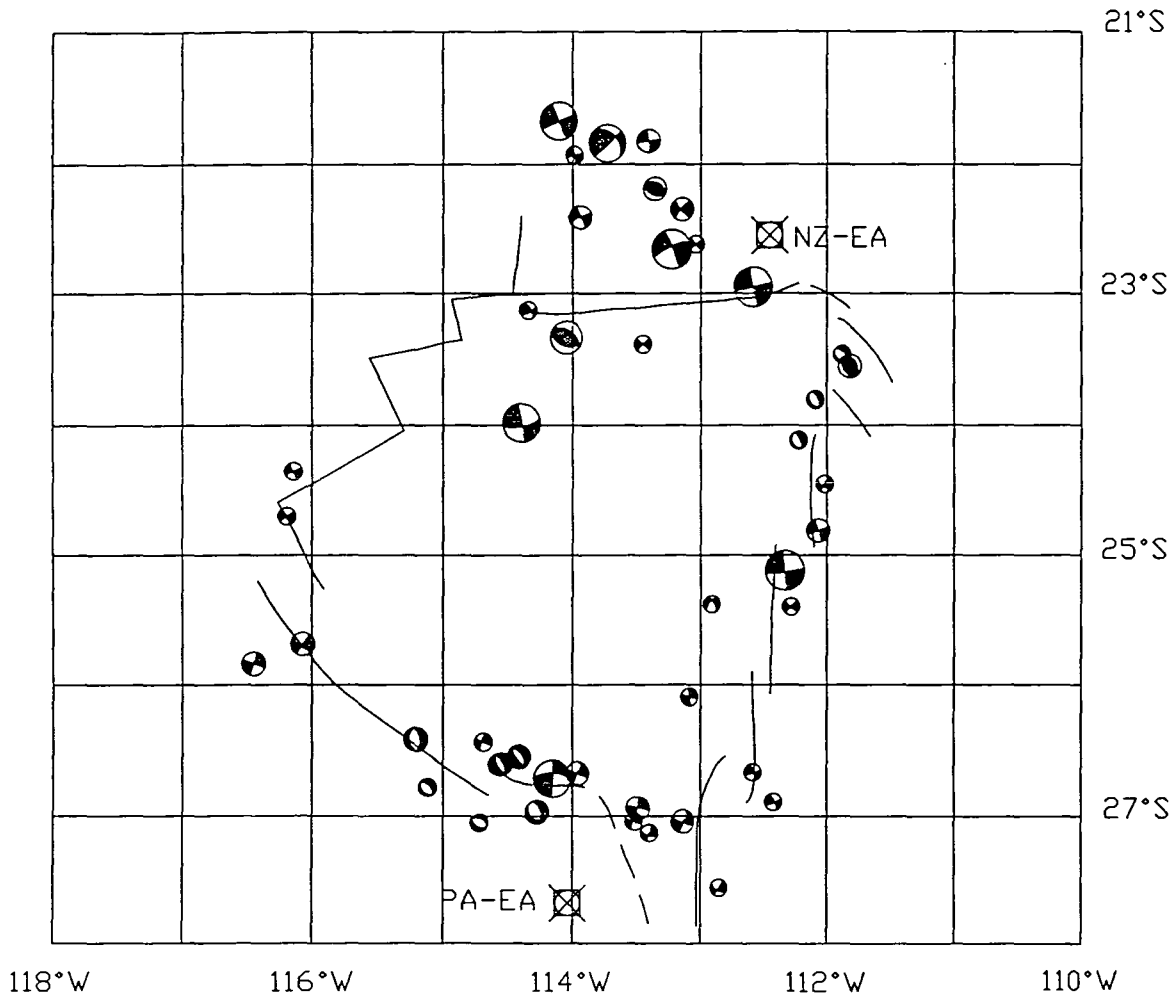

Fig. 2.9 Earthquake focal plane solutions listed in Table 2.1, compiled from Engeln and Stein (1984) for earthquakes until 1965, and from the Centroid Moment Tensor solutions (Dziewonski and Woodhouse, 1983) for earthquakes after 1965. The crossed squares show the location of the NZ-EA and PA-EA three-plate closure poles calculated by Rusby and Searle (1995). P axis in the white quadrant. Size indicates the earthquakes relative magnitudes.

The axes of maximum compression along the East and West rifts follow approximately the rift strikes, with the axes of maximum extension being perpendicular to them. This means that the earthquakes along the East and West rifts are only representative of the state of stress within the spreading boundaries. Similarly to the earthquake focal mechanisms the tectonic pattern of the East and West boundaries does not provide particular information about the state of stress of Easter microplate. Thus, the West and East boundaries of the microplate display a tectonic pattern typical of other propagating rifts and spreading segments of the EPR: normal faulting roughly parallel to the spreading axis, pseudofaults associated with the propagating rifts, and tectonically rotated fabric at the Overlapping Spreading Centres and propagating rifts.

In the northern part of the microplate, and in the adjacent Nazca plate, the direction of the compression axis is consistently NNE-SSW. Such direction of maximum compression explains the high relief and strike of both the northern boundary and the anomalous ridges in the Nazca plate. The large majority of the earthquakes show strike-slip motion combined with a component of thrust. The strike-slip mechanisms are consistent with left lateral motion along ENE-WSW fault planes. The component of thrust is substantiated by two thrust mechanisms, one observed in Nazca and the other in the NW corner of the microplate.

The earthquake focal mechanisms along the southern boundary of the microplate indicate a NW-SE direction of maximum compression. The strike of the Orongo fracture zone is WNW-ESE, so the earthquakes can be related with right-lateral strike-slip motion along WNW-ESE fault planes. To the east, between the Orongo fracture zone and the East Pacific Rise, there is no defined plate boundary, so it is not possible to decide if the observed earthquakes are related to right-lateral strike slip motion along NW-SE planes or left-lateral strike slip motion along NE-SW planes. However, since the earthquakes are relatively concentrated along the southern boundary they probably reflect the motion along the boundary, rather than the regional stress field.

In this sense the ridges observed along the southern boundary are better stress

indicators. In the western part of this boundary the high relief of the Orongo fracture zone, as well as the anomalous elevation of the two ridges to the west of it, indicate a strong component of N-S compression. In the eastern part of the southern boundary, the shallow NW-SE trending ridge identified as the southern continuation of the Orongo fracture zone is consistent with NE-SW compression.

The stress release in the South is relatively concentrated along the southern boundary, consisting of many small magnitude earthquakes. In the north of the microplate the earthquake distribution is broader, extending to the adjacent Nazca plate. Despite the fact that the magnitude of the earthquakes in the north is on average higher than in the south, it is not possible to conclude that there is a decrease in the stress level from the north to the south, because the density of earthquakes along the southern boundary is larger.

Chapter 3

Stress and the finite element method

3.1 Introduction

The essence of any stress problem is to find the response of a structure, or structures, to the applied loading. The solution of stress problems in general requires the satisfaction of the equilibrium conditions and rheological laws, which determine a set of differential equations with prescribed boundary conditions. The boundary conditions and material properties in geodynamic problems often have complex distributions, and therefore the equations have to be solved numerically. The finite element method is one of the most versatile numerical tools in structural analysis and its applications to geodynamics.

The basic principle of the method is to divide the structure to be analysed into elements, to form a finite element grid. Each element is characterised by material properties that depend on the rheology. In the present modelling the elastic, the viscoelastic and the elasto-plastic rheologies are used.

Boundary conditions, specifying the applied loads, are assigned to the relevant elements. The finite element equations are then derived and assembled to form the stiffness equation (section 3.3). The elastic displacements, and from these the elastic strains and the elastic stresses, are computed by solving the stiffness equation. The

viscoelastic and elasto-plastic analysis is carried out using the initial strain method which is based on the iterative solution of the stiffness equation.

Many commercial finite element programs are nowadays available. However, a finite element program specifically designed for geodynamic analysis has been developed over the years at Durham University (Bott, private communication) and has been used in this study. The DURHAM TECTONIC FINITE ELEMENT PACKAGE is in the form of a FORTRAN subroutine library and a master calling program. That facilitates the addition and modification of subroutines, and allows great flexibility in the program applications. The aim of this chapter is to introduce the finite element method, and outline the rheologies and techniques used in the modelling.

3.2 Elastic stress analysis

The rheology defines the relation between stress and strain. Among the rheologies the elastic is of fundamental importance because it describes the behaviour of almost all solid materials at low temperatures and pressures, provided the stress does not exceed a critical level. Elastic behaviour is characterised by instantaneous deformation upon application of the load and by instantaneous recovery of the original shape upon removal of the load.

The theory of elasticity is a good first order approximation for the long-term behaviour of rocks in the upper lithosphere. Direct evidence of the elastic behaviour of the upper lithosphere is provided by the general observation that surface tectonic plates do not deform significantly on geological time scales. For example, the topography in the continental crust, and the linearity of fracture zones in the oceanic crust, can be preserved on a time scale of the order of 10^8yr or more (Turcotte and Schubert, 1982). The bending of the oceanic lithosphere under surface loads constitutes another indication of the lithosphere's long-term elastic behaviour.

The development of the theory of elasticity can be found in many books (e.g. Jaeger, 1969; Ranalli, 1995) so only some relevant definitions will be given here. Consider a set of three mutually perpendicular coordinate axes (x, y, z) with (u, v, w)

being the components of the displacement in that reference system. Under the assumption of infinitesimal strain (i.e. assuming that the displacements vary slowly so that the squares and products of their derivatives are negligible), the strain components at any point in a material are defined by (e.g. Jaeger, 1969),

$$\epsilon_x = \frac{\partial u}{\partial x}, \quad \epsilon_y = \frac{\partial v}{\partial y}, \quad \epsilon_z = \frac{\partial w}{\partial z},$$

$$\gamma_{yz} = \gamma_{zy} = \frac{\partial w}{\partial y} + \frac{\partial v}{\partial z}, \quad \gamma_{xz} = \gamma_{zx} = \frac{\partial w}{\partial x} + \frac{\partial u}{\partial z}, \quad \gamma_{xy} = \gamma_{yx} = \frac{\partial v}{\partial x} + \frac{\partial u}{\partial y}, \tag{3.1}$$

where ϵ_x, ϵ_y, ϵ_z are the extensions of lines in the directions of the axis and $\pi/2 - \gamma_{yz}$ is the angle in the strained state between lines initially parallel to the y and z axis. Similarly to the definition of principal stress (section 2.2) three orthogonal axes can always be chosen such that $\gamma_{yz} = \gamma_{xz} = \gamma_{xy} = 0$. The three principal normal strains in these coordinate directions are denoted ϵ_1, ϵ_2 and ϵ_3.

The constitutive equation for the linear elastic behaviour, known as Hooke's law, postulates that the strain components are linear functions of the stress components. In the isotropic approximation (usually satisfactory for the Earth's crust and mantle) Hooke's law may be written as,

$$\begin{aligned} \sigma_1 &= (\lambda + 2G)\epsilon_1 + \lambda\epsilon_2 + \lambda\epsilon_3 \\ \sigma_2 &= \lambda\epsilon_1 + (\lambda + 2G)\epsilon_2 + \lambda\epsilon_3 \\ \sigma_3 &= \lambda\epsilon_1 + \lambda\epsilon_2 + (\lambda + 2G)\epsilon_3 \end{aligned} \tag{3.2}$$

where λ and G are the Lamé's parameters. More commonly used elastic constants are the Youngs modulus (defined as the ratio of tension to extension in a cylinder which is under axial tension and is unrestricted laterally),

$$E = \frac{\sigma_1}{\epsilon_1} = \frac{G(3\lambda + 2G)}{\lambda + G}, \tag{3.3}$$

and the Poisson's ratio (defined as the ratio of lateral contraction to longitudinal extension for the cylinder considered above),

$$\nu = \frac{\lambda}{2(\lambda + G)} \tag{3.4}$$

When a threshold stress termed strength (essentially a function of the material, temperature and pressure) is reached, solids diverge from the linear elastic behaviour and eventually fail, in either a brittle or ductile manner. The material is termed brittle if it fails by fracture or ductile if it fails by flow. In models of lithospheric stress, instantaneous plastic failure may be used to predict the occurrence of brittle failure. Plastic failure is considered in section 3.5.

3.3 Derivation of the element equations for elastic stress analysis

Before deriving the equations of the finite element method it is necessary to introduce the concept of shape function. The shape functions are interpolation polynomials that relate the position within an individual element to its nodal location. The displacements, from which the strains and stresses are derived, are also described by interpolation functions. As an example consider the one dimensional element shown in Fig. 3.1 with nodes i and j placed at distances x_i and x_j from the origin respectively.

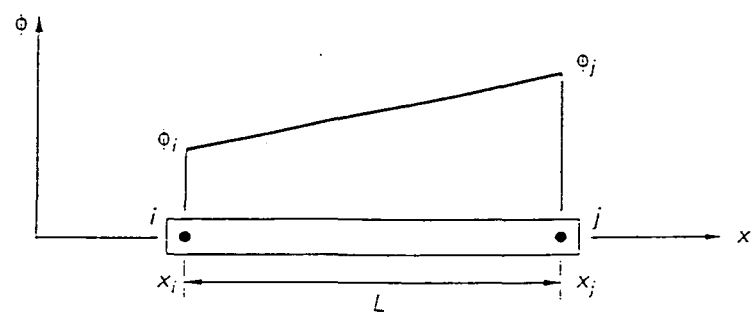

Fig. 3.1 Simplex element example to illustrate the concept of shape function. The one-dimensional element has two nodes i and j placed at distances x_i and x_j from the origin. The interpolation function ϕ is a linear function of x (after Fagan, 1992).

The general form of the interpolation function in this element is,

$$\phi = \alpha_1 + \alpha_2 x, \tag{3.5}$$

where α_1 and α_2 are constants and x is the distance from the origin. The constants can be found by evaluating ϕ at each node,

$$\alpha_1 = \frac{\phi_i x_j - \phi_j x_i}{x_j - x_i} = \frac{\phi_i x_j - \phi_j x_i}{L}, \tag{3.6}$$

$$\alpha_2 = \frac{\phi_j - \phi_i}{x_j - x_i} = \frac{\phi_j - \phi_i}{L}. \tag{3.7}$$

Substitution of Eq. 3.6 and Eq. 3.7 into Eq. 3.5 gives,

$$\phi = \frac{x_j - x}{L}\phi_i + \frac{x - x_i}{L}\phi_j, \tag{3.8}$$

that is,

$$\phi = N_i\phi_i + N_j\phi_j, \tag{3.9}$$

where $N_i = (x_j - x)/L$ and $N_j = (x - x_i)/L$ are the shape functions. Each node is associated with one shape function. As the order of the interpolation function (and the number of constants to determine) increases, the number of nodes defining the element must also increase.

Suppose for instance that the interpolation function ϕ is the displacement, and that a two-dimensional element with eight nodes is being considered. The displacement at any point in the element can be specified by (Fagan, 1992),

$$\begin{Bmatrix} u \\ v \end{Bmatrix} = \begin{bmatrix} N_1 & 0 & \cdots & N_8 & 0 \\ 0 & N_1 & \cdots & 0 & N_8 \end{bmatrix} \begin{Bmatrix} u_1 \\ v_1 \\ \vdots \\ u_8 \\ v_8 \end{Bmatrix}, \tag{3.10}$$

where the shape functions N_1 to N_8 are quadratic polynomials, u_1 and v_1 are the displacements at node 1 in the x and y directions respectively, and so on. In condensed form Eq. 3.10 may be written as,

$$\mathbf{u} = \mathcal{N}\mathbf{U}, \tag{3.11}$$

where $\mathbf{u}$ is the generic displacement vector at any point in the element, $\mathcal{N}$ is the shape function matrix and $\mathbf{U}$ is the vector of nodal displacements.

The equations of equilibrium in the finite element method are obtained using the variational approach to mechanics, more specifically the principle of virtual work (e.g. Lanczos, 1970). The principle demands that the work of the applied forces is zero for any infinitesimal variation of the equilibrium configuration of the system, and leads to the condition that the potential energy must assume a minimum for equilibrium to be stable. Consider that an infinitesimal small displacement $\delta\mathbf{u}$ is imposed on the nodes of a finite element with volume V and surface S. The virtual work done by the external loads acting on the element is,

$$\delta w = \int \delta \mathbf{u}^T \mathbf{G} dV + \int \delta \mathbf{u}^T \mathbf{P} dS + \delta \mathbf{u}^T \mathbf{C}, \tag{3.12}$$

where $\mathbf{G}$ is the vector of the body forces (e.g. gravitational), $\mathbf{P}$ is the vector of the surface tractions and $\mathbf{C}$ is the vector of nodal loads. The superscript ^{T} denotes a matrix or column vector transpose.

The virtual strain energy is,

$$\delta\Omega = \int \delta\epsilon^T \boldsymbol{\sigma} dV, \tag{3.13}$$

where $\boldsymbol{\epsilon}$ is the vector of total strains and $\boldsymbol{\sigma}$ is the vector of the stress components.

The aim of the following derivation is to express the potential energy of the model ($\Pi = \Omega - w$) in terms of the nodal displacements ($\mathbf{u}$). Substitution of Eq. 3.11 into Eq. 3.12 gives,

$$\delta w = \int \delta \mathbf{u}^T \mathcal{N}^T \mathbf{G} dV + \int \delta \mathbf{u}^T \mathcal{N}^T \mathbf{P} dS + \delta \mathbf{u}^T \mathbf{C}. \tag{3.14}$$

The theory of elasticity is used to set up the equations relating the stress, the strain and the displacements. Stress and stain are related through the laws of elasticity by,

$$\boldsymbol{\sigma} = \mathcal{D}(\boldsymbol{\epsilon} - \boldsymbol{\epsilon}_0) + \boldsymbol{\sigma}_0, \tag{3.15}$$

where $\boldsymbol{\epsilon}_0$ is the initial strain vector, $\boldsymbol{\sigma}_0$ is the initial stress vector and $\mathcal{D}$ is the elásticity matrix. Under the plane stress assumption the elasticity matrix is,

$$\mathcal{D} = \frac{E}{1-\nu^2} \begin{bmatrix} 1 & \nu & 0 \\ \nu & 1 & 0 \\ 0 & 0 & \frac{1-\nu}{2} \end{bmatrix}. \tag{3.16}$$

Under the plane strain assumptions it becomes,

$$\mathcal{D} = \frac{E}{(1+\nu)(1-2\nu)} \begin{bmatrix} 1-\nu & \nu & 0 \\ \nu & 1-\nu & 0 \\ 0 & 0 & \frac{1-2\nu}{2} \end{bmatrix}. \tag{3.17}$$

Substitution of Eq. 3.15 into Eq. 3.13 gives,

$$\delta\Omega = \int \delta\epsilon^T \mathcal{D}\epsilon dV - \int \delta\epsilon^T \mathcal{D}\epsilon_0 dV + \int \delta\epsilon^T \mathcal{D}\sigma_0 dV. \tag{3.18}$$

Since $\mathcal{D}^T = \mathcal{D}$ we deduce that $\delta(\frac{1}{2}\epsilon^T\mathcal{D}\epsilon) = \delta\epsilon^T\mathcal{D}\epsilon$. Consequently, integrating the variations δw and $\delta\Omega$ leads to the potential energy of the element,

$$\Pi = \left\{\frac{1}{2}\int \epsilon^T \mathcal{D}\epsilon dV - \int \epsilon^T \mathcal{D}\epsilon_0 dV + \int \epsilon^T \mathcal{D}\sigma_0 dV\right\} - \\ -\left\{\int \mathrm{u}^T \mathcal{N}^T \mathrm{G} dV + \int \mathrm{u}^T \mathcal{N}^T \mathrm{P} dS + \mathrm{u}^T \mathrm{C}\right\}. \tag{3.19}$$

The strain results from displacement gradients (Eq. 3.1) and so it can be equated to the nodal displacements as,

$$\epsilon = \mathcal{B}\mathrm{u}, \tag{3.20}$$

where $\mathcal{B}$ is the strain matrix, derived by the proper differentiation of the shape functions. Substituting Eq. 3.20 into Eq. 3.19, and summing the energies of all the elements in the model, gives the potential energy of the whole system,

$$\Pi = \sum\left\{\frac{1}{2}\int \mathrm{u}^T \mathcal{B}^T \mathcal{D}\mathcal{B}\mathrm{u} dV - \int \mathrm{u}^T \mathcal{B}^T \mathcal{D}\epsilon_0 dV + \int \mathrm{u}^T \mathcal{B}^T \mathcal{D}\sigma_0 dV\right\} - \\ -\sum\left\{\int \mathrm{u}^T \mathcal{N}^T \mathrm{G} dV + \int \mathrm{u}^T \mathcal{N}^T \mathrm{P} dS + \mathrm{u}^T \mathrm{C}\right\}. \tag{3.21}$$

For the model to be in equilibrium its total potential energy must be a minimum. Hence, for the n components of the displacement vector (two for each node in a 2D model) we must have,

$$\frac{\partial\Pi}{\partial u_1} = \frac{\partial\Pi}{\partial v_1} = \cdots = \frac{\partial\Pi}{\partial v_n} = 0. \tag{3.22}$$

This gives n equations in n unknowns. In a condensed form it can be written as,

$$\frac{\partial\Pi}{\partial \mathrm{u}_s} = 0, \tag{3.23}$$

where $\mathbf{u}_s$ is the vector of all the degrees of freedom in the model. Differentiation of Eq. 3.21 yields the stiffness equation, which is the fundamental equation of the finite element method,

$$\mathcal{K}\mathbf{u}_s = \mathbf{F}, \tag{3.24}$$

where

$$\mathcal{K} = \sum \int \mathcal{B}^T \mathcal{D} \mathcal{B} dV, \tag{3.25}$$

is known as the global stiffness matrix and,

$$\mathbf{F} = \sum \left\{ \int \mathcal{B}^T \mathcal{D} \epsilon_0 dV - \int \mathcal{B}^T \mathcal{D} \sigma_0 dV + \int \mathcal{N}^T \mathbf{G} dV + \int \mathcal{N}^T \mathbf{P} dS + \mathbf{C} \right\}, \tag{3.26}$$

is the global force vector. The global force vector includes the contribution from the initial strains ϵ_0, the initial stresses σ_0, the body forces $\mathbf{G}$, the surface tractions $\mathbf{P}$ and finally the nodal forces $\mathbf{C}$.

The stiffness matrix depends only on the geometry of the model (through $\mathcal{B}$) and on the material properties (through $\mathcal{D}$). A solution to Eq. 3.24, by matrix inversion, can be accomplished using the Gaussian elimination method (e.g. Conte and de Boor, 1981). The strains are computed from the displacements $\mathbf{u}_s$ using Eq. 3.20 and the stresses are then obtained from the strains using Eq. 3.15.

Throughout the modelling triangular and quadrilateral isoparametric elements are used. The elements are isoparametric when the displacement interpolation function and the geometric interpolation function are polynomials of the same order (Fagan, 1992). Elements with mid- point nodes along their sides, such as those used in this thesis, have quadratic interpolation functions. Isoparametric elements of order 2 or higher are favoured not only because of their increased accuracy but also because they allow curved element boundaries. They are particularly useful in problems involving bending.

As seen above, the finite element method involves integration of functions of the shape function (Eq. 3.25 and Eq. 3.26). For elements with order 2 or higher the integrations must be performed numerically. The numerical method for carrying out the integrations is Gauss quadrature (e.g. Conte and de Boor, 1981). This technique

requires the limits of integration to be -1 to 1, or 0 to -1, and so a transformation of coordinates is needed. Instead of expressing the coordinates of the nodes in the global coordinate system, they are expressed in natural coordinates (Fig. 3.2). For quadrilateral elements with eight nodes, the shape functions are defined in terms of natural coordinates as,

$$
\begin{aligned}
N_1 &= -\frac{1}{4}(1-\xi)(1-\eta)(1+\xi+\eta) & N_2 &= \frac{1}{2}(1-\xi^2)(1-\eta) \\
N_3 &= -\frac{1}{4}(1+\xi)(1-\eta)(1-\xi+\eta) & N_4 &= \frac{1}{2}(1+\xi))(1-\eta^2) \\
N_5 &= -\frac{1}{4}(1+\xi)(1+\eta)(1-\xi-\eta) & N_6 &= \frac{1}{2}(1-\xi^2)(1+\eta) \\
N_7 &= -\frac{1}{4}(1-\xi)(1+\eta)(1+\xi-\eta) & N_8 &= \frac{1}{2}(1-\xi))(1-\eta^2).
\end{aligned}
\tag{3.27}
$$

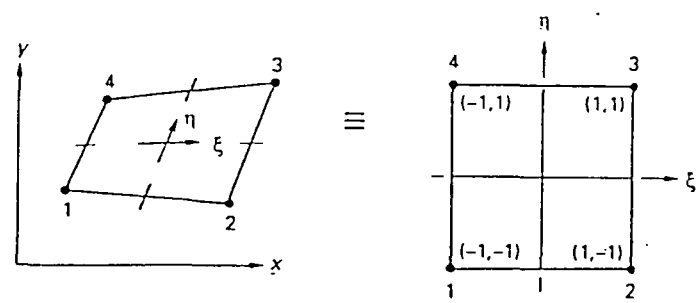

Fig. 3.2 Natural coordinate system for the simplest two-dimensional quadrilateral element (with four nodes, one at each corner). For this element the axes ξ and η are defined by lines drawn from the mid-side of opposite faces (after Fagan, 1992).

The calculations of the element equations then need a change of the integration variable. For instance,

$$\int_V \mathcal{B}^T \mathcal{D} \mathcal{B}\, dV = t \int \mathcal{B}^T \mathcal{D} \mathcal{B}\, dxdy = t \int_{-1}^{1} \int_{-1}^{1} \mathcal{B}(\xi,\eta)^T \mathcal{D} \mathcal{B}(\xi,\eta) |J| d\xi d\eta, \tag{3.28}$$

where t is the thickness of the element, considered 1 in the modelling, and $|J|$ is the Jacobian of the coordinate transformation.

Gauss quadrature works by evaluating the function to be integrated at a number of sampling points (called the Gauss points), multiplying these values by weighting functions and summing the products,

$$\int_{-1}^{1} \int_{-1}^{1} f(\xi,\eta) d\xi d\eta = \sum_{i=1}^{n} H_i f(\xi_i \eta_i), \tag{3.29}$$

where n is the number of integration points (n points evaluate a polynomial of order $2n-1$ exactly) and H_i is the weighting function at the sample point i with natural coordinates (η_i,ξ_i). The location of the Gauss points and the values of the weighting functions are available in the literature (e.g. Fagan, 1992).

3.4 Viscoelastic analysis

Fluids show steady-state flow under constant deviatoric stress. Newtonian or linearly viscous fluid behaviour is characterised by a strain rate linearly proportional to the stress, and is described by,

$$\dot{\epsilon} = \frac{\sigma^D}{2\eta}, \tag{3.30}$$

where η is the dynamic viscosity of the fluid and σ^D is the deviatoric stress.

Materials that deform elastically on short time scales and viscously on long time scales, such as the mantle and possibly the lower crust, are represented by the viscoelastic rheology. In a viscoelastic (or Maxwell) body the instantaneous elastic deformation is followed by linear viscous deformation. The mechanical analogue consists of a dashpot (a fluid filled cylinder containing a porous piston) in series with a spring. The rheological equation for a Maxwell body is obtained by superposition of the elastic and viscous responses (e.g. Ranalli, 1995),

$$\dot{\epsilon} = \frac{\dot{\sigma^D}}{2\mu} + \frac{\sigma^D}{2\eta}, \tag{3.31}$$

where $\mu = E/2(1+\nu)$ is the rigidity. The strain under constant stress σ_0 is,

$$\epsilon = \frac{\sigma_0}{2\mu} + \frac{\sigma_0}{2\eta}t, \tag{3.32}$$

where t is time. For a constant imposed strain the initial elastic response is gradually converted into permanent viscous deformation. In that case $\dot{\epsilon} = 0$ and solving Eq. 3.31 in order to get the stress gives,

$$\sigma^D = \sigma_0 exp\left[-\frac{\mu}{\eta}t\right]. \tag{3.33}$$

After the initial elastic response the deviatoric stresses approach zero exponentially, with a time constant $t_m = \eta/\mu$ called the Maxwell relaxation time.

The initial strain method is used to implement the time-dependent viscoelastic behaviour in the finite element programme. The basis of the method is the division of the total stress relaxation time in time increments, of specified length. At each time increment the creep strain if found using the Newton-Raphson method (Owen and Hinton, 1980). For simplicity only the fundamental steps of the method are listed:

1. Given the applied loads, material properties and model geometry, the elastic stresses σ_0 are computed at $t = 0$.

2. Assuming that the stress remains unchanged during the time increment, the creep strains at the end of the time increment are computed according to $\epsilon = \dot{\epsilon}\, t$.

3. The creep strains are set up as initial strains, and a new global force vector is calculated.

4. The stiffness equation is solved for the new force vector, to find the stresses at the end of the time increment.

5. The residual force vector is calculated and subsequently used to correct the initial solution.

6. The obtained stress is used as σ_0 at the onset of the next time increment, and the whole process is repeated.

3.5 Elasto-viscoplastic analysis

Viscous rheology is unable to describe the behaviour of materials that only undergo non-elastic deformation when the stress reaches a critical value termed the *yield stress*. The yield stress of viscous bodies is zero, and therefore they flow at any stress. Materials that behave elastically below the yield stress, but flow above it, are called

elasto-plastic. Perfectly plastic rheology describes the behaviour of materials that fail instantaneouly without loss of continuity, in contrast with viscous deformation which is time dependent. An empirical failure criterion may be used to predict the occurrence of plastic failure. The Von-Mises criterion states that plastic yielding occurs when

$$(\sigma_1 - \sigma_2)^2 + (\sigma_1 - \sigma_3)^2 + (\sigma_2 - \sigma_3)^2 = 6J_2 = 2\sigma_Y{}^2, \tag{3.34}$$

where J_2 is the second invariant of the deviatoric stress and σ_Y is the Von-Mises yield strength (Jaeger, 1969). When there is no strain hardening the Von-Mises criterion also specifies the relation between the stress components after failure.

Another rheological model combining elastic and plastic rheology is the elasto-viscoplastic body. Its behaviour is illustrated in Fig. 3.3.

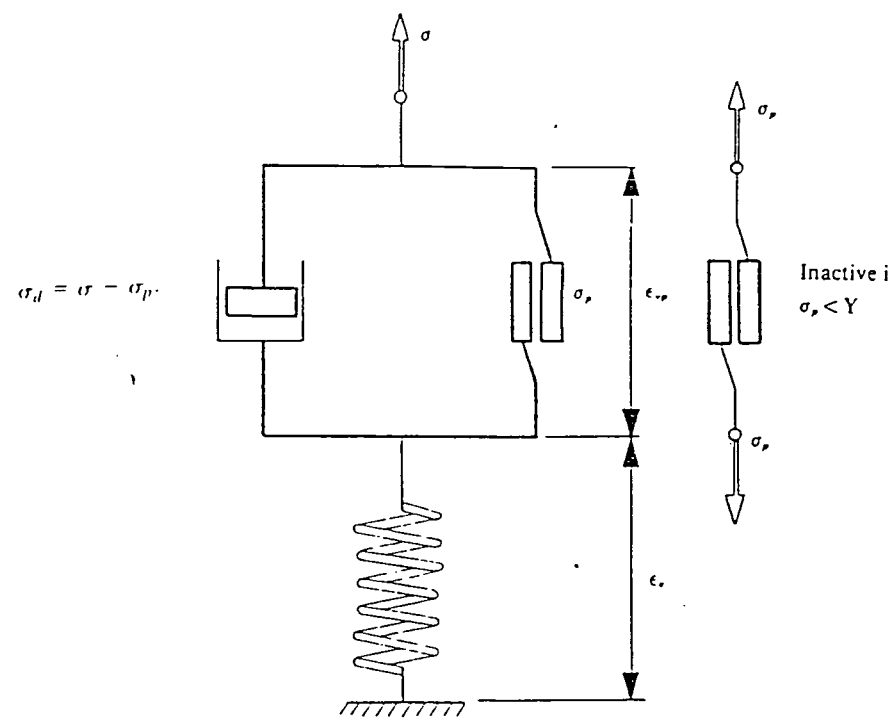

Fig. 3.3 Mechanical analogue of the elasto-viscoplastic model. The spring provides the instantaneous elastic response. The friction slider develops a stress σ_p becoming active only when the stress σ exceeds the yield strength Y. The excess stress $\sigma_d = \sigma - \sigma_p$ is released by the dashpot. The total strain is the sum of the elastic ϵ_e and viscoplastic ϵ_{vp} strains (after Owen and Hinton, 1980).

Instantaneous elastic response below the yield stress is provided by the linear spring. A stress σ_p arises on the slider, only when the applied force exceeds the frictional resistance, or in other words when the stress is at or slightly above the yield stress. The excess stress $\sigma_d = \sigma - \sigma_p$ is released by the dash pot. The dash pot represents linear viscous flow, which occurs above the yield strength, with a strain rate proportional to σ_d. The stress level may instantaneously exceed the yield strength, but the viscous solution tends asymptotically to the elasto-plastic solution as the excess stress progressively decays.

The elasto-viscoplastic model can be used to simulate elastic-perfectly plastic behaviour (Owen and Hinton, 1980). Throughout the modelling when elasto-plastic rheology is referred to I am in fact using the elasto-viscoplastic model. The numerical procedure to evaluate the viscous response in the elasto-viscoplastic analysis is similar to that used for viscoelastic analysis. The actual viscosity value imparted to elasto-viscoplastic materials is not relevant, because the transient viscous response is a technical procedure to achieve the elasto-plastic solution. The viscosity controls the amount of time required to obtain viscous stress relaxation.

3.6 The dual node technique for fault modelling

The method of modelling faults used in this thesis was initially developed by Mithen (1980) based on the work of Goodman et al. (1968). The fault is represented as a plane boundary between pairs of elements. The nodes defining the fault are 'dual' because each node on one side of the fault has a counterpart on the other side. Initially the dual nodes have the same spatial coordinates, but they can move independently along the fault plane.

The fault is divided into fault elements and for each of these a local stiffness matrix is calculated. The local stiffness matrix ensures the fault planes remain in contact but allows sliding to take place. The derivation of the local stiffness matrix, which is expressed in terms of the fault's shear and normal stiffness (k_s and k_n, respectively), is here omitted for the sake of simplicity.

The work done on a fault section can be written as (Mithen, 1980),

$$w = \frac{1}{2}\mathbf{u}_f{}^T K_f \mathbf{u}_f, \tag{3.35}$$

where $\mathbf{u}_f$ is the vector of nodal displacements in the fault section, and K_f is the stiffness matrix for the fault section. Minimizing the work with respect to the nodal displacements gives,

$$\frac{\partial w}{\partial \mathbf{u}_f} = K_f \mathbf{u}_f = 0 \tag{3.36}$$

The global stiffness equation for a model containing a fault is therefore (from Eq. 3.24),

$$(\mathcal{K} + K_f)\mathbf{u}_s = \mathbf{F}. \tag{3.37}$$

The version of the DURHAM TECTONIC FINITE ELEMENT PROGRAM which I used could only work with two limiting values of the frictional fault strength. The faults modelled have either zero frictional strength ($k_s = 0$) or a frictional strength so high that displacement along the fault is prevented ($k_s = 10^{16}$). In order to maintain the fault closed, the fault normal stiffness k_n is always assigned a high value such as 10^{16}.

Chapter 4

The anomalous subsidence of the East Pacific Rise

4.1 Introduction

The stress distribution and the ridge push developed in oceanic lithosphere have been modelled by Bott (1991) for normal and hot-spot affected ridges. He modelled a semi-ocean bordered by a passive margin and continental crust. The same methodology, restricted to young oceanic lithosphere, is now used to investigate the stress field in the region of Easter microplate. The original aim of this study was to explore the relation between the anomalous subsidence of the Pacific plate and the existence of Easter microplate.

The anomalous asymmetric subsidence of the East Pacific Rise, at about 20°, is assumed to be due to a thermal anomaly in the asthenosphere, as indicated by geophysical observations and other modelling (section 1.10). To begin with, the thermal anomaly in the asthenosphere is estimated to fit the anomalously shallow bathymetry observed on the western flank of the rise. Then, the stress field is modelled by elastic/viscoelastic finite element analysis. Comparison between the symmetric normal model and the asymmetric anomalous model allows me to analyse the effect of the asthenospheric thermal anomaly. Finally, the results are discussed

in the light of observations.

4.2 Grid and rheology

The models represent a vertical section of the Earth across the East Pacific Rise. They include an elastic layer, representing the strong upper lithosphere, overlying a viscoelastic layer representing the lower lithospheric mantle. Beneath the lithosphere, the asthenospheric mantle is also represented by a viscoelastic material, but with a lower viscosity.

The finite element grid used in the modelling is shown in Fig. 4.1. The grid contains 104 isoparametric elements, 99 of which are quadrilateral and 5 are triangular. The elastic and the viscoelastic lithospheric layers are each only one element thick.

The lateral extent of the grid is 1200 km on each side of the East Pacific Rise. The spreading velocities observed at about 19°S are 65 mm/yr for the Pacific plate and 80 mm/yr for the Nazca plate (Cormier et al., 1994). Using these velocities the ages at the ends of the model are 18.5 Ma and 15 Ma on the western and eastern flanks of the East Pacific Rise respectively.

The vertical extent of the grid is 400 km. Fleitout and Froidevaux (1982) suggested that mass anomalies beneath the 200-300 km depth do not contribute to topography, so a maximum depth of 400 km should be enough to include density anomalies which affect the seafloor subsidence.

The structure of the grid in the ridge region, at the centre of the model, is more detailed to allow the inclusion of density anomalies related to the asthenosphere upwelling. Also, to simulate the ascent of the asthenosphere to the surface, the viscoelastic asthenospheric rheology is used in the central elements of the grid up to the surface. The width of the surface viscoelastic element at the ridge axis is 2 km.

Fig. 4.1 Finite element grid used in the modelling. It represents a cut across the East Pacific Rise, at about 20°S. At the centre of the grid the column of elements 10 km wide represents the mid-ocean ridge conduit. At the surface, the conduit narrows to 2 km wide. On the ridge flanks, the one element thick top layer corresponds to the elastic lithosphere, which is delimited at the base by the 600°C isotherm of Parsons and Sclater (1977) model. The layer below, also one element thick, corresponds to the viscoelastic lithosphere, which is delimited at the base by the 1000°C isotherm. The asthenosphere extends from the base of the lithosphere to 400 km depth. An average half spreading rate of 65 mm/yr in the Pacific plate (on the left flank of the ridge) and an average half spreading rate of 80 mm/yr in the Nazca plate (on the right flank of the ridge) were assumed to compute the thickness of the elastic and viscoelastic lithospheric layers.

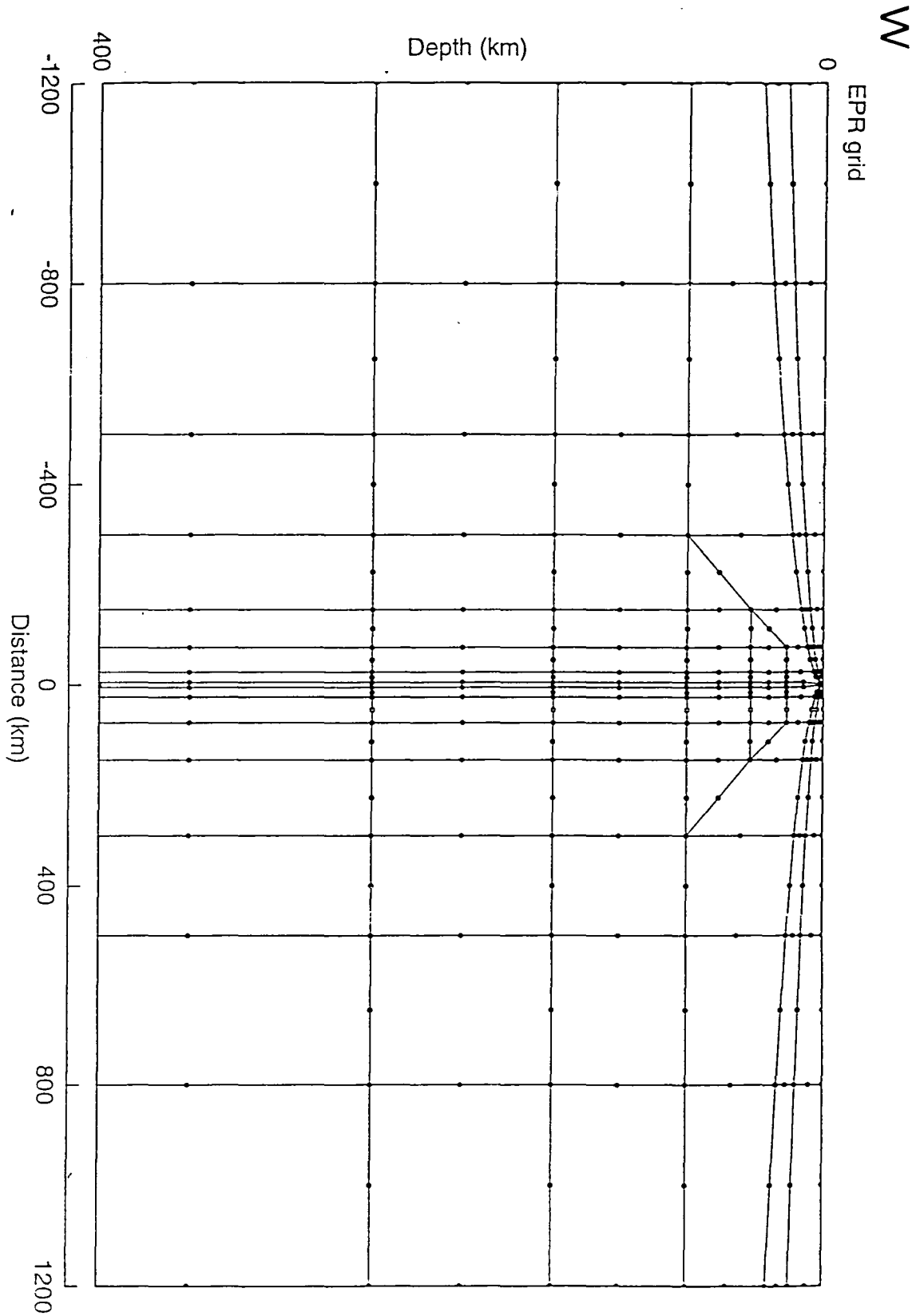
W
EPR grid
0
Depth (km)
400
-1200
-800
-400
0
400
800
1200
Distance (km)
E

The isotherms predicted by the half space cooling model (David and Lister, 1974) are used to delimit the different rheologic layers,

$$T(z,t) = T_m erf(z/2\sqrt{kt}), \tag{4.1}$$

where $T(z,t)$ is the temperature, which is a function of the depth, z, and of age, t. T_m is the mantle temperature at the ridge axis and k is the thermal diffusivity of the mantle.

Flexural studies show that the lithosphere responds to long term surface loads like a thin elastic layer overlying a weak fluid (e.g. Walcott, 1970). When plotted as a function of lithospheric age, the estimated effective elastic plate thickness lies between the depths of the 300°C and 600°C isotherms, according to the thermal model of Parsons and Sclater (1977) (Watts et al., 1980). According to the same thermal model, the 800°C isotherm limits the maximum depth of the oceanic intraplate seismicity (Weins and Stein, 1984; Bergman and Solomon, 1984). As a compromise between the seismicity and flexural indications for the thickness of the stronger upper lithosphere, the 600°C isotherm has been chosen to delimit the base of the elastic layer.

The depth to the top of the low velocity zone inferred from Rayleigh wave dispersion studies in the Pacific approximately follows the 1000°C isotherm of Parsons and Sclater's model (Leeds et al., 1974). For that reason the 1000°C isotherm has been chosen to separate the lower lithospheric mantle from the asthenosphere.

The depth of the isotherms was computed by setting $T(z,x)$ in Eq. 4.1 to 600°C and to 1000°C and solving to obtain the depth. Using the values of the material parameters and thermal model parameters listed in table 4.1, the depth of the 1000°C isotherm (the thickness of the lithosphere, L) as a function of age t is given by,

$$L = 8\sqrt{t}, \tag{4.2}$$

where L is in kilometres and t in million years.

The minimum viscosity value attributed to the viscoelastic materials determines the length of the time step in the initial strain method (section 3.4). Provided

Table 4.1 Modelling parameter values

Young modulus (lithosphere and asthenosphere)	1.75×10^{11}Pa
Poisson's ratio (lithosphere and asthenosphere)	0.27
Viscosity of viscoelastic lithosphere	1.0×10^{22}Pa s
Viscosity of asthenosphere	1.0×10^{20}Pa s
Mantle thermal diffusivity k	0.8 mm^2s
Mantle coefficient of thermal expansion α	3.2×10^{-5}°C^{-1}
Mantle temperature at the ridge axis T_m	1350°C
Mantle reference density ρ_m	3300 kgm^{-3}
Seawater density ρ_w	1030 kgm^{-3}
Half-spreading rate for the Pacific plate	65 mm/yr
Half-spreading rate for the Nazca plate	80 mm/yr
Subsidence rate for the Pacific plate	198 m $Ma^{-1/2}$
Subsidence rate for the Nazca plate	356 m $Ma^{-1/2}$

that the total number of time steps is enough for nearly complete deviatoric stress relaxation to occur in the most viscous material, the actual viscosity values do not influence the results. It is, however, desirable that the different material viscosities do not differ by more than two orders of magnitude. Otherwise the total number of 'small' time steps needed would be excessive, as would be the time needed to run each model. Viscosity values of 10^{22} Pa s and 10^{20} Pa s have been used for the lithospheric mantle and the asthenospheric mantle respectively.

The oceanic crust is neglected in the modelling. There are two main reasons for this. First, away from mid-ocean ridges the crust seems to play only a passive role in plate deformation, as indicated by the lack of intraplate oceanic earthquakes above the Moho (Bergman and Solomon, 1984). Second, a crust with constant thickness and density does not contribute to the density anomalies. Multichannel seismic reflection data in the South Pacific Superswell region indicates that, apart from local crustal thickening beneath the islands and seamounts, the thickness of the crust in this region is normal and uniform(McNutt, 1998).

4.3 Modelling principles

At the onset of the modelling, the surface of the model is horizontal and at 'zero' depth. Density anomalies are specified in the lithosphere and in the asthenosphere. These generate anomalous pressures which produce vertical displacements of the surface of the model, so that isostatic equilibrium can be reached.

The seafloor depth (the depth of the model's surface) and the density structure of the lithosphere, are referenced to the seafloor depth and to the density structure of lithosphere 75 Ma old.

The density anomalies in the asthenosphere, which give rise to the anomalous subsidence, are relative to the reference mantle density $\rho_m = 3300$ kg m^{-3}.

The viscoelastic solution for the specified lithospheric and sublithospheric loading is computed using the initial strain method. As viscous relaxation takes place in the lower layers, the stress concentrates upwards into the elastic layer, as recognised by Kusznir and Bott (1977). The uplift of the surface of the models increases until viscoelastic equilibrium is approached, i.e. until almost complete deviatoric stress relaxation has taken place in the most viscous layer. The process of achievement of viscoelastic equilibrium does not have geological significance because its timescale is much shorter than that of geological processes such as the anomalous subsidence of the East Pacific Rise.

By the time viscoelastic equilibrium is achieved, the surface uplift relative to the initial zero depth must isostatically balance the subsurface mass anomalies. The isostatic equilibrium is flexural and consequently there is a combination of loading and bending stresses. Because the loads in this study are wide (the extent of the load is the extent of the model, 1200 km to each side of the EPR) bending stresses are negligible.

The out-of-plane stress is assumed to be the arithmetic mean of the two in-plane principal stresses. This is equivalent to the assumption of plane strain with a Poisson's ratio of 0.5. In viscoelastic modelling this is conceptually more satisfactory

than the plane strain assumption with a more realistic Poisson's ratio (Table 4.1) because of the high pressures within the Earth (e.g. Whittaker et al., 1992). As a consequence the in-plane deviatoric stresses are equal and opposite.

The 'observed' subsidence rates calculated by Cochran (1986) are used to set up the bathymetric profiles my models try to fit. The average subsidence rate for the Pacific plate is 198 m $Ma^{-1/2}$. For the Nazca plate it is 356 m $Ma^{-1/2}$. These subsidence rates have been derived for lithosphere aged between 0 and 5 Ma (Cochran, 1986), so they are extrapolated to 18.5 Ma on the Pacific plate and to 15 Ma on the Nazca plate. This extrapolation is supported by observations that the anomalous subsidence of the Pacific plate extends out to at least 12 Ma lithosphere (Cochran, 1986). Furthermore, the shallow depths of the South Pacific Superswell are observed out to about 100 Ma lithosphere (McNutt, 1998).

4.4 The density structure in normal plate cooling models

Normal oceanic subsidence results from the cooling of the lithosphere. For lithospheric ages less than about 70 Ma, the normal subsidence rate of 350 m $Ma^{-1/2}$ is predicted by both the half space cooling model and the plate cooling model (Parsons and Sclater, 1977). Assuming a zero depth at the ridge crest, this subsidence rate is used to compute the normal depth of the seafloor, ignoring flexural effects.

The seafloor depth and the density profile of lithosphere 75 Ma old are used as reference. The normal seafloor depth of lithosphere 75 Ma is 3031 m. At each point, the vertical displacement W of the surface of the model relative to the reference depth produces a vertical load that must be balanced by the subsurface loading, that is,

$$(\rho_m - \rho_w)W = \int_0^{L_e} \Delta\rho_1 dz + \int_{L_e}^{L} \Delta\rho_2 dz + \int_L^D \Delta\rho_3 dz, \tag{4.3}$$

where ρ_m is the reference mantle density, ρ_w is the seawater density, $\Delta\rho_1$ is the density anomaly in the elastic lithosphere, with thickness L_e, $\Delta\rho_2$ is the density anomaly in the viscoelastic lithosphere and $\Delta\rho_3$ is the density anomaly in the asthenosphere distributed between the base of the lithosphere, at depth L, and the compensation depth D.

At depths less then the base of 75 Ma old lithosphere, the temperatures in the model are higher than the temperature of the reference lithosphere at the same depth. It is assumed that the density disturbances have only a thermal origin, that is,

$$\Delta\rho = -\rho_m \alpha \Delta T, \tag{4.4}$$

where $\Delta\rho$ is the density anomaly, ρ_m is the reference mantle density, α is the mantle coefficient of thermal expansion and ΔT is the temperature anomaly.

For each grid element in the lithosphere the temperature anomaly ΔT, relative to the temperature of the 75 Ma lithosphere at the same depth, is computed according to

$$\Delta T = T(z,t) - T(z, 75\text{Ma}), \tag{4.5}$$

where T(z,t) is the temperature at depth z and age t, calculated from Eq. 4.1. Eq. 4.4 then gives the density anomalies $\Delta\rho_1$ and $\Delta\rho_2$ in the lithosphere.

The density anomaly in the asthenosphere is determined by solving Eq. 4.3 for $\Delta\rho_3$.

4.5 The density structure in anomalous subsidence models

To model the anomalous subsidence of the western flank of the East Pacific Rise anomalous low densities in the asthenosphere must be combined with $\Delta\rho_3$.

The anomaly in the subsidence ΔS is defined as the difference between the 'observed' subsidence computed by Cochran (1986) and the normal subsidence of the model of Parsons and Sclater (1977)(Fig. 4.2). The anomaly in the subsidence can be related to the anomalous density in the asthenosphere $\Delta\rho_a$ through,

$$\Delta S = \frac{1}{\rho_m - \rho_w} \int_L^D \Delta\rho_a dz. \tag{4.6}$$

Assuming that the anomalous density in the asthenosphere arises from a constant lateral temperature gradient, starting at the ridge crest and extending westwards, Eq. 4.4 and Eq. 4.6 give,

$$\Delta S = \frac{1}{\rho_m - \rho_w} \int_L^D (-\rho_m \alpha G_T x) dz. \tag{4.7}$$

where x is the lateral distance to the ridge axis and G_T is the constant lateral temperature gradient in the asthenosphere. Assuming that G_T is constant throughout depth, the anomaly in the subsidence becomes,

$$\Delta S = -\frac{\alpha\rho_m}{\rho_m - \rho_w}\, x\, G_T\, [D - L)]. \tag{4.8}$$

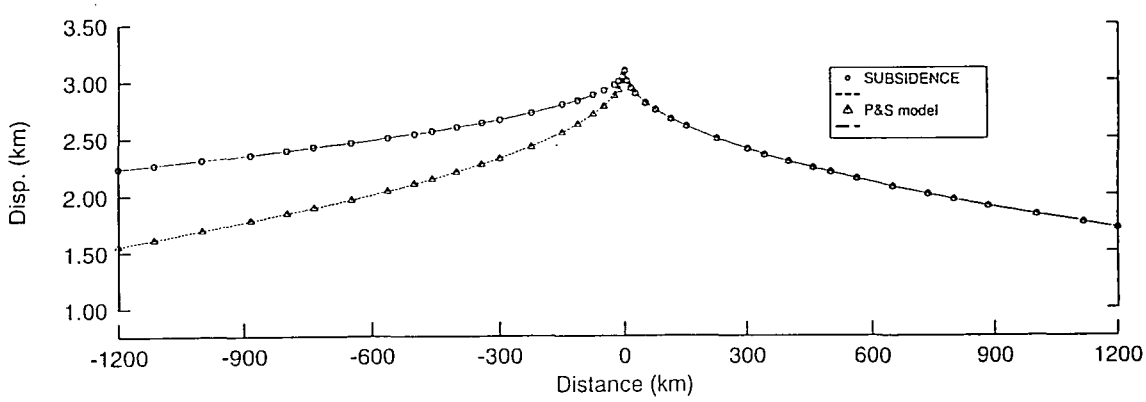

Fig. 4.2 The normal subsidence curve (P&S) corresponds to the empirical subsidence rate determined by Parsons and Sclater (1977). The observed subsidence curve (SUBSIDENCE) corresponds to the subsidence rates calculated by Cochran (1986) from stacked bathymetric profiles between 14°S and 21°S along the EPR. The displacements are relative to the 3031 m depth, which is the normal depth of 75 Ma old seafloor.

Different values of the compensation depth correspond to different temperature gradients in the asthenosphere. There is a good correlation between the pattern

of shallow depth and the slow shear wave velocities in the upper 150 km of the mantle (McNutt, 1998), suggesting that the source for the anomalous subsidence of the western flank of the East Pacific Rise lies above 150 km depth. Therefore, a compensation depth $D = 150$ km is assumed.

Consider the anomaly in the subsidence on the western end of the model. There, $x = 1200$ km, $t = 18.5$ Ma, $\Delta S = 198\sqrt{18.5} - 350\sqrt{18.5} = -653.8$ m and $L = 8\sqrt{18.5} = 34.4$ km. Solving Eq. 4.8 using these values and the constant values listed in table 4.1 we obtain $G_T = 0.101°$ C/km. This result is in agreement with the linear temperature gradient in the asthenosphere beneath the western flank of the East Pacific Rise estimated by Cochran (1986).

4.6 The density structure at the ridge axis

Thermal models of lithospheric cooling such as that of Parsons and Sclater (1977) predict the heat flow and subsidence rates on the ridge flanks but do not reproduce the ridge axial bathymetry. The details of the stress field and temperature structure at the ridge axis are not the subject of this work, so no attempt is made to match the vertical displacements of the surface of the model with the East Pacific Rise axial high. Nevertheless there is evidence for additional low density material beneath the ridge crest and that must be accounted for in the modelling.

Constraints on the magnitude, extent and depth of the density anomalies beneath the EPR have been advanced from the modelling of bathymetric and gravimetric data (e.g. Madsen et al., 1984; Wang and Cochran, 1993). These studies indicate that the density anomalies are concentrated within 5 to 10 km from the ridge axis, and that the product of the anomaly and its depth extent is within the range of 10^5 to 10^6 kg/m^2. A density anomaly of this magnitude has been specified at the ridge axis. It is confined to a triangular shaped conduit 2 km wide at the surface and 10 km wide at the bottom, reaching a maximum depth of 20 km.

4.7 Boundary conditions

The nodes at the left and right ends of the model are constrained to zero horizontal displacement but remain free vertically. These constraints allow us to determine the force exerted by the ridge in the absence of underside drag.

Free boundary conditions are used at the base of the model, representing an inviscid substratum at 400 km depth without density change.

Isostatic boundary conditions are applied at the surface of the model, representing the bathymetric load relative to 75 Ma ocean floor. The isostatic boundary conditions are restoring forces that must be applied when vertical displacements change the vertical loading. The restoring forces are proportional to the product of the vertical displacement at the surface and the change in density. Because the crust is neglected, the change in density is the difference between the seawater density ρ_w and the reference mantle density ρ_m. The isostatic boundary conditions effectively constrain the surface of the model in the vertical direction, so no further constraints are necessary to guarantee the convergence of the finite element program to a solution.

4.8 Presentation of the models

In the stress diagrams only the nearest to horizontal deviatoric stresses are displayed, as the in-plane deviatoric stresses are equal but opposite. The stresses are averaged over the Gauss points and plotted at the centre of each element. In the elastic layer, which is only one element thick, this implies that the small bending stresses in the layer are averaged out. Tensional stresses are represented by a broken line, and compressional stresses by a solid line. When the magnitude of the stress is small, it is often not possible to discern if the line is solid or broken. In such case the stress sign is indicated in the legend of the figure. The stress scale is displayed at the right top of the diagrams and is the same for all models.

Two stress diagrams, with different horizontal scales, are displayed in each figure. The bottom diagram shows the whole length of the model and the stress in the elements away from the ridge. The top diagram is an enlargement of the central part of the model and shows the stresses within 150 km of the ridge axis. Only the top 40 km of the models is depicted, because the deviatoric stress below is negligible. The name of the model, the compensation depth D, and the total relaxation time T is displayed at the left top of each diagram. Three models are presented:

- Model EPR.C2T has a normal density structure relative to 75 Ma lithosphere, and a stress relaxation time of 25000 yr. It fits the normal, although asymmetric, idealised subsidence profile (Fig. 4.3).
- Model EPR.C2 has the same density structure as model EPR.C2T but a different stress relaxation time of 50000 yr. It also fits the normal idealised subsidence profile (Fig. 4.4).
- Model EPR.A150 has an anomalous density structure in the asthenosphere, and a stress relaxation time of 50000 yr. It fits the anomalously shallow bathymetry observed on the western flank of the East Pacific Rise (Fig. 4.5).

The stress diagrams of models EPR.C2T, EPR.C2, and EPR.A150 are presented in Fig. 4.6, Fig. 4.7, and Fig. 4.8 respectively.

4.9 General description of the results

An important feature common to all models is the viscoelastic surface element at the ridge axis, having the same viscosity as the underlying asthenosphere. Incomplete relaxation of deviatoric stress in this element causes a local decrease in elevation of about 250 m at the ridge axis (Fig. 4.3, Fig. 4.4 and Fig. 4.5). This simulates the head-loss effect caused by the resistance to viscous inflow into a constricted region.

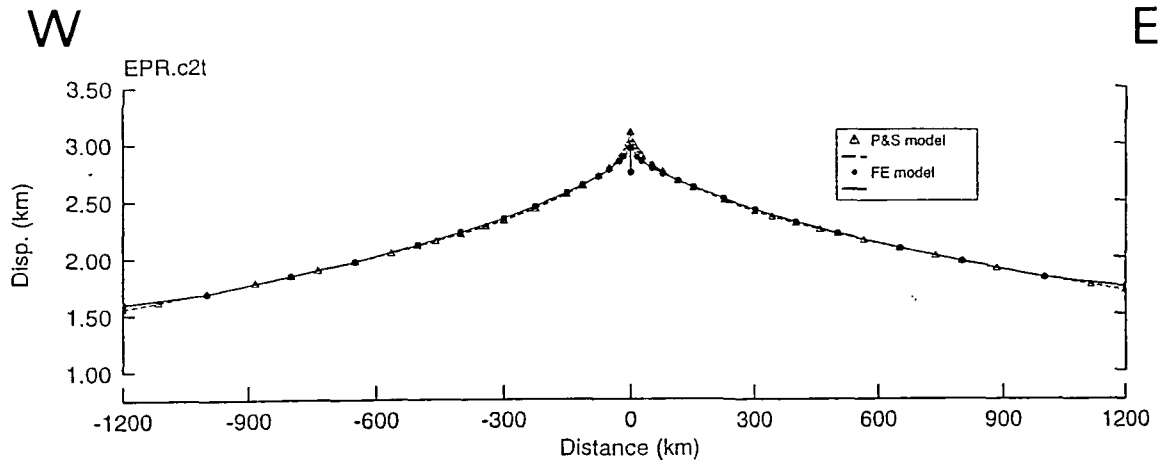

Fig. 4.3 The flexural profile of the finite element model EPR.C2T compared to the Parsons and Sclater (1977) predicted bathymeric profile. Model EPR.C2T is a normal subsidence model with an assumed compensation depth of 150 km. The viscoelastic relaxation time is 25000 yr.

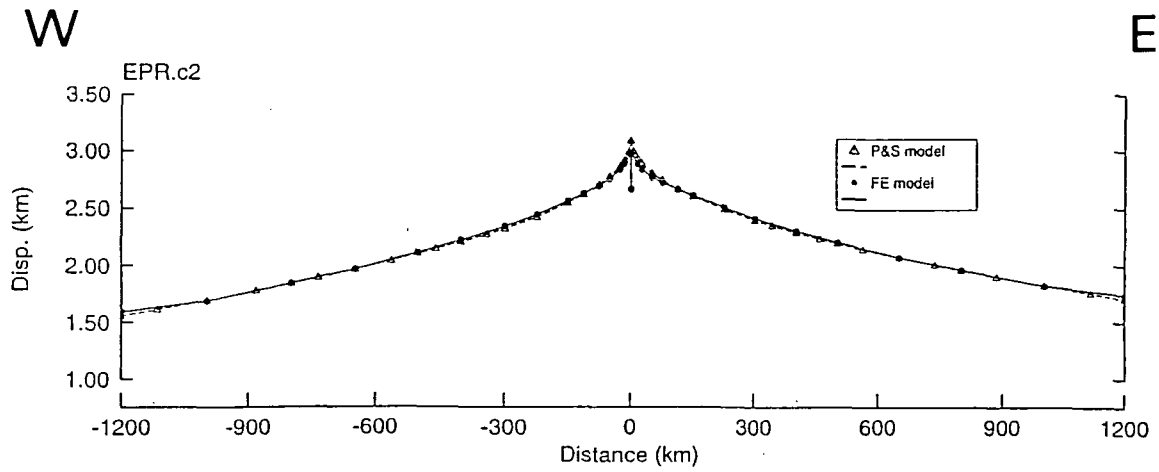

Fig. 4.4 The flexural profile of the finite element model EPR.C2 compared to the Parsons and Sclater (1977) predicted bathymeric profile. Model EPR.C2 is a normal subsidence model with an assumed compensation depth of 150 km. The viscoelastic relaxation time is 50000 yr.

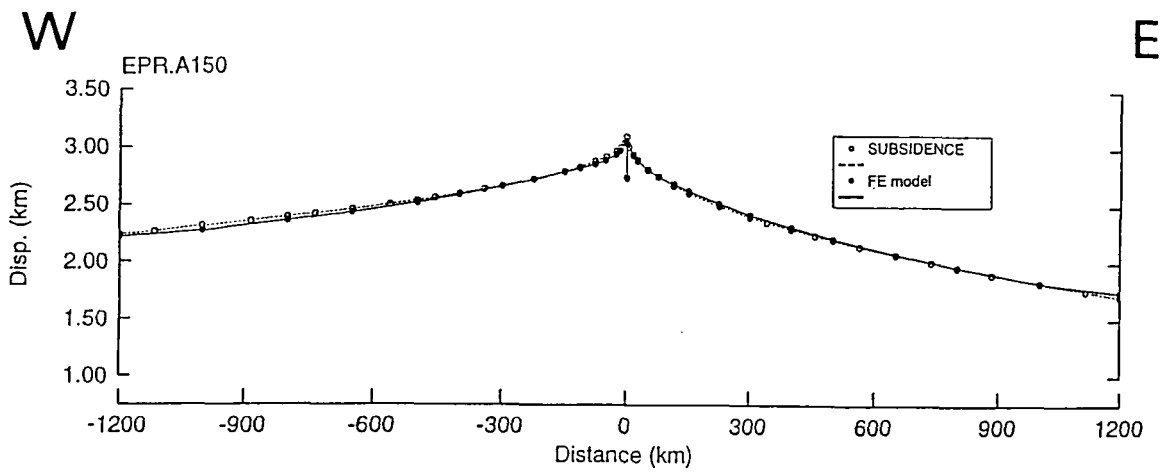

Fig. 4.5 The flexural profile of the finite element model EPR.A150 compared to the subsidence observed by Cochran (1986). Superimposed on the normal density structure referenced to 75 Ma lithosphere, model EPR.A150 contains density anomalies between the base of the lithosphere and the 150 km compensation depth. The density anomalies in the asthenosphere correspond to a temperature gradient of 0.1°C/km starting at the ridge axis and increasing westwards.

The weak element at the ridge axis has a radical effect on the stress pattern. It imposes a push on the adjacent elements and superimposes compressional stresses on the elastic layer. The push results from the increase of the horizontal principal compression in the weak element, as viscoelastic relaxation causes it to approach the high vertical principal compression due to high ridge topography.

Effective complete relaxation of the deviatoric stress in the most viscous material was deliberately not reached, so that small deviatoric compressions remain in the lower lithosphere. The lower lithosphere, defined between the 600°C and the 1000°C isotherms, has a small average strength consistent with the maximum depth of earthquakes delimited by the 800°C isotherm (e.g. Bergman and Solomon, 1984). Also, the base of the lithosphere is usually defined as the depth below which the ductile strength drops below a chosen value (e.g. Kirby, 1980).

The stress pattern in the elastic lithosphere is tensional at the ridge axis and compressional in the plate interiors. The modelling predicts that the transition from tension to compression is gradual and depends fundamentally on the material properties of the weak element at the ridge crest and the extent to which the stress has relaxed.

4.10 Changing the strength of the ridge

The ridge strength can be regarded as the deviatoric stress supported by the axial viscoelastic element. The depth integrated effect of this deviatoric stress constitutes the ridge resistance. The amount of deviatoric stress in the axial viscoelastic element is controlled by the viscoelastic relaxation time.

Model EPR.C2T (Fig. 4.6) has a relaxation time of 25000 yr. It shows a tensile deviatoric stress of 40 MPa at the ridge axis, and a compressive deviatoric stress of 30 MPa at the ends of the model. The transition from tension to compression occurs at $\sim$ 150 km from the ridge axis on both flanks.

Model EPR.C2 (Fig. 4.7) has a relaxation time of 50000 yr. It shows a tensile deviatoric stress of 15 MPa at the ridge axis, and a compressive deviatoric stress of 35 MPa at the ends of the model. The distance from the ridge axis at which the transition from tension to compression occurs is $\sim$ 25 km on the western flank and $\sim$ 75 km on the eastern flank. This asymmetry in the extent of the tensile stresses near the ridge is due to the asymmetry in the spreading rate. At a given distance from the ridge axis the lithosphere is younger, and the density anomalies larger, to the east than to the west.

Although a stress level of 30-35 MPa at 1000 km from the ridge axis is compatible with other stress estimates in oceanic plate interiors (e.g. Bott, 1991), a ridge strength of 40 MPa is certainly too high for the fast spreading East Pacific Rise. A tensile stress of 15 MPa at the ridge axis is more in agreement with estimates of the ridge resistance at fast spreading ridges (section 2.5.3), so a stress relaxation time of 50000 yr is preferred and used in the following section.

Fig. 4.6 The stress pattern of model EPR.C2T. In the elements adjacent to the ridge axis the tensile stress is 42 MPa in the western flank and is 47 MPa in the eastern flank of the ridge. Between 75 km and 150 km from the ridge axis a tensile stress of 2 MPa exists in the western flank and a tensile stress of 7 MPa exists in the eastern flank. Beyond 150 km off axis the stress becomes compressional, reaching 30 MPa at 1000 km from the ridge in both flanks. A small residual stress of less than 5 MPa is present in the viscoelastic layer.

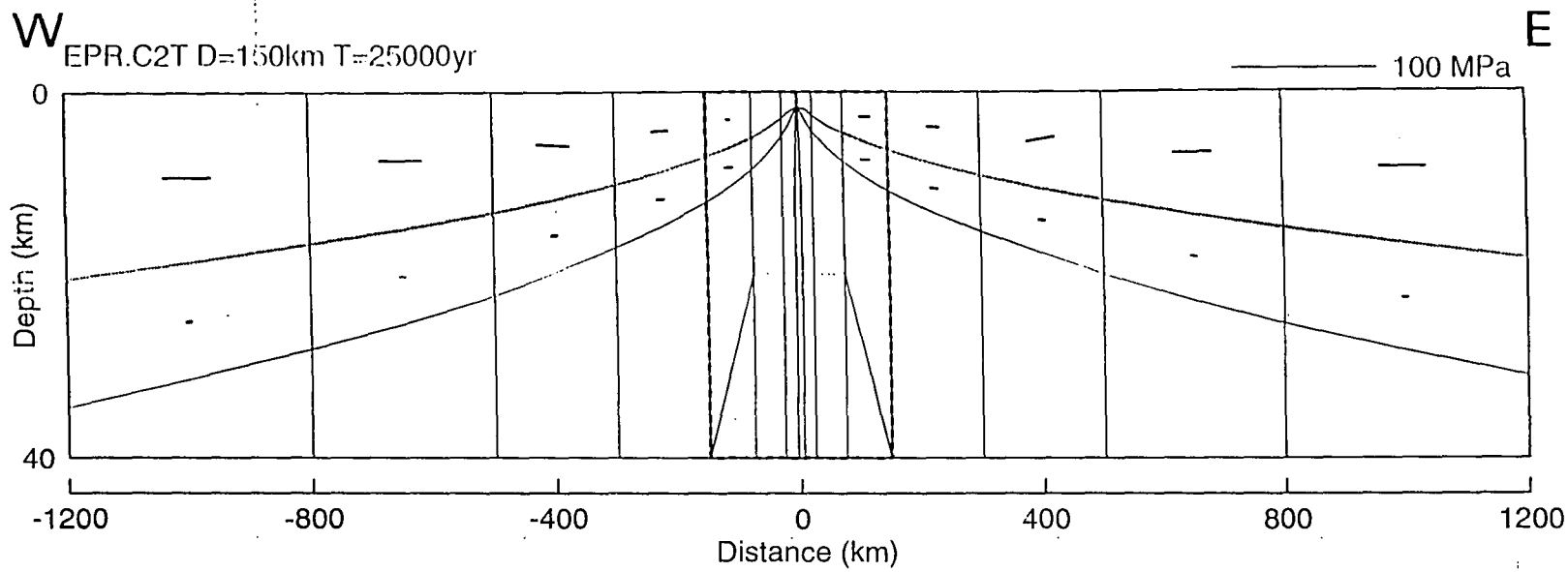
W
E
EPR.C2T D=150km T=25000yr
100 MPa
0
40
Depth (km)
-1200
-800
-400
0
400
800
1200
Distance (km)

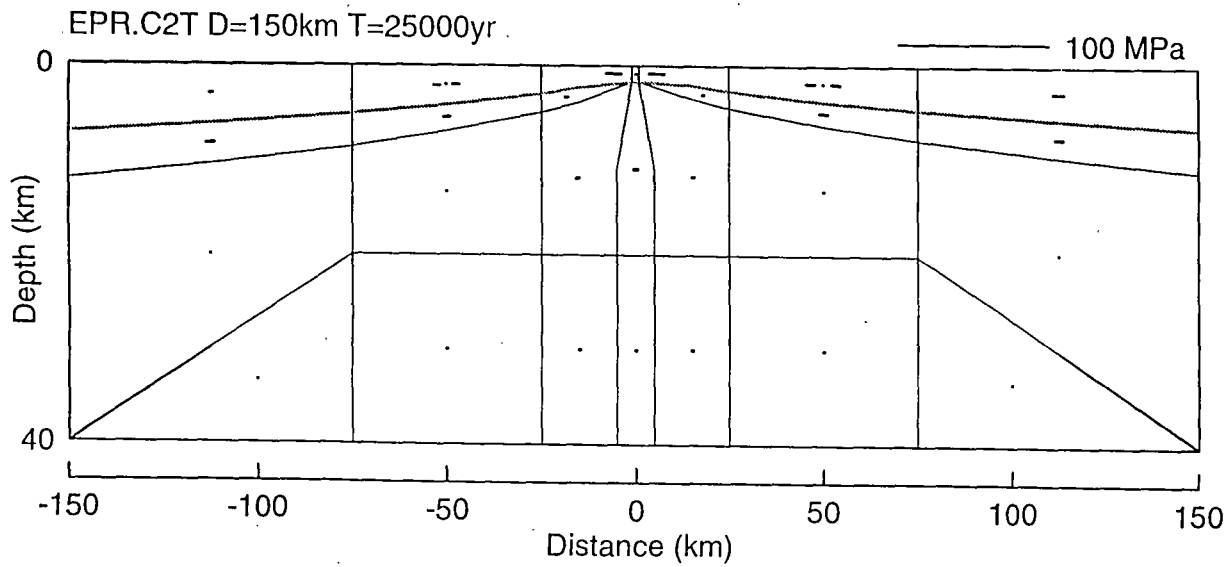
EPR.C2T D=150km T=25000yr
100 MPa
0
40
Depth (km)
-150
-100
-50
0
50
100
150
Distance (km)

Fig. 4.7 The stress pattern of model EPR.C2. At the ridge axis there is a tensile stress of 15 MPa. Between 25 km and 75 km from the ridge axis the stresses are so small that tensile and compressional stresses are not distinguished in the diagrams. Inspection of the output files has shown that a small compressional stress of 3 MPa exists on the western flank, and a small tensile stress of 1.5 MPa exists on the eastern flank. At 1000 km from the ridge axis the compressional stress is about 35 MPa on both flanks.

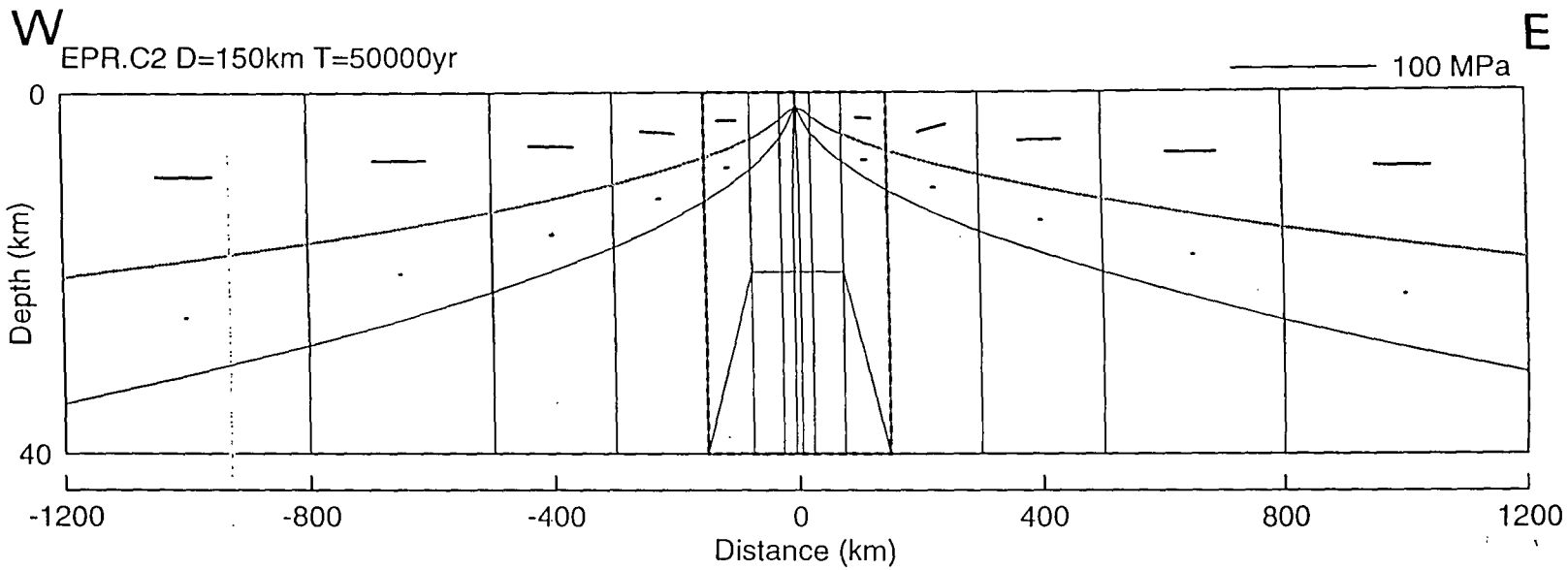
W
E
EPR.C2 D=150km T=50000yr
100 MPa
0
40
Depth (km)
-1200
-800
-400
0
400
800
1200
Distance (km)

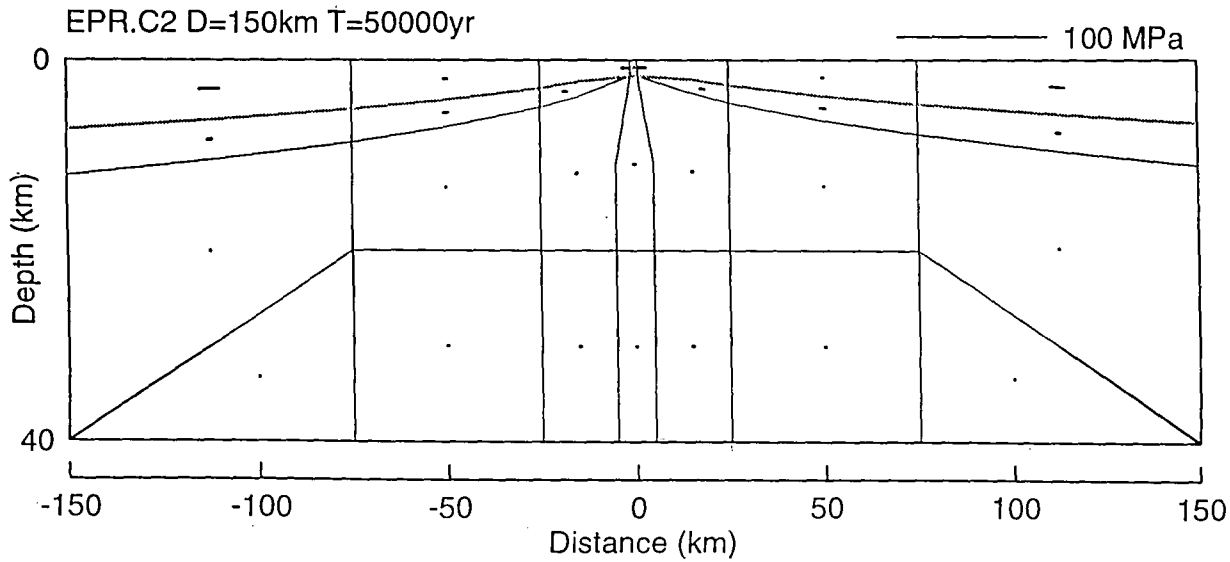
EPR.C2 D=150km T=50000yr
100 MPa
0
40
Depth (km)
-150
-100
-50
0
50
100
150
Distance (km)

4.11 Anomalous versus normal subsidence

To model the anomalous subsidence, density anomalies are added to model EPR.C2, between the base of the lithosphere and the 150 km compensation depth. The resulting model is called EPR.A150. The additional density anomalies correspond to the 0.101°C/km asthenospheric temperature gradient as specified in section 4.5. Although this gradient was calculated for a specific distance from the ridge of 1200 km, the fit between the flexure profile of model EPR.A150 and the anomalous subsidence profile (Fig. 4.5) shows it applies all along the western flank of the ridge.

The stress in model EPR.A150 (Fig. 4.8) becomes compressional at $\sim$ 75 km and $\sim$ 25 km from the ridge axis on the western and eastern flank respectively. At 1000 km from the axis the compressional stress reaches 20 MPa on the western flank, and 40 MPa on the eastern flank. Comparison with the normal subsidence model EPR.C2 (Fig. 4.7) allow us to conclude that (1) the asthenospheric temperature gradient increases the tensile stresses within the western flank of the ridge, and (2) has the greatest effect at the western end of the model where the compressional stresses are reduced by 50%.

The effect of the thermal anomaly beneath the western flank extends across the ridge. Thus, the compressive stresses on the eastern flank are 5-10 MPa higher in the anomalous subsidence model EPR.A150 than in the normal subsidence model EPR.C2. This increase in the compressive stress within the eastern flank can be understood in terms of the normal and shear stresses in the viscoelastic layers. The most obvious effect of the anomalously low asthenospheric densities beneath the western flank is to create an anomalous pressure above the load, which acts at the base of the lithosphere and produces the flexural uplift. The other effect, which is less obvious but gives a substantial contribution to the deviatoric stress, is caused by the advection of mantle material driven by the load. As a result of this advection, eastwardly directed shear stress acts at the base of the elastic layer below the eastern flank of the ridge, increasing the compressive stress there. Beneath the western flank of the rise the advection in the asthenosphere contributes to increase the tension.

Fig. 4.8 The stress pattern of model EPR.A150. In the elements adjacent to the ridge axis the tensile stress is about 10 MPa. Between 25 km and 75 km from the ridge axis it is not possible to distinguish the tensile and the compressional stresses in the diagrams. Inspection of the output files has shown that there is a small tensile stress of 3 MPa on the western flank, and a small compressional stress of 5 MPa on the eastern flank of the rise. On the western flank the stress becomes compressional at a distance of approximately 75 km from the ridge axis, reaching 4 MPa and 20 MPa at 100 km and 1000 km from the ridge respectively. On the eastern flank of the ridge the compressional stress reaches 40 MPa at 1000 km from the ridge axis. The anomalously hot asthenosphere on the western flank greatly reduces the compressional stresses directly above the anomaly, and slightly increases the compressional stress on the other flank of the ridge.

4.12 Estimate of neglected factors

There is an error in the asthenospheric temperature gradient introduced by neglecting the thermal expansion of the lithosphere. Assuming that the thermal expansion of the lithosphere can be approximated by the thermal expansion of a half-space having a time-dependent surface boundary condition, the elevation caused by the thermal expansion of the lithosphere is (Cochran, 1986),

$$el = 0.7523 K t^{3/2} k^{1/2} \alpha \tag{4.9}$$

where K is the asthenospheric temperature gradient per unit of plate age, t is the age, k is the thermal diffusivity and α is the coefficient of thermal expansion of the lithosphere. This elevation is maximum at the end of the western flank of the model, where the age is 18.5 Ma. Using a half space model temperature gradient of 0.1°C/km, a spreading velocity of 65 km/Ma, the coefficient of thermal expansion and the thermal diffusivity values listed in table 4.1, the elevation at the western end of the model predicted by Eq. 4.9 is 60 m. The anomaly in the subsidence at 1200 km from the EPR, used to estimate the temperature gradient in the asthenosphere in section 4.5 is 653.8 m. Therefore, to neglect the thermal expansion of the lithosphere introduces an error of $\sim$ 9% in the computation of the asthenospheric temperature gradient. A change of $\sim$ 9% in the asthenospheric temperature gradient affects the deviatoric stress pattern only marginally.

To estimate the stress arising from possible asthenosphere basal drag, suppose that the asthenosphere exerts a constant shear stress σ_{xz}^{L} on the base of the lithosphere. The effect of a resistive basal drag, directed towards the ridge, is to reduce the intraplate compression. The magnitude of the induced tension can be estimated from the horizontal condition of mechanical equilibrium in two dimensions,

$$\frac{\partial \sigma_{xx}}{\partial x} + \frac{\partial \sigma_{xz}}{\partial z} = 0. \tag{4.10}$$

where x is the lateral distance to the ridge axis and z is the depth. Neglecting the shear stress caused by viscous advection driven by the asthenospheric density

anomalies, $\sigma_{xz} = \sigma_{xz}^{L}$ at the base of the lithosphere and $\sigma_{xz} = 0$ at the surface of the elastic layer. Under this assumption the variation of the depth averaged horizontal stress $\bar{\sigma_{xx}}$ in the lithosphere is,

$$d\bar{\sigma_{xx}} = -\frac{\sigma_{xz}^{L}}{L(x)}dx, \tag{4.11}$$

where L(x) is the lithosphere thickness at a given distance x to the ridge axis. Expressing L(x) in terms of age t according to Eq. 4.2 and making $dx = Vdt$ where V is the spreading velocity, the variation in the depth averaged horizontal stress between the ridge axis (x=t=0) and the western end of the model (x=1200km, t=18.5 Ma) is,

$$\Delta\bar{\sigma_{xx}} = -\frac{\sigma_{xz}^{L}V}{8}\int_{0}^{18.5} t^{-1/2}dt. \tag{4.12}$$

Assuming a constant shear stress $\sigma_{xz}^{L} = 0.1$ MPa and a spreading velocity V=65 km/Ma, the maximum variation in the depth averaged horizontal stress for my models is approximately -7 MPa. Neglecting any contribution of the basal drag to the vertical stress in the lithosphere, then the maximum contribution of the basal drag to the deviatoric stress in the lithosphere is a tensile stress of about 7 MPa. The main results of my modelling would still apply if such stress was superimposed on the elastic layer.

In chapter 7 it will be argued that a basal shear stress of 0.1 MPa is consistent with an asthenosphere viscosity beneath oceans of the order of 10^{19}Pa s, which is more likely than the value assumed in the modelling here (10^{20}Pa s). However, the value of the asthenosphere viscosity used in the modelling does not affect the results significantly, only the computational time.

4.13 Discussion

The modelling indicates that the intraplate compressional deviatoric stresses are greatly reduced above the anomalously hot asthenosphere. At a distance of about one thousand kilometres from the East Pacific Rise, the compressional deviatoric

stresses in the Pacific plate are predicted to be reduced by 50% relatively to normal ocean floor. To confirm these results there should be less evidence of intraplate compression in the Pacific than in the Nazca plate.

The stress indicators in the region (Fig. 4.9) reveal a different reality. To the north of Easter microplate, tensional stresses give way to compressional stresses as the plate age increases, in agreement with the transition from tension to compression predicted by the modelling. However, at the latitude of Easter the stress indicators concentrate over the Pitcairn-Gambier and Tuamotu seamount chains in the Pacific plate, and over the Easter-Sala y Gomez seamount chains in the Nazca plate.

Seamount loading induces flexural stresses that can reach hundreds of megapascals, and can perturb the regional stress field for hundreds of kilometers (e.g. Bodine et al., 1981; McNutt and Menard, 1982). At shallow depths, compressive bending stresses occur beneath the center of the load, and tensile bending stresses occur in the peripheral bulge regions. Bending stresses of opposite sign occur at depth. Therefore, bending stresses can account for the diversity of faulting styles observed at the latitude of Easter microplate, particularly in the Pacific plate (e.g. Okal et al, 1980).

Bending stresses may easily swamp the small stresses predicted by the modelling in the Pacific plate. In the Nazca plate, another source of stress may explain why evidence for intraplate compression is so weak. This source of stress is slab pull, which is expected to superimpose tension in old ocean floor (e.g. Whittaker et al., 1992). In summary, what the comparison between the modelling results and the stress indicators points out, is that other sources of stress are superimposed on the loading distribution that has been assumed, dominating the stress field in the region of Easter microplate.

Fig. 4.9 World-Stress-Map maximum horizontal stress orientation S_{Hmax} in the Southeast Pacific. The stress orientations are plotted on a base of average topography (after Mueller et al., 1997).

Qualities:
A - stress orientations to within $10 - 15°$
B - stress orientations to within $15 - 20°$
C - stress orientations to within $20 - 25°$

Red data NF - normal faulting regime $S_V > S_{Hmax} > S_{hmin}$
Green data SS - strike-slip faulting regime $S_{Hmax} > S_V > S_{hmin}$
Blue data TF - thrust faulting stress regime $S_{Hmax} > S_{hmin} > S_V$
Black data U - unknown stress regime

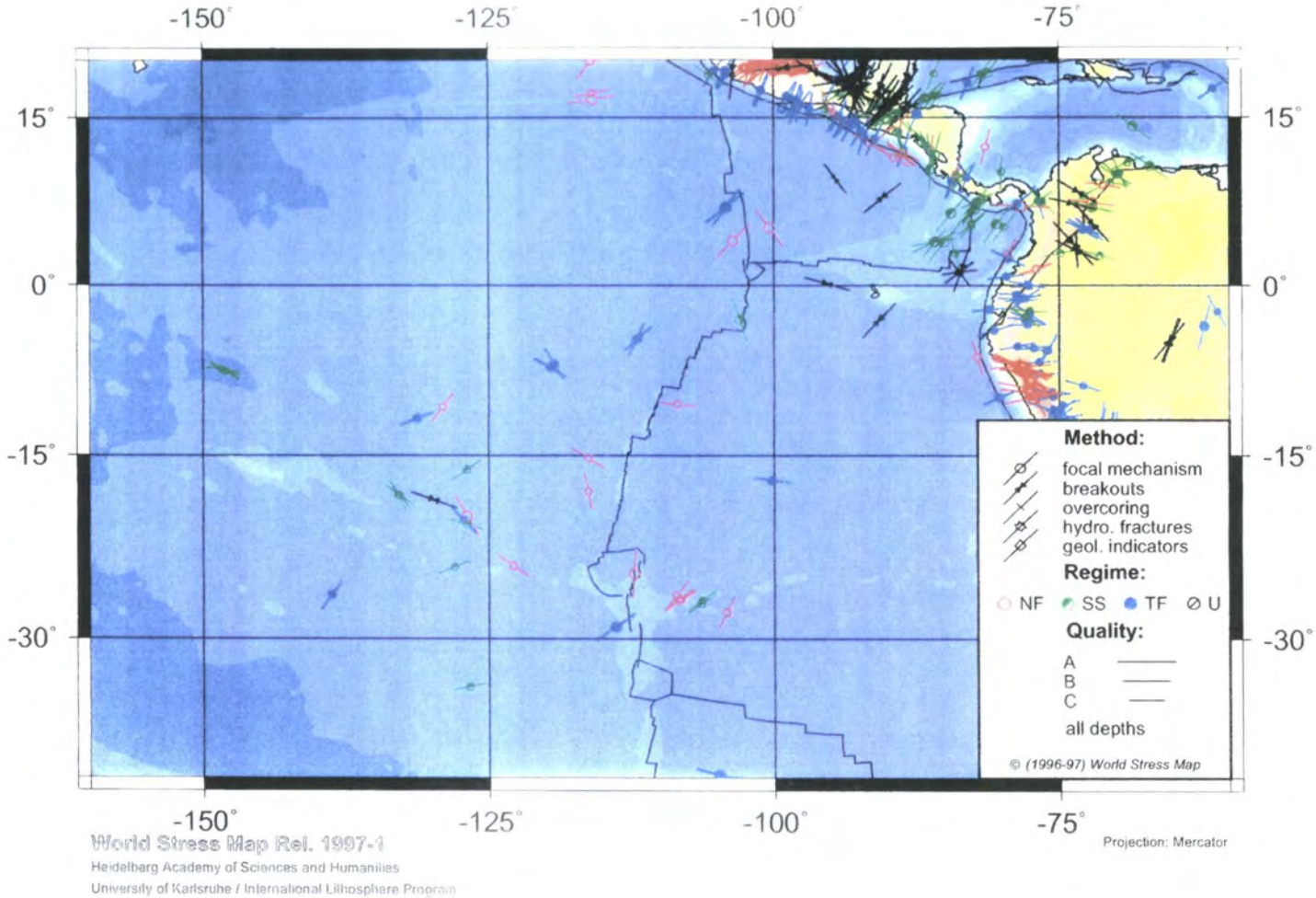
-150°
-125°
-100°
-75°
15°
0°
-15°
-30°
Method:
focal mechanism
breakouts
overcoring
hydro. fractures
geol. indicators
Regime:
NF
SS
TF
U
Quality:
A
B
C
all depths
© (1996-97) World Stress Map
World Stress Map Rel. 1997-1
Heidelberg Academy of Sciences and Humanities
University of Karlsruhe / International Lithosphere Program
Projection: Mercator

Chapter 5

Elasto-plastic models of normal faulting in the oceanic lithosphere

5.1 Introduction

Flexural models of normal faults have been mainly applied to continental lithosphere. Among such models a few refer to the importance of plastic failure and discuss its implication on estimates of the effective elastic plate thickness (e.g. Buck, 1988; Kusznir et al., 1991; Forsyth, 1992). Recently Bott (1997) proposed a model of development of half-grabens in continental lithosphere including the effect of plastic yielding. He verified that plastic deformation may reduce the effective elastic plate thickness by up to 70%, helping to explain the anomalously low values of the elastic thickness associated with normal faulting. He also showed that plastic yielding places a limit on the maximum amount of subsidence and fault displacement that can occur.

Until now flexural models of faulting in oceanic lithosphere, including plastic yielding of the elastic plate, have only been applied to thrust faulting at oceanic trenches (McAddoo et al., 1978; Goetze and Evans, 1979). Because plastic yielding plays such an important role in the evolution of normal faults and associated plate flexure in the continents, we expect the same will happen in the oceans.

The main purpose of this chapter is to investigate the influence of plastic yielding on the evolution of normal faults in the oceanic lithosphere. The stress, the pattern of failure and the flexure profile produced when extension is applied to a brittle plate containing a pre-existing normal fault is modelled using elasto-plastic finite element analysis. An oceanic type of strength envelope is inferred and used. The effects of changing the brittle layer thickness and the fault dip angle are also investigated.

5.2 Rheology

Models of the lithosphere as an elastic plate that bends under applied loads, overlying an inviscid fluid, have been successful in matching bathymetric and gravity observations at seamounts, oceanic volcanic chains and trench-rise systems (e.g. Walcott, 1970; Bodine and Watts, 1979; McNutt and Menard, 1982). Matching between observed and theoretical elastic plate profiles produces estimates of the flexural rigidity D and the elastic plate thickness h. The flexural rigidity D relates the local bending moment M to the local plate curvature, $M(x) = -D(dw^2/dx^2)$, where w is the vertical deflection and x the horizontal distance. The flexural rigidity is expressed in terms of the elastic plate thickness h, Poisson's ratio ν and Young's modulus E through $D = Eh^3/[12(1-\nu^2)]$ (e.g. Turcotte and Schubert, 1982).

The thickness of the elastic plate is often interpreted as the thickness of the high-strength brittle layer assuming no plastic failure. The comparison between estimates of h from flexural studies and the isotherms of the Parsons and Sclater (1977) plate cooling model, suggests that a) the elastic thickness is determined by a particular isotherm, and b) that D and h increase with the age of the lithosphere at the time of loading (e.g. Watts et al., 1980; Bodine et al., 1981). Although the elastic plate model of the lithosphere works well as a first order model, by the early 1980s there were already a number of reasons to consider it an oversimplification. For instance (1) observed plate curvatures and bending strains at trench-rise systems are more localised than those predicted by elastic models, (2) the large value of the bending stresses at the surface of the elastic models is unrealistic, (3) the literal

interpretation of the flexural data would place the elastic layer thickness at the 450°C isotherm instead of the 700°C isotherm indicated by the flow law of olivine, and (4) the calculated values of D and h vary more than would be expected if they only depended on the temperature structure (Kirby, 1983).

As an alternative model, an elastic-plastic rheology has been proposed for the high strength layer (defined as the layer that extends to the depth of the 700°C isotherm). Such elastic-plastic models, where bending stresses larger than the strength are relaxed by plastic flow, were particularly successful in explaining the observed localised high plate curvatures and the variability in the values of D and h along some trench-rise systems (e.g. McAdoo et al., 1978). They also explained the discrepancy between the estimates of the elastic thickness, roughly limited by the 450°C isotherm, and the thickness of the high-strength lithosphere, defined by the 700°C isotherm.

The models in this chapter represent vertical sections of the brittle lithosphere cut by a high angle planar fault, overlying an inviscid substratum of the same density. It is assumed that the oceanic crust mainly consists of basalt, gabbro and diabase, while the brittle mantle mainly consists of peridotite and dunite. For these rocks, Young's modulus ranges from 0.6×10^{11} Pa to 1.6×10^{11} Pa (Turcotte and Schubert, 1982). A Poisson's ratio equal to 0.27 and a Young's modulus equal to 1.0×10^{11} Pa are assumed in the modelling.

5.3 Strength envelope

Strength profiles, also termed strength envelopes, depict the variations of lithospheric strength with depth, by limiting the maximum stress difference $S = \sigma_1 - \sigma_3$ that rocks can support at a given pressure, temperature and strain rate (recall that σ_1 and σ_3 are respectively the maximum and minimum principal compressive stress). The maximum shear stress in a three dimensional state of stress is one half the difference between the minimum and maximum principal stresses. Therefore strength profiles provide a limit to the maximum shear stress.

The widespread existence of fractures at shallow depths suggests that the overall stress in the brittle lithosphere is the stress at which rocks can slide along pre-existing faults and joints when opposed by friction. The magnitude of the shear stress (τ) that must be applied across a fault to initiate sliding when there is a normal compressive stress (σ_n) acting on the fault is $\mid \tau \mid = f_s \sigma_n$, where f_s is the coefficient of friction (Turcotte and Schubert, 1982, p.351).

It has been found in laboratory experiments that the coefficient of friction which determines the peak stress necessary to cause sliding on optimally oriented fractures is constant and the same for almost all rocks except clays (Byerlee, 1978). This result is known as Byerlee's law. Later Brace and Kohlstedt (1980) verified that the laboratory measurements of rock strength during frictional sliding provide a good fit for observations of in-situ stress (McGarr and Gay, 1978). Consequently the strength of the brittle lithosphere is usually assumed to be given by Byerlee's law.

The presence of water along a fault creates a fluid pressure (P_w) which decreases the normal stress across the fault surface, and consequently the shear stress required for sliding. On a wet fault the shear stress necessary to initiate sliding is therefore related to the effective normal stress which is the actual normal stress across the fault less the pore fluid pressure (Hubbert and Rubey, 1959; Turcotte and Schubert, 1982, p.352),

$$\mid \tau \mid = f_s(\sigma_n - P_w). \tag{5.1}$$

Values of the pore fluid pressure range from zero to the lithostatic pressure, constituting the main source of uncertainty when applying Byerlee's law. The Byerlee law applied to dry friction is an upper bound to stress measurements in the uppermost crust, while a pore fluid pressure equal to the lithostatic pressure gives the lower bound. An intermediate pore fluid pressure, especially the hydrostatic pressure, is often assumed and gives good agreement with stress measurements (Brace and Kohlstedt, 1980).

According to Anderson's theory of faulting (Anderson, 1951), normal faulting is associated with a state of stress in which the maximum compressive stress is the

vertical stress and the minimum compressive stress is the horizontal stress. The vertical stress σ_{zz} is the lithostatic pressure. The horizontal stress σ_{xx} is the sum of the lithostatic pressure and a tectonic tensile horizontal stress $\Delta\sigma_{xx}$ (negative). Under these assumptions the maximum and minimum compressive stress at a depth z below the seabed are

$$\sigma_1 = \sigma_{zz} = \rho_w g h_w + \rho g z, \tag{5.2}$$

$$\sigma_3 = \sigma_{xx} = \sigma_{zz} + \Delta\sigma_{xx} = \rho_w g h_w + \rho g z + \Delta\sigma_{xx}, \tag{5.3}$$

where ρ_w is the density of seawater, g is the acceleration due to gravity, h_w is the seawater depth and ρ is the rock density. The difference between the maximum and minimum compressive principal stresses corresponds to the tectonic horizontal stress,

$$S = |\sigma_1 - \sigma_3| = |\sigma_{zz} - \sigma_{xx}| = |\Delta\sigma_{xx}|. \tag{5.4}$$

The strength is defined as the maximum horizontal tectonic stress rocks can support.

The normal and shear stress across a fault are related to the vertical and horizontal components of stress (assumed to be the principal stresses) by (Turcotte and Schubert, 1982, p.354),

$$\sigma_n = \frac{1}{2}(\sigma_{xx} + \sigma_{zz}) + \frac{1}{2}(\sigma_{xx} - \sigma_{zz})\cos 2\theta, \tag{5.5}$$

$$\tau = -\frac{1}{2}(\sigma_{xx} - \sigma_{zz})\sin 2\theta, \tag{5.6}$$

where θ is the angle of the fault plane with respect to the vertical (the hade). Upon substituting Eqs. 5.2 and 5.3 into Eqs. 5.5 and 5.6 the normal and the shear stress on the fault are,

$$\sigma_n = \rho_w g h_w + \rho g z + \frac{1}{2}\Delta\sigma_{xx}(1 + \cos 2\theta), \tag{5.7}$$

$$\tau = -\frac{\Delta\sigma_{xx}}{2}\sin 2\theta. \tag{5.8}$$

We can now substitute σ_n and τ into Eq. 5.1 to relate the tectonic stress to the coefficient of friction and the angle of dip of the fault. But first we have to compute the pore fluid pressure at a depth z below the seabed, which for hydrostatic conditions is,

$$P_w = \rho_w g h_w + \rho_w g z. \tag{5.9}$$

Eq. 5.1 then becomes

$$-\frac{\Delta\sigma_{xx}}{2}\sin 2\theta = f_s\left[\rho gz - \rho_w gz + \frac{\Delta\sigma_{xx}}{2}(1+\cos 2\theta)\right]. \tag{5.10}$$

The yield strength, that is the maximum tectonic stress the brittle layer can withstand without sliding along pre-existing normal faults, is therefore,

$$\Delta\sigma_{xx} = \frac{2f_s(\rho gz - \rho_w gz)}{-\sin 2\theta - f_s(1+\cos 2\theta)}. \tag{5.11}$$

Under the hypothesis that reactivation of pre-existing normal faults will occur at angles that minimise the tectonic stress (i.e. making $d\Delta\sigma_{xx}/d\theta = 0$), it is found that

$$\tan 2\theta = \frac{1}{f_s}. \tag{5.12}$$

Substituting Eq. 5.12 in Eq. 5.11 we obtain the tectonic stress needed to cause slip on optimally oriented normal faults as,

$$\Delta\sigma_{xx} = \frac{-2f_s(\rho gz - \rho_w gz)}{(1+{f_s}^2)^{1/2} + f_s}. \tag{5.13}$$

This is the strength in extension. In the modelling program a modified formula is used, which has been deduced by Bott (private comunication) for directions of tectonic principal stress making an angle Φ with the horizontal,

$$\Delta\sigma_{xx} = \frac{-2f_s(\rho gz - \rho_w gz)}{(1+{f_s}^2)^{1/2} + f_s\cos 2\Phi}. \tag{5.14}$$

To find the strength in compression we follow the same reasoning but assume that the maximum compressive stress is the horizontal stress (equal to the lithostatic stress plus a compressive tectonic stress) and that the minimum compressive stress is the vertical stress (equal to the lithostatic stress). Either in tension or in compression, the strength increases from zero at the seabed. This result differs from other estimates of the strength in the oceanic lithosphere, particularly near spreading ridges (e.g. Norrell, 1991).

If the depth below the sea bed is less than the crustal thickness, the lithostatic stress in the modelling program is $\rho_c gz$, where ρ_c is the density of rock in the oceanic crust. The Moho is assumed to be at 6 km depth below the seabed, so that if the

Symbol	value
ρ_w	1030 kg/m^3
ρ_c	2950 kg/m^3
ρ_m	3300 kg/m^3
g	9.8 m/s^2
f_s	0.75

Table 5.1: Values for the parameters used in the computation of the strength envelope

model thickness is larger than 6 km the mantle density ρ_m must also be used to compute the contribution of mantle rock to the lithostatic pressure. Table 5.1 lists the values of the constants used in the modelling.

The plane strain formulation was used throughout the modelling. This is the best assumption for modelling of bending problems since it implies zero bending in the out-of-plane direction (Bott, 1997). In the finite element program viscous relaxation reduces the stress to the yield strength according to the Von-Mises criterion (section 3.5). In plane strain the Von Mises yield strength σ_Y is related to the strength S (the maximum stress difference) by a factor equal to $\sqrt{3}/2$, provided that the principal stresses are horizontal and vertical, and is a reasonable approximation more generally.

5.4 Model length and thickness

To investigate the evolution of normal faulting at mid-ocean ridges, the length of the model must correspond to the distance from the ridge axis characterised by extension and active faulting. The distribution of active normal faults at mid-ocean ridges has been inferred from seismic data and from high resolution bathymetric or side-scan sonar data. Both data sets indicate that active normal faulting at slow spreading ridges is confined to a maximum distance from the ridge axis of 10-20 km (section 1.3). At fast spreading ridges the same range of activity applies.

Given the above occurrence of active faulting it was decided to model a normal fault placed at 15 km from the ridge axis. An inward facing fault is modelled because

these faults are predominant at slow spreading ridges. In the finite element model the position of the ridge axis corresponds to the left edge of the grid. The length of the downthrown block, between the fault and the left end of the model, is therefore 15 km. The length of the upthrown block, between the fault and the right end of the model, is also 15 km. This makes a total length of the finite element model equal to 30 km, which approximately agrees with estimates of the extent of extension at mid-ocean ridges given by ridge push stress models (Fleitout and Froidevaux, 1983; Bott, 1991).

The thickness of the finite element model is the thickness of the layer that can be affected by brittle failure. The best constraints on the brittle layer thickness at mid-ocean ridges are supplied by seismic experiments. At slow spreading ridges the maximum focal depth of microearthquakes and teleseismically recorded earthquakes indicate that the brittle layer thickness ranges from 2 to 10 km (section 1.2). From this range of brittle layer thicknesses, minimum values occur in the middle of the segment and maximum values occur at segment ends (e.g. Kong et al., 1992; Wolfe et al., 1995). At fast spreading ridges, the depth to the top of axial magma chambers, inferred from seismic reflection sections, indicates a brittle layer thickness ranging from 1 to 2 km (e.g. Detrick et al., 1987). Given these estimates for the brittle layer thickness, two main models are used. One, 8 km thick, represents sections of the brittle lithosphere at slow spreading segment ends. The other, 2 km thick, represents sections of the brittle lithosphere either at fast spreading ridges or in the middle of slow spreading segments.

5.5 Fault parameters

Four parameters characterise the planar fault considered in the finite element models: the fault's maximum depth, the fault dip angle, the fault's coefficient of friction, and the fluid pressure.

The maximum depth of observed earthquakes at mid-ocean ridges was used to estimate the thickness of the brittle layer, and thus, the thickness of the finite

element model. Taking into account that earthquakes result from slip along faults, it is reasonable to consider a fault that cuts the entire brittle thickness. Therefore it is assumed that the maximum depth of the fault corresponds to the maximum depth of the model. The underlying region is treated as inviscid.

Seismic observations at mid-ocean ridges suggest that the mean dip of faults is 45° (section 1.3). However, high angle normal faults (up to 90°) are observed both at segment centres and segment ends (e.g. Tucholke and Lin, 1994). Moreover, it has been suggested that the exposure of mafic and ultramafic rocks at inside corners results from low angle normal faulting (e.g. Karson, 1990; Tucholke et al., 1998).

Given the range of possible fault dips, and the implication of fault dip on models of ridge segmentation, it was decided to model: (1) a fault dipping at 63° representing high angle faulting, (2) a fault dipping at 45° representing the average faulting, and (3) a fault dipping at 33° representing low angle faulting. Because low and high angle normal faulting are more important at segment ends of slow spreading ridges, especially at inside corners, the fault dip angle is studied using the 8 km thick model.

Friction at mid-ocean ridge normal faults has not yet been quantified. The best constraint on the amount of friction existent at oceanic faults is provided by observations at transform faults (section 2.8). These observations suggest that transform faults have a much smaller coefficient of friction than indicated by Byerlee's law, thus seeming to have a much smaller strength than the surrounding lithosphere (e.g. Zoback, 1991). I assume that normal faults at mid-ocean ridges, like transform faults, have negligible effective friction.

The fault is modelled using the dual node technique (section 3.6). Bott (1996) demonstrated that the dual node technique produces a good fit to theoretical flexure profiles in which the fault planes are constrained to remain parallel and in contact as slip proceeds.

5.6 Grid

The 4 finite element grids displayed in Fig. 5.1 correspond to the combinations of fault dip angle, length and thickness of the model assumed in the previous sections.

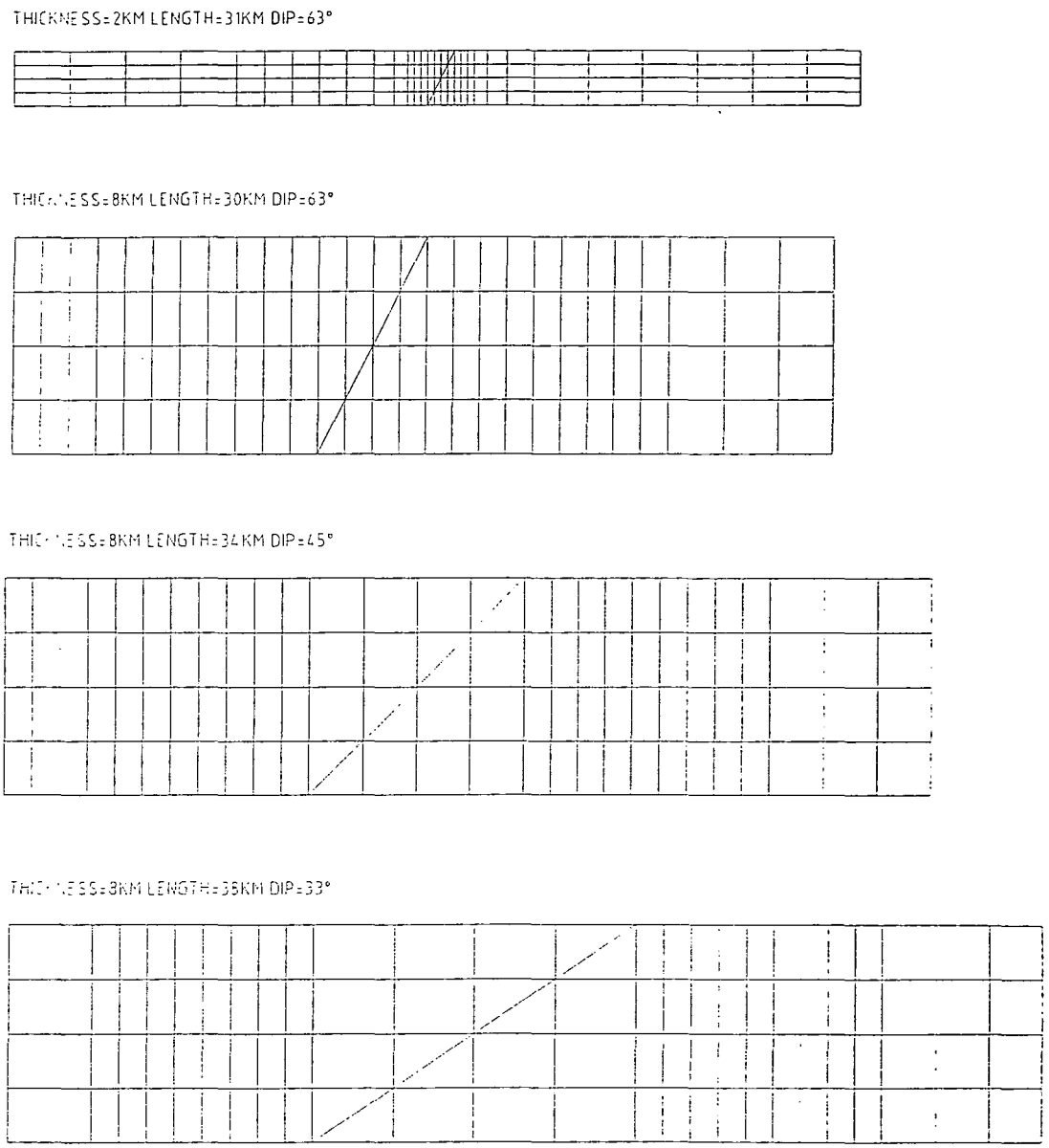

Fig. 5.1 The 4 finite element grids used in the modelling. From top to bottom, the first grid corresponds to models F* and FL*, the second grid to model S*, the third grid to model D45* and the fourth grid to model D33*.

In all the grids triangular elements were used to define the fault. Apart from the triangular elements bordering the fault, there are otherwise only quadrilateral elements. The triangular elements have 6 nodes each and the quadrilateral elements have 8 nodes each. The number of Gauss points used to evaluate the stress was 3 in the triangular elements and 4 in the quadrilateral elements.

The grid at the top of Fig. 5.1 is 2 km thick and 31 km long. It contains a linear fault at a distance of 15 km from the left end of the model (this distance is averaged over the fault thickness), dipping at 63°. The grid contains a total of 124 isoparametric elements, of which 116 are quadrilateral and 8 triangular.

The second grid from top is 8 km thick and 30 km long. It also contains a linear fault at a distance of 15 km from the left end of the model, dipping at 63°. The grid contains a total of 112 isoparametric elements, from which 104 are quadrilateral and 8 triangular.

The third grid is identical to the second in number of elements and topology. However, the elements surrounding the fault are wider so that the fault dips at 45°. This grid is 8 km thick, 34 km long, and the fault is at 15 km from the left end of the model.

The grid at the bottom of the Fig. 5.1 is 8 km thick and 38 km long. It also results from a widening of the second grid but the number of elements and the topology remain the same. The fault dips at 33° and the distance between the fault and the left end of the model, averaged over the fault thickness, is 17 km.

5.7 Application of extension

Extension is applied to the finite element model by fixing the right edge of the grid and incrementally extending the left edge. At each increment of extension the elasto-plastic solution is computed. Before the next increment of extension is applied the model geometry is updated by modifying the stiffness matrix. The response of the model to the applied extension is mainly controlled by the brittle layer thickness

and the fault dip angle. Therefore the magnitude of the increments of extension and the total amount of applied stretching vary with the model geometry.

The tectonic force equivalent to the applied displacement at the edge of the model can be found by integration of the stress difference ($\sigma_{xx} - \sigma_{zz}$) over the depth of the plate. Since the stresses are corrected by the strength profile, after plastic failure the stress difference at the edge of the model reflects the Byerlee strength envelope.

5.8 Infill loading

The role of sedimentation in the evolution of continental half-grabens was analysed by Bott (1997). He concluded that the density of the infill that fills the half-graben is a determining factor in the final amount of subsidence and half-graben width. Lowering the density of the infill reduced the final half-graben width and the amount of subsidence. Sediment and volcanic infill in the oceanic crust is insignificant compared to sedimentation in the continents. Thus, infill thickness in the oceans is usually less than 0.5 km (e.g. Fowler, 1990). Nevertheless in the vicinity of mid-ocean ridges infill in the form of extrusive volcanism may be important. For that reason, the effect of volcanic/sediment loading on the evolution of mid-ocean ridge normal faults deserves investigation.

The infill is assumed to mainly consist of extrusive rocks, and its density is assumed to be 2500 kg/m^3. Seismic studies along the East Pacific Rise have reported that the thickness of the extrusive layer 2A, about 200 m beneath the rise axis, almost doubles within 1-2 km off axis (e.g. Kent et al., 1994). The extrusive layer is characterised by low seismic velocities suggesting low rock densities. Bottom gravity measurements indicate a density range of 2400-2600 kg/m^3 for these near surface rocks (Stevenson et al., 1994). The infill is assumed to occur in regions of subsidence, and to fill the space between the surface of the model and the initial datum.

Vertical displacements cause modified vertical loading to act on the plate. To maintain isostatic equilibrium, restoring forces are applied through isostatic boun-

dary conditions at each density interface. They are proportional to the product of the vertical displacement and the change of density at each interface. When there is no infill the density contrast along the surface of the model is 2950-1030=1920 kg/m^3, which is the density difference between the basaltic oceanic crust and the seawater. When there is infill the density contrast at the surface of the model is 2950-2500=450 kg/m^3.

For the thicker models there is also a density contrast of 3300-2950=350 kg/m^3 at 6 km depth (the Moho). Tests have shown that the same density contrast (350 kg/m^3) at the base of the 2 km thick model does not significantly affect the results.

As extension proceeds, the edge of the subsiding region migrates slightly towards the fault. The location of the half-graben hinge-line and the updating of the isostatic boundary conditions are done iteratively. At each stage of extension I first run the model to locate the edge of the subsiding region. Then, the isostatic boundary conditions are updated, and the model run again to determine the new position of the half-graben hinge-line. The updating of the isostatic boundary conditions continues until the edge of the subsiding region is at the same location as in the preceding step.

5.9 Presentation of the models

Four types of model were computed, corresponding to the four grids presented in section 5.6:

- Model F* (Fig. 5.2) is 2 km thick and has a fault dipping at 63°. It represents a section of the brittle lithosphere at a fast spreading ridge segment, or in the middle of a slow spreading segment.
- Model FL* (Fig. 5.3) is used to study the effect of loading by infill. It is otherwise identical to model F*.
- Model S* (Fig. 5.4) is 8 km thick and has a fault dipping at 63°. It represents a section of the brittle lithosphere at the end of a slow spreading segment.

- Model D45* (Fig. 5.5) is 8 km thick and has a fault dipping at 45°. It is used to study the effect of changing the fault angle while maintaining all the other parameters.
- Model D33* (Fig. 5.6) is 8 km thick and has a fault dipping at 33°. It is also used to study the effect of changing the fault angle.

In the 2 km thick models the asterisk is replaced by the number of 10 m increments by which the model was extended. Models F* and FL* are presented at 10, 50, 100, and 150 m of applied extension.

In the 8 km thick models the asterisk is replaced by the number of 100 m increments by which the model was extended. Models S*, D45* and D33* are presented at 100, 300, 500, and 700 m of applied extension.

In the stress diagrams, tensile non-lithostatic stresses are represented by outward pointing arrows. Compressive non-lithostatic stresses are represented by inward pointing arrows. Within the model, stresses are plotted at the centre of each element, corresponding to the average stress over the Gauss points of each element. For plane strain the maximum and minimum stresses are always in-plane. The out-of-plane stresses, which are intermediate, are not plotted. The in-plane stresses are scaled relative to the maximum stress. The maximum stress is labelled in MPa and is plotted at the right of the 2 km thick model and at the top of the 8 km thick models.

Two different scales are used to display the results of the model 2 km thick, due to the wide range of element widths in the grid. For each stage of stretching two diagrams are presented, one with the results for the larger elements and another with the results for the region close to the fault. For the models 8 km thick only one diagram is presented for each stage of stretching.

The plastic failure symbols are plotted at each Gauss point. Plastic failure in extension is represented by a circle. Plastic failure in compression is represented by a square.

Fig. 5.2 Stress and failure pattern of model F* (2 km thick, 63° fault). The * denotes the number of 10 m increments of applied extension. There is no volcanic/sediment loading. Outward pointing arrows represent tensile stresses and inward pointing arrows represent compressive stresses. The circles with a cross inside denote plastic failure in extension and the squares with the cross inside denote plastic failure in compression. The results are presented at two different scales, each scale in a separate diagram, with the first showing the whole model with the central section blank, and the second showing an enlargement in the vicinity of the fault. The maximum stress and the fault throw are shown at the right of each model.

'F1.DAT 10 m no sediments'

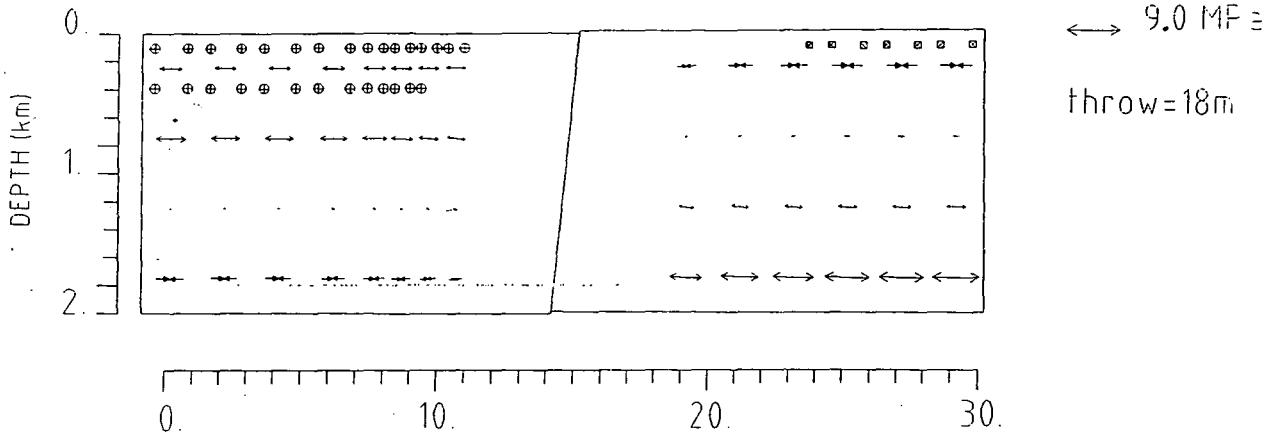

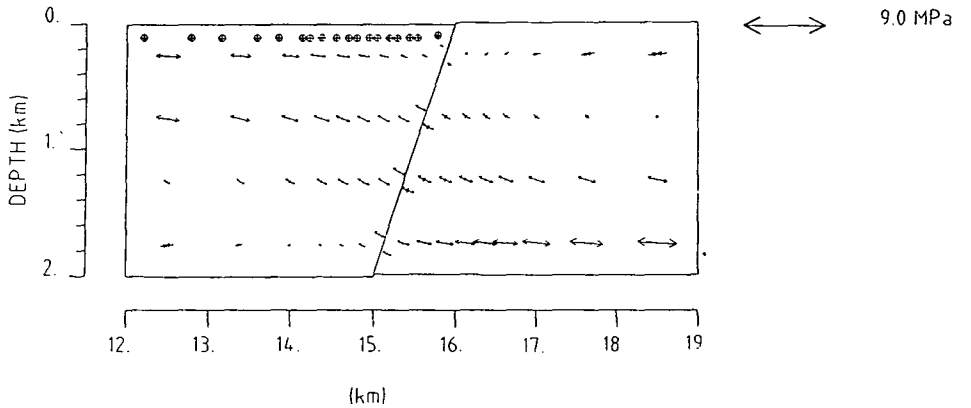

'F5.DAT 50 m no sediments'

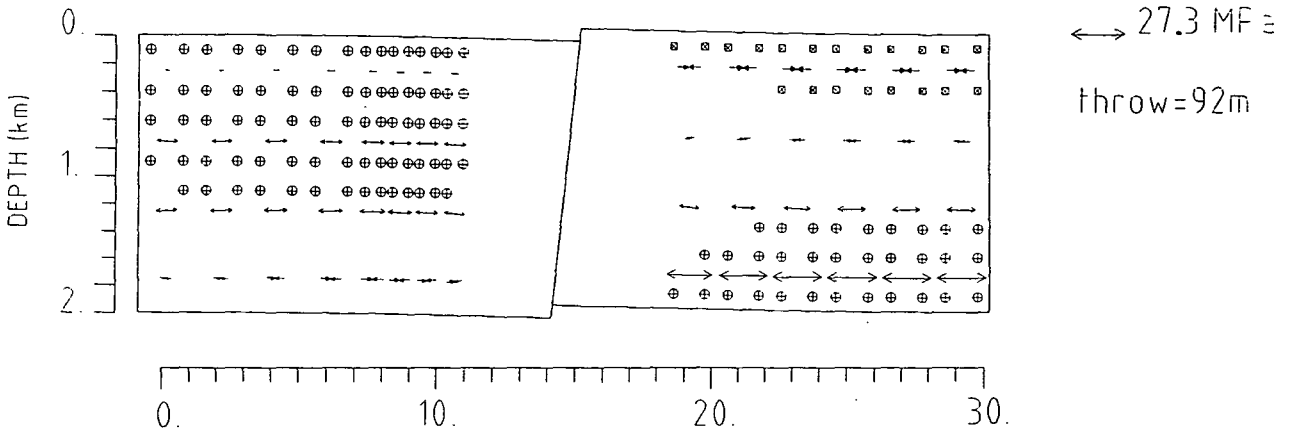

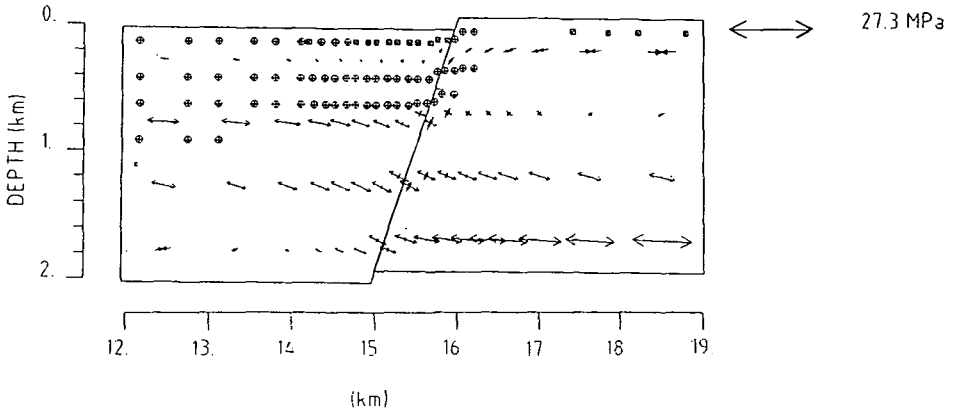

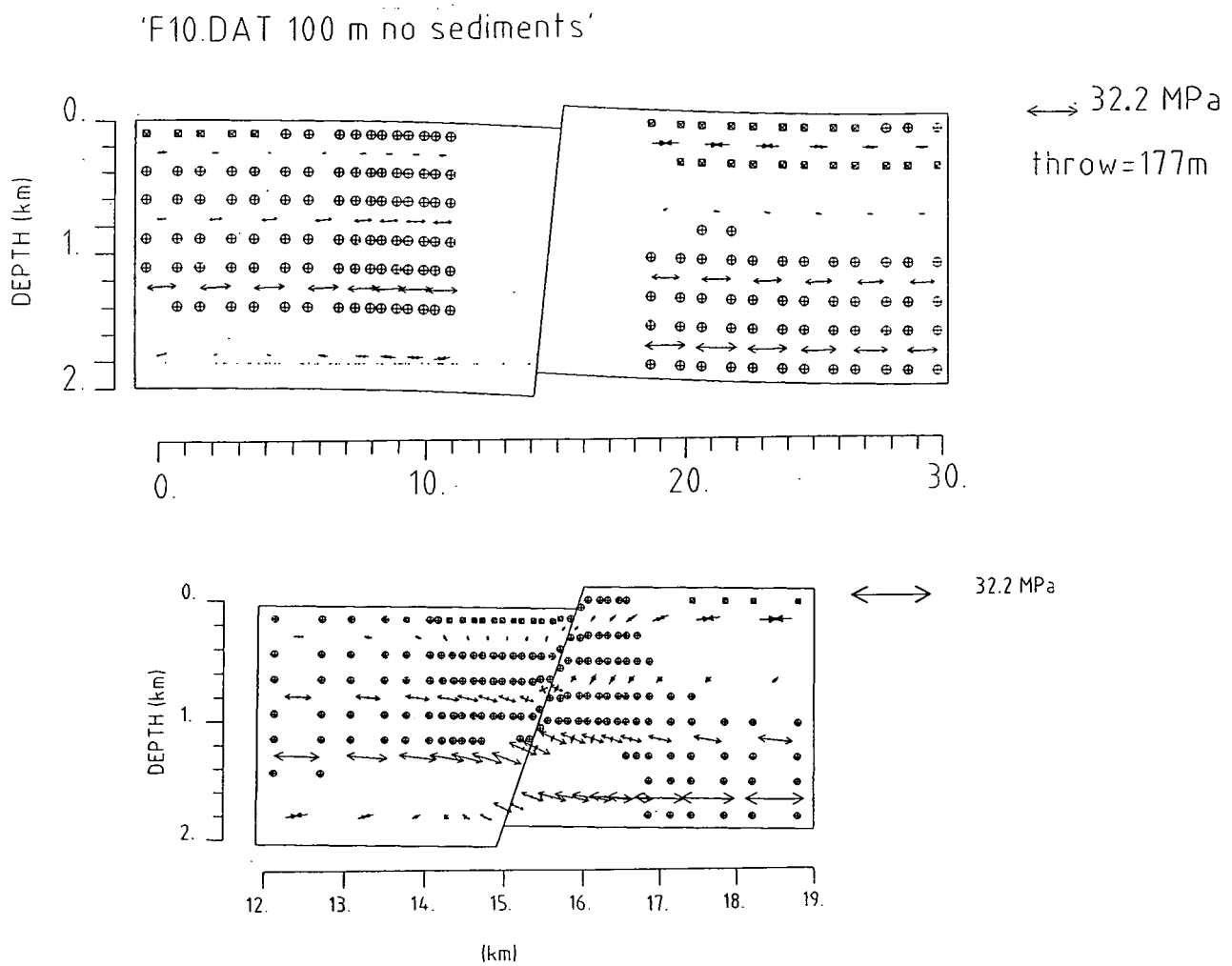

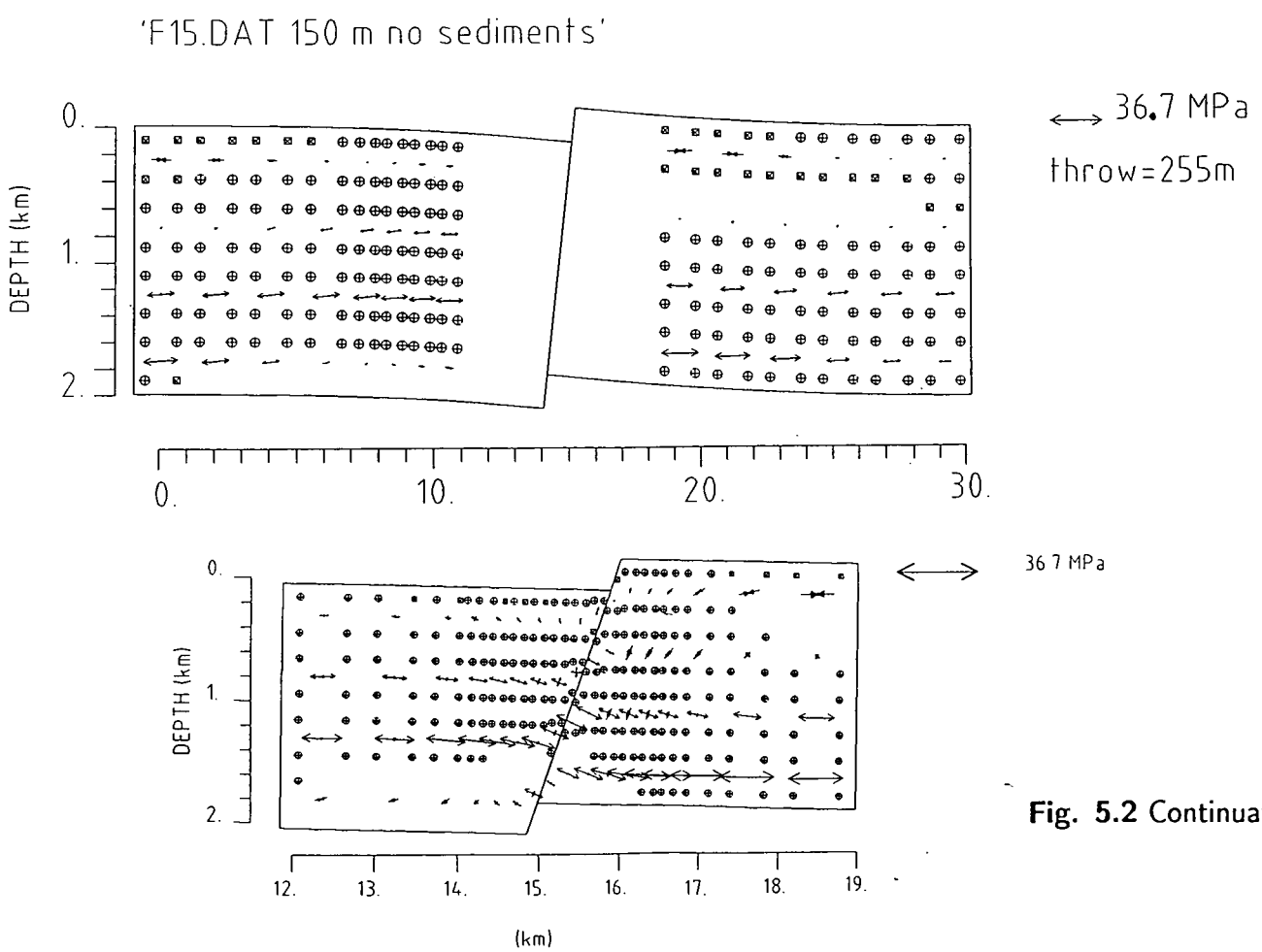

Fig. 5.2 Continuation

Fig. 5.3 Stress and failure pattern of model FL* (2 km thick, 63° fault). Volcanic infill of density 2500kg/m^3 fills the half-graben to the initial datum (at zero depth). Symbols and labels are as described in the caption of figure 5.2. As in figure 5.2 each stage of extension is shown on two different scales.

'FL1.DAT 10 m with loading'

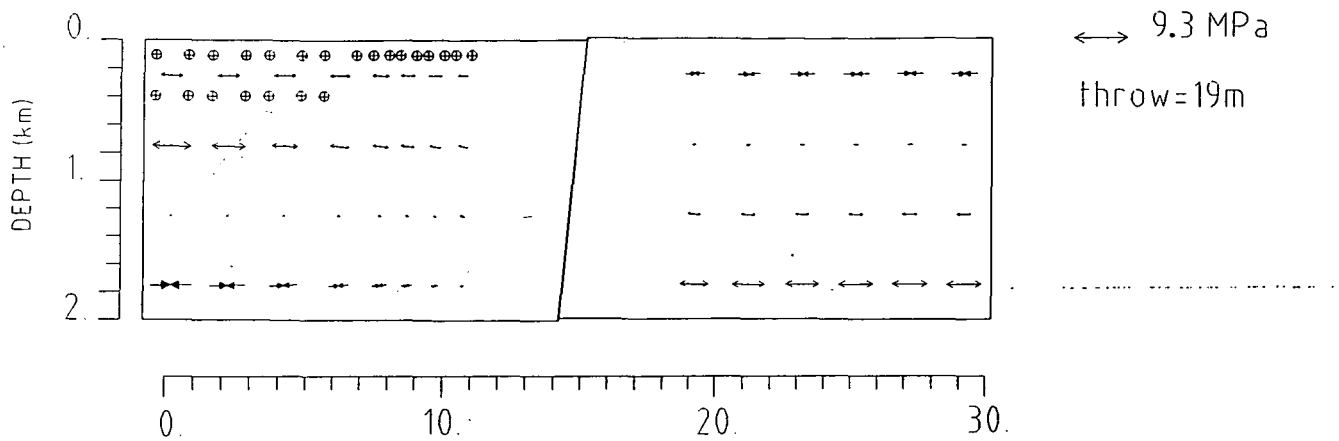

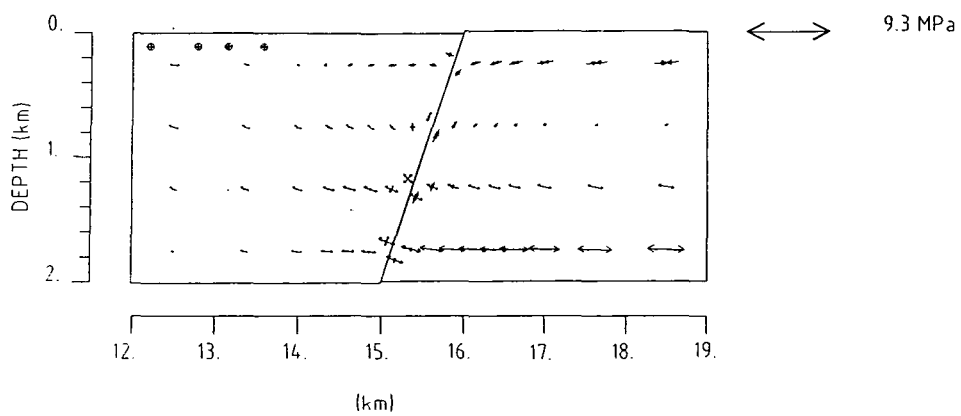

'FL5.DAT 50 m with loading'

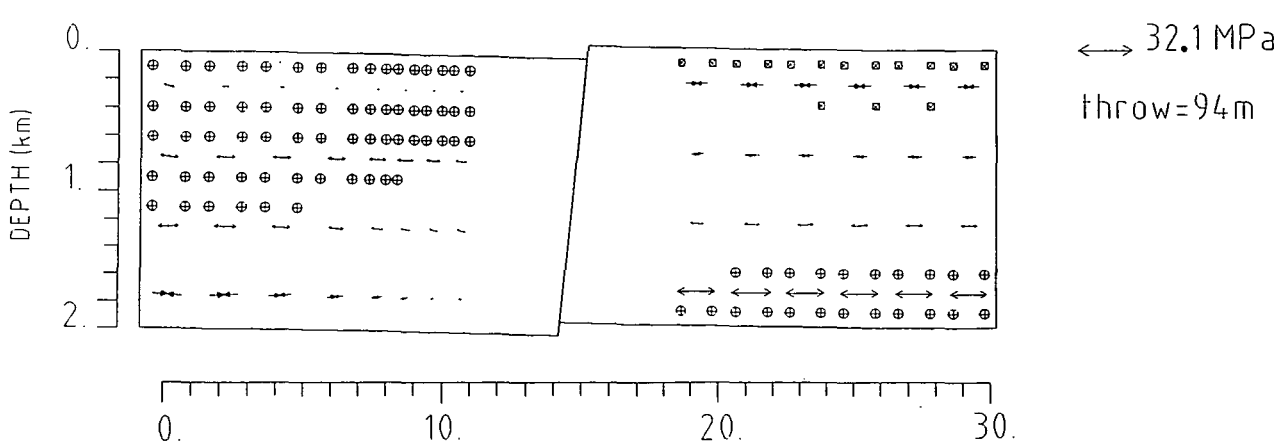

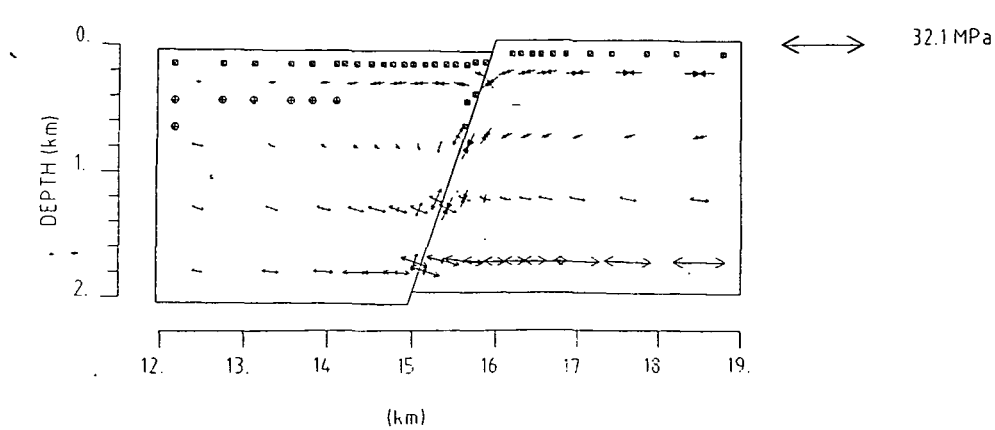

'FL10.DAT 100 m with loading'

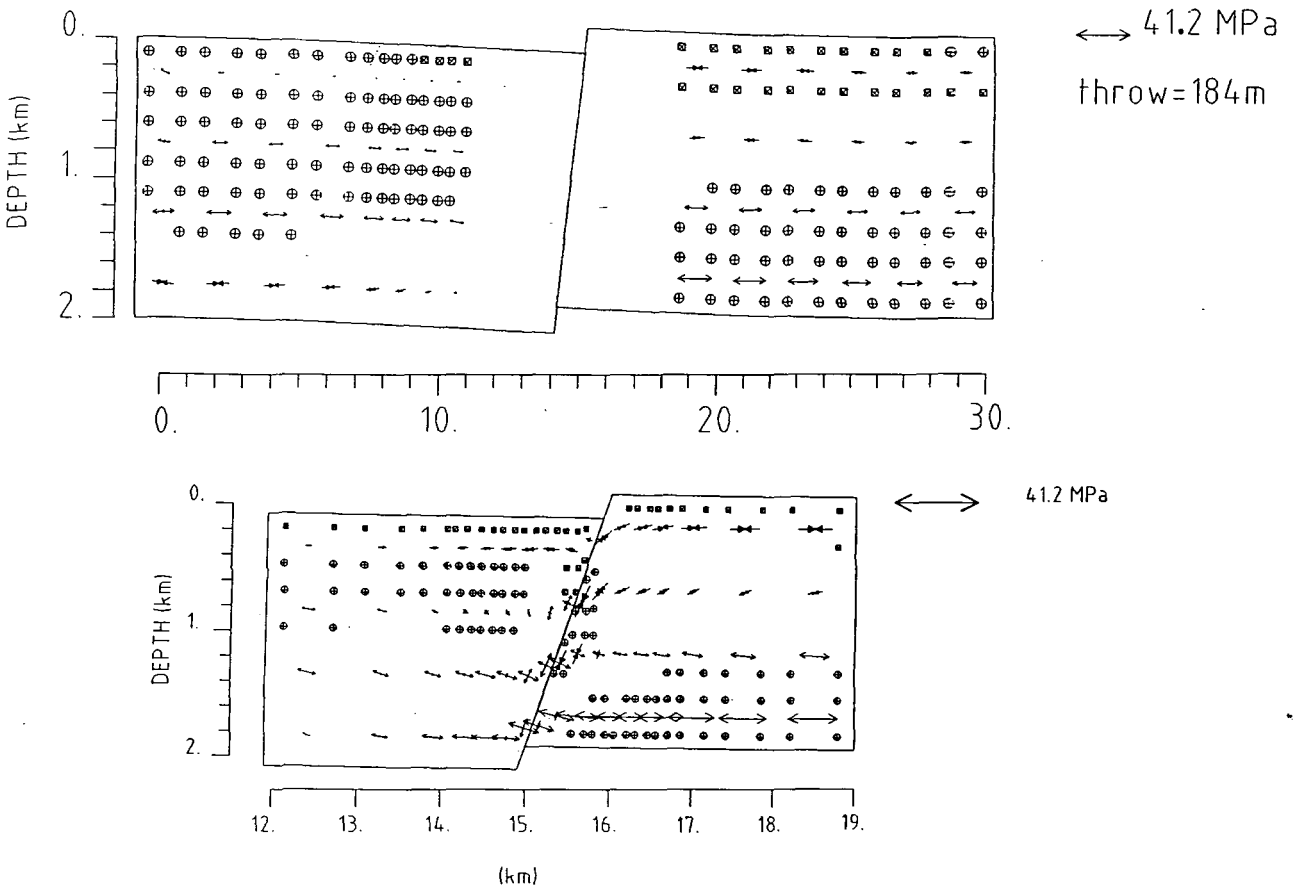

'FL15.DAT 150 m with loading'

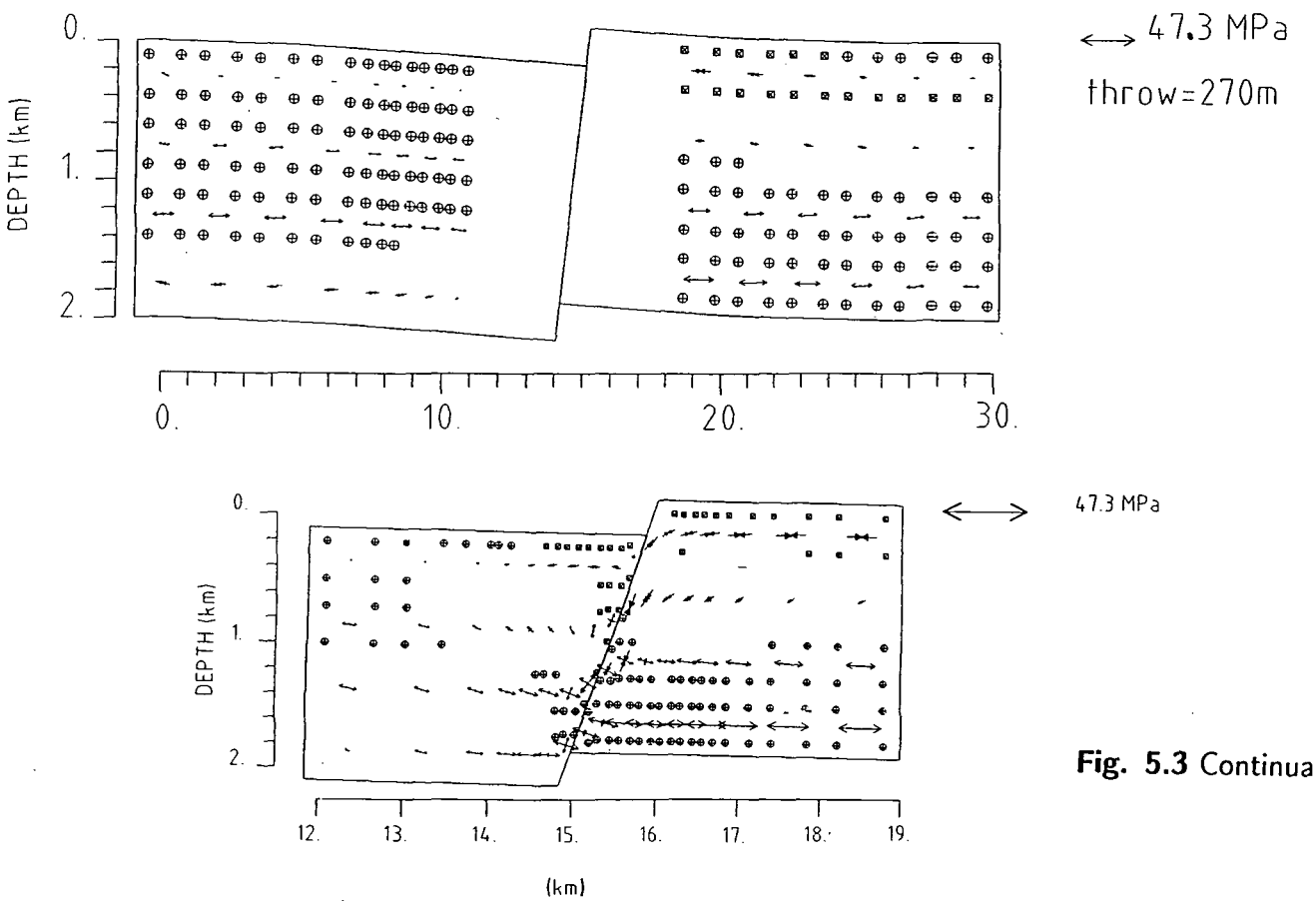

Fig. 5.3 Continuation.

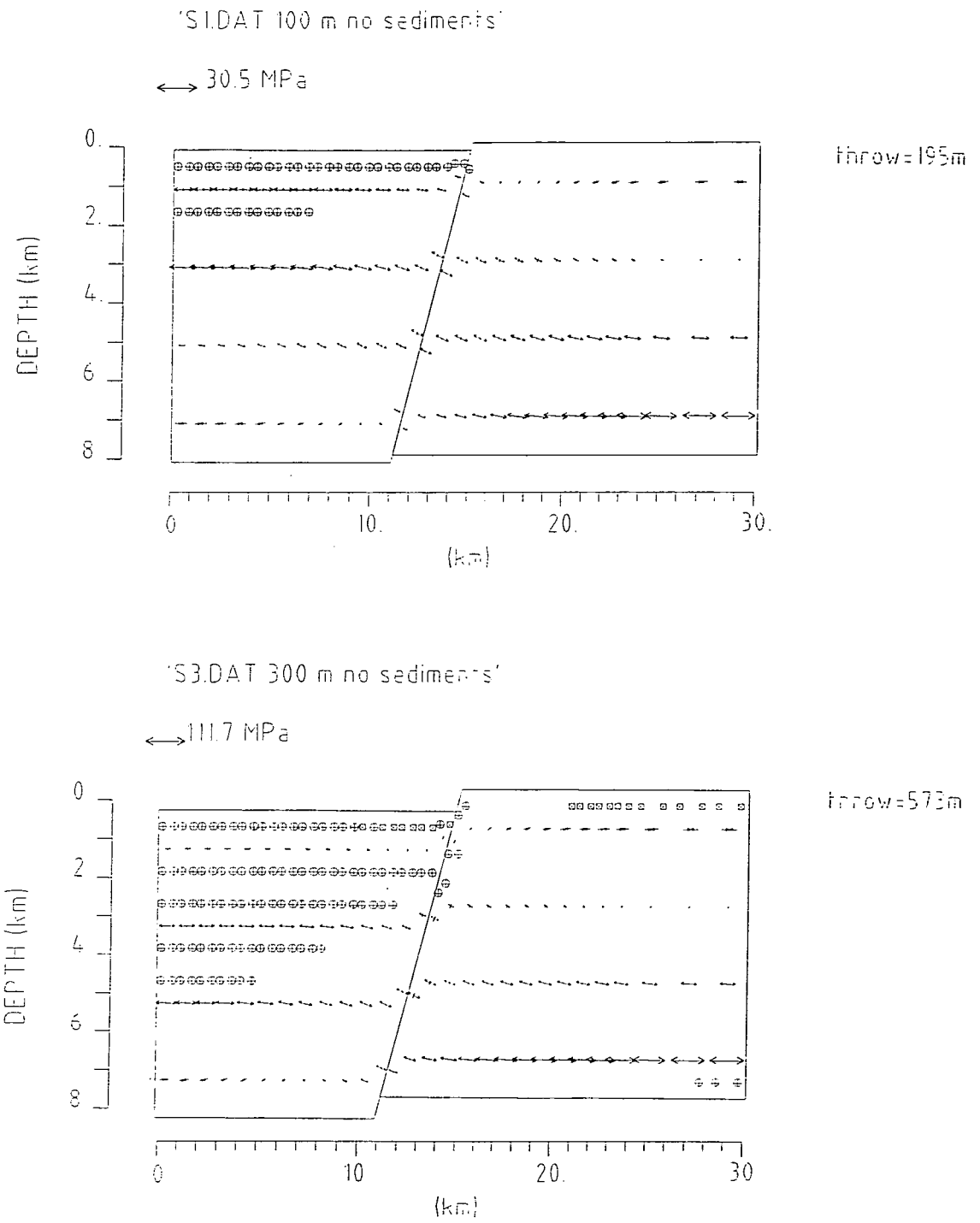

Fig. 5.4 Stress and failure pattern of model S* (8 km thick, 63° fault). The * denotes the number of 100 m increments of applied extension. There is no loading by infill. The maximum stress is shown at the top and the fault throw is shown at the right of each model. All symbols are as described in figure 5.2.

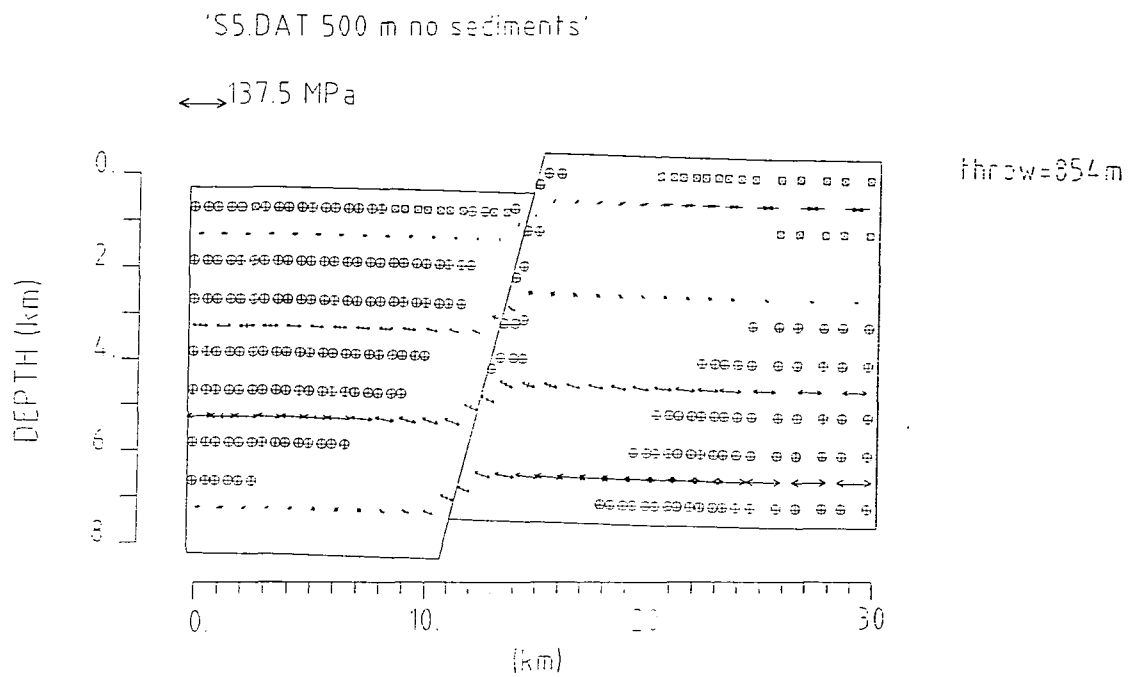

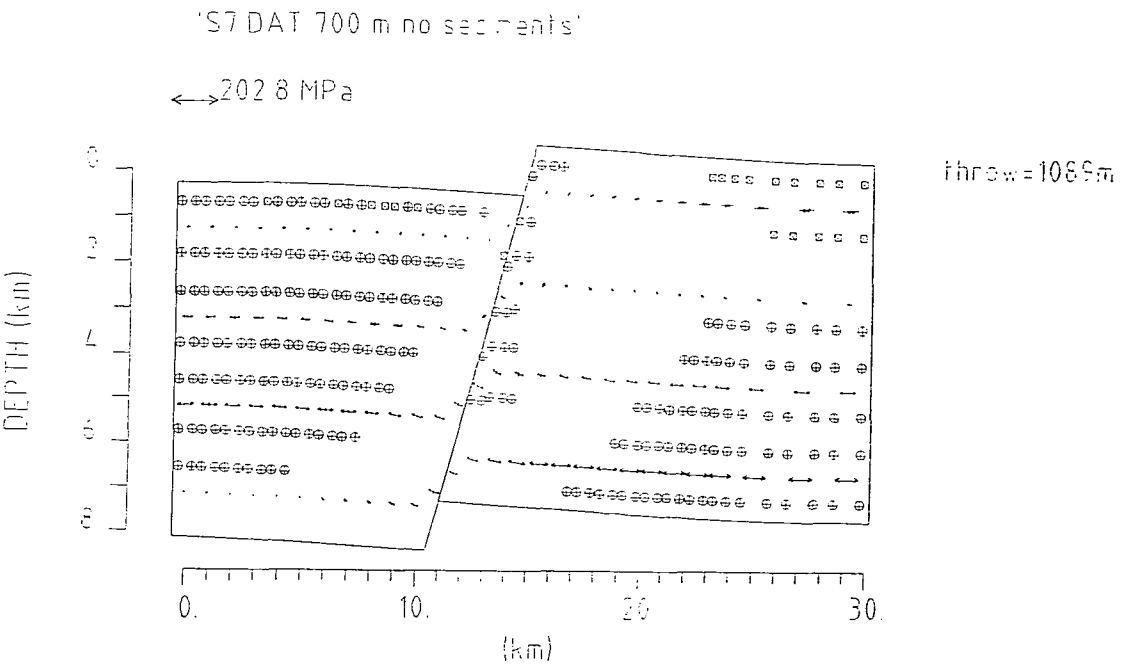

Fig. 5.4 Continuation.

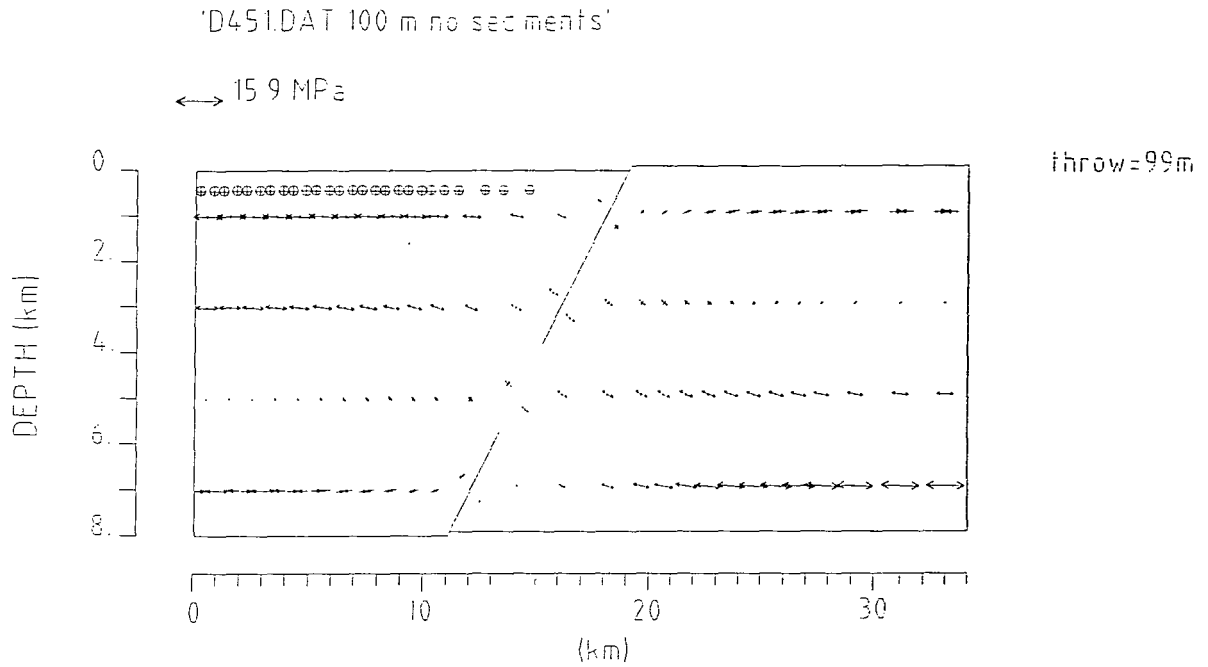

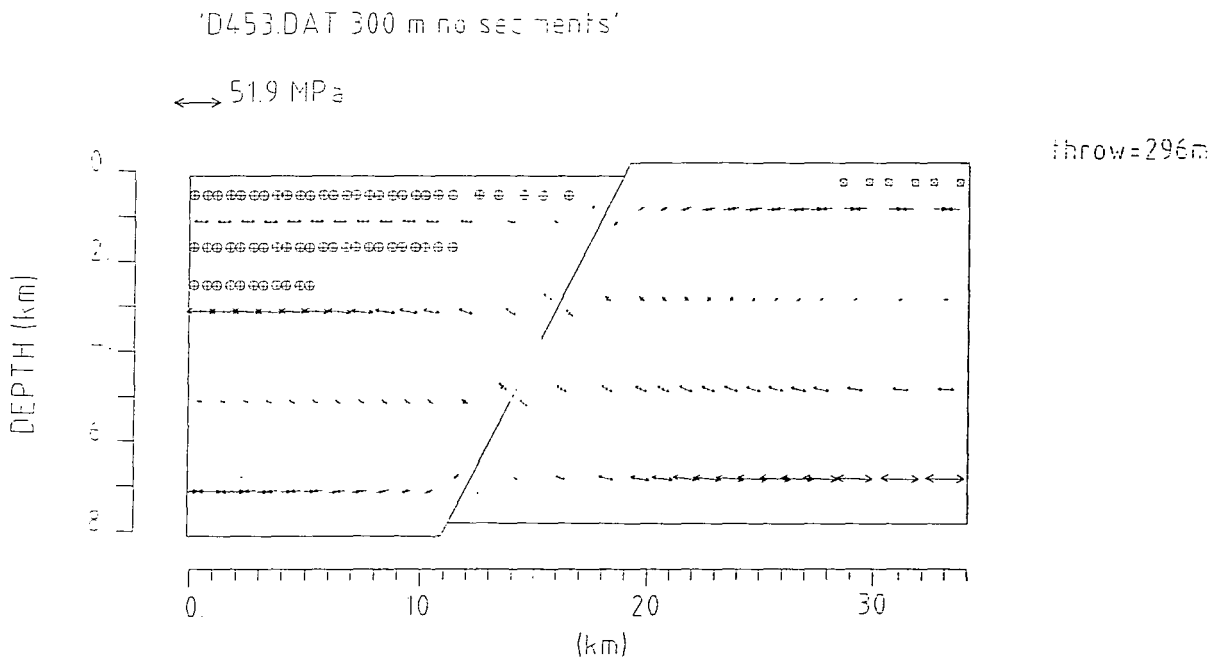

Fig. 5.5 Stress and failure pattern of model D45* (8 km thick, 45° fault). The * denotes the number of 100 m increments of applied extension. There is no loading by infill. The maximum stress is shown at the top and the fault throw is shown at the right of each model. All symbols are as described in figure 5.2.

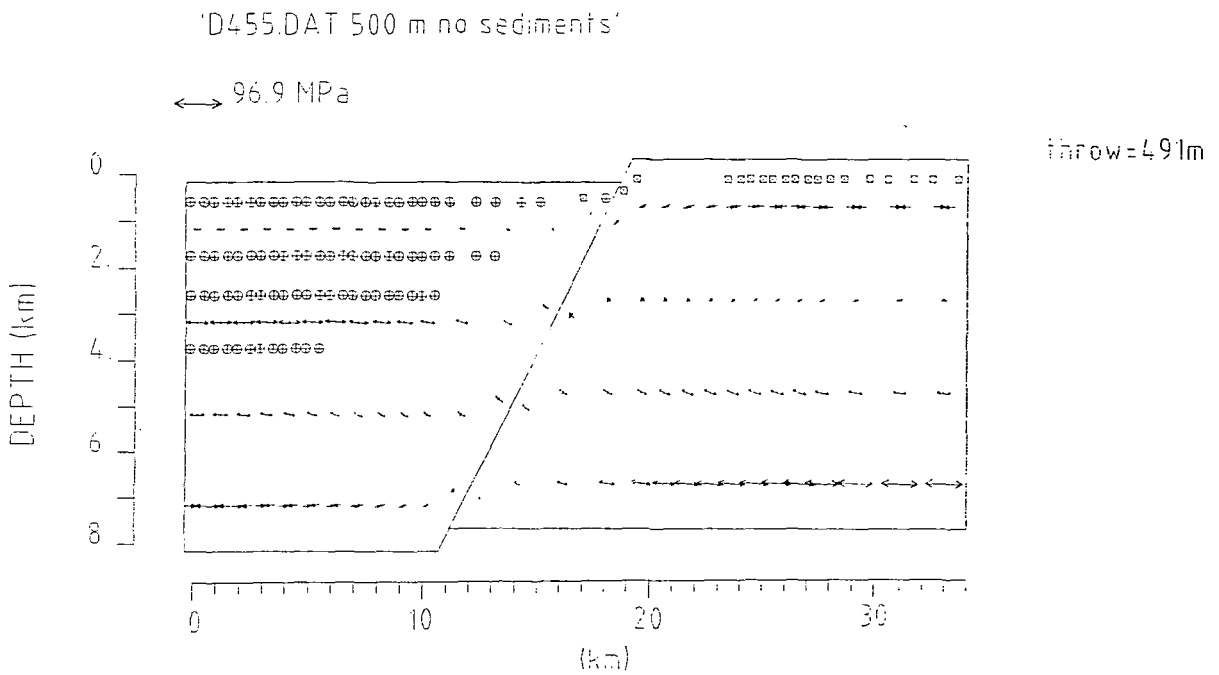

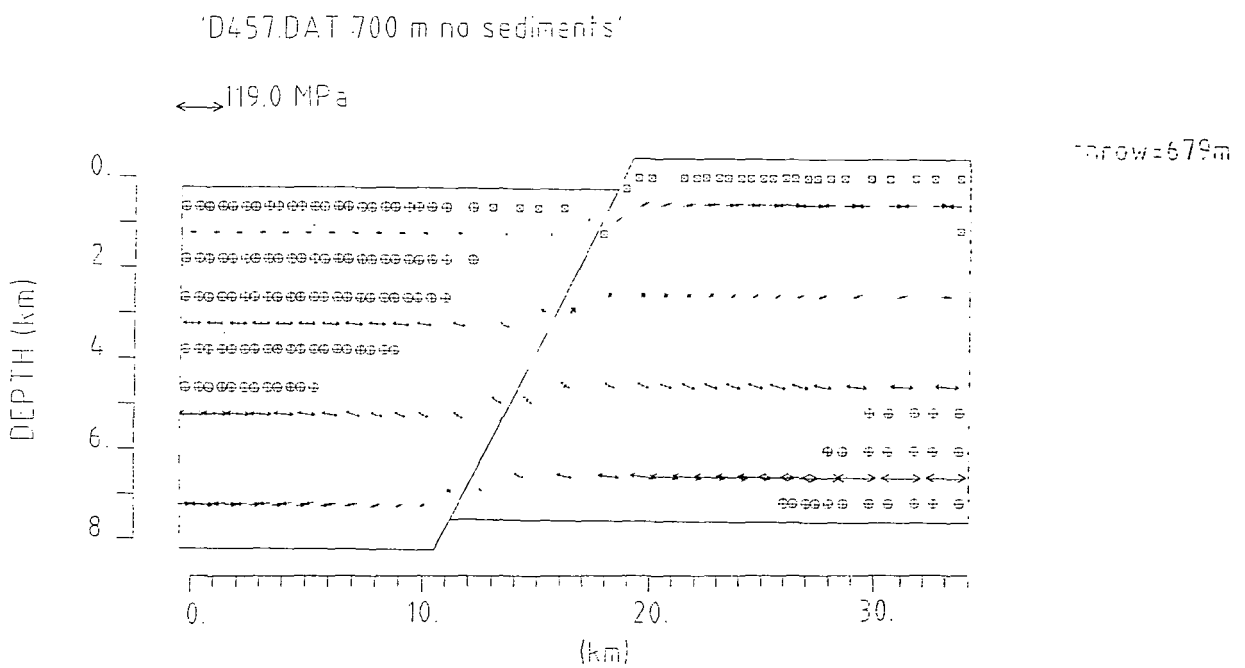

Fig. 5.5 Continuation.

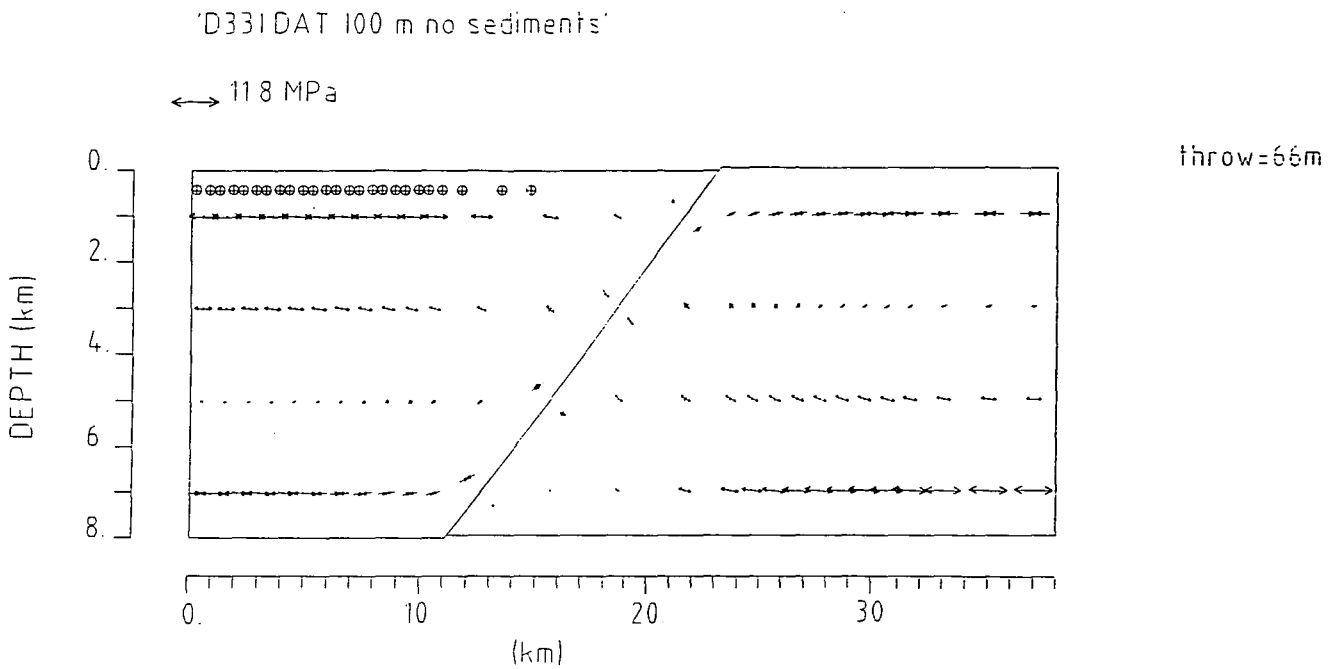

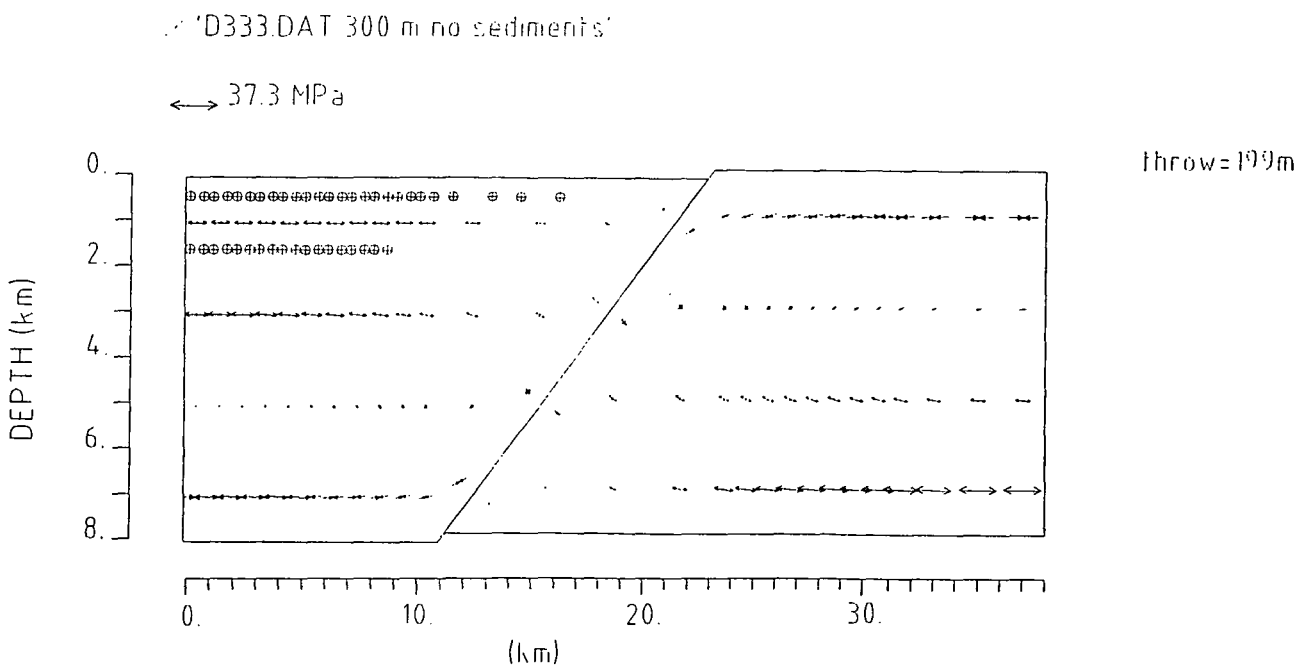

Fig. 5.6 Stress and failure pattern of model D33* (8 km thick, 33° fault). The * denotes the number of 100 m increments of applied extension. There is no loading by infill. The maximum stress is shown at the top and the fault throw is shown at the right of each model. All symbols are as described in figure 5.2.

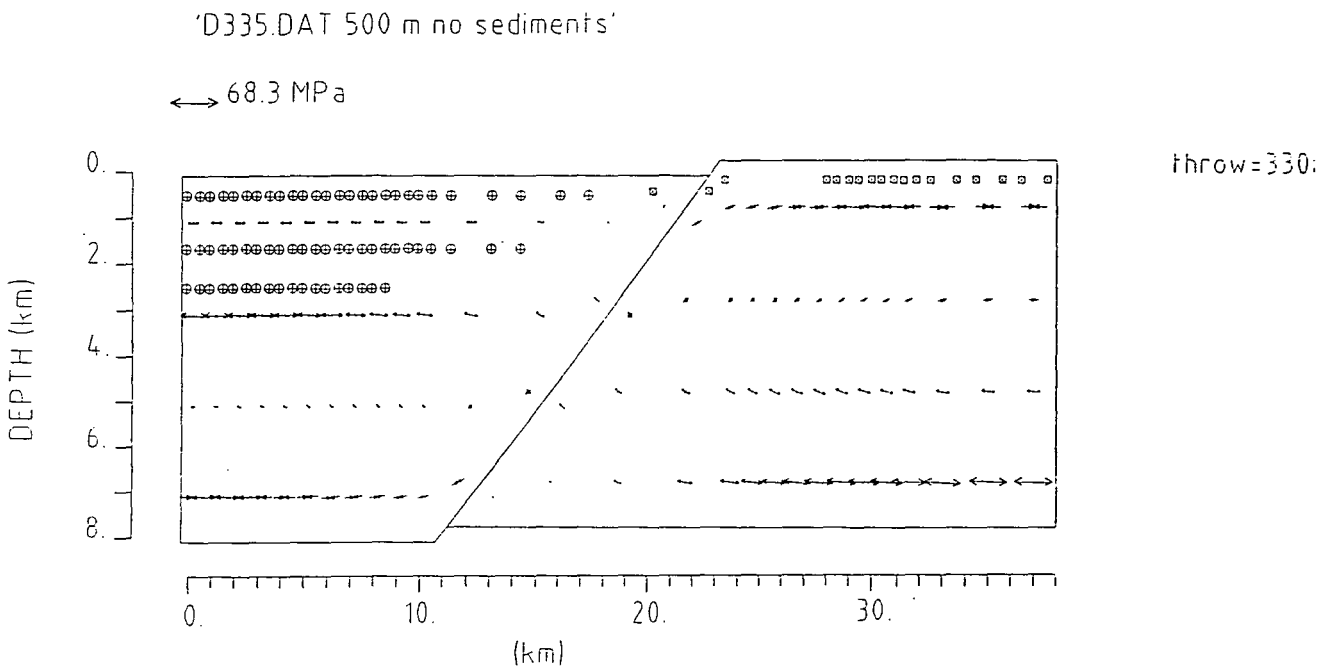

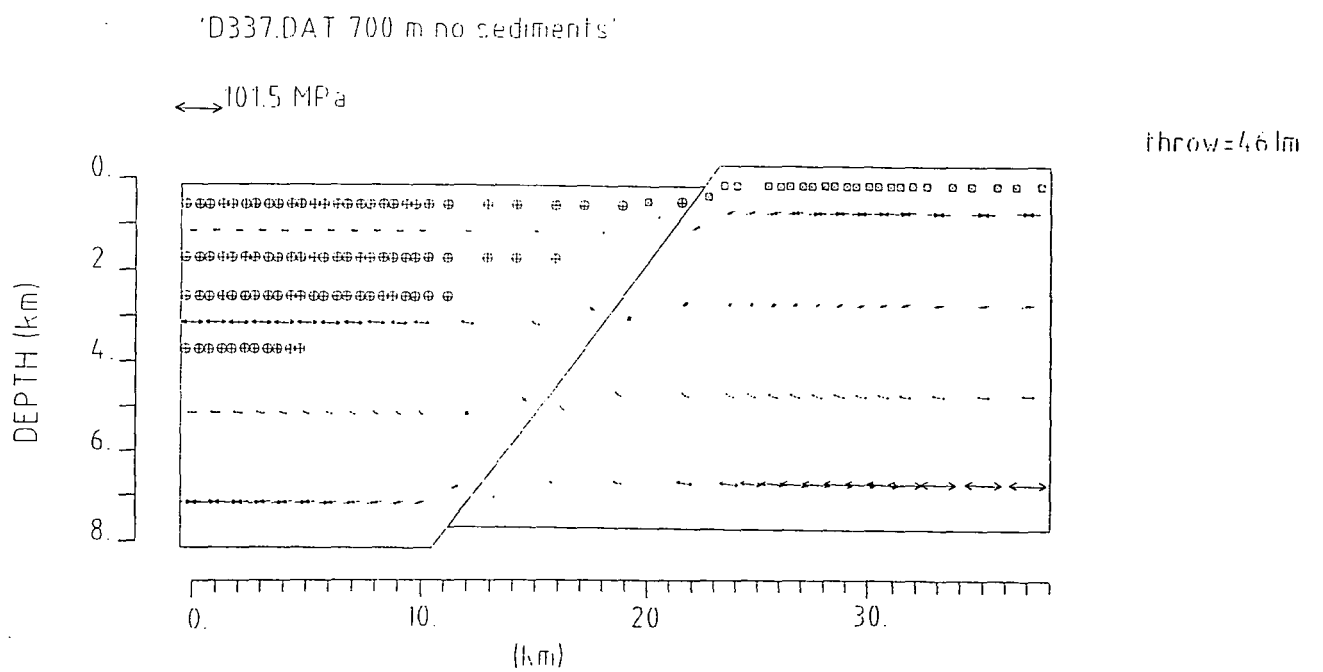

Fig. 5.6 Continuation.

Models S*, D45*, and D33* have lengths of 30 km, 34 km and 38 km respectively. To check if the difference in length between the 8 km thick models affected the results, the length of model S* was increased by 10 km, by adding four more columns of quadrilateral elements to the left edge of the grid. The stress and failure patterns and the flexure profile of model S* were not affected by this modification. Consequently, in the analysis of the results the difference in length between the 8 km thick models is ignored.

5.10 General description of the results

Problems arise due to the small length to thickness ratio of the 8 km thick models. The natural width of flexure is proportional to the flexural parameter, defined as $\alpha = [4D/(\rho_m - \rho_w)g]^{1/4}$ when there is no loading by infill (Turcotte and Schubert,1982). Using the definition of the flexural rigidity D (section 5.2), and the elastic parameter values listed in Table 5.1, the flexural parameter for an elastic plate 8 km thick is $\sim$ 170 km. The 8 km thick models are less than 40 km long and are fixed in the horizontal direction at the edges. These boundary conditions imply that the edges cannot rotate in a vertical plane, and thus the flexure profile must be horizontal at the edges of the model. The plate is forced to bend in the close vicinity of the fault and simultaneously remains unbended at less than 20 km away from it. For large applied extension this causes distortions of the grid and generates numerical instabilities that prevent the convergence of the program to a solution. Therefore, the extension applied to the 8 km thick models is limited to a maximum of 700 m. The 2 km thick model is not seriously affected by the above problem, and so it is extended until almost complete plastic failure through the whole thickness of the layer is achieved.

There are some general features of the results regardless of the layer thickness or the fault dip angle. These are described in terms of the stress distribution, pattern of plastic failure, and vertical displacement of the model's surface.

STRESS DISTRIBUTION (e.g. Fig. 5.2 and Fig. 5.4). As first recognised by Bott (1997) the non-lithostatic stress at each stage of extension is the superposition of three different types of stress:

(1) Tensional stresses caused by the stretching of the layer. The tensional stresses produced by the stretching of the layer are horizontal, and if it was not for the fault would be equally distributed throughout the layer thickness, except where the strength is exceeded and the failure envelope is followed.

(2) Bending stresses caused by the displacement along the fault. The bending stresses are dominant in these models. In the hanging wall they are tensile near the surface and compressive near the bottom of the layer. In the footwall they are compressive near the surface and tensile near the bottom of the layer. Bending stresses are parallel to the surface and nearly horizontal.

(3) Topographical stresses arising from the excess of mass in the upthrown block and deficiency of mass on the downthrown block. Topographical or loading stresses are mainly vertical, being tensile beneath the half-graben because of the low density infill, and compressive beneath the footwall uplift because of the anomalous topographic load. The vertical stresses are much smaller in magnitude than the stretching or bending stresses. Nevertheless they have some influence in the failure pattern as will be seen in section 5.8 where loading is investigated.

As the fault is approached the principal stresses rotate to remain parallel and tangential to the fault plane. This is consistent with the lack of friction along the fault so that it cannot sustain shearing stresses.

PATTERN OF PLASTIC FAILURE (e.g. Fig. 5.2 and Fig. 5.4). Failure first occurs in extension at the surface of the downthrown block. Next, failure in compression occurs at the surface of the upthrown block. The bottom of the upthrown block

close to the right edge of the models also begins to fails in extension at early stages of stretching.

At relatively early stages of stretching, failure in compression develops at the surface of the downthrown block, close to the fault (e.g. model S3 in Fig. 5.4). The compressional failure at shallow levels of the downthrown block is partially caused by unbending close to the fault. As the tensile stresses due to the stretching increase, failure in compression is progressively replaced by failure in extension.

As stretching proceeds, the shallow region of extensional failure in the downthrown block extends laterally and enlarges downwards. At the same time the region of extensional failure at the bottom of the upthrown block grows upwards and towards the fault.

The maximum observed stresses are tensile and occur at the bottom of the upthrown block, at some distance from the fault. There, the strength is maximum, and the extensional bending stresses reinforce the stretching stresses. In contrast, at the bottom of the downthrown block the compressive stresses caused by the bending oppose the extensional stresses due to the stretching. As a result this region remains mainly unaffected by failure.

FLEXURE PROFILE (e.g. Fig. 5.7 and Fig. 5.8). In general, the bending of the plate increases with stretching, becoming more localised with increasing plastic failure. As slip takes place, the hanging wall and the footwall are displaced in opposite senses from the initial datum at zero depth.

For small amounts of extension there is only slight bending. As stretching proceeds the plate's curvature and the displacement relative to the initial datum depend on the model thickness. In the 2 km thick model (Fig. 5.7), the left end of the downthrown block moves slightly above the initial datum, while the remaining part of the block moves below the initial datum. In the upthrown block the opposite happens, with uplift occurring close to the fault and subsidence occurring near the right end of the model.

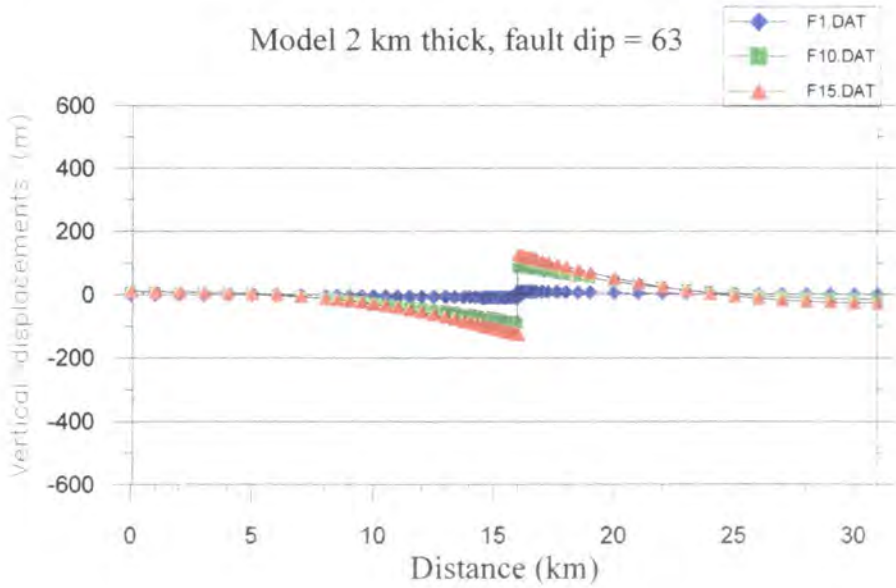

Fig. 5.7 The flexure profile of model F* (2 km thick, 63° fault) at 10, 100, and 150 m of applied extension. Bending increases with stretching and affects the whole length of the model.

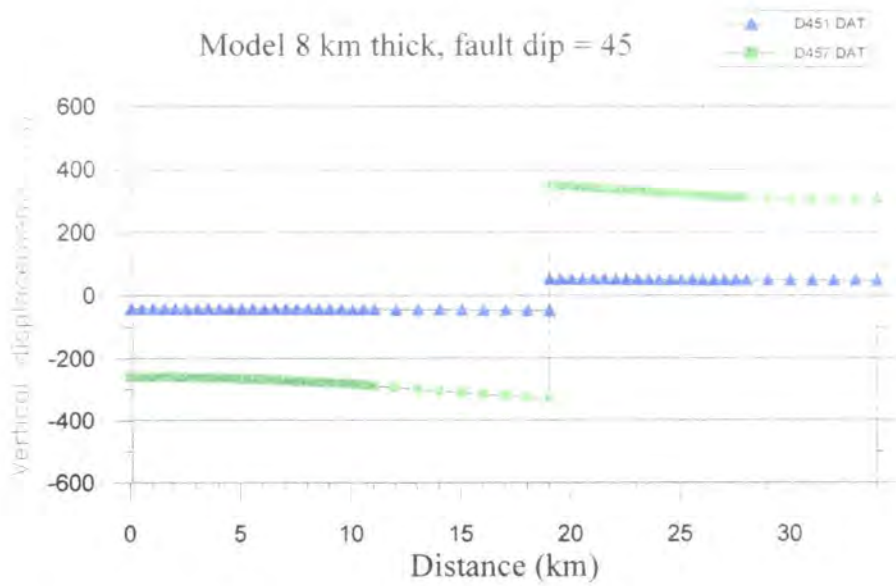

Fig. 5.8 The flexure profile of model D45* (8 km thick, 45° fault) at 100 and 700 m of applied extension. The vertical displacements relative to the initial datum are greatly affected by the boundary conditions. The flexure profile is much nearer the horizontal than it should be for a longer or rotationally unconstrained model.

In the 8 km thick model (Fig. 5.8), slip along the fault shifts the entire downthrown block downwards and the entire upthrown block upwards. However, this result is vitiated by the length to thickness ratio problem referred to at the beginning of this section.

5.11 The effect of changing the brittle layer thickness

Differences between fault observations at fast and slow spreading ridges, and along the axis of slow spreading ridges, have been attributed to differences in the plate's strength. Since strength increases with depth, the larger the brittle layer thickness the larger the plate's strength. To investigate how differences in the brittle layer thickness affect the stress, the pattern of plastic failure is compared for models F* (Fig. 5.2) and S* (Fig. 5.4). The main results are:

- The 2 km thick model (F*) undergoes almost throughgoing plastic failure at 150 m of applied extension, when the fault throw is 270 m. It is difficult to envisage how slip may continue along the fault when the whole layer is flowing plastically in response to extension. As a consequence it is considered that throughgoing plastic failure places a limit on the maximum possible fault throw.

- The 8 km thick model (S*) sustains a maximum stretching of 700 m due to the development of numerical instabilities. However, stretching this model beyond 700 m would result in a fault throw larger than 1100 m. Maximum observed fault throws at slow spreading ridges are about this value, so that it would be unrealistic to stretch this model further.

These results show that the strength profiles can explain why faulting is more well developed at slow spreading ridges than at fast spreading ridges.

The flexural profiles of models F15 and S7 are compared in Fig. 5.9. The main results are:

- The plate curvature in the thinner model is smaller.
- The final fault throw in the thinner model is smaller.
- The departure of the surface from the initial datum is much smaller in the thinner model. However, this large discrepancy between the two models is artificially caused by the boundary conditions at the edges.

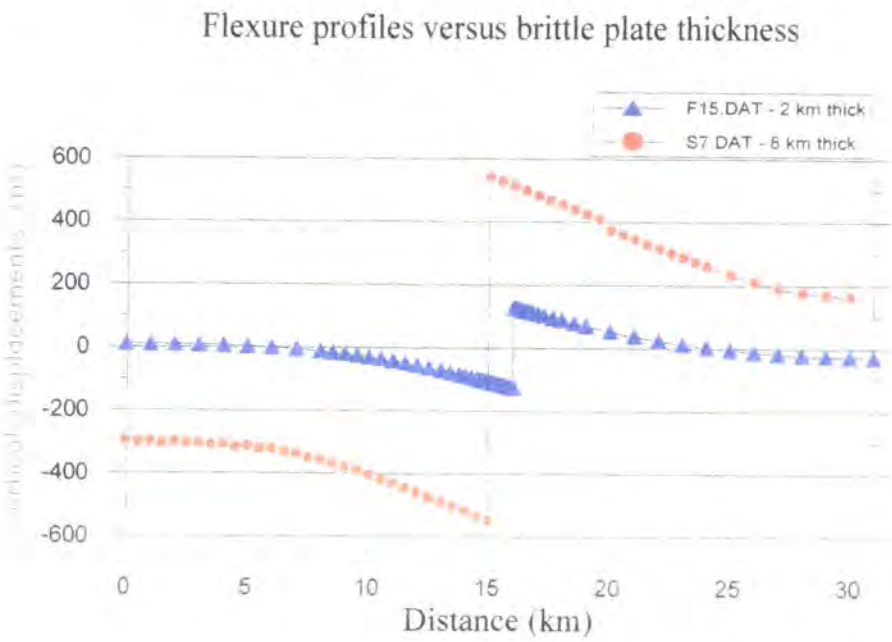

Fig. 5.9 Flexure profile versus brittle layer thickness, for model F* at maximum applied extension (model 2 km thick, 63° fault, 150 m of stretching) and model S* at maximum applied extension (model 8 km thick, 63° fault, 700 m of stretching). The fault throw and the plate curvature are greater for the thicker brittle layer.

In summary, the thickness of the brittle layer varies in the same sense as (1) the maximum stretching the model can sustain, (2) the maximum fault throw, (3) the plate's curvature, and varies in the opposite sense to the degree of plastic failure. Assuming that the amount of extension applied is directly proportional to time, it is concluded that the period of brittle activity of a fault increases with the thickness of the lithosphere.

5.12 The effect of changing the fault dip angle

According to Anderson's theory of faulting (Anderson, 1951) and for a fault coefficient of friction $f_s = 0.85$, the optimal dip angle for normal faults is 65.2° from the horizontal (e.g. Turcotte and Schubert, 1982). Slightly different coefficients of friction yield preferred orientations for active normal faults between 45° and 70° from the horizontal. The purpose of this section is to investigate how the stress and the failure patterns depend on the fault dip angle. At mid-ocean ridges such an investigation is relevant not only because a wide range of fault dip angles are observed, but also because the existence of low-angle faults at segment ends has been used to explain the observed segmentation of slow spreading ridges.

Comparison between models S* (Fig. 5.4), D45* (Fig. 5.5) and D33* (Fig. 5.6) indicates the following:

(1) For a fixed amount of extension, the extent of plastic failure and the fault throw are directly proportional to the fault dip angle. For a given extension, for instance 700 m, the fault throw and plastic failure incidence is maximum in model S* and minimum in model D33*. Since the three models have the same strength envelope, the difference in the failure pattern at a given stage of extension is only due to the inclination of the fault plane. The stretching stresses are basically the same for the three models. The loading stresses are also similar. The difference in the failure pattern of the three models is attributed to the bending stresses and to the amount of extension taken up by the fault's heave. The bending stresses decrease as the fault throw and fault dip angle decrease. Morover, the lower the fault dip the more of the extension is taken up by the heave of the fault.

(2) Plastic failure of the whole layer limits the brittle slippage along the fault. If plastic failure increases with the fault dip angle, then faults dipping at higher angles will cease to be active before faults dipping at

lower angles. These results agree with Forsyth's model (1992) in which the regional stress required to continue sliding against the flexure induced stresses increase with the dip of the fault. Forsyth (1992) predicted that high-angle normal faults, with normal coefficients of friction (around 0.75) cannot accommodate much extension before a new fault forms. His elastic model did not take into account plastic failure. Thus, the higher the fault dip the larger the bending stresses, independently of the model being elastic or elasto-plastic. The results now presented imply that plastic failure further contributes to reduce the ability of the high-angle normal faults to withstand large amounts of extension.

5.13 The effect of loading by infill

Lava flows are more extensive and continuous at fast spreading ridges than at slow spreading ridges. Also, at slow spreading ridges the magmatic budget is higher at segment centres where the brittle plate is thinner. For this reason the effect of loading by infill is studied using the 2 km thick model. The main difference between the failure patterns of the unloaded F* (Fig. 5.2) and loaded FL* (Fig. 5.3) models is:

- Beneath the half-graben, near vertical tensile stresses arise as a result of the effective replacement of crustal rock by lower density infill. These vertical tensile stresses reduce the horizontal deviatoric tensile stresses and increase the horizontal deviatoric compressive stresses. Plastic failure is proportional to the deviatoric stress, so that failure in extension is reduced and failure in compression is enhanced.

The flexure profiles of the loaded and of the unloaded models are compared in Fig. 5.10.

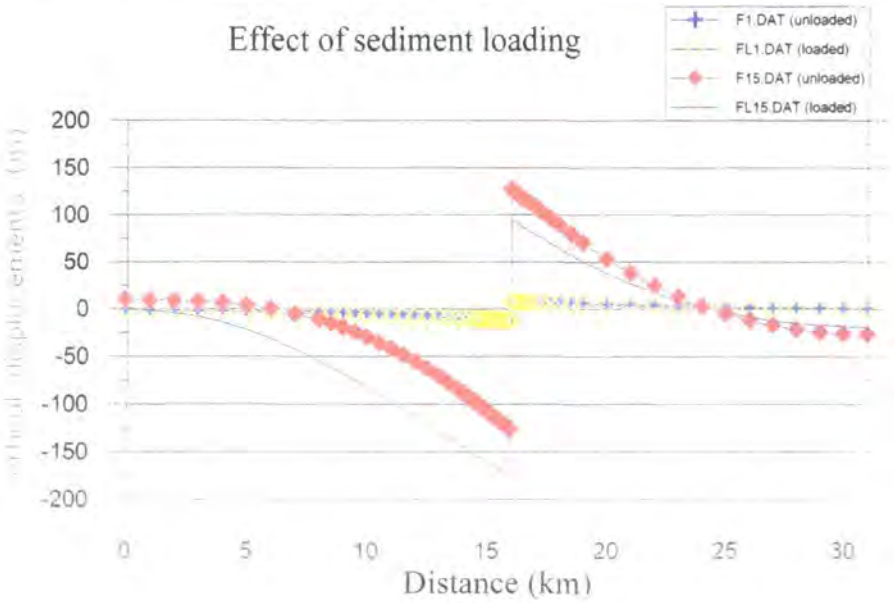

Fig. 5.10 The flexure profiles of model F* (2 km thick, 63° fault) and of model FL* (2 km thick, 63° fault, with infill on the half-graben) at 10 and 150 m of applied tension. Loading by infill increases the subsidence of the hanging wall, reduces the uplift of the footwall, and increases the width of the half-graben.

Loading by infill causes no visible difference at 10 m of extension, when vertical displacements in both models are small. At 150 m of extension the loading increases the subsidence of the downthrown block by 50 m, but also decreases the uplift of the upthrown block by 35 m. As a result the throw of the fault is only 15 m larger in the loaded model. The most significant difference between the two models concerns the width of the half-graben:

- Loading by infill widens the half-graben significantly. The reason for this is apparent from simple flexure theory. The width of the half-graben is proportional to the flexural parameter (section 5.10), which is inversely proportional to the density contrast between water/infill and substratum. The density contrast is larger for water than for infill. Consequently, the unloaded model displays a much narrower half-graben.

5.14 Comparison between elastic and elasto-plastic models

The elastic solution for the 2 km thick, unloaded model F* has been computed. The elastic and elasto-plastic flexure profiles are compared at 10, 100 and 150 m of applied extension (Fig. 5.11).

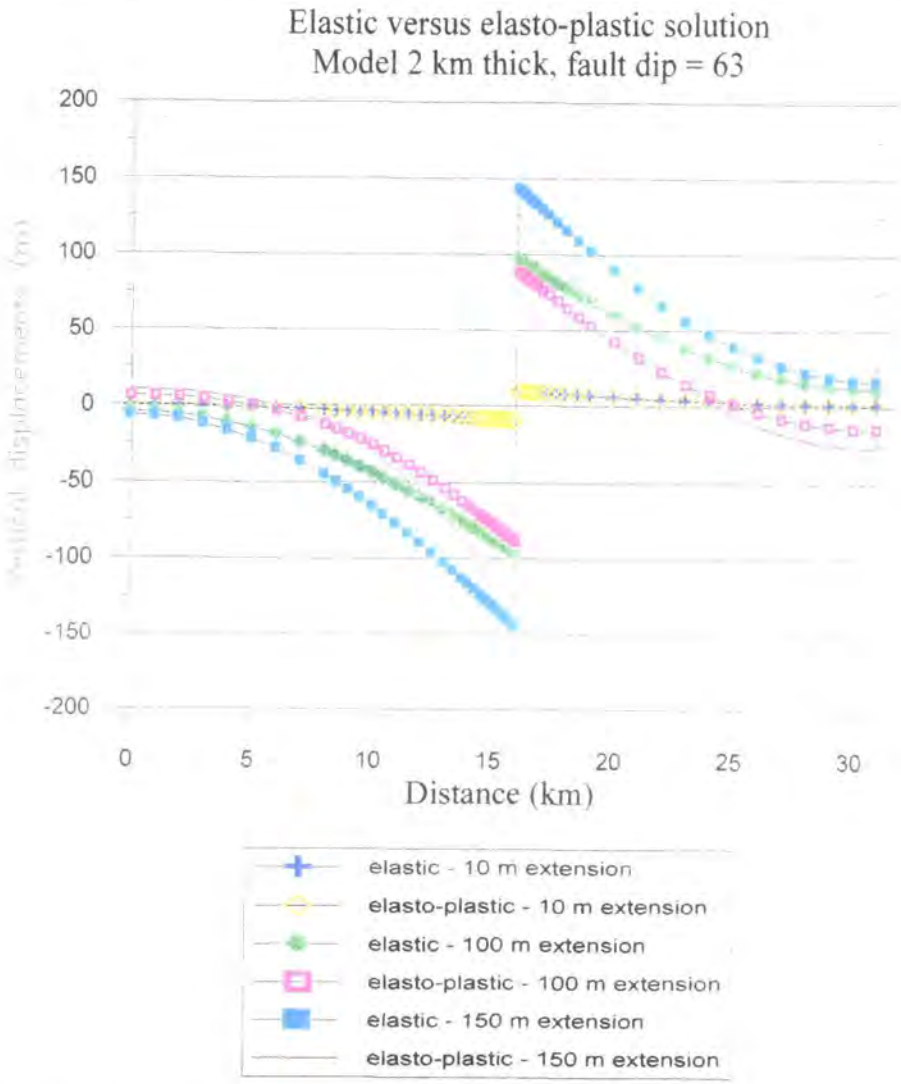

Fig. 5.11 The elastic and elasto-plastic flexure profiles of model F* (2 km thick, 63° fault) are compared at 10, 100 and 150 m of applied extension. Relative to the elastic solution, plastic failure sharpens the plate curvature and reduces the width of the half-graben. It also slightly reduces the subsidence of the hanging wall and the uplift of the footwal.

For small amounts of extension the elastic and elasto-plastic flexure profiles are practically coincident, but as extension and plastic failure increase the two profiles separate. At 150 m of extension, the displacements relative to zero depth at the ends of the elastic model have opposite signs from those observed at the ends of the elasto-plastic model. Nevertheless the vertical distance between the two profiles is never greater than 50 m, and at the fault is only about 35 m. This result shows that in this example plasticity does not significantly modify the fault throw, although it places a limit on the maximum throw that can be reached.

The most important effect of plasticity is to sharpen the plate's curvature and to decrease the width of the half-graben. The width of the half-graben is proportional to the flexural parameter (section 5.10), which decreases for decreasing elastic plate thickness. Plastic failure reduces the equivalent elastic plate thickness, and consequently causes the narrowing of the half-graben.

5.15 Discussion

5.15.1 Comparison with observations

The flexure profiles associated with normal faults cannot be directly compared with observations at mid-ocean ridges. The main reason for this is that in reality fault spacing is too close to allow the measurement of the half-graben width (section 1.3). Nevertheless, it is possible to compare the modelled and observed fault throws.

At fast spreading ridges lava flows are expected to fill up the half-graben to the initial datum. In this case only the footwall uplift can be observed. The loaded 2 km thick model yields a maximum footwall uplift of 95 m. Footwall uplifts reported along the East Pacific Rise and other fast spreading ridges range from a few tens of meters to about 150 m (e.g. Carbotte and Macdonald, 1994), consistent with the modelled value.

At slow spreading segments sediment and/or volcanic infill is small, and consequently it is not expected to affect the fault throw observations. The unloaded

models yield maximum fault throws of 255 m and 1100 m for the 2 km and 8 km thick brittle layers, respectively. These values are consistent with fault throws observed along the MAR, of 200-600 m at segment centres and 800-1200 m at segment ends (e.g. Shaw, 1992).

From the above comparisons it is concluded that the models provide a good fit to observations of fault throws at mid-ocean ridges. More importantly, the modelling shows that (1) plastic failure prevents large fault throws from occurring in thin strong layers at fast spreading ridges, in contrast to slow spreading ridges, and (2) variations in the brittle layer thickness can account for the observed dependence of the fault throw on the spreading rate and along axis position.

5.15.2 Tectonic strain

The tectonic strain is the total strain accommodated by brittle deformation. It is usually calculated from the fault heave and spacing. Estimates of the tectonic strain at the East Pacific Rise range from 5% to 10% (Cowie et al., 1993; Bicknell et al., 1987). At the Mid-Atlantic Ridge recent estimates based on high resolution side-scan sonar data suggest tectonic strains between 10% and 25% (Escartin et al., 1999).

The tectonic strain in the modelling can be computed using $e = H/L_i$, where H is the heave of the fault after maximum applied extension and L_i is the initial length of the model. The 2 km thick, unloaded model after 150 m of extension yields $e = 0.43\%$. The 8 km thick model after 700 m of extension yields $e = 1.84\%$. The modelled tectonic strains are therefore much less than the observed ones, simply because just one fault is used in the modelling whereas multiple faults occur in reality. This result also implies that the stretching applied to the models has not reached unrealistic values.

The modelled tectonic strain can be compared with the modelled total extensional strain, which is given by $\mathsf{E} = (L_f - L_i)/L_i$, where L_f is the final length of the model after maximum applied extension. Application to the 2 km thick, unloaded

model after 700 m of extension gives $\mathsf{E} = 2.33\%$. The fraction of the modelled strain that can be attributed to elasto-plastic extension $(\mathsf{E} - e)/\mathsf{E}$ is thus much less than the fraction attributed to the fault heave e/E.

5.15.3 Fault longevity

Fault longevity is important in the context of ridge segmentation models that involve detachment faults at slow spreading segment ends. Fault longevity corresponds to the period of activity of the fault, i.e. the period of time while there is slip on the fault. Observations at slow spreading ridges suggest that faults at segment ends are active for longer periods of time than faults at segment centres, because (1) fault throws at segment ends are larger, and (2) the oceanic analogues to metamorphic core complexes have only been found at segment ends, more specifically at inside corners.

The oceanic analogues to continental metamorphic complexes, found at several inside corners along the MAR, have been termed megamullions (Tucholke et al., 1998). Dredging at some of these structures revealed the exposure of lower crust gabbros and serpentinized upper mantle peridotites. It has therefore been suggested that prolonged slip along low-angle detachment faults is responsible for the exposure of such rocks, and that the occurrence of detachment faults at slow spreading ridges is restricted to inside corners (Karson, 1990). The dip at fossil off-axis terminations of megamullions average 23°, and the active (or recently active) detachment faults observed have dips of about $35° - 38°$ (Tucholke et al., 1998). Therefore, detachment faults at inside corners are assumed to have lower dip angles than normal faults at segment centres or outside corners.

According to Tucholke et al. (1998) two main factors can explain why detachment faults accommodate slip for so long: (1) detachment faulting is active during phases of amagmatic extension. The average duration of an amagmatic phase of extension, which is characterised by elevated values of Residual Mantle Bouguer Anomaly (RMBA) and thinner crust, is about 1.6 m.y, and (2) detachment faults

are exceptionally weak. Detachment faults may be exceptionally weak due to the presence of serpentinites along the fault.

In my modelling the total amount of extension applied is assumed to be proportional to the total amount of elapsed time. Accordingly, two main factors can explain the longer longevity of normal faults at slow spreading segment ends:

1. The larger brittle plate thickness at segment ends. It was shown that the larger the brittle thickness the larger the amount of extension the model can withstand.

2. The lower dip angle of the detachment faults presumed to exist at inside corners. It was also shown that the lower the dip fault angle the larger the amount of extension the model can withstand.

If the longevity of detachment faults is due to their low dip, what remains to be explained is why low angle faults should be favoured at segment ends. The answer may be that enhanced serpentinisation occurs at segment ends as proposed by Escartin et al. (1997). The presence of serpentinites lowers the coefficient of internal friction of the lithosphere. The Coulomb-Navier criterion of fracture predicts that the optimum dip angle for fault formation decreases with the coefficient of internal friction. Thus, low angle dipping faults may occur preferentially where serpentinites are abundant, i.e. at inside corners.

Finally, Tucholke et al. (1998) noted that megamullions represent only a small fraction of the inside corner highs observed along the MAR. They suggest this happens because even minor magmatic episodes within an amagmatic phase may lead to the termination of slip along detachment faults. Two alternative explanations can be proposed based on my work: (1) the brittle layer thickness at inside corners may not always be large enough and (2) the formation of low angle normal faults at inside corners may not always happen.

Chapter 6

Models of stress at mid-ocean ridge offsets

6.1 Introduction

The study of major plate dynamics, and of the state of stress at mid-ocean ridge offsets, has been mainly done with two-dimensional numerical models which neglect sources of vertical stress (e.g. Richardson et al., 1979; Phipps Morgan and Parmentier, 1984). These models, which rely on the thin sheet approximation, have been relatively successful and provide important constraints on plate boundary forces. However, at the local scale of mid-ocean ridge offsets, sources of vertical stress may be important. Without wanting to develop a full 3D numerical method, a formulation that allows one to include vertical stresses into 2D horizontal models is presented in section 6.2.3. In this formulation the most relevant source of vertical stress in young oceanic lithosphere is the topographic load created by the elevation of mid-ocean ridges relative to old seafloor. In order to test the modelling method, simple models of stress at mid-ocean ridge offsets are presented. The stress patterns obtained are then compared with structural observations at transform faults and non-transform offsets.

The formulation derived in this chapter constitutes an alternative to previous modelling efforts, in which the reproduction of the observed structures at mid-ocean ridge offsets was done by varying the ratio between the ridge resistance force and

the transform resistance force (e.g. Phipps Morgan and Parmentier, 1984; Grindlay and Fox, 1993). These modelling efforts failed to explain the existence of extensional structures striking at high angles (> 35°) to the ridge trend, often found at ridge-transform intersections (e.g. Karson and Dick, 1983; Searle, 1983, Fornari et al., 1989). The generation of such structures is predicted here.

6.2 Modelling assumptions and procedure

6.2.1 Rheology

The oceanic lithosphere is represented by a 2D horizontal plate of constant thickness. It is divided into two distinct mechanical regions. The brittle and relatively strong plate outside the ridge axial zone is represented by elastic rheology. The elastic behaviour is characterised by specifying the Young's modulus (E) and the Poisson's ratio (ν). The values assumed, $E = 1.0 \times 10^{11}$ Pa and $\nu = 0.25$, are generally accepted for the oceanic lithosphere (e.g. Turcotte and Schubert, 1982).

The ridge axial zone, characterised by extensive fissuring and normal faulting, is described by elasto-plastic rheology (section 3.5). Plastic flow is often adopted as a continuum description of deformation on distributed faults, provided the distance between faults is small compared to the size of the deforming zone (e.g. Lin and Parmentier, 1989). I assume this condition is met at mid-ocean ridges, where the spacing between fractures (tens to hundreds of metres) and between well developed normal faults (on average about 1.5 km) is small compared to the width of the region affected by active normal faulting (up to 20 km)(section 1.3). The width of the elasto-plastic axial zone is 10 km, to be consistent with the average width of the region of active normal faulting at mid-ocean ridges.

The elasto-plastic or elasto-viscoplastic material is characterised by the strength value. Provided the relaxation time is sufficient, viscous stress relaxation will continue until the strength value is approximately attained. The strength of the elasto-plastic material in the ridge axial region was determined from estimates of the ridge

resistance force. A strength of 30 MPa and 15 MPa at slow and fast spreading ridges respectively, is assumed based on the work of Lachenbruch (1973).

6.2.2 Grid geometry and boundary conditions

All models presented in this Chapter are based on the finite element grid presented in Fig. 6.1. The grid contains 64 identical quadrilateral elements 10 km × 10 km each, having a total area of 80 km × 80 km. Each element has 8 nodes and 4 gauss points. The main differences between the models are the location of the ridge segments (i.e. of the elasto-plastic elements), and the inclusion or not of a fault between ridge segments.

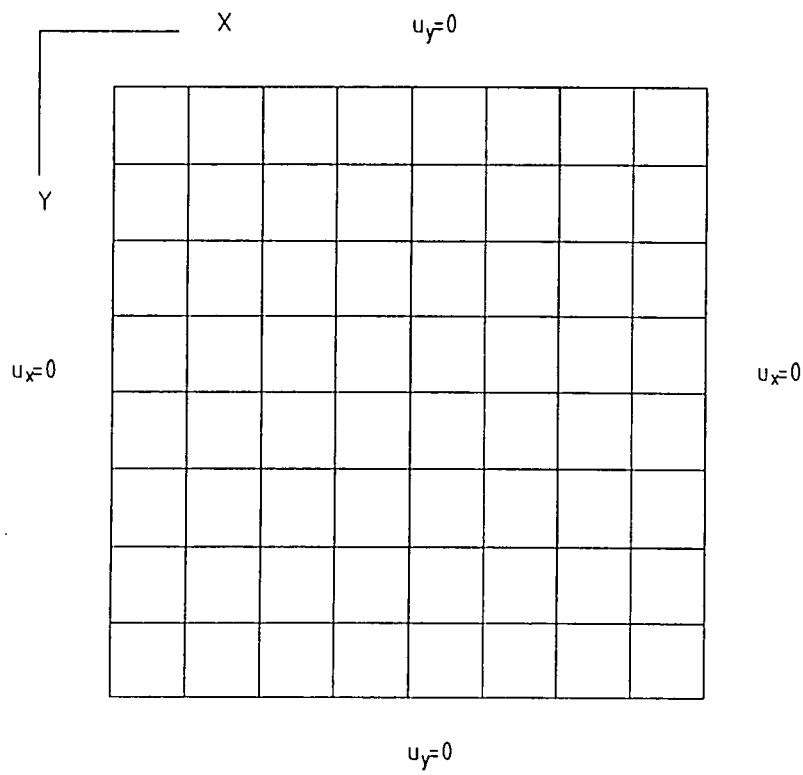

Fig. 6.1 The finite element grid used in the modelling. It contains 64 identical isoparametric quadrilateral elements. Normal displacements to the outer boundaries are set to zero.

The external boundaries of the model are either parallel or perpendicular to the ridge axis. At all outer boundaries the displacements in the normal direction to the boundary were set to zero.

At boundaries perpendicular to the ridge axis the boundary conditions imply that convergence or divergence across transforms is not allowed. Although evidence of deformation in the normal direction to the fault's strike has been found in some transforms (e.g. Fornari et al., 1989, Wilcock et al., 1990; Pockalny, 1997), pure strike-slip movement is the dominant process and the most general situation to model.

At boundaries parallel to the ridge axis the boundary conditions are artificial. They are imposed to obtain a stress field consistent with observations. More specifically, it was found necessary to fix the boundaries parallel to the ridge axis to obtain a negligible level of deviatoric extension, or some small deviatoric compression, at about 80 km from the ridge axis. Free boundary conditions parallel to the ridge axis were tested (section 6.3.2) and not used for producing tensile deviatoric stresses perpendicular to the ridge axis in plate interiors.

Faults are incorporated in the finite element model using the dual node technique. Only completely locked and completely unlocked faults are modelled due to software limitations. Nevertheless, this allows one to analyse the behaviour of offsets when their strength is either very large (locked) or very weak (unlocked). Unlocked and locked faults are modelled by attributing to the fault's shear stiffness a zero or high value respectively. Alternatively, in section 6.4.4 transform fault offsets are modelled as finite width weak elasto-plastic zones.

Taking into account all the evidence suggesting that transform faults are weak it seems a better approximation to model transforms with zero frictional strength. How can locked transform faults and locked non-transform offsets be justified? Locking can occur for short periods of time or along some sections of the fault. For instance, the San Andreas fault apparently contains some locked sections (e.g. Turcotte and Schubert, 1982), and ridge parallel structures can be traced across the extensions of some second-order discontinuities of the Mid-Atlantic Ridge, indicating temporal locking (Grindlay et al., 1991). Temporal locking at ridge-transform intersections may occur as the base of the newly formed lithosphere periodically welds to the older juxtaposed plate (Fox and Gallo, 1984).

6.2.3 Application of the topographic loading

The topographic load created by the elevation of ridges relative to old seafloor generates a non-lithostatic vertical stress inside the oceanic plate. It is assumed that the topography exerts a vertical normal stress equal in magnitude but opposite in sign to the normal stress caused by buoyancy of low density asthenosphere beneath the plate. The surface and subsurface loads must be equal and opposite to guarantee local isostatic equilibrium (Fig. 6.2).

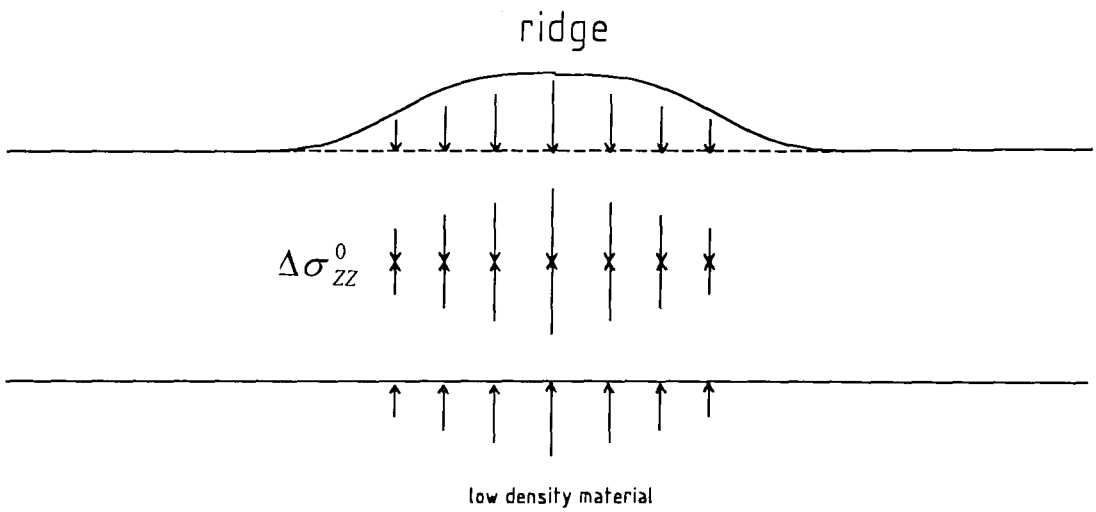

Fig. 6.2 The surface and subsurface loads associated with the topography of mid-ocean ridges produce vertical non-lithostatic stresses $\Delta\sigma^0_{zz}$ in the lithospheric plate.

In the region between the loads the vertical non-lithostatic stress is,

$$\Delta\sigma^0_{zz} = (\rho_m - \rho_w)gh, \tag{6.1}$$

where ρ_m is the density of the mantle, ρ_w is the density of the seawater, g is the acceleration of gravity and h is the height of the seafloor relative to the reference depth of old seafloor.

The actual depth of the seafloor can be calculated from the empirical relation, $d = d_r + 350\,t^{1/2}$, where d_r is the seafloor depth at the ridge axis (in meters) and t is the age of the seafloor (in million years)(Parsons and Sclater, 1977). It is assumed

that $d_r = 2500$ m, which is a good approximation to observations at both slow and fast spreading ridges. Two end member models of mid- ocean ridges and associated bathymetric profiles, are represented in Fig. 6.3. Profile (a) corresponds to a (slow) ridge spreading at a half rate of 15 mm/yr. Profile (b) corresponds to a (fast) ridge spreading at a half rate of 60 mm/yr.

The depth of lithosphere 75 Ma old (5531 m) is chosen as reference. Therefore, the height of the seafloor in Eq. 6.1 is $h = 5531 - d$, where d is the actual depth of the seafloor.

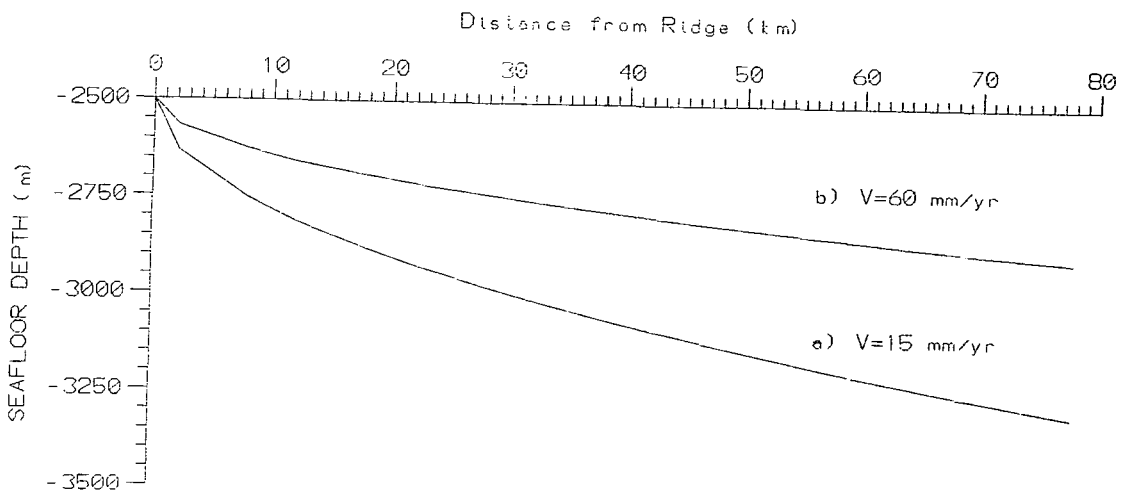

Fig. 6.3 Seafloor depth as a function of distance to the ridge axis, as predicted by the empirical relationship of Parsons and Sclater (1977) for two half-spreading rates: a) 15 mm/yr and b) 60 mm/yr. The depth at the ridge crest is assumed to be 2500 m.

The actual topography at the ridge axis is neglected, that is, the existence of a median valley or an axial high is ignored. What justifies this approximation is that the region of axial topography is represented by the elasto-viscoplastic rheology. As a result, the deviatoric stress in the ridge axial zone is primarily determined by the strength of the material and only secondarily determined by the applied topographic load.

The plane stress approximation was adopted, implying that the plate is thin relative to its horizontal dimensions. The plane stress approximation also implies that only horizontal loading is considered. How can we then implement in the models the effect of a vertical topographic load? By evaluating the effect of the vertical loading on the horizontal non-lithostatic stress as follows.

First, consider the stress-strain relations for a perfectly elastic isotropic solid (e.g. Jaeger, 1969),

$$\Delta\sigma_{xx} = \frac{E(1-\nu)}{(1+\nu)(1-2\nu)}\left(e_{xx} + \frac{\nu}{1-\nu}\, e_{yy} + \frac{\nu}{1-\nu}\, e_{zz}\right), \tag{6.2}$$

$$\Delta\sigma_{yy} = \frac{E(1-\nu)}{(1+\nu)(1-2\nu)}\left(\frac{\nu}{1-\nu}\, e_{xx} + e_{yy} + \frac{\nu}{1-\nu}\, e_{zz}\right), \tag{6.3}$$

$$\Delta\sigma_{zz} = \frac{E(1-\nu)}{(1+\nu)(1-2\nu)}\left(\frac{\nu}{1-\nu}\, e_{xx} + \frac{\nu}{1-\nu}\, e_{yy} + e_{zz}\right) \tag{6.4}$$

Now, let the actual vertical stress be equal to a specified stress, that is $\Delta\sigma_{zz} = \Delta P_{zz}$. Solving Eq. 6.4 in order to obtain the vertical strain gives,

$$e_{zz} = \frac{(1+\nu)(1-2\nu)}{E(1-\nu)}\,\Delta P_{zz} - \frac{\nu}{1-\nu}(\, e_{xx} + e_{yy}) \tag{6.5}$$

Upon substitution of Eq. 6.5 into Eq. 6.2 and Eq. 6.3 the horizontal tectonic stresses become,

$$\Delta\sigma_{xx} = \frac{E}{1-\nu^2}(e_{xx} + \nu e_{yy}) + \frac{\nu}{1-\nu}\,\Delta P_{zz}, \tag{6.6}$$

$$\Delta\sigma_{yy} = \frac{E}{1-\nu^2}(\nu e_{xx} + e_{yy}) + \frac{\nu}{1-\nu}\,\Delta P_{zz}. \tag{6.7}$$

According to Eqs. 6.6 and 6.7 the specified vertical stress ΔP_{zz} gives rise to initial horizontal stresses equal to,

$$\Delta\sigma^0_{xx} = \frac{\nu}{1-\nu}\,\Delta P_{zz}, \tag{6.8}$$

$$\Delta\sigma^0_{yy} = \frac{\nu}{1-\nu}\,\Delta P_{zz}. \tag{6.9}$$

In the modelling the specified stress ΔP_{zz} is equal to the non-lithostatic stress created by the ridge topographic load σ^0_{zz}, that is,

$$\Delta\sigma^0_{xx} = \frac{\nu}{1-\nu}(\rho_m - \rho_w)gh, \tag{6.10}$$

$$\Delta\sigma^0_{yy} = \frac{\nu}{1-\nu}(\rho_m - \rho_w)gh. \tag{6.11}$$

The spreading is assumed to be orthogonal to the ridge, and no bathymetric variations along isochrons are considered. Consequently, the vertical loading only varies in the direction perpendicular to the ridge axis. The vertical loading is computed at each Gauss point, assuming $\rho_m - \rho_w = 2300\,\mathrm{kg/m^3}$ and $g = 9.8\,\mathrm{m/s^2}$, and input to the model. At each Gauss point the elevation h is determined by the distance of the Gauss point to the ridge axis. Since the axial morphology is neglected, inside the ridge axial zone a constant vertical load is assumed (Fig 6.4).

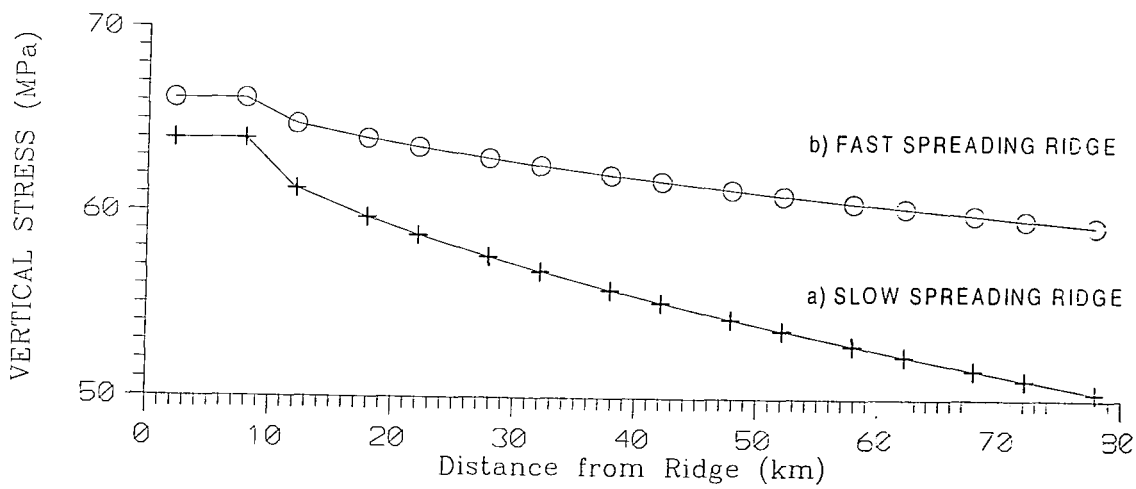

Fig. 6.4 The vertical non-lithostatic stress as a function of distance from the ridge. Profile a corresponds to the topographic load associated with a slow spreading ridge (profile a in Fig. 6.3), and profile b corresponds to the topographic load associated with a fast spreading ridge (profile b in Fig. 6.3). The points along the profiles correspond to the location of the Gauss points in the finite element model.

6.3 Models of stress from mid-ocean ridges to intraplate regions

The principal aspect of the stress field that is modelled in this section is the fading of the ridge perpendicular tensile stresses, and eventually the transition from extension to compression, observed as we move away from mid- ocean ridges (section 2.7). This is accomplished through the combination of topographic loading, boundary conditions and rheologic assumptions.

The ridge axial zone is 10 km wide and is represented by the light dotted pattern at the left end of the models (e.g. Fig. 6.5). The horizontal stresses are scaled relative to the value displayed at the right of each model (e.g. 15 MPa in Fig. 6.5), and are plotted at the centre of each element. Compressive stresses are represented by inward pointing arrows and tensile stresses are represented by outward pointing arrows. Both the principal and the deviatoric stress fields are displayed.

Recall that deviatoric stresses are related to the principal stresses through Eq. 2.5 (section 2.2). Using the assumption of plane stress, with an initial vertical stress $\Delta\sigma^0_{zz}$ that remains always constant, the relation between the deviatoric and principal stresses becomes,

$$\begin{aligned}
\Delta\sigma^D_{xx} &= \Delta\sigma_{xx} - \frac{1}{3}(\Delta\sigma_{xx} + \Delta\sigma_{yy} + \Delta\sigma^0_{zz}), \\
\Delta\sigma^D_{yy} &= \Delta\sigma_{yy} - \frac{1}{3}(\Delta\sigma_{xx} + \Delta\sigma_{yy} + \Delta\sigma^0_{zz}), \\
\Delta\sigma^D_{zz} &= \Delta\sigma^0_{zz} - \frac{1}{3}(\Delta\sigma_{xx} + \Delta\sigma_{yy} + \Delta\sigma^0_{zz}).
\end{aligned} \tag{6.12}$$

6.3.1 Elastic model (slow spreading ridge)

In a horizontally confined elastic model, with boundaries fixed all around the model as explained in section 6.2.2, we have $\epsilon_{xx} = \epsilon_{yy} = 0$. Using $\nu = 0.25$ and a constant topographic load corresponding to $\sigma^0_{zz} = 10\,\text{MPa}$ we obtain from Eq. 6.6 and Eq. 6.7 compressive principal stresses $\Delta\sigma_{xx} = \Delta\sigma_{yy} = 3.33\,\text{MPa}$, and from Eq. 6.12

tensile deviatoric stresses $\Delta\sigma^D_{xx} = \Delta\sigma^D_{yy} = -2.22\,\mathrm{MPa}$. In this case the stresses are constant and uniform all over the model.

When the topographic load is as represented in profile a of Fig. 6.4, corresponding to a spreading rate of 15 mm/yr, we obtain the results of model RISEL (Fig. 6.5 and Fig. 6.6). The magnitudes of the principal and deviatoric stresses, nearly equal at each point, decrease with distance from the ridge due to the decrease of the topographic load. Nevertheless, the deviatoric ridge perpendicular stresses in the ridge axial zone (dotted pattern) should be unequivocally larger than the deviatoric ridge parallel stresses, to fit observations. A more realistic stress pattern is accomplished through the use of a viscous rheology in the ridge axial zone as shown in the following subsection.

6.3.2 Elasto-plastic model (slow spreading ridge)

When viscous relaxation is allowed inside the ridge axial zone, the three components of principal stress become closer in magnitude, in order to reduce the deviatoric stress in excess of the yield value. This means that the horizontal principal stresses ($\Delta\sigma_{xx}$ and $\Delta\sigma_{yy}$) must get more compressive in order to become closer to the value of the initial vertical stress ($\Delta\sigma^0_{zz}$). As they get more compressive, they exert a push on the adjacent plate. As a result of this push the adjacent elastic plate experiences an increase in the principal compressive stress, hence a decrease in the deviatoric tensile stress. In this way the viscous relaxation in the axial zone at least partially simulates the push resulting from the high pressure at mid-ocean ridges, that is, the ridge push.

Model RIDSL is identical to previous model RISEL except that the ridge axial zone is elasto-plastic, with 30 MPa of strength. Viscous relaxation in this zone stops when the strength is achieved according to the Von-Mises criterion. The principal and deviatoric stresses are presented in Fig. 6.7 and Fig. 6.8 respectively.

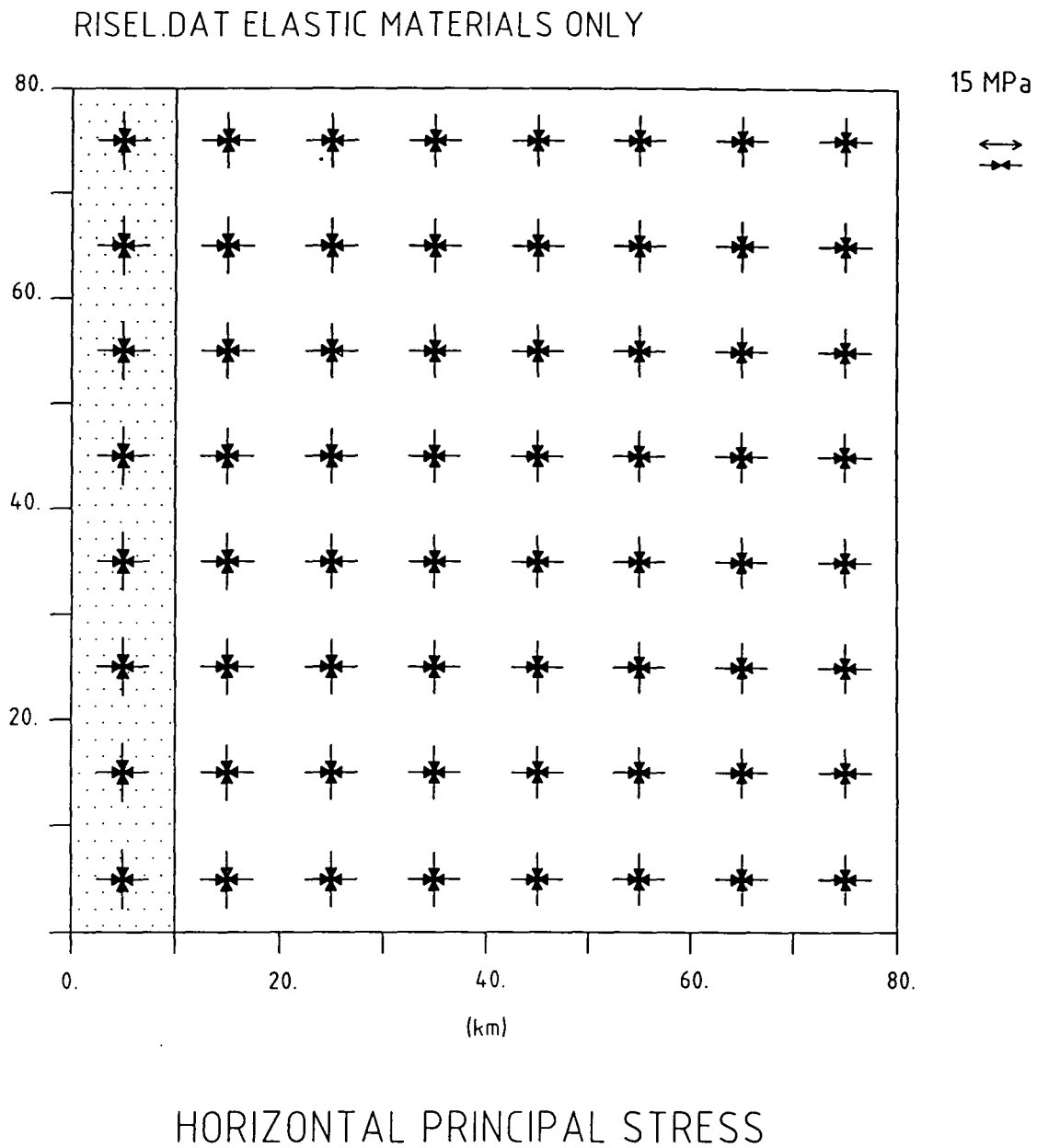

Fig. 6.5 Principal stress pattern of model RISEL, which represents a slow spreading ridge and the adjacent plate. Both the 10 km wide ridge axial zone, with the dotted pattern, and the surrounding lithosphere have elastic rheology. The lithosphere subsides at a rate corresponding to a half-spreading velocity of 15 mm/yr. Compressive stresses are represented by inward pointing arrows and tensile stresses are represented by outward pointing arrows. The stresses, plotted at the centre of each element, are scaled relative to 15 MPa.

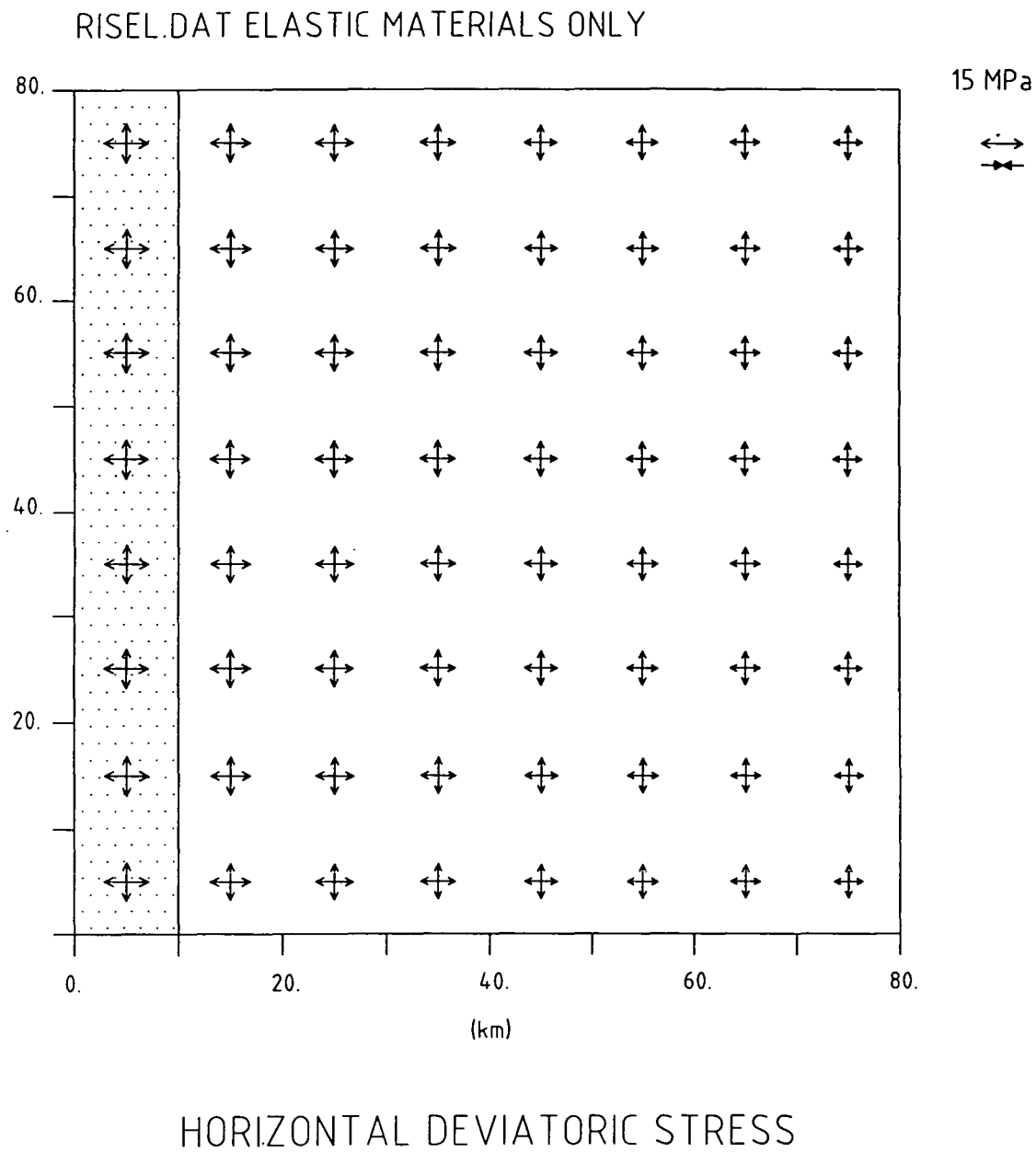

Fig. 6.6 Deviatoric stress pattern of the elastic model RISEL. Topographic loading and symbols are as in Fig. 6.5. The observed stress pattern is the result of the topographic load and the requirement of no displacement in the normal direction to the outer boundaries of the model.

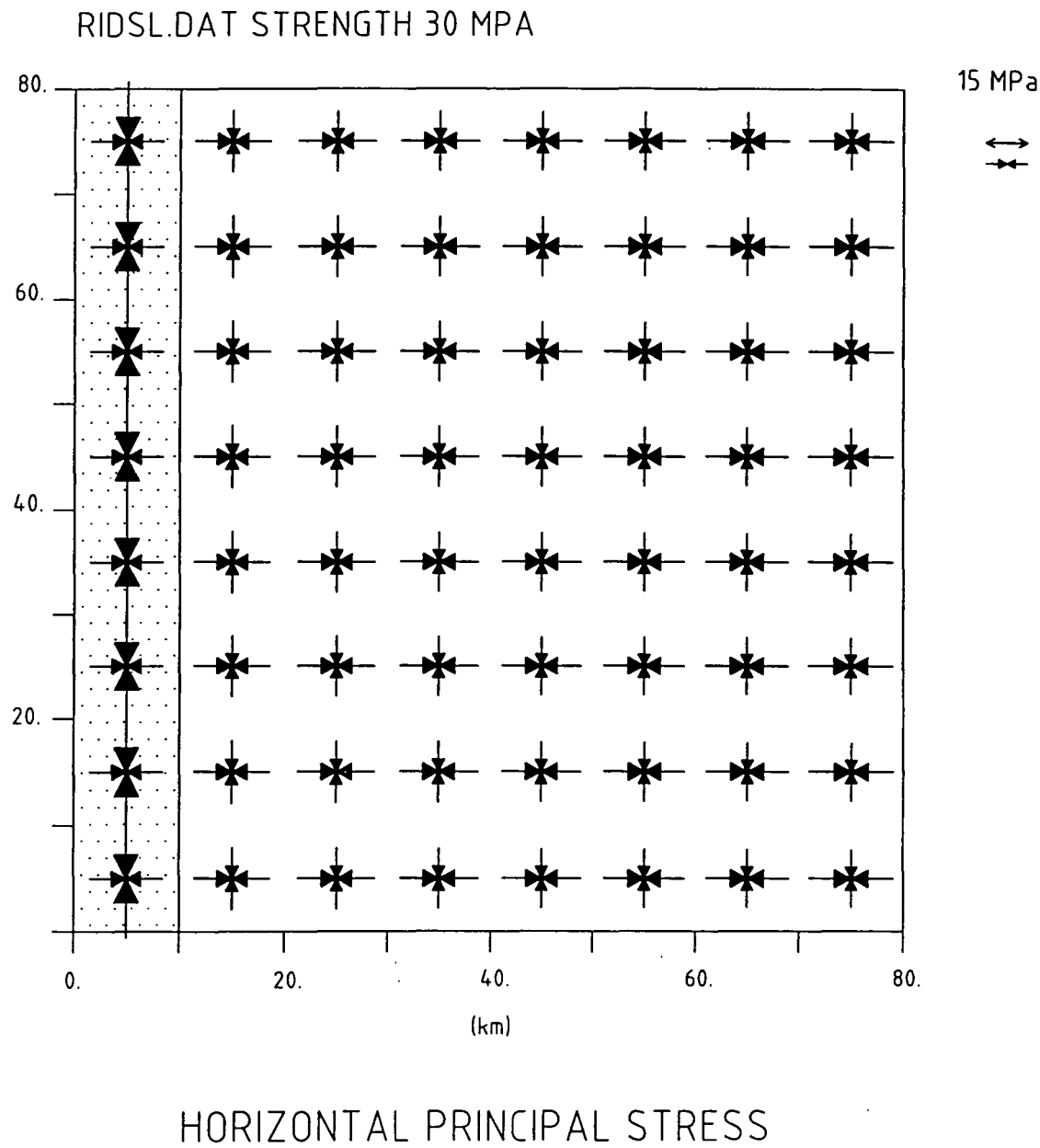

Fig. 6.7 Principal stress pattern of model RIDSL. The dotted 10 km wide ridge axial zone has elasto-plastic rheology, with a strength value of 30 MPa. The adjacent lithosphere has elastic rheology. Topographic loading and symbols are as in Fig. 6.5. Viscoplastic stress relaxation in the axial zone effectively applies a push on the adjacent elastic plate, increasing the magnitude of the ridge perpendicular compressive principal stresses.

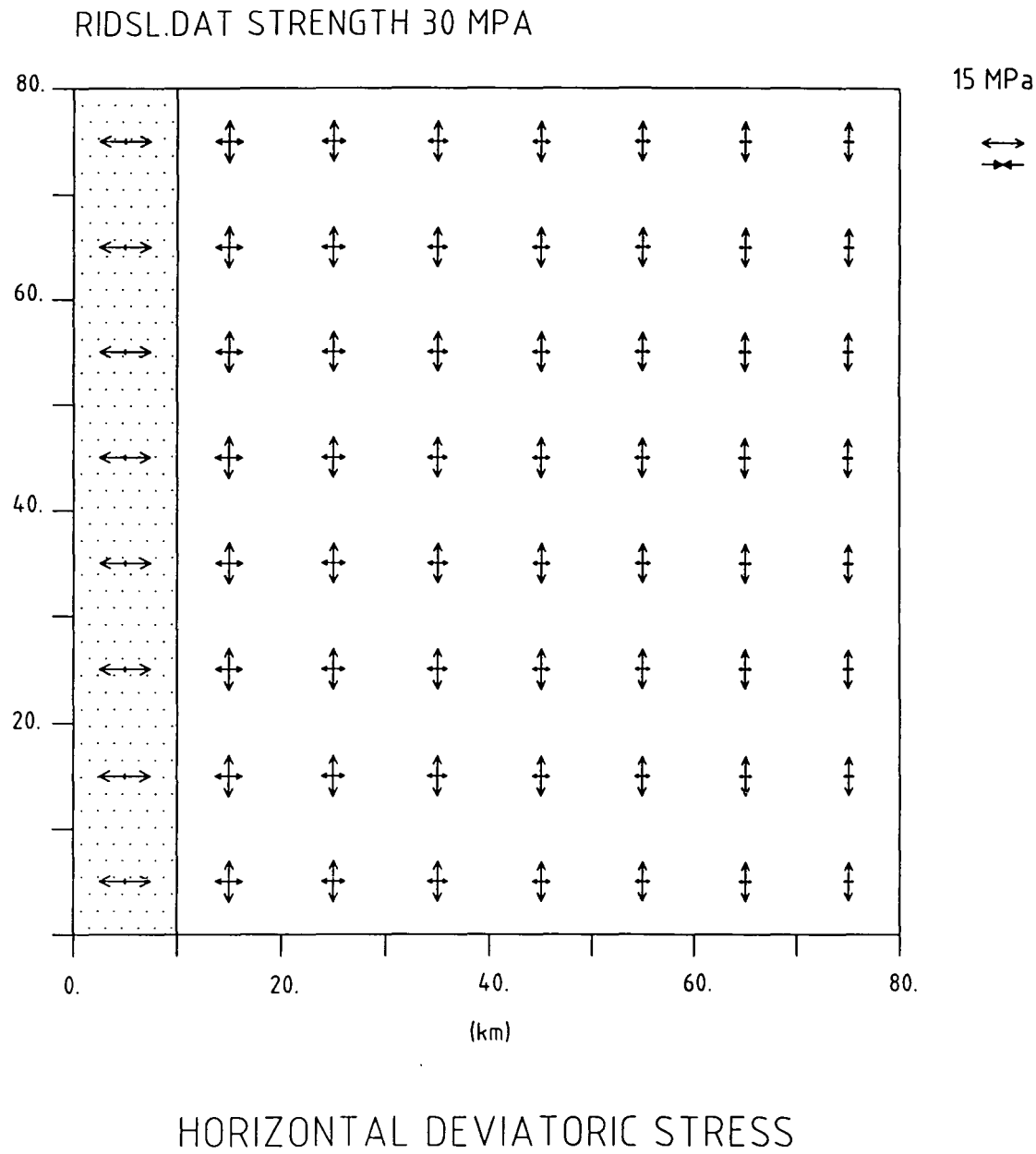

Fig. 6.8 Deviatoric stress pattern of the elasto-plastic model RIDSL. Topographic loading and symbols are as in Fig. 6.5. Viscoplastic stress relaxation in the axial zone effectively applies a push on the adjacent elastic plate, increasing the magnitude of the ridge parallel tensile deviatoric stresses.

The two components of stress in the ridge axial zone no longer have similar magnitudes. The deviatoric stress parallel to the ridge relaxes towards zero, and the deviatoric stress perpendicular to the ridge relaxes towards the strength. This happens in part because the along axis continuity of the viscoplastic finite elements allows a better performance of the viscous relaxation method, but can also be interpreted as a lower resistance to along axis compared to across axis viscous flow. Also, normal stresses must be continuous across interfaces, and in the adjacent elastic plate the stresses due to the topographic loading cannot relax. A dominant deviatoric extension perpendicular to the ridge agrees with the near axis stress indicators. In the adjacent elastic plate, some amount of ridge parallel extension is preserved. Focal mechanism interpretations indicate that ridge parallel extension is common in young oceanic seafloor (section 2.7).

In Fig. 6.8 the magnitude of the deviatoric tensile stress perpendicular to the ridge decreases from approximately 18 MPa at the ridge axis to 3 MPa at 70 km of distance from the ridge. Beyond 80 km of distance from the ridge axis the deviatoric stress will eventually become compressive. Tests have shown that the distance from the ridge axis at which the transition occurs depends on the ridge strength. This result is similar to that of the East Pacific Rise models, despite the contrasting approach (2D horizontal instead of 2D vertical).

What is the result of using a free boundary opposite to the ridge in model RIDSL (Fig. 6.7 and Fig. 6.8)? The result is shown in Fig. 6.9 and Fig. 6.10 for a model called RIFRE. The stresses in the perpendicular direction to the ridge are pervasively tensile reflecting the action of the ridge resistance. Although the spatial range of the ridge resistance is unknown, there is no evidence of consistent extension perpendicular to the ridge axis at distances from the ridge greater than $\sim$ 20 km (the upper bound estimate for the extent of normal fault activity at mid-ocean ridges). Therefore, the confinement perpendicular to the ridge is favoured in order to produce a negligible level of ridge perpendicular deviatoric stress at 80 km from the ridge, as shown in model RIDSL (Fig. 6.8).

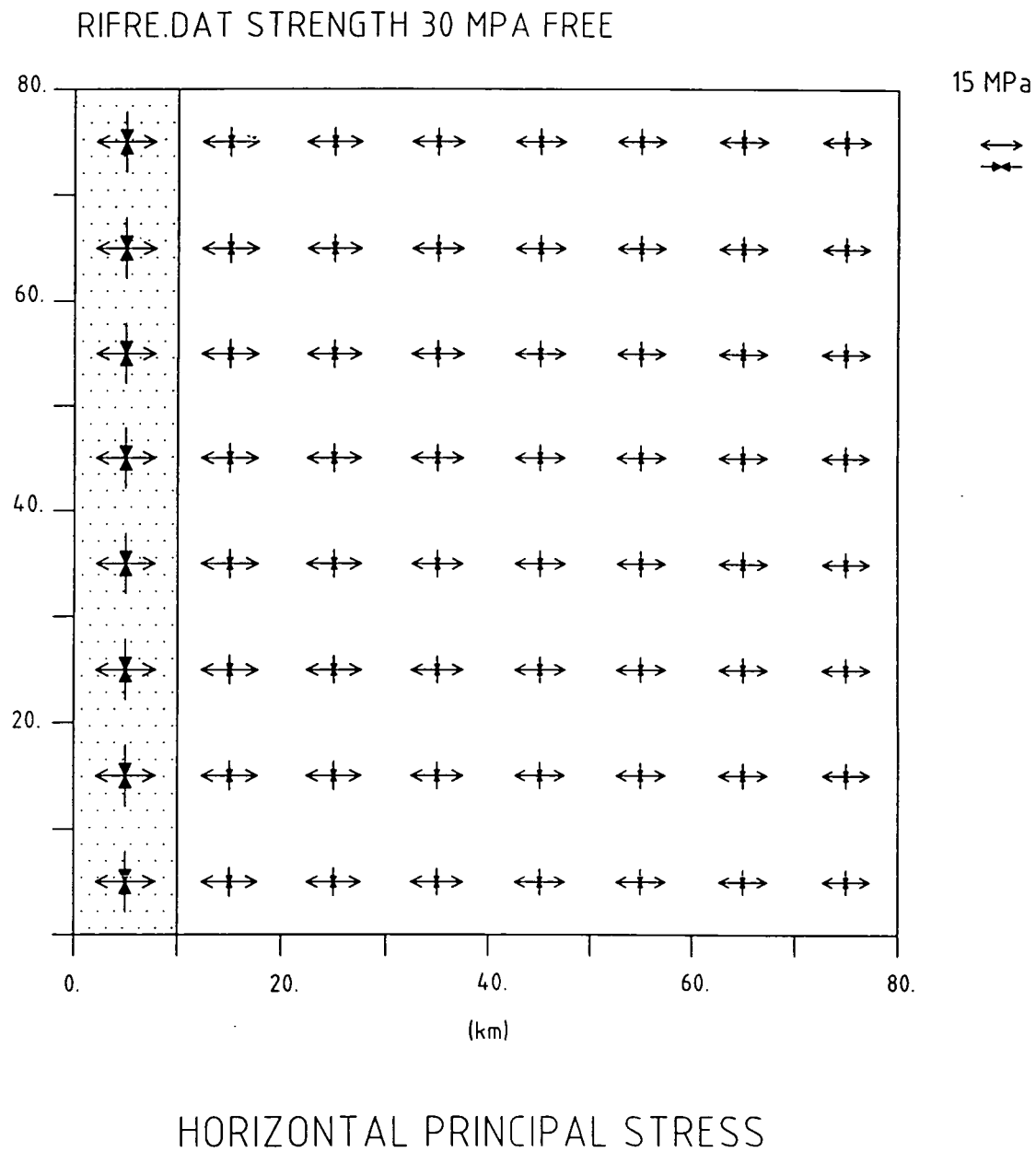

Fig. 6.9 Principal stress pattern of model RIFRE, which is identical to model RIDSL (Fig. 6.7) except for the boundary conditions. The edge of model RIFRE opposite to the ridge axis is free, but all the other boundaries are restrained in the normal direction to the boundary. The combination of topographic loading and viscoplastic stress relaxation in the axial zone generates tensile principal stresses perpendicular to the ridge direction all over the model.

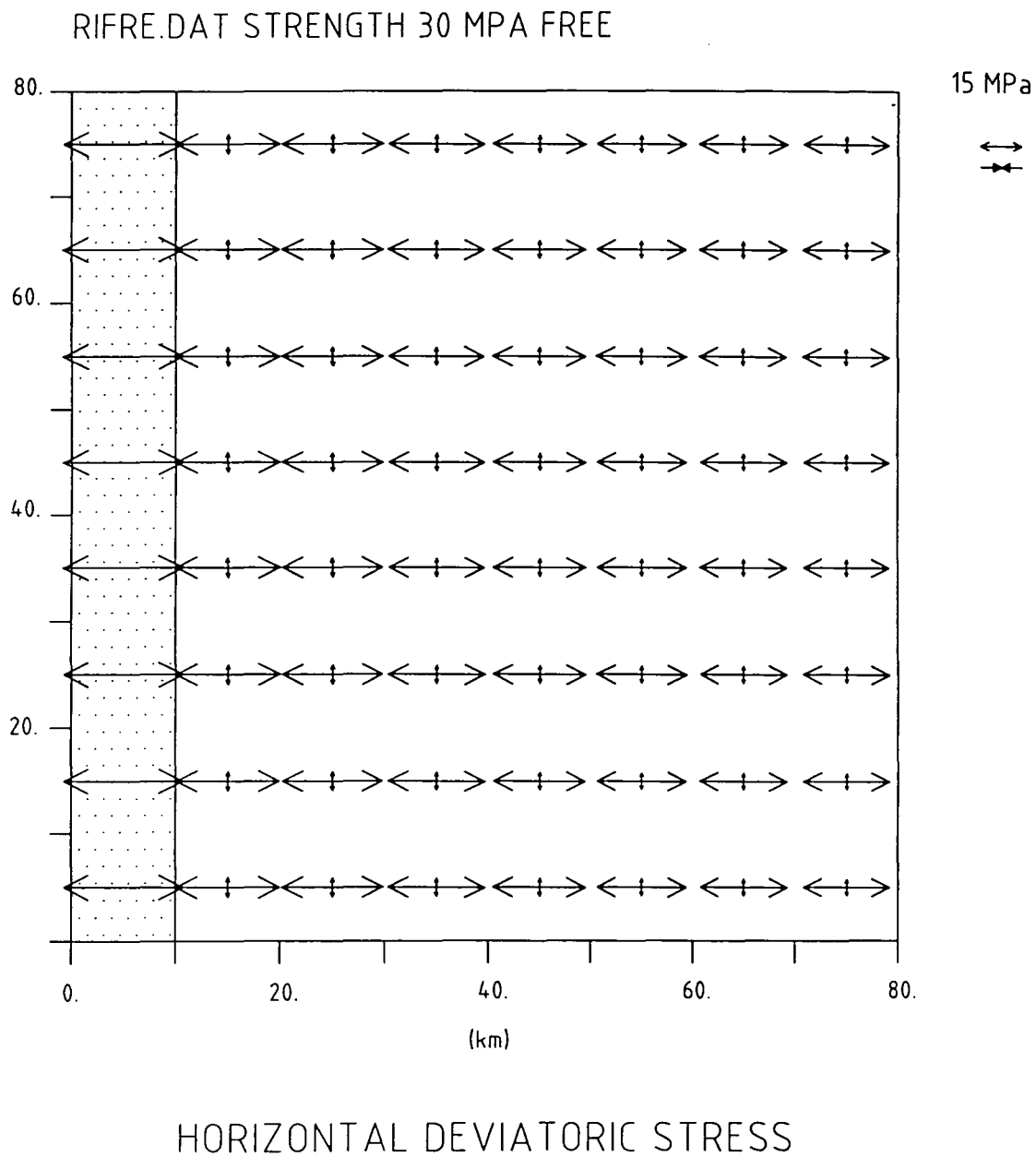

Fig. 6.10 Deviatoric stress pattern of model RIFRE, which has a free boundary condition at the edge opposite to the ridge axis. The deviatoric stress pattern reflects the action of the 'ridge resistance'.

6.3.3 Fast versus slow spreading ridges

Model RIDFS has the topographic load of a fast spreading ridge (profile b of Fig. 6.4) and a ridge strength of 15 MPa. Its deviatoric stress pattern (Fig. 6.11) shows an abrupt transition from ridge perpendicular stress to ridge parallel stress, at the ridge axial zone interface. This abrupt transition is unrealistic. Moreover, the ridge parallel deviatoric stress magnitude is relatively larger in model RIDFS than in its slow spreading ridge analogue (model RIDSL, Fig. 6.8). A lower ridge strength implies a greater amount of viscous relaxation in the ridge axial zone. With more viscous relaxation in the axial zone, the ridge perpendicular compressive principal stress increases, and so does the ridge parallel tensile deviatoric stress.

The dependence of the ridge parallel deviatoric tensile stress on the ridge strength lacks observational support. The half-spreading rates in the Central Indian Ridge and the Southeast Indian Ridge, where nearby evidence of tensile parallel stresses is strongest, are about 25-30 mm/yr (e.g. Mitchell and Parson, 1993), within the intermediate spreading range classification (section 1.2). In other oceanic areas, the number of earthquake focal mechanisms indicating ridge parallel tensile stresses is not enough to establish a relation between the ridge parallel tensile stresses and the spreading velocity. Ridge parallel tensile stresses due to lithospheric cooling must be a function of the lithospheric age, decreasing with distance from the ridge, but be otherwise independent of the spreading rate.

In order to prevent the artificial features of model RIDFS (Fig. 6.11) the ridge strength has to be chosen carefully. This a shortcoming of the modelling method. Nevertheless, when applied to ridge offsets the method predicts similar stress patterns regardless of the amount of viscous relaxation at the ridge axis (section 6.4.3).

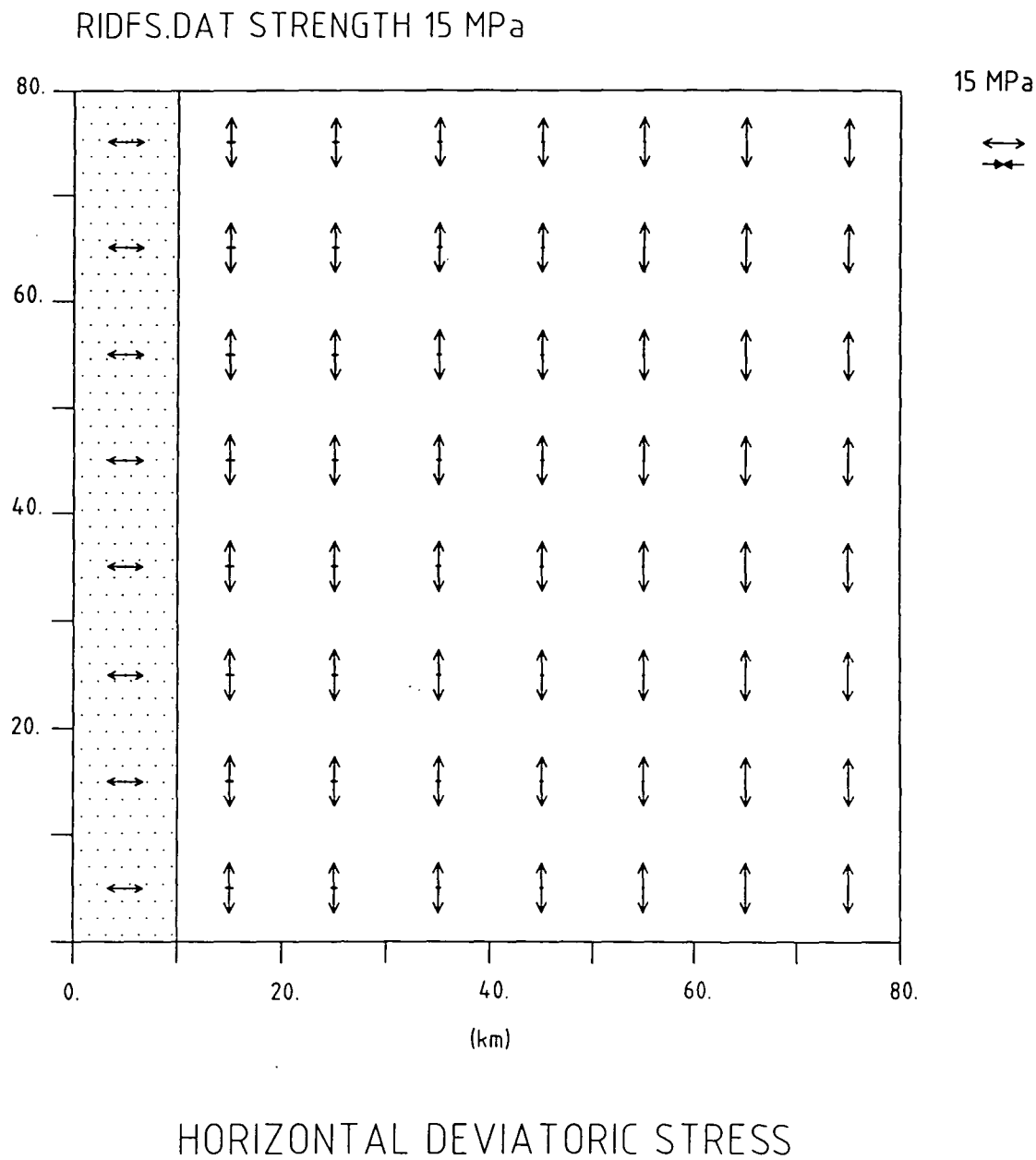

Fig. 6.11 Deviatoric stress pattern of model RIDFS, which represents a fast spreading ridge and the adjacent plate. The dotted 10 km wide ridge axial zone has viscoplastic rheology, with a strength value of 15 MPa. The adjacent plate is elastic. The lithosphere subsides at a rate correspondent to a half-spreading velocity of 60 mm/yr. Symbols are as in Fig. 6.5.

6.4 Models of stress at transform faults

6.4.1 Locked versus unlocked faults

In this section, two slow spreading ridge segments are offset by a 40 km long transform fault. The topographic load associated with each one of the ridge segments is displayed in Fig. 6.12.

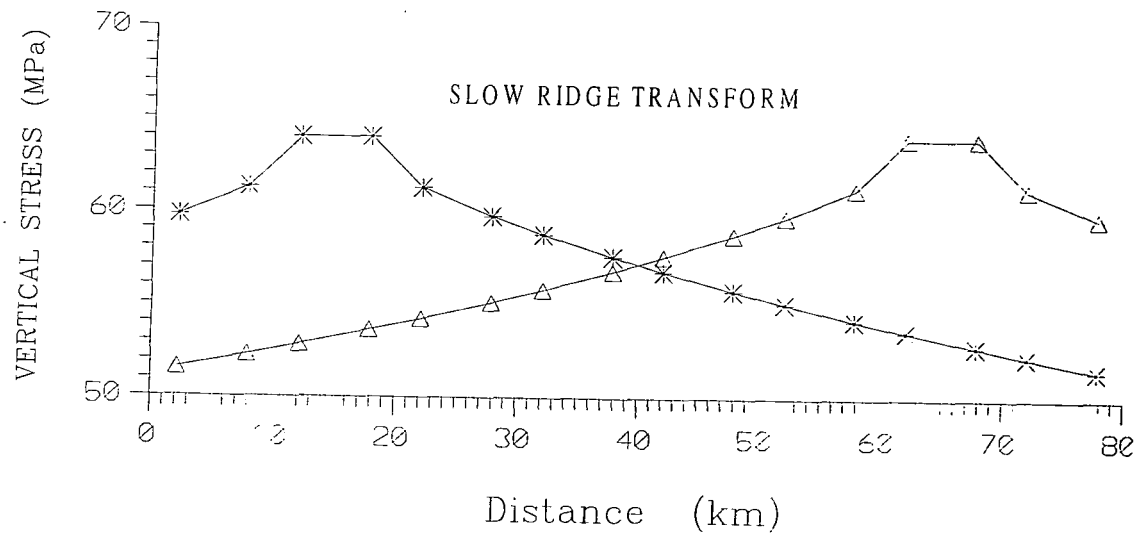

Fig. 6.11 The vertical non-lithostatic stress as a function of distance from the ridge, for two ridge segments bounding a 40 km long transform fault. Each profile corresponds to the topographic loading associated with a slow spreading ridge, relative to lithosphere 75 Ma old. The points along the profiles correspond to the location of the Gauss points in the finite element model.

In the following models only deviatoric stresses are displayed as they are more easily related to failure. The transform fault location is indicated by the line joining the two ridge segments which are represented by the dotted pattern. The stresses are plotted at each Gauss point and are scaled relative to 30 MPa.

Model SL30U (Fig. 6.13) includes an unlocked transform fault. As can be observed such an unlocked transform fault has only a minor influence on the stress field associated with the ridge segments. The ridge parallel and perpendicular deviatoric tensile stresses remain practically undisturbed by the presence of the fault. This model also shows that the change in seafloor depth across the fault, caused by the age offset, does not by itself produce any significant rotation of stresses in the fault's vicinity.

Model SL30 (Fig. 6.14) includes a locked transform fault. Now, the stress magnitudes increase in the fault's vicinity and are maximum ($\sim$ 28 MPa) at the inside corners of the ridge-transform intersections, where the tensile stresses rotate 30° relative to the ridge trend.

It is assumed that the ridge and the immediately adjacent plate have the same strength. The ridge is in a state of thoroughgoing failure, so the deviatoric stress observed inside the ridge axial zone is the maximum that can be supported. If the deviatoric stress in the plate exceeds the deviatoric stress in the ridge axial zone, the plate is expected to release the excess stress by brittle failure.

Under the above assumption the plate in model SL30 is predicted to fail at the places marked by the circles in Fig. 6.14, within 5 km of the ridge-transform intersections. The type of faulting that may occur is predicted using Anderson's theory of faulting (section 2.3). Since the maximum compressive principal stress (i.e. the minimum tensile deviatoric stress) is vertical, normal faults should develop perpendicular to the minimum compressive principal stress (i.e. the maximum tensile deviatoric stress). Accordingly, a normal fault regime is predicted to occur at the inside corners of the ridge-transform intersection, trending up to 60° oblique to the ridge axis.

Dyke intrusions should occur in the perpendicular direction to the maximum tensile deviatoric stress. Consequently the ridge will tend to propagate in the perpendicular direction to the maximum tensile deviatoric stress at the ridge-transform intersections, i.e. towards the transform.

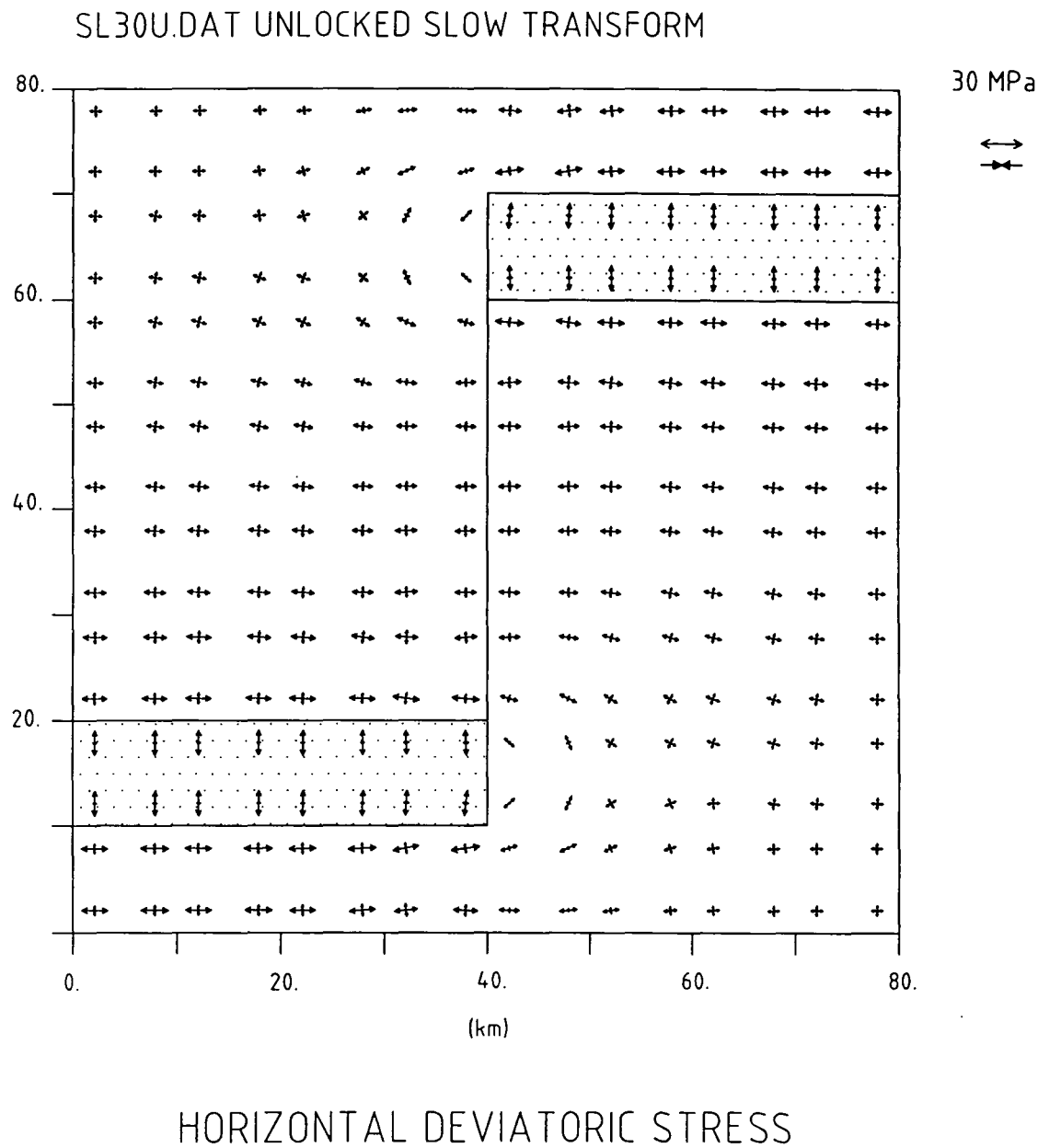

Fig. 6.13 Deviatoric stress pattern of model SL30U, which represents two slow spreading ridges separated by a transform fault 40 km long. The 10 km wide dotted ridge axial zones have elasto-plastic rheology with a strength of 30 MPa. The adjacent plate is elastic. The fault is unlocked with respect to slip. Compressive stresses are represented by inward pointing arrows, tensile stresses are represented by outward pointing arrows. The stresses, plotted at the Gauss points, are scaled relative to 30 MPa.

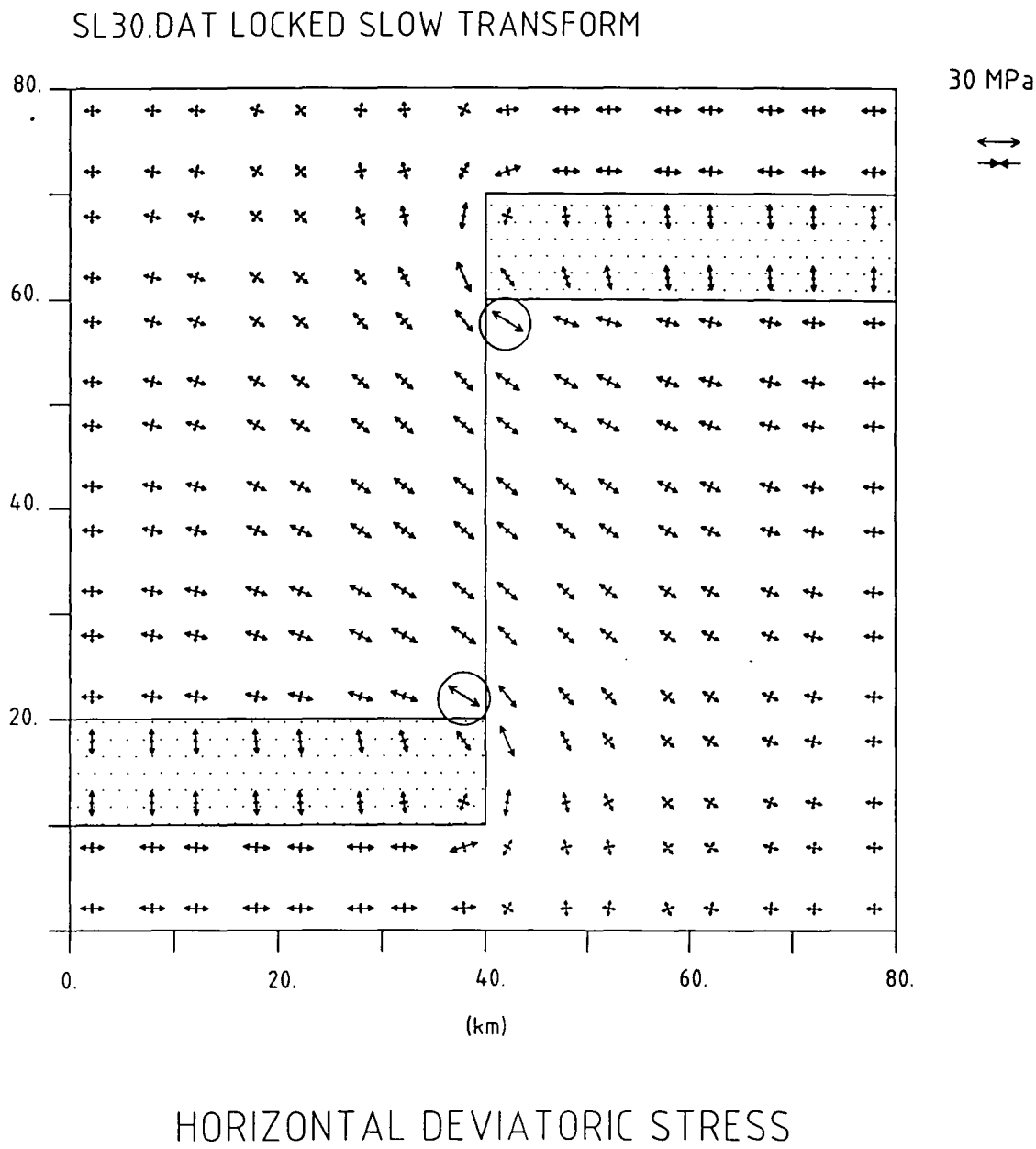

Fig. 6.14 Deviatoric stress pattern of model SL30, which is identical to model SL30U (Fig. 6.13) except that the fault is now locked with respect to slip. Large inside corner stresses favour the overshooting of dikes and the curvature of the ridge towards the transform. The circles mark the regions where normal faults trending up to 60° oblique to the ridge axis are predicted. Other symbols are as in Fig. 6.13.

6.4.2 The effect of topography

To verify how the stress pattern at a locked offset is affected by the subsidence rate, a model having the strength of a slow spreading ridge (30 MPa) but the vertical load of a fast spreading ridge is considered. The model is called FS30 (Fig. 6.15). It shows the same stress pattern as model SL30 (Fig. 6.14) except for a slight increase ($\sim$ 1 MPa) in the deviatoric stress magnitude. It can be concluded that the distinction between the topographic load of fast and slow spreading ridges is not important along locked offsets.

6.4.3 The effect of ridge strength

What is the effect of changing the ridge strength from 30 MPa to 15 MPa at a locked offset? Let us compare model FS15L (Fig. 6.16), which has the topographic load and the strength of a fast spreading ridge, with its slow spreading ridge analogue, model SL30 (Fig. 6.14).

The comparison shows a remarkable increase in the magnitude of the deviatoric stress when the ridge strength is reduced. At the ridge transform intersections a maximum deviatoric stress of $\sim$ 38 MPa is obtained in model FS15L, against the $\sim$ 28 MPa obtained in model SL30. This increase in the stress magnitude at the RTIs is caused by the artificial increase of the ridge parallel tensile stresses at low strength ridges (section 6.3.3). Nevertheless, the amount of stress rotation at the RTI predicted by the locked offset models (30° relative to the ridge trend) is the same regardless of the ridge strength. Supporting this result is the fact that observations at ridge-transform intersections do not indicate any correlation between stress rotation and slipping rate.

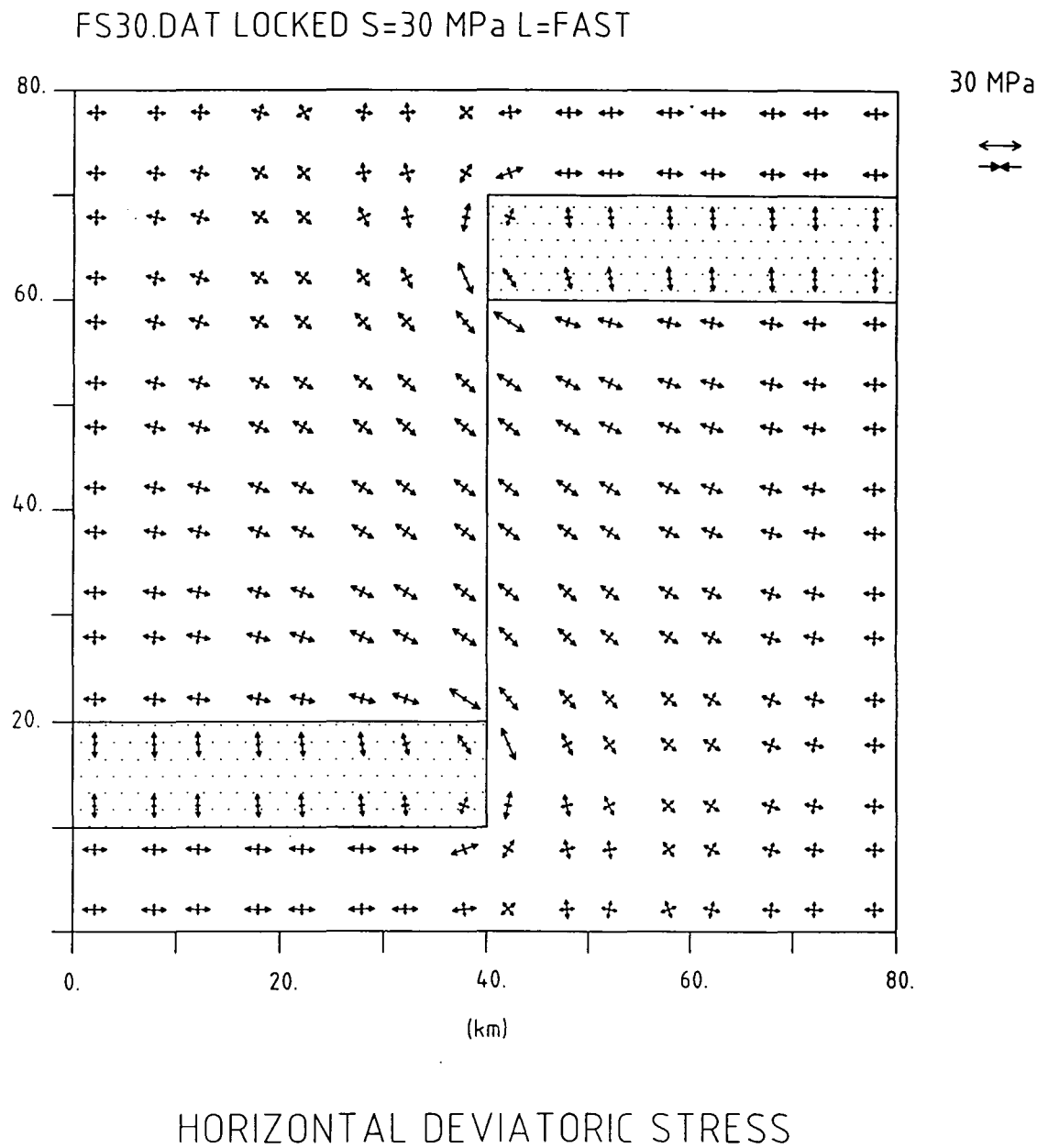

Fig. 6.15 Deviatoric stress pattern of model FS30, which represents a locked transform fault between two ridge segments. Although the ridge strength is that of a slow spreading ridge (30 MPa), the topographic loading associated with each segment is that of a fast spreading ridge. Symbols are as in Fig. 6.13. Comparison with Fig. 6.14 shows that the dependence of the topographic loading on the spreading rate does not significantly affect the results.

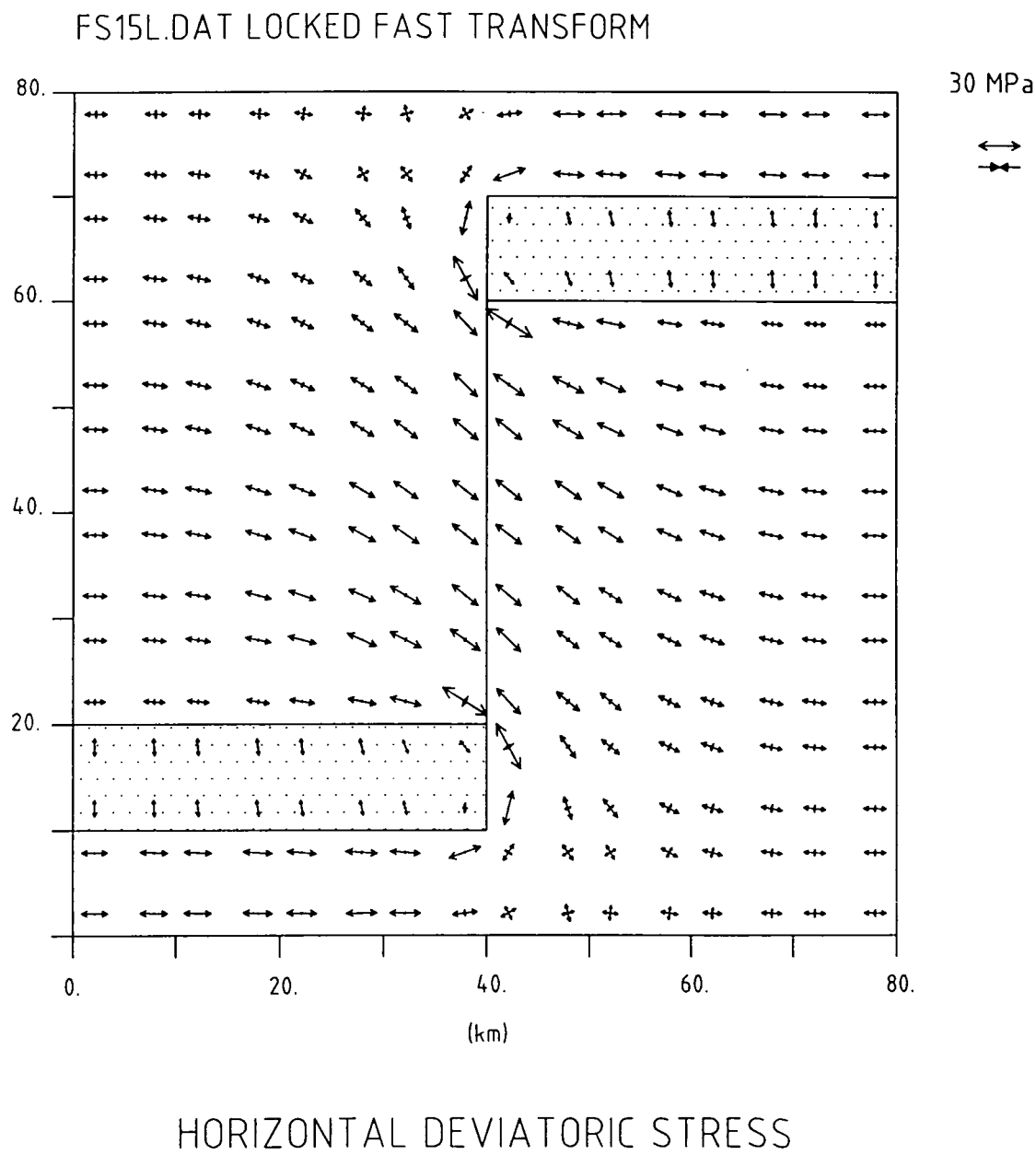

Fig. 6.15 Deviatoric stress pattern of model FS15L, which represents a locked transform fault between two fast spreading ridge segments. The topographic loading associated with each ridge segment and the ridge strength (15 MPa) are as in model RIDFS (Fig. 6.11) . Symbols are as in Fig. 6.13. The amount of stress rotation at ridge-transform intersections is the same of model SL30 (Fig. 6.14) regardless the differences in the ridge strength and in the topographic loading.

6.4.4 Transform as finite width weak zones

In this section, transform offsets are modelled as 10 km wide elasto-plastic zones. The width of the 'transform tectonized zone' at most transform faults is 10 to 20 kilometres, depending on the slipping rate (Mauduit and Dauteuil, 1996). This finite width 'weak' zone, containing closely spaced fractures and faults, may be represented by elasto-plastic rheology, just as the ridge axial zone has been.

The strength of the offset bounding ridges is kept at 30 MPa, and the topographic load is that characteristic of slow spreading ridges. The strength of the transform is varied to analyse the effect of changing the ridge to transform strength ratio:

- In model WT30SL (Fig. 6.17) the offset strength is 30 MPa, so the ridge to transform strength ratio is 1:1.
- In model WT15SL (Fig. 6.18) the offset strength is 15 MPa, so the ridge to transform strength ratio is 2:1.
- In model WT5SL (Fig. 6.19) the offset strength is 5 MPa, so the ridge to transform strength ratio is 6:1.

In Figs. 6.17, 6.18 and 6.19, the elasto-plastic transform domain is bounded by the rectangle between the two ridge segments. The deviatoric stress within the transform domain relaxes towards zero in the direction parallel to the transform, and relaxes towards the strength in the direction perpendicular to the transform. As the transform strength diminishes the deviatoric tensile stress within the offset becomes more ridge parallel. Simultaneously the magnitude of the ridge parallel tensile stresses in the adjacent elastic plate decreases.

At all ridge to transform strength ratios the maximum deviatoric stress in the elastic plate is observed at the inside corner of the ridge-transform intersections, at the places marked by the circles in the figures. There, normal faulting may develop at an angle to the ridge trend that depends on the transform strength.

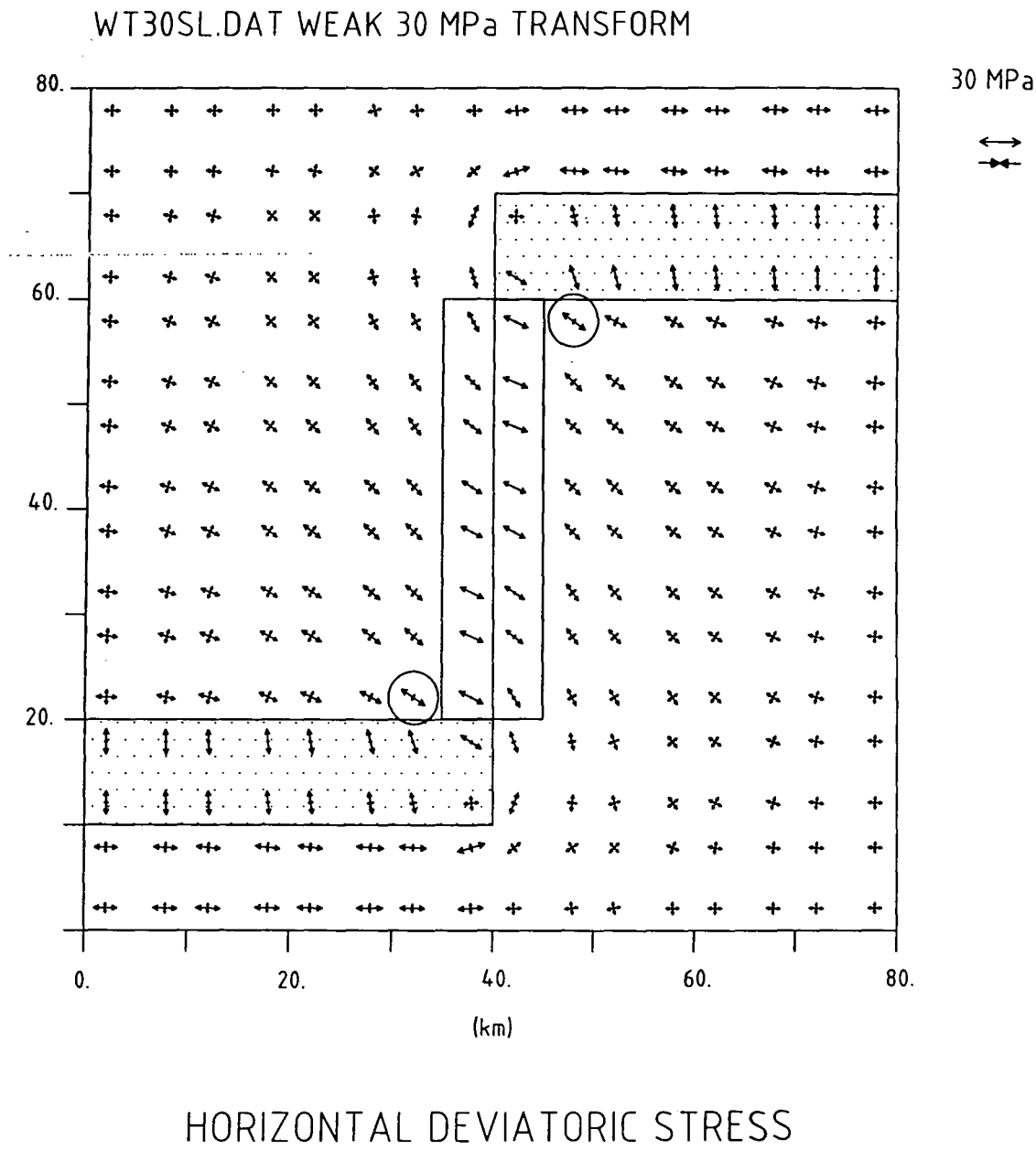

Fig. 6.17 Deviatoric stress pattern of model WT30SL. Two slow spreading ridges, having a strength of 30 MPa, are offset by a finite width transform zone. The transform is 10 km wide and has an elasto-plastic rheology with 30 MPa of strength. At the ridge-transform intersection inside corners of the elastic plate (indicated by the circles) the maximum tensile stress makes an angle of 35° to the ridge axis. At the inside corners of the elasto-plastic transform domain it makes an angle of 30° to the ridge axis.

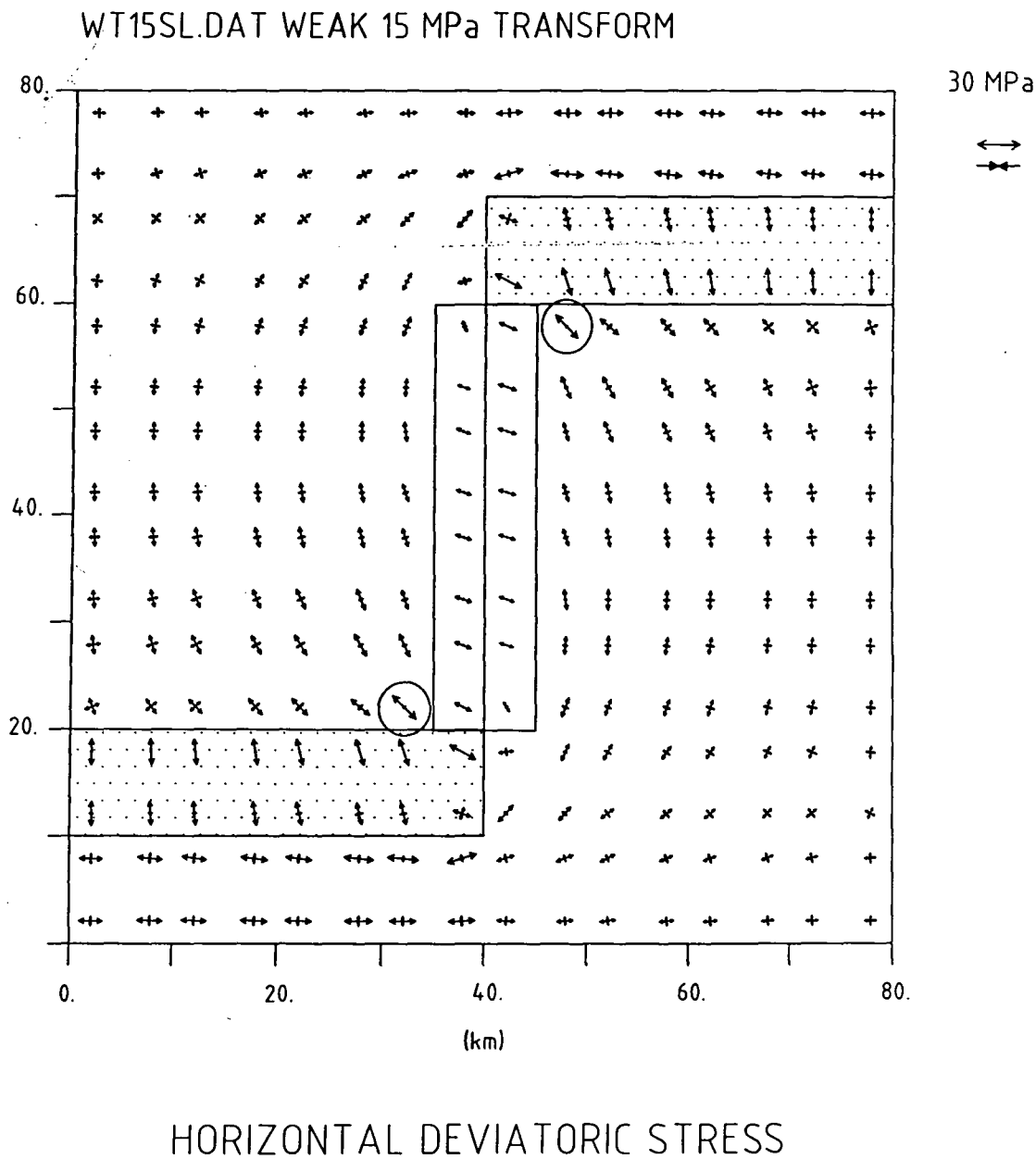

Fig. 6.18 Deviatoric stress pattern of model WT15SL. Two slow spreading ridges, having a strength of 30 MPa, are offset by a finite width transform zone. The transform is 10 km wide and has an elasto-plastic rheology with 15 MPa of strength. At the ridge-transform intersection inside corners of the elastic plate (indicated by the circles) the maximum tensile stress makes an angle of 45° to the ridge axis. At the inside corners of the elasto-plastic transform domain it makes an angle of approximately 20° to the ridge axis.

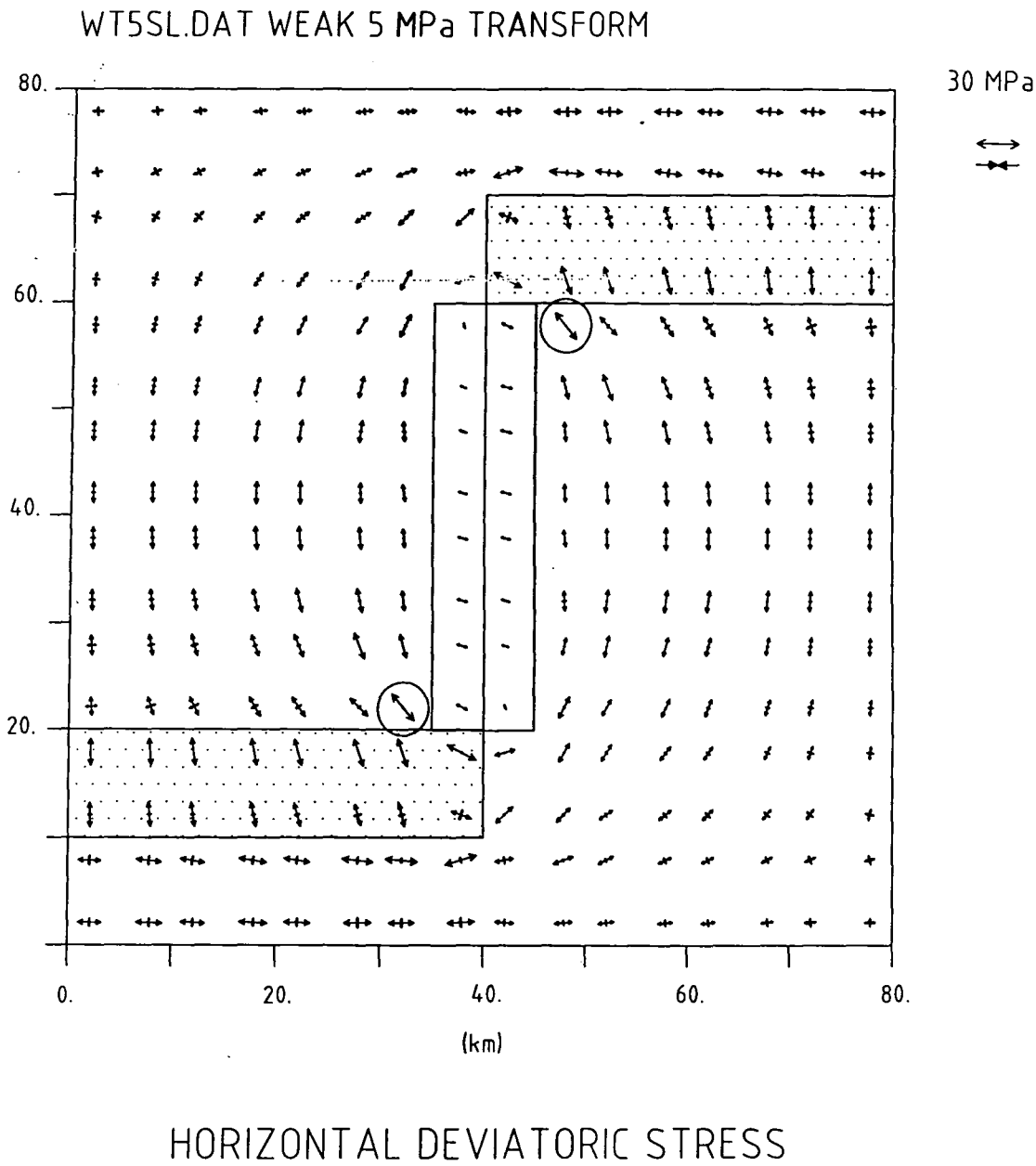

Fig. 6.19 Deviatoric stress pattern of model WT5SL. Two slow spreading ridges, having a strength of 30 MPa, are offset by a finite width transform zone. The transform is 10 km wide and has an elasto-plastic rheology with 5 MPa of strength. At the ridge-transform intersection inside corners of the elastic plate (indicated by the circles) the maximum tensile stress makes an angle of 50° to the ridge axis. At the inside corners of the elasto-plastic transform domain it makes an angle of approximately 20° to the ridge axis.

6.5 Comparison of the results with observations at transform faults

The curvature of the ridge axis towards transforms and the development of oblique extensional structures at ridge-transform intersections, predicted by the modelling, are observed at most well surveyed transforms. One example is the Vema transform fault, which offsets the Mid-Atlantic Ridge by 320 km, at approximately 11° N (Macdonald et al., 1986). At its eastern ridge-transform intersection, normal faults and the axial zone of dyke injection curve along trends on average 30° oblique to the regional North-South trend of the ridge axis (Fig. 2.3).

Another good example occurs at the Clipperton transform, which offsets the East Pacific Rise by 85 km, at approximately 10°15′ N (Kastens et al., 1986). At the Clipperton eastern ridge-transform intersection the ridge crest bends clockwise rotating through 25° from 350° to 015° (Fig. 2.4). Then it terminates abruptly against a north facing scarp that constitutes the northern edge of the intersection high, characteristic of fast slipping transforms. Within 5 km of the transform, well developed oblique NE-SW trending scarps replace the ridge parallel scarps at the inside corners of the ridge-transform intersection. In contrast, the outside corner is characterized by well developed ridge-parallel terrain of ridges and troughs, that bend sharply to merge with the northern end of the transform valley.

At the Siqueiros transform, which offsets the East Pacific Rise by 138 km at approximately 8°25′ N, the seafloor at the outside corner is also characterised by faults and volcanic ridges that parallel the trend and mimic the morphology of the associated ridge segments. At the inside corners, the structural fabric is composed of short ridges and troughs that trend at oblique ($\sim$ 45°) angles to the spreading segments (Fornari et al., 1986).

Normal faults that strike more than 45° oblique to the spreading segments have been reported at the Quebrada-Gofar transform complex, at approximately 4° S along the EPR (Searle, 1983). In this region the ridge parallel normal faults start to

curve 4-10 km from the transforms, curving more strongly within 2-3 km of them. Commonly, the normal faults strike at an angle of up to 55° relative to the ridge trend, but in some places they curve all the way around into the transform direction.

In general, other transforms show similar features, with the range of obliquity at the inside corners estimated to be 20° – 50° (Fox and Gallo, 1986). Focal mechanisms at transforms also confirm oblique stress at ridge-transform intersections (e.g. Lilwall and Kirk, 1985; Cessaro and Hussong, 1986).

The modelling of different ridge to transform strength ratios has shown that the degree of obliquity of extensional structures, at ridge-transform intersections, varies with the transform strength. The maximum angle of the extensional structures predicted at RTIs (60°), relative to the ridge axis, occur for model SL20, that is for a locked offset. A variety of normal fault trends at ridge-transform intersections is expected if the offset strength varies with time. The strength of the offset, particularly at the ridge-transform intersection, may vary due to changes in lithospheric thickness. Cyclic variations in lithospheric thickness (with a period of 2-3 m.y.), presumably caused by alternating magmatic and amagmatic phases, are supported by gravity measurements at the MAR (Tucholke et al., 1998).

Fracture zone valleys often contain transform-parallel normal faults, tension fractures and small-scale grabens (Searle, 1992). Transform-parallel dyke intrusions and earthquake focal mechanisms indicating ridge parallel tensile stresses have been reported at the Kane fracture zone (Tucholke and Schouten, 1988; Wilcock et al., 1990). Transform parallel normal faults and dykes have also been found in a fracture zone exposed in Iceland (Gudmundsson, 1995). At ridge transform intersections, normal faults oriented within 20° of the transform fault have been reported at the Kane (Karson and Dick, 1983), Quebrada-Gofar (Searle, 1983) and Vema (Macdonald et al., 1986) transform faults. According to the modelling all these observations may be explained by the weakness of the transform domain relative to the surrounding plate. Thus, models WT15SL (Fig. 6.18) and WT5SL (Fig. 6.19) indicate that low strength transforms are characterised by ridge parallel tensile stresses within the transform domain.

6.6 Models of stress at non-transform offsets

At non-transform offsets the shear deformation between ridge segments is not localised along a narrow fault. Non-transform offsets of slow spreading ridges are mainly oblique shear zones and rift valley jogs. The structural geometry of many non-transform discontinuities along the Mid-Atlantic Ridge has been successfully modelled by Grindlay and Fox (1993). However, their models could not explain the orientation of the 45° oblique basins and fault patterns observed for instance at the 33°35′S discontinuity (Fig. 2.5).

The 45° oblique structural trends at non-transform offsets are relatively common. They were first observed at the Kurchatov fracture zone (Searle and Laughton, 1977), which is a 20 km offset of the MAR at 40°30′ N. The Kurchatov offset is characterized by a 45° oblique linear trough, with no sign of a tectonic lineament that might indicate the presence of a transform fault. However, there is a well developed fracture valley that can be traced for more than 150 km, where 45° oblique scarpments are also seen (Searle and Laughton, 1977). Several such oblique offsets have also been found in the Gulf of Aden, and in one of these a normal faulting earthquake confirms the 45° stress rotation relative to the spreading axis (Searle, 1986).

Model SL30S (Fig. 6.20) represents a 20 km non-transform offset of a slow spreading ridge. The offset does not contain any defined plane of weakness. The stress pattern shows maximum tensile stresses occurring along the offset, particularly at the inside corners of the ridge-offset intersections. These tensile stresses are larger than the tensile stresses inside the ridge axial zone, and trend 35° – 50° oblique to the ridge axis. The strength of the lithospheric plate along the offset must be more or less constant because the offset is small. In that case failure at the ridge-offset intersections must be accompanied by failure along the offset as well. As a result failure in extension is predicted for the whole non-transform offset, at an angle on average about 45° oblique to the ridge axis.

The models reproduce the observational data referred to above, and indicate

that non-transform offsets characterized by extensional structures 45° oblique to the ridge axis are strong offsets without defined planes of weakness.

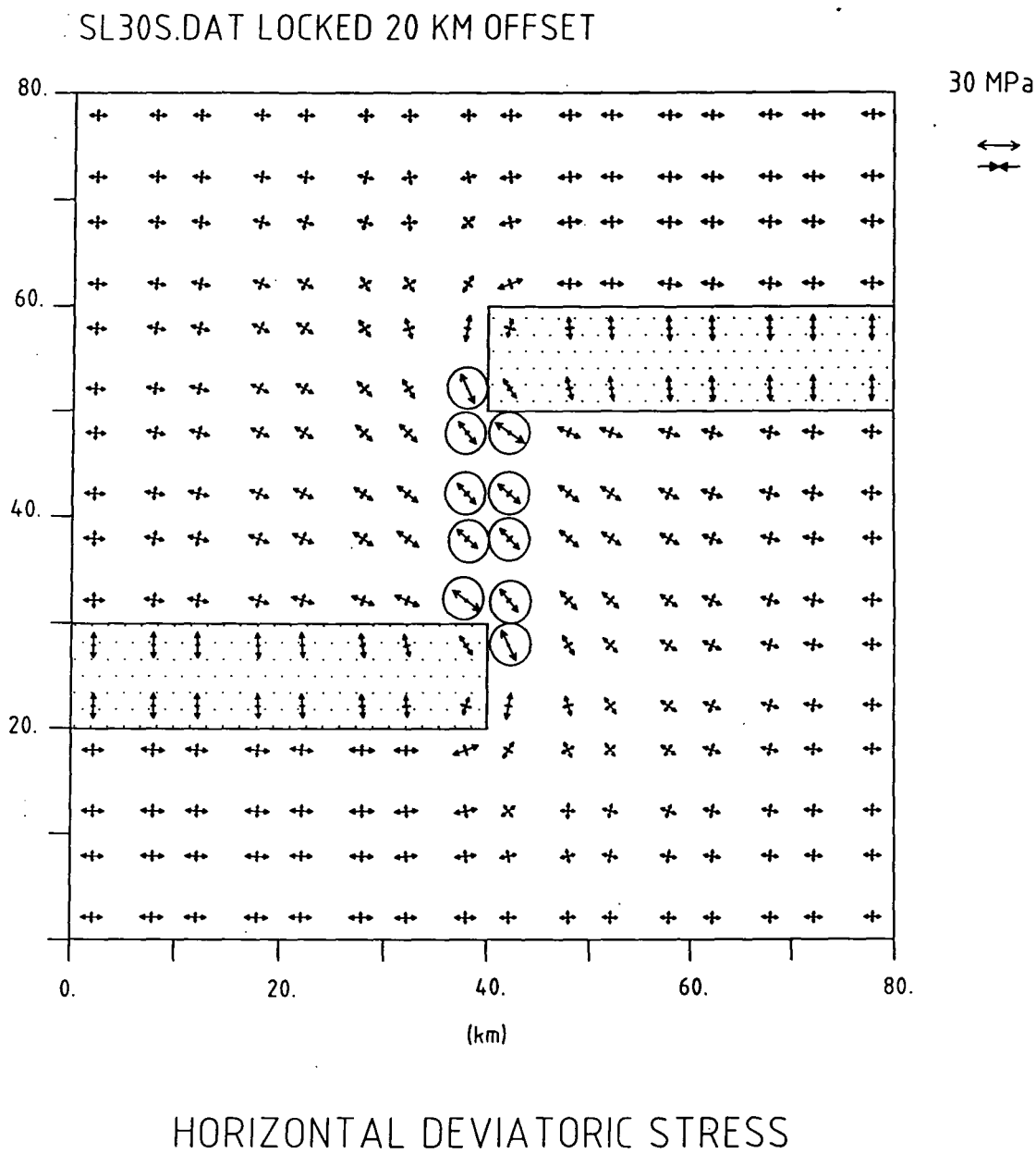

Fig. 6.20 Deviatoric stress pattern of model SL30S, which represents a 20 km non-transform offset between two slow spreading ridges. Rheologies and topographic loading are as in Fig. 6.13. The circles mark the regions where normal faults trending 35°-50° oblique to the ridge axis are predicted. Other symbols are as in Fig. 6.13. The deviatoric stress pattern is consistent with the 45° oblique basins and structural trends characteristics of some non-transform offsets.

6.7 Discussion

The modelled stress pattern at mid-ocean ridges is the result of three effects: (1) the topographic loading relative to old ocean floor, (2) the elasto-plastic deviatoric stress relaxation within the axial zone, and (3) the assumed boundary conditions. The topographic loading generates similar tensile deviatoric stresses in the ridge perpendicular and ridge parallel directions. The elasto-plastic stress relaxation in the axial zone simulates the ridge resistance, and imposes a push on the adjacent plate. The boundary conditions, in particular the confinement of the model in the spreading direction, allows me to model the transition from ridge perpendicular tension to ridge perpendicular compression at a relatively short distance from the ridge axis.

The modelling method that has been used in this chapter produces unrealistic stress patterns for low values of the ridge strength, particularly away from ridge offsets. However, when applied at ridge offsets the method produces the same results independently of the ridge strength that has been chosen.

Ridge perpendicular tensile stresses within the axial zone are supported by seismicity data and normal fault observations at mid-ocean ridges. At more than 10-20 km from the ridge there is no evidence that ridge perpendicular tensile stresses are consistently larger than ridge parallel tensile stresses. On the contrary, earthquake focal mechanisms in young oceanic lithosphere indicate that ridge parallel tensile stresses are often dominant.

This study has shown that the topographic loading may generate significant ridge parallel tensile stresses in young oceanic lithosphere. It is however necessary that no significant deformation is allowed in the normal direction to transform faults. In thermo-elastic stress models, ridge parallel tensile stresses are also predicted under the condition that no significant thermal contraction in the ridge axis direction is allowed at transform faults (Turcotte, 1974).

Independently of having a thermal or topographic loading origin, significant

ridge parallel tensile stresses just outside the ridge axial zone have important implications at ridge offsets.

In previous stress modelling at ridge-transform intersections the curving of normal faults as the transforms were approached was attributed to the rotation of ridge perpendicular tensile stresses (Phipps Morgan and Parmentier, 1984; Grindlay and Fox, 1993). In these and other models at ridge-transform intersections (Fujita and Sleep, 1978) normal faults were predicted to deviate up to 30° from the ridge trend. Normal faults that strike at larger angles to the ridge remained as unexplained phenomena (e.g. Macdonald et al., 1986).

At transform and non-transform offset models I tested free boundary conditions at outer boundaries parallel to the ridge segments (as in model RIFRE, Fig. 6.10). As a result of changing the boundary conditions, the ridge perpendicular tensile stresses became dominant all over the elastic plate. At ridge-transform intersections the stress rotates up to a maximum of only 35°, very much as in previous modelling efforts (Phipps Morgan and Parmentier, 1984; Grindlay and Fox, 1993; Fujita and Sleep, 1978).

The modelling in this chapter shows that normal faulting at high angles (> 35°) to the ridge trend can be explained by the rotation of ridge parallel tensile stresses. The obliquity of normal faulting relative to the strike of the ridge segments may reach 55°/60° in strong/locked transforms.

Ridge parallel tensile stresses at transform faults had already been used by Gudmundsson (1995) to explain the transform parallel extensional structures sometimes observed. However, he did not quantify the amount of stress rotation at ridge-transform intersections, nor did he make the point that ridge parallel tensile stresses are necessary to explain the high obliquity of normal faulting at ridge-transform intersections. Also, Gudmundsson regards the ridge parallel tensile stresses at transform faults, as an applied far field stress (section 1.6) that may dominate the stress field temporarily. In contrast, my models of transform faults as finite width zones suggest that ridge parallel tensile stresses within the transform domain are an intrinsic property of weak transforms.

Chapter 7

Easter microplate dynamics

7.1 Introduction

Easter is probably the best documented microplate. It has been comprehensively surveyed using long-range sidescan sonar, multibeam echosounders and magnetic profiling (section 2.9). These data have been used to test models of deformation of ridge overlap systems (Engeln et al., 1988). Plate reconstructions based on Easter magnetic and structural evidence favour a model of microplate rigid behaviour, rather than a shear zone model (Naar and Hey, 1991; Rusby and Searle, 1995). Assuming this rigid behaviour Schouten et al. (1993) proposed a kinematic model in which microplates are driven by shear couples imposed on them by the motions of their bounding plates (section 1.8). One of the aims of this chapter is to verify if the Schouten et al. kinematic model is compatible with the stress indicators in Easter microplate.

Although the tectonics, kinematics and evolution of Easter microplate are reasonably well established, its dynamics has never been investigated. In this chapter, the methodology used in other plate dynamic studies (e.g. Cloetingh and Wortel, 1986; Richardson and Reding, 1991; Wang et al., 1997) is for the first time applied to a ridge overlap system. Finite element stress modelling is used to infer the forces governing Easter microplate rotation, leading to an estimate of their relative magnitudes. A new dynamic model for Easter microplate is proposed, in which the driving

forces for the microplate rotation are due to the ridge resistance gradient along the East and West Rifts. This new 'ridge driven' model contrasts with the Schouten et al. hypothesis, which involves driving forces acting along the northern and southern boundaries of the microplate (Fig. 7.1).

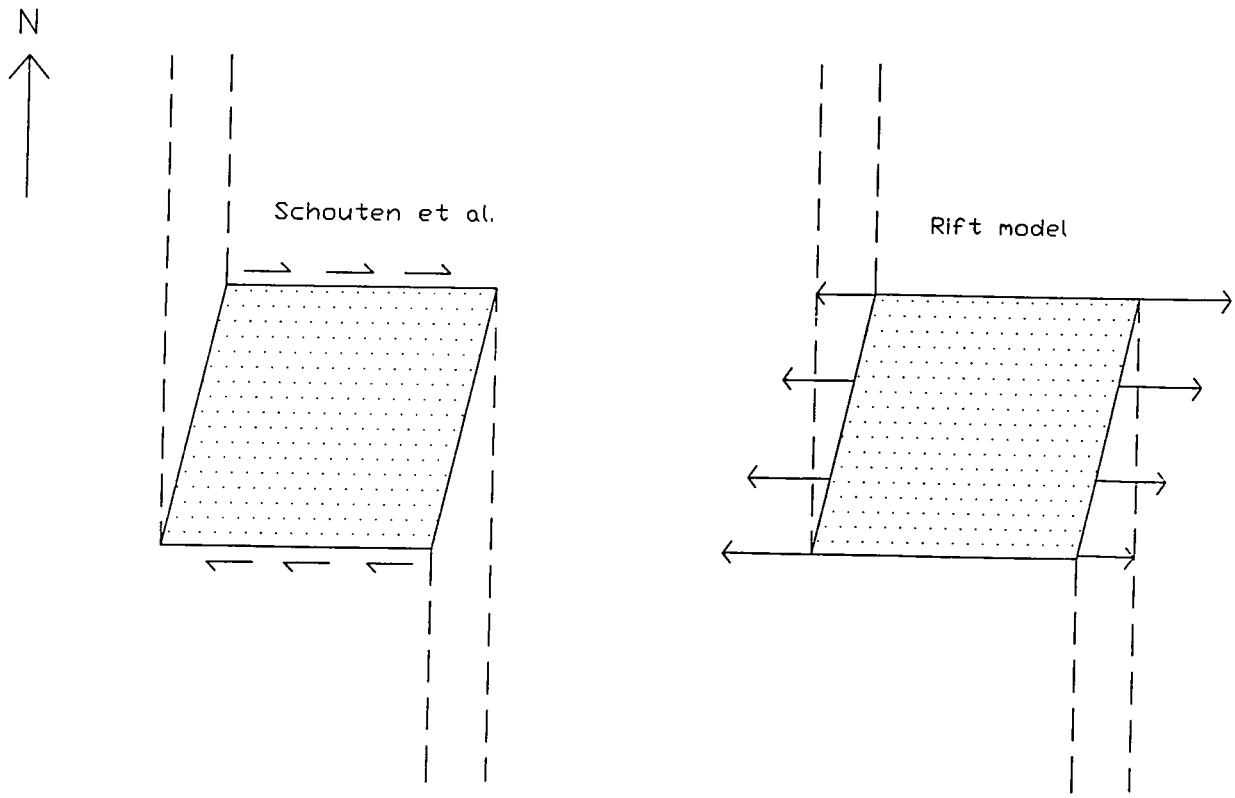

Fig. 7.1 Schouten at al. (1993) versus the new rift model. The dotted area represents the microplate, bounded at the top and bottom by the northern and southern boundaries respectively, and bounded laterally by the East and West Rifts. Dashed lines represent isochrons and illustrate the accretion gradient along the microplate margins (the spreading rate decreases northwards along the East Rift and decreases southwards along the West Rift). In the Schouten et al. model, the microplate is driven by shear forces along the northern and southern boundaries, produced by the drag of the main plates. In the new rift model, the microplate is driven by the clockwise torque produced by the gradient in the ridge resistance along the East and West Rifts.

7.2 Modelling assumptions and procedure

In the following sections I analyse the forces governing Easter Microplate rotation, using 2D horizontal finite element models of stress. To avoid boundary effects, Easter geometry is initially simplified and represented by a square. This simple geometry can also outline other microplates. The finite element grid, the same as used in chapter 6 (Fig. 6.1), contains 64 quadrilateral elements, each with eight nodes and four Gauss points. The square grid side dimension is 480 km, sensibly the same as the diameter of Easter microplate. The right and left boundaries of the grid represent the East and West rifts respectively. The top and bottom sides of the square represent the northern and southern boundaries of the microplate.

The models are elastic. This hypothesis applies inside the microplate, where the observations indicate small total deformation. The elastic constants assumed are $E = 0.7 \times 10^{11}$ Pa and $\nu = 0.25$. As in previous chapters only the non-lithostatic stress is modelled. All the quantities in the models are averaged over the plate thickness, and the plate is treated as weightless. The plate thickness is assumed to be constant. Since the tectonic force is approximately conserved, variations in the plate thickness cause inversely proportional variations in the stress magnitude.

The plane stress assumption is used. The applied and resistive forces are all horizontal, and the top surface of the plate is free, implying that there are no vertical stresses. Since there are no vertical stresses there is no need to compute the horizontal deviatoric stresses. Therefore, all the models display only the horizontal principal stresses. As the vertical stress (less lithostatic component) is zero, thrust, normal and transcurrent regimes can be readily identified using Anderson's theory of faulting (section 2.3).

The fundamental hypothesis of the modelling procedure is that the microplate is in dynamical equilibrium. Tectonic plates move at very slow rates, so in general the acceleration of the plates can be neglected. Also, the rotation rate of Easter microplate has been constant over the last 3 Ma, so there is no angular acceleration. The relatively small dimensions of Easter microplate justify the flat plate approxi-

mation. In a flat plate model the equilibrium condition implies that the total torque about a vertical axis, exerted by all the forces acting on the plate, must be zero.

I assume that there are three main types of force acting on Easter microplate: (1) the mantle basal drag, distributed over the base of the microplate, (2) the boundary forces distributed along the East and West Rifts, and (3) the boundary forces distributed along the northern and southern boundaries of the microplate. The mantle basal drag is estimated and input to the finite element models. The two remaining force distributions are the unknowns of the problem.

The three types of force can be combined to produce a zero net torque. However, since there are two unknown forces there is an infinite number of such combinations. In order to limit the number of possibilities, initial combinations include the mantle basal drag and either normal forces along the East and West Rifts, or shear forces along the southern and northern boundaries. Then, after critical assessment, the three types of force are superimposed.

A numerical plate model fixed so that no net translation or rotation is allowed, automatically satisfies the equilibrium condition. This ensures that the finite element system of equations has a unique solution. Here I fix the nodal points along the boundaries of the microplate to find the boundary forces as the reaction to the mantle basal drag.

A boundary can be fixed in one or in two directions. If a boundary is fixed in both directions then both shear and normal forces can exist along that boundary. If a boundary is only fixed in the parallel or perpendicular direction to the boundary then only shear or normal forces, respectively, can exist along that boundary. The boundary forces, which are the forces per unit of length and of thickness of the plate boundary, can be linearly extrapolated from the stresses at the Gauss points in the elements adjacent to the boundaries.

In the diagrams showing the results, inward pointing arrows represent compressive principal stresses and outward pointing arrows represent tensile principal stresses. The stresses are averaged over the Gauss points of each grid element, and displayed at the centre of each element. The stresses at the Gauss points adjacent to the plate boundaries are therefore slightly different from those displayed at the centre of the elements. The scale of the depicted stresses is shown by the labelled arrow at the top right of each diagram.

7.3 The strength of the microplate

In the thrust and normal fault regimes the strength of the brittle lithosphere is determined from the Byerlee law, which for hydrostatic pore fluid pressure can be written as (section 5.3),

$$S = \left| \frac{\mp 2 f_s (\rho g z - \rho_w g z)}{(1 + f_s^2)^{1/2} \pm f_s} \right| \tag{7.1}$$

where the upper sign gives the strength in extension and the lower sign gives the strength in compression. The meaning and value of the symbols are listed in Table 5.1 (chapter 5). In the transcurrent fault regime, the vertical stress, which is usually assumed to be the lithostatic pressure, is the intermediate stress. In this case the strength is harder to determine because both the maximum and minimum principal stresses are unknown. Nevertheless, the strength can be derived by writing the intermediate stress as,

$$\sigma_{zz} = \sigma_3 + \delta(\sigma_1 - \sigma_3), \tag{7.2}$$

where σ_{zz} is the vertical stress, σ_3 is the minumum principal stress, δ is a dimensionless factor $0 < \delta < 1$ and σ_1 is the maximum principal stress. Following a derivation analogous to that presented in section 5.3 the strength in the transcurrent fault regime is defined as,

$$S = \left| \frac{2 f_s (\rho g z - \rho_w g z)}{(1 + f_s^2)^{1/2} - f_s (1 - 2\delta)} \right|. \tag{7.3}$$

For a fault with coefficient of friction $f_s = 0.75$ and $\delta = 0.5$ equations 7.1 and 7.3 can be written in the condensed form,

$$S = \alpha(\rho g z - \rho_w g z), \tag{7.4}$$

where α depends on the fault type. Under the present assumptions $\alpha = 3.0$ for thrust faults, $\alpha = 1.2$ for strike-slip faults and $\alpha = 0.75$ for normal faults. The density ρ is equal to the density of the crust ρ_c for depths less than 6 km and equal to the density of the mantle ρ_m for depths greater than 6 km.

The rock strength integrated over the lithospheric thickness yields the maximum tectonic force that it can withstand, and will be referred to as the lithospheric strength (see Eq. 2.12 and Eq. 5.4). Estimates of the lithospheric strength in the normal, strike-slip, and thrust faulting regimes for several estimates of the brittle layer thickness are listed in Table 7.1 (the strength of the ductile lower lithosphere is neglected).

The mean strength of the lithosphere $\bar{S}$ can be defined as the tectonic force averaged over the lithopheric thickness, that is $\bar{S} = \int_0^L S dz/L$, where L is the brittle lithospheric thickness and S is the strength given by Eq. 7.4. At the East Pacific Rise, an estimated brittle thickness of 2 km implies a mean tensile strength of 14 MPa. This value is in agreement with estimates of the ridge resistance force (per unit of plate thickness) at fast spreading ridges, provided by other theoretical and numerical models (section 2.5.3).

Estimates of the strike-slip strength based on Byerlee's law are known to overestimate the strength of transform faults. Estimates of the transform resistance at the San Andreas fault have an upper bound of 20 MPa (Lachenbruch, 1973), and numerical plate dynamic models indicate shear stress values along transform faults less than 10 MPa (e.g. Wortel et al., 1991; Richardson and Reding, 1991). Although the northern and southern boundaries of Easter microplate are not well developed transform faults, some parts of these boundaries have been interpreted as such. Hence, the analogy with transform faults suggests that the shear stresses along the northern and southern boundaries are likely to be less than 15 MPa.

Table 7.1: Lithospheric strength (maximum tectonic force F)

Brittle thickness (km)	F_{normal} ($\times 10^9$ N/m)	$F_{strike-slip}$ ($\times 10^9$ N/m)	F_{thrust} ($\times 10^9$ N/m)
2	28	46	112
4	112	180	452
8	488	784	1952

7.4 Estimating the basal drag force

The mantle basal drag force quantifies the interaction between the lithosphere and the asthenosphere. In plate tectonic numerical models the basal drag is commonly computed from (section 2.5.1):

$$\vec{F}_D = D\vec{V}, \tag{7.5}$$

where $\vec{F}_D$ is the mantle drag force per unit area, D is a constant of proportionality and $\vec{V}$ is the absolute velocity of the plate in a fixed hotspot reference frame. If D is positive then the basal drag acts in the same direction as the absolute plate velocity, and is considered a driving force. If D is negative, than the basal drag is a force opposing the plate motion.

The absolute motion of Easter microplate can be derived from the absolute motion of either Pacific or Nazca plates, and from the motion of Easter relative to Pacific or Nazca respectively. Since Easter is rotating relative to Nazca and Pacific plates, its absolute motion can be decomposed into a rotation about an axis fixed to the microplate and a translation of that axis. The component of translation has no relevance when the forces governing Easter rotation are being analysed. Therefore the absolute velocity of the microplate, $\vec{V}$, is replaced by the vector product of the angular velocity $\vec{w}$ (about a vertical axis fixed to the microplate) and the distance to the rotation axis, $\vec{r}$. That is,

$$\vec{F}_D = D(\vec{w} \times \vec{r}), \tag{7.6}$$

The angular velocity of Easter during the last 3 Ma, estimated from the magnetic anomalies and predicted by the roller-bearing model, has been fairly constant and is about 18°/Ma (Schouten et al., 1993, Searle et al., 1993). According to the roller-bearing model, the broad curvature of the Eastern Inner Pseudofault (EIPF) suggests that the microplate rotation axis is located at about 24.2°S, 112.5°W, much closer to the northern boundary than to the southern one. This implies larger magnitudes of linear velocities in the south than in the north of the microplate, but this detail will not be taken into account at first. Initially, it is assumed that the microplate is rotating about a vertical axis located at the centre of the square grid, with an angular velocity $w = 18°/\text{Ma}$.

If the rotation of the microplate is driven by the asthenospheric flow, then there must be a vortex in the asthenosphere having increasing angular velocity with depth. This hypothesis is disregarded on the grounds of implausibility, and consequently it is assumed that the mantle basal drag resists the microplate rotation. The asthenosphere is considered to be a low-viscosity constant-thickness channel, bounded at its top by a moving lithosphere and at its bottom by a motionless mesosphere. To determine the constant of proportionality D of equations 7.5 and 7.6, I approximate the basal drag to the shear produced by the asthenosphere flow at the top of that channel. The asthenosphere is assumed to behave like a Newtonian fluid. Because circular flow can be regarded as the composition of two unidimensional flow components, it is assumed that circular flow produces the same shear stress as 2D channel Couette flow (e.g. Liggett, 1994). The velocity profile of a Newtonian fluid moving with velocity u in the horizontal x direction, in a channel of constant thickness h, under no applied horizontal pressure gradient, and with boundary conditions $u = V$ at the top of the channel (y=0), and $u = 0$ at the base (y=h), is (e.g. Turcotte and Schubert, 1982),

$$u = V(1 - y/h). \tag{7.7}$$

As a result of the gradient in the velocity profile, a shear stress is exerted on horizontal planes in the asthenosphere and at the base of the lithosphere. The shear

stress at the base of the lithosphere is,

$$\tau = \eta|\frac{du}{dy}| = \eta\frac{V}{h}, \tag{7.8}$$

where η is the viscosity of the asthenosphere. Making τ of eq. 7.8 equal to F_D of eq. 7.5 gives $D = \eta/h$. Then, the expression of the basal drag becomes,

$$\vec{F_D} = \frac{\eta}{h}(\vec{w} \times \vec{r}) \tag{7.9}$$

According to Eq. 7.9 the magnitude of the basal drag increases with the distance from the rotation axis. The basal drag, being a resisting force acts in an anticlockwise direction since the microplate rotates in a clockwise direction.

The existence of a channel of low viscosity mantle, 100-200 km thick, is supported by postglacial rebound data, and also by seismic studies showing a low-velocity layer beneath the lithosphere (Dziewonski and Anderson, 1981). Beneath continents, upper mantle viscosity values of about 10^{21}Pa s are inferred from postglacial rebound data (Peltier, 1989). Beneath oceans, geophysical studies suggest lower viscosity values. For instance, models of mantle convection require a 100-200 km thick asthenosphere with viscosity of about 2×10^{19}Pa s to explain the topographic and geoid anomalies associated with oceanic fracture zones (Robinson et al., 1988). Taking into account postglacial rebound data, plate driving force models, geoid anomalies and heat flow data, Hager (1991) proposed a compromise average asthenosphere viscosity under oceans of the order of 10^{19}Pa s.

Near mid-ocean ridges upper mantle viscosities are probably lower. Studies on the temperature and pressure dependence of the mantle viscosity indicate smallest viscosities where the asthenosphere is both hot and shallow (Weertman and Weertman, 1975), as it is beneath spreading centres. The presence of partial melt at mid-ocean ridges may further weaken the asthenosphere (Kohlstedt, 1992), although that is not entirely clear (Karato, 1986). The few observational constraints on the viscosity of the asthenosphere near mid-ocean ridges indicate values between 10^{18}Pa s and 10^{19}Pa s. For instance, models of small-scale mantle convection consistent with the gravity lineations observed in satellite data near the East Pacific

Rise, suggest a minimum of 10^{18}Pa s (Buck and Parmentier, 1986). Postglacial rebound data in Iceland requires upper mantle viscosity values lower than 10^{19}Pa s (Sigmundsson, 1991).

Easter microplate is a large mid-ocean ridge offset, so the asthenosphere viscosity value beneath the microplate is likely to be close to that beneath mid-ocean ridges. Furthermore, the regional tectonic setting of the microplate, including several hotspots and an anomalously hot asthenosphere (chapter 4), favours a low value of asthenosphere viscosity. For that reason I assume that the asthenosphere viscosity beneath Easter may have a value in the range between 1×10^{18}Pa s and 1×10^{19}Pa s. It is also assumed that the asthenosphere channel is 200 km thick.

In the finite element model the magnitude of the basal drag is maximum at the boundaries of the grid, that is, for $r = 240$ km. Using $r = 240$ km, $w = 18°/\text{Ma}$ and $h = 200$ km in Eq. 7.9 gives,

$$F_D \sim 0.012 \text{ MPa} \quad \text{for} \quad \eta = 1 \times 10^{18} \text{ Pa s},$$
$$F_D \sim 0.12 \text{ MPa} \quad \text{for} \quad \eta = 1 \times 10^{19} \text{ Pa s}.$$

These values are in conformity with generally accepted estimates of the basal drag magnitude in the range $10^{-1} - 10^{-2}$ MPa (section 2.5.1).

The shear stress exerted by the asthenosphere at the base of the lithosphere produces a shear stress profile within the lithospheric plate. The distribution of the shear stress within the plate is unknown, but it is zero at the plate's surface and equal to the basal drag F_D at the base of the plate. Since the models are 2D horizontal, the variation of the shear stress within the plate is neglected, and the basal drag has to be averaged over the plate thickness.

In order to find the boundary forces, the basal drag must be averaged over the plate thickness at the edges of the microplate. Seismic studies provide estimates of the lithosphere thickness at the EPR in the range of 1-2 km (section 1.2). Here, an average plate thickness of 2 km is assumed at the East and West Rifts. The value of the basal drag that is input to the models is F_D divided by 2 km. This input

input value has the dimensions of a force per unit volume (i.e. a stress per unit length). This force per unit volume is first computed at each Gauss point position and then included in the input file of the main modelling program. I programmed a new subroutine of the main program that deals with the basal drag as an horizontal body force. Testing has proved that this procedure is equivalent to the input of direct nodal forces.

As the plate thickens away from the ridge the stress will be proportionately reduced. Therefore, within the microplate there is a relative error in the stress magnitudes predicted by the modelling. More critical than this relative error are the limits of validity of the assumptions and approximations made to estimate the basal drag. The simplifying assumptions concerning the asthenosphere flow, in particular the negligence of the vertical flow (i.e. the asthenosphere upwelling), is certainly not valid near spreading centres. The mid-ocean ridge boundary zones are also ignored in the definition of the model's rheology. Thus, the elastic rheology assumed for the microplate is not appropriate to represent the low-strength ridge axial region. In conclusion, the mantle basal drag model just derived does not take into account local sources of stress in the vicinity of the spreading segments.

To find the order of magnitude of the torque exerted by the mantle drag in the microplate, let us compute the torque, $T = |\vec{F_D} \times \vec{r}|$, about the central point of the square grid. After expressing the basal drag force in rectangular coordinates the total (vertical) torque per unit of thickness of the microplate is,

$$\frac{T}{L} = \int_{-240}^{240} \int_{-240}^{240} \frac{\eta}{h} w(x^2 + y^2) dx dy. \tag{7.10}$$

Using $w = 18°/\text{Ma}$ and $h = 200$ km in the above equation the magnitude of the mantle basal drag torque averaged over a 2 km thick microplate is,

$$T = 8.8 \times 10^{11} \text{ Nm} \quad \text{for} \quad \eta = 1 \times 10^{18} \text{ Pa s},$$

$$T = 8.8 \times 10^{12} \text{ Nm} \quad \text{for} \quad \eta = 1 \times 10^{19} \text{ Pa s}.$$

7.5 Estimating possible driving forces

This section calculates possible driving forces opposing the basal drag. The possibilities considered are the two alternative models depicted in Fig. 7.1.

7.5.1 The Schouten et al. hypothesis

In the ideal kinematic model described in section 1.8, the rotation of the microplate is due to the drag of the main plates at two single points, which are simultaneously the tips of the propagating rifts and the instantaneous poles of rotation of Easter relative to Nazca and Pacific plates. With the exception of these two points, there is slip everywhere along the microplate's margins. In reality the tips of the propagating rifts do not coincide with the instantaneous poles of Pa-Ea and Na-Ea motion (Rusby and Searle, 1995). Also, the poles do not exactly lie along the microplate's margins. This implies that the model of Schouten et al. cannot be strictly applied. If it is applied, there must be some slip along the microplate boundaries.

Here I test the idea of a microplate being driven by drag forces distributed along its boundaries. In practice this is more reasonable than having all the drag concentrated at only two points. The hypothesis of a drag force along the East and West rifts is excluded, because these boundaries are more likely weak decoupling zones between the microplate and the main plates. If at the ridge axis the crust is separated by low viscosity material, or is formed by just a thin solid layer on top of a magma chamber, then it can only support very low stresses, and behave like a decoupling zone. This hypothesis is more appropriate at the fast spreading rates typical of the EPR. But even if the ridge's strength is significant, as at slow spreading rates (near the rift tips), the local tensile stress perpendicular to the strike of the ridge is expected to dominate any drag force. Hence, to examine the dynamics of the roller-bearing model, free boundary conditions along the East and West rifts are assumed.

In the Schouten et al.'s ideal model the drag forces at the rift tips are tangent to the microplate boundaries, so they are shear forces. In my approach the drag

forces are no longer concentrated at the rift tips, so the question arises whether they can be normal to the northern and southern boundaries. This hypothesis seems implausible because the location of the Pa-Ea and Na-Ea instantaneous relative poles of rotation (close to the rift tips) implies that the convergence rate between the major plates and the microplate increases with the distance from the rift tips (Fig. 7.2). Thus, the normal forces along the northern and southern boundaries, imposed by the motion of the major plates, produce an anticlockwise torque, and consequently cannot drive the microplate.

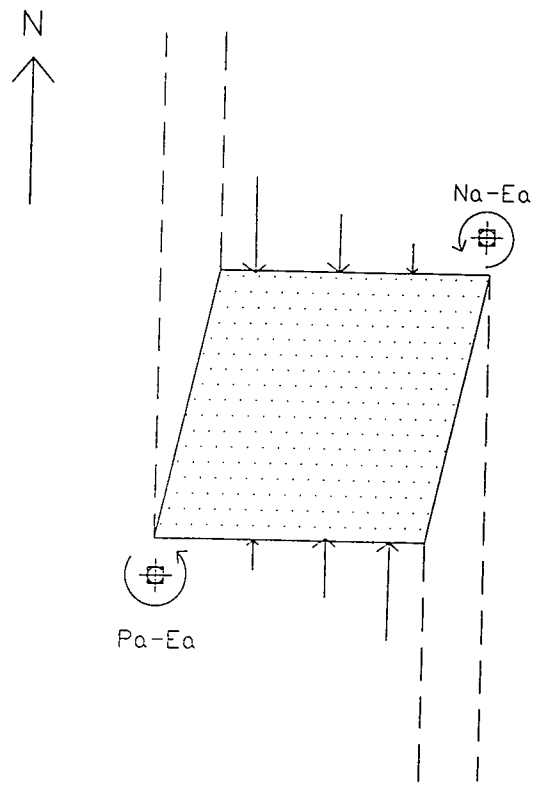

Fig. 7.2 Hypothetical normal force distribution resulting from the drag of the main plates. The dotted area represents the microplate. Dashed lines represent isochrons and illustrate the accretion gradient along the microplate margins. Symbols near the rift tips represent the instantaneous rotation axes Na-Ea and Pa-Ea, which describe the instantaneous motion of Nazca and Pacific plates relative to Easter microplate. The normal force distributions along the northern and southern boundaries, consistent with the location of the Pa-Ea and Na-Ea instantaneous relative poles of rotation, produce an anticlockwise torque on the microplate.

The driving forces consistent with Schouten el al. hypothesis are therefore shear forces distributed along the northern and southern boundaries of the microplate. These forces are included in model BNS (Fig. 7.3), which has the following boundary conditions:

- The resisting basal drag acting at the base of the plate is anticlockwise, and is computed for an asthenosphere viscosity value of 5.0×10^{18} Pa s.
- The northern and southern boundaries of the grid are only fixed in the x direction (E-W). This boundary condition implies there are no normal forces along the northern and southern boundaries of the microplate.
- The east and west boundaries of the grid are free.
- The centre of the grid is fixed in the y direction to ensure the numerical stability of the model. This condition does not affect the results.

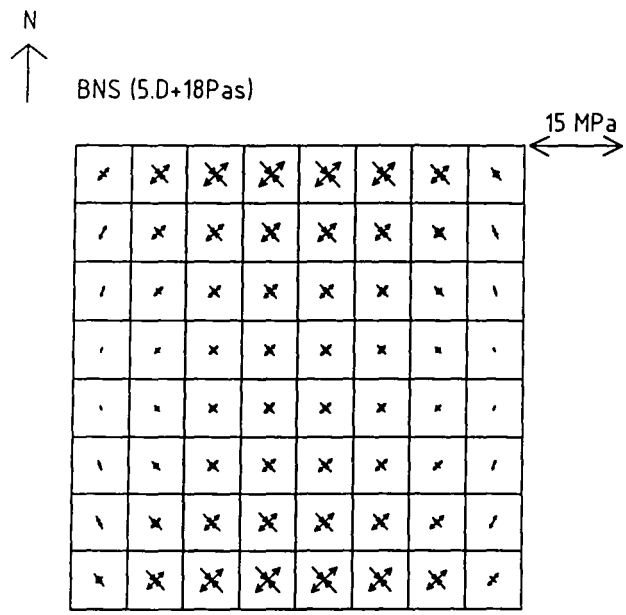

Fig. 7.3 Model BNS. The driving forces along the northern and southern boundaries are derived as the reaction to an anticlockwise mantle basal drag (computed for an asthenosphere viscosity equal to 5×10^{18} Pa s). In order to produce only shear driving forces, the northern and southern boundaries are only fixed in the tangential direction to the boundary.

In model BNS (Fig. 7.3) the shear driving stresses have a maximum value of 7.5 MPa in the central part of the northern and southern boundaries, and decrease towards the boundary ends.

7.5.2 The rift driven hypothesis

The absence of shear stresses at mid-ocean ridges in general is confirmed by earthquake focal mechanism evidence, showing principal stress directions parallel and perpendicular to ridge trends (e.g. Bergman and Solomon, 1984). So if the microplate is driven by forces along the East and West Rifts, these must be normal forces. The driving normal forces along the East and West Rifts are included in model BEW (Fig. 7.4), which has the following boundary conditions:

- The resisting basal drag acting at the base of the plate is anticlockwise, and is computed for an asthenosphere viscosity value of 5.0×10^{18} Pa s.
- The northern and southern boundaries of the grid are free.
- The east and west boundaries are only fixed in the x direction (E-W), perpendicular to the boundary. This condition implies there are no shear forces along the East and West Rifts.
- The centre of the grid is fixed in the y direction to ensure the numerical stability of the model. This condition does not affect the results.

In model BEW (Fig. 7.4) the normal driving stresses along the East and West boundaries have a maximum value of 15 MPa at the rift extremities. Principal stresses are compressive at one end of the rift and tensile at the other.

Fig. 7.4 shows that driving forces along the East and West Rifts, varying between -15 MPa and +15 MPa, balance a resisting torque equal to 4.4×10^{12}Nm (which is the torque of the mantle basal drag computed for an asthenosphere viscosity equal to 5.0×10^{18}Pa s).

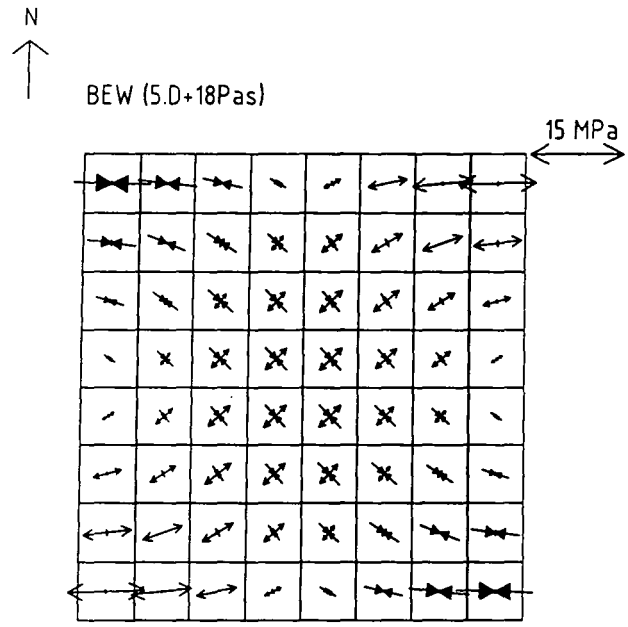

Fig. 7.4 Model BEW. The driving forces along the East and West Rifts are derived as the reaction to an anticlockwise mantle basal drag (computed for an asthenosphere viscosity equal to 5×10^{18} Pa s). The east and west boundaries are only fixed in the normal direction to the boundary because there are no shear forces along spreading centres.

Testing has proved that a mantle basal drag computed for an asthenosphere viscosity equal to 1.0×10^{19}Pa s produces a maximum stress magnitude at the rift extremities equal to 30 MPa. Therefore, a driving force distribution along the East and West Rifts, varying between -30 MPa and +30 MPa, produces a driving torque equal to 8.8×10^{12}Nm (which is the torque of the mantle basal drag computed for an asthenosphere viscosity equal to 1.0×10^{19}Pa s).

Several kinds of evidence suggest that the ridge resistance decreases as the spreading rate increases (section 2.5.3). The variation of the spreading rate along the East and West Rifts has been derived by Rusby (1992) from magnetic anomaly data, and is listed in Table 7.2.

Table 7.2 Spreading rates and azimuths at the East and West Rifts. Data from Rusby (1992)

	Latitude/°S	Longitude /°W	Rate (mm/yr)	Azimuth/°
West rift	23.12	114.87	136.10	261
	23.39	115.26	130.45	256
	23.78	115.48	121.07	252
	24.33	116.00	111.50	243
	24.88	116.11	98.98	237
	25.73	116.00	77.24	229
	26.22	115.54	58.36	228
	26.68	115.00	38.77	230
	26.78	114.13	26.64	265
	27.00	113.82	20.86	286
	27.36	113.51	16.76	326
East rift	27.22	113.04	138.57	097
	26.50	112.60	116.55	092
	26.00	112.49	101.76	091
	25.50	112.47	87.03	090
	24.78	112.11	66.43	082
	24.27	112.09	51.68	079
	23.92	111.82	43.89	067
	23.41	111.67	33.06	050
	23.00	112.00	18.06	047
	23.00	112.51	-13.38	097
	23.04	113.00	-20.81	136
	23.08	113.50	-32.56	151
	23.16	114.00	-45.83	157

The full spreading rate along the East rift decreases from $\sim$ 139 mm/yr at 27°S to $\sim$ 18 mm/yr at 23°S. Similarly, the full spreading rate along the West rift changes from $\sim$ 136 mm/yr at 23°S to $\sim$ 20 mm/yr at 27°S. As a consequence the ridge resistance must increase northwards along the East Rift and southwards along the West Rift, that is, must increase towards the tip of each rift.

The above reasoning justifies a distribution of the ridge resistance force along the East and West Rifts as depicted in Fig. 7.5 (a).

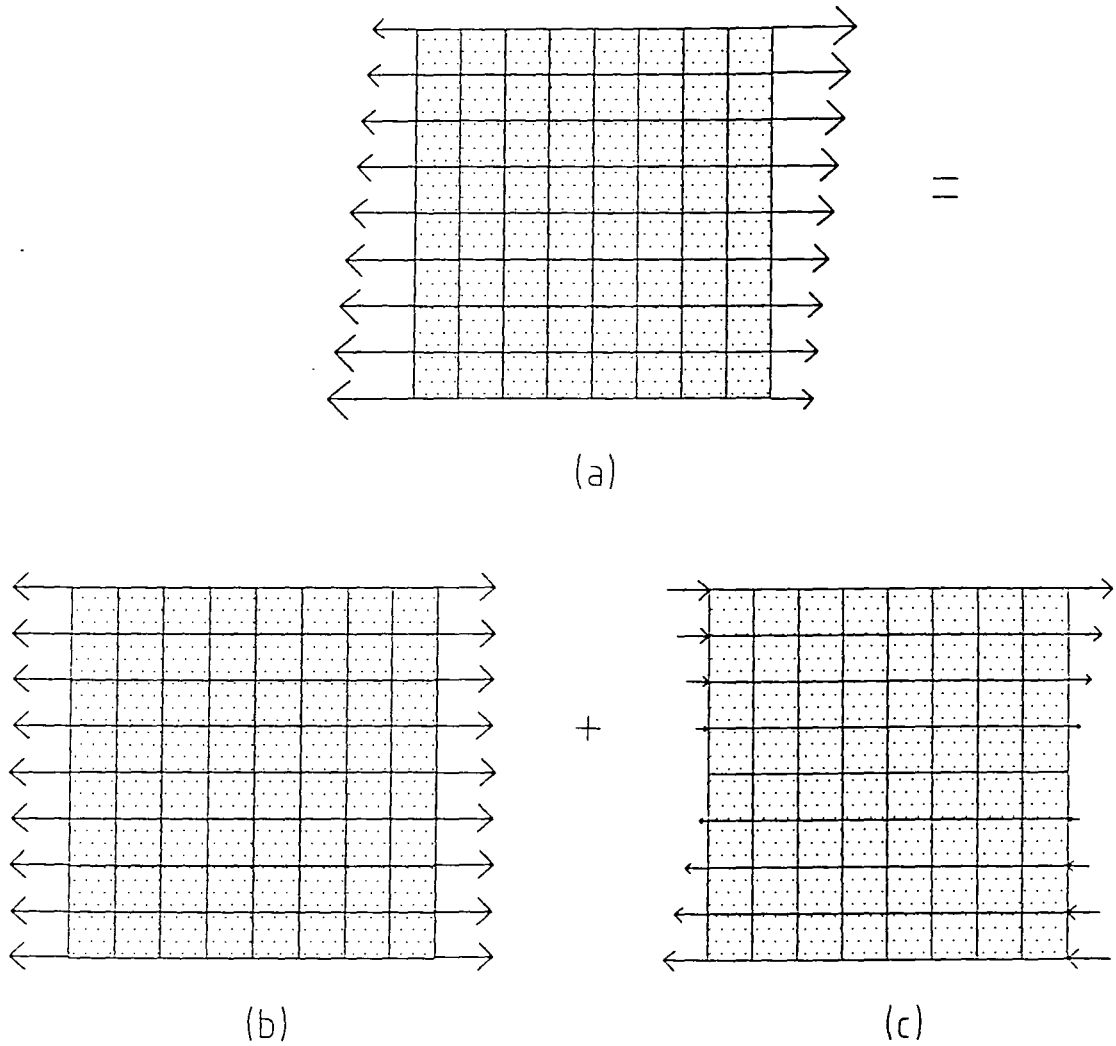

Fig. 7.5 The tensile normal stress along the East and West boundaries of the model, representing the ridge resistance, varies in the inverse proportion to the spreading rate. It increases southwards along the West Rift and northwards along the East Rift. The net force represented in (a) can be decomposed into the force distributions of diagram (b) and (c). Diagram (b) represents the average ridge resistance, which does not contribute to the torque about the centre of the microplate. Diagram (c) corresponds to the force distribution along the East and West Rifts inferred from model BEW (Fig. 7.4). It provides the driving torque for the rotation of the microplate.

The force distribution in Fig. 7.5 (a) may be decomposed in the two components displayed in Fig. 7.5 (b) and (c). The constant tensile stress of (b) corresponds to the average ridge resistance along the East and West Rifts. This component can only cause uniform stress and does not contribute to the torque about the centre of the microplate. The force distribution in (c) is that inferred from the stress pattern of model BEW (Fig. 7.4). This component produces the driving torque for the rotation of the microplate.

In order to maintain a net tensile force at the rifts, the maximum stresses at the rift extremities in Fig. 7.5 (c) must not overcome the average ridge resistance in Fig. 7.5 (b). The effect of the average ridge resistance, which is to superimpose an E-W tension on the stress distribution, is neglected.

7.6 Expanding the rift driven hypothesis

Model BEW (Fig. 7.4) shows that forces applied along the East and West Rifts, having the distribution of Fig. 7.5 (c), can drive the rotation of the microplate against the mantle basal drag. In this section the ridge driven model is expanded to include possible resisting forces along the northern and southern boundaries of the microplate.

Contrary to the East and West Rifts, the northern and southern margins of Easter are not typical plate boundaries, so there is no a priori information about the forces acting on them. Nonetheless, the stress indicators at Easter suggest that both shear and normal forces may exist along these boundaries. The existence of shear forces is supported by the observed strike-slip earthquake focal mechanisms, and also by structural observations. The Orongo fracture zone at the southern boundary, and the Pito fracture zone at the eastern end of the northern boundary have been recognised as transform faults (Francheteau et al., 1988). Although small, there is some shear resistance along transform faults. Additionally, the prominent elevation of some of the ridges observed at the northern and southern boundaries of the microplate, indicates the existence of forces normal to the boundaries. At

the northern boundary the evidence for normal forces comes also from the thrust earthquake focal mechanisms indicating strong N-S compression.

To produce both shear and normal forces along the boundaries they must be fixed in both the x (E-W) and y (N-S) directions. The problem is that in some parts of the boundaries there may be both shear and normal forces, and in others either shear or normal forces alone. To be able to model these possibilities I consider five distinct types of boundary conditions:

1. Both the x and y directions are fixed along the whole length of the northern and southern boundaries (model DEW1, Fig. 7.6; model DEWRB1, Fig. 7.7).
2. Only the x direction is fixed along the whole length of the northern and southern boundaries (model DEW2, Fig. 7.6; model DEWRB2, Fig. 7.7).
3. Only the y direction is fixed along the whole length of the northern and southern boundaries (model DEW3, Fig. 7.6; model DEWRB3, Fig. 7.7).
4. The half length of the northern and southern boundaries adjacent to the rift tips are let free. The other half lengths are fixed in both the x and y directions (model DEW4, Fig. 7.6; model DEWRB4, Fig. 7.7).
5. The half length of the northern and southern boundaries adjacent to the rift tips are free. Those away from the rift tips are fixed only in the y directions. The centre of the grid is fixed in the x direction to ensure the numerical stability of the model (model DEW5, Fig. 7.6; model DEWRB5, Fig. 7.7).

The justification for boundary condition type (4) is that the crust is much weaker in tension than in compression. Because the crust near the rift tips is subjected to tension, the halves of the northern and southern boundaries adjacent to the rift tips are assumed to have free boundary conditions, and the other halves to have transcurrent faulting conditions. The halves subjected to transcurrent faulting conditions may subsequently become weak relatively to shear displacement, so that the boundary becomes constrained only in the normal N-S direction (boundary condition (5)).

Fig. 7.6 The rift driven model is expanded to include resisting forces along the northern and southern boundaries. There is no mantle basal drag. The force distribution along the East and West Rifts represented in Fig. 7.5 (c), varying between -15 MPa and +15 MPa, is input to the models. Five types of boundary conditions are used along the northern and southern boundaries of the microplate: (1) in model DEW1 they are fixed in both directions, (2) in model DEW2 they are only fixed in the direction parallel to the boundary, (3) in model DEW3 they are only fixed in the direction perpendicular to the boundary, (4) in model DEW4 the half of the northern boundary adjacent to the East Rift tip and the half of the southern boundary adjacent to the West Rift tip are free; the other halves are fixed in both directions, and (5) in model DEW5 the half of the northern boundary adjacent to the East Rift tip and the half of the southern boundary adjacent to the West Rift tip are free; the other halves are fixed in the direction perpendicular to the boundary.

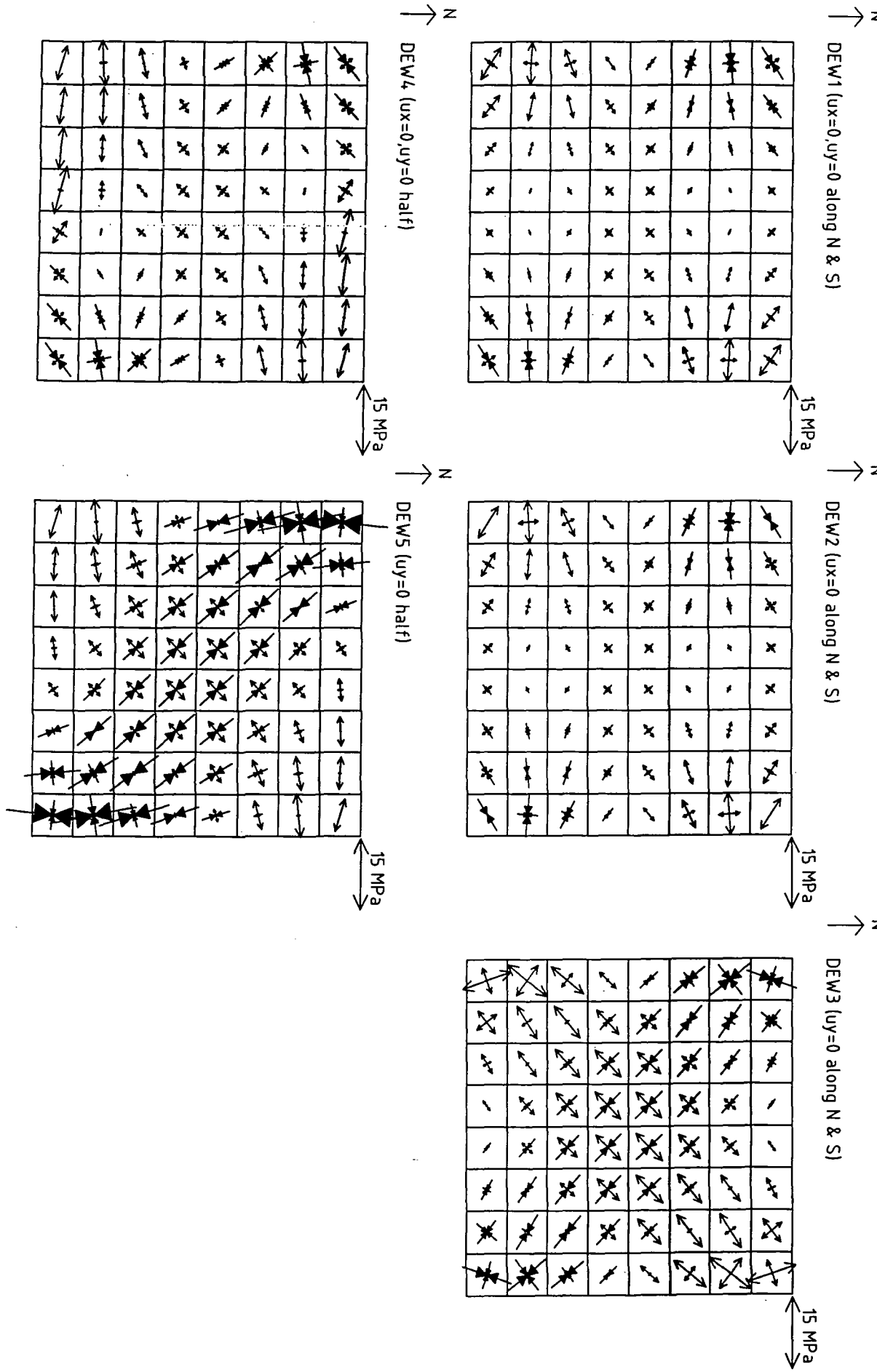
N
DEW1 (ux=0,uy=0 along N & S)
15 MPa
N
DEW2 (ux=0 along N & S)
15 MPa
N
DEW3 (uy=0 along N & S)
15 MPa
N
DEW4 (ux=0,uy=0 half)
15 MPa
N
DEW5 (uy=0 half)
15 MPa

Fig. 7.7 The expanded rift driven model includes an anticlockwise mantle basal drag, computed for an asthenosphere viscosity equal to 5×10^{18} Pa s. The force distribution applied along the East and West Rifts varies between -30 MPa and +30 MPa. Five types of boundary conditions are used along the northern and southern boundaries, as in Fig. 7.6.

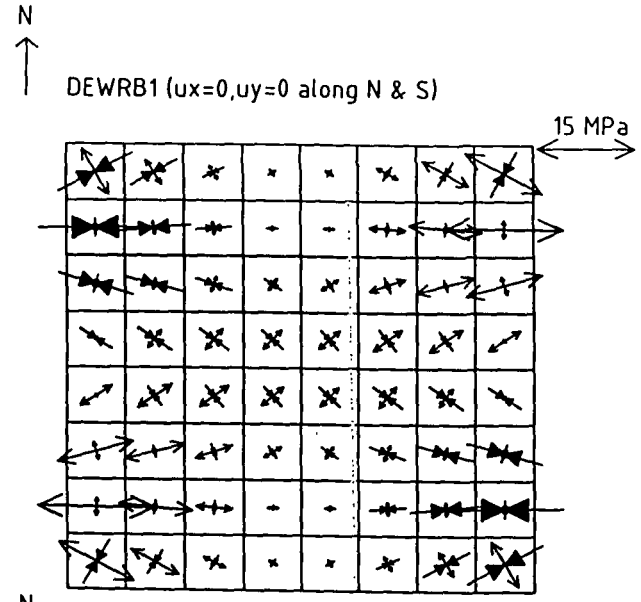
N
DEWRB1 (ux=0,uy=0 along N & S)
15 MPa

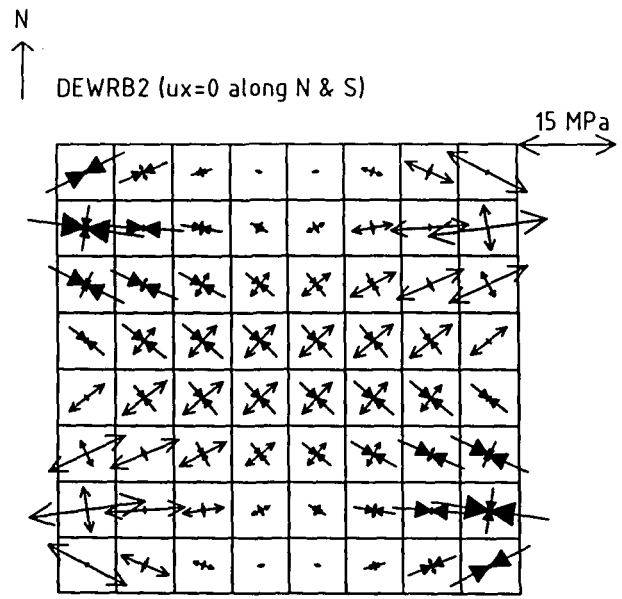
N
DEWRB2 (ux=0 along N & S)
15 MPa

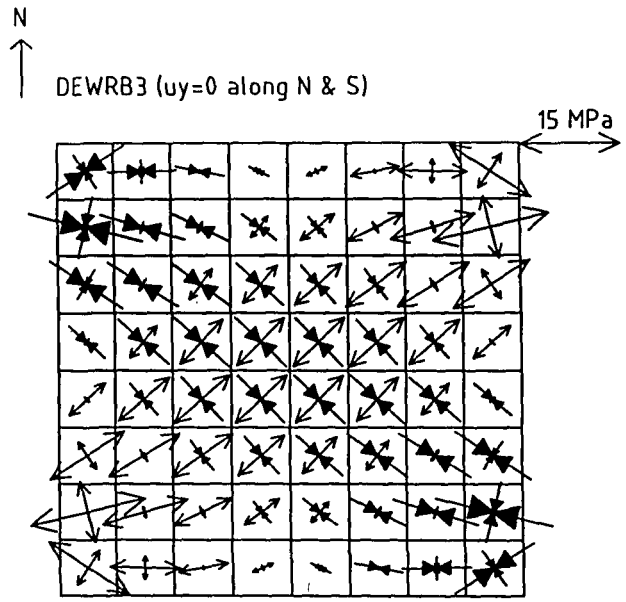
N
DEWRB3 (uy=0 along N & S)
15 MPa

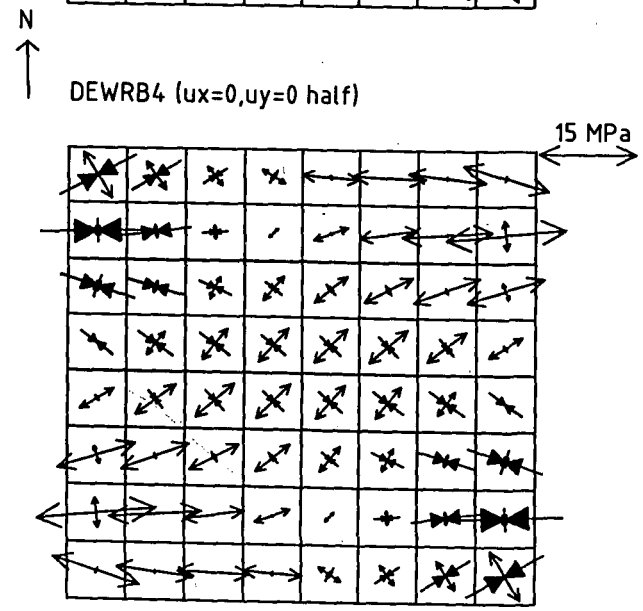
N
DEWRB4 (ux=0,uy=0 half)
15 MPa

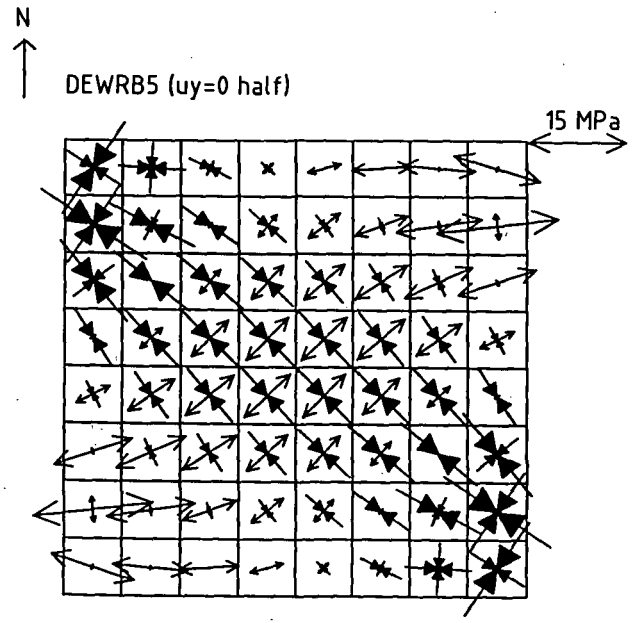
N
DEWRB5 (uy=0 half)
15 MPa

In models DEW1 to DEW5 (Fig. 7.6) the effect of the mantle basal drag is neglected and all the resistance to rotation is assumed to take place along the northern and southern boundaries of the microplate. The driving force distribution applied along the East and West boundaries varies between -15 MPa and +15 MPa.

In models DEWRB1 to DEWRB5 (Fig. 7.7) the mantle basal drag, computed for an asthenosphere viscosity of 5.0×10^{18} Pa s, is included. The driving forces applied along the East and West Rifts oppose both the mantle basal drag and the resistances along the northern and southern boundaries, so they are increased by a factor of two (i.e. vary between -30 MPa and +30 MPa).

The comparison between Fig. 7.6 and Fig. 7.7 shows that the mantle basal drag has an important effect on the stress orientations. However, that effect depends on the relative contribution of the mantle basal drag to the total resisting torque. In models DEWRB1 to DEWRB5 (Fig. 7.7) the torque of the driving forces along the East and West Rifts is 8.8×10^{12} Nm, and the torque of the mantle basal drag is 4.4×10^{12} Nm. In this case the mantle basal drag contributes to half, and the resistances along the northern and southern boundaries to the other half, of the total resisting torque needed to meet the condition of dynamic equilibrium. For other ratios of resisting torques the stress pattern is expected to be different from that of Fig. 7.7.

7.7 Comparison with observations at Easter microplate

This section compares the results of model BNS (Fig. 7.3), corresponding to the Schouten et al. hypothesis, and of models DEW1 to DEW5 (Fig. 7.6) and DEWRB1 to DEWRB5 (Fig. 7.7), corresponding to the expanded rift driven hypothesis, with the stress indicators at Easter microplate. The comparison is used to argue in favour of the ridge driven hypothesis, and to choose the best boundary conditions along the northern and southern boundaries of the microplate. However, the examination of Schouten et al. hypothesis presented in this chapter is incomplete because normal

resistances along the northern and southern boundaries have not been included in model BNS (it is not possible to simultaneously apply shear forces and derive the resistances by fixing the nodal displacements). A fuller investigation, outside the scope of my modelling, is needed to examine it properly.

According to the evidence given in section 2.10, one would like to have a model predicting **(A)** NE-SW compression along the whole length of the northern boundary, and **(B)** approximately N-S compression in the western side of the southern boundary. Alternatively, taking into account the existence of E-W compressional ridges in the Nazca plate, as well as the strike and elevation of the northern boundary, one would like to have a model predicting **(C)** strong N-S compression in the western part of the northern boundary.

The orientation of the principal stresses in model BNS (Fig. 7.3) is not consistent with either **(A)**, **(B)**, or **(C)**. Normal resisting forces along the northern and/or southern boundaries, not included in model BNS, can produce the N-S direction of maximum compression required to fit the stress indicators. In this case the shear driving forces would have to drive the microplate against both the normal resistances and the mantle basal drag. The lack of shear strength at transform faults suggests that the northern boundary of the microplate cannot transmit large shear stresses. Therefore, although shear driving stresses along the northern and southern boundaries cannot be disregarded, it is unlikely that they fully account for the microplate rotation.

Fig. 7.6 and Fig. 7.7 show that the stress orientations in the rift driven models are essentially determined by the boundary conditions along the northern and southern boundaries, although they also depend on the magnitude of the basal drag. In order to propose a new dynamic model for Easter microplate, it is necessary to chose the boundary conditions along the northern and southern boundaries that best fit the stress indicators.

The best fit to **(A)** (NE-SW direction of maximum compression along the whole length of the northern boundary) is produced by the transcurrent faulting conditions of model DEW1 (Fig. 7.6) and DEWRB1 (Fig. 7.7). The fit to **(B)** (N-S

compression in the western side of the southern boundary) is not achieved in any of the models in Fig. 7.6 or Fig. 7.7, but can only occur if that part of the boundary is fixed in both directions or in the y direction only. The best fit to (C) (strong N-S compression in the western part of the northern boundary) is produced by the thrust faulting conditions of model DEW5 (Fig. 7.6) and DEWRB5 (Fig. 7.7).

In summary, the comparison of the stress indicators with the modelling results shows that:

- The earthquake focal mechanism evidence in the northern region of the microplate and adjacent Nazca plate (indicating a NE-SW direction of maximum compression along the whole length of the northern boundary) can be explained by locked boundary conditions along the northern boundary.

- The thrust faulting observed on the Nazca plate to the north of Easter, and the elevation of the northern boundary (indicating strong N-S compression), can be explained by a northern boundary that is weak relatively to shear displacement, but offers significant resistance to normal displacement away from the rift tips.

7.8 A new dynamic model for Easter

The previous section suggests that a new dynamic model for Easter microplate, alternative to the Schouten et al. hypothesis, must include: (1) driving forces along the East and West boundaries having the distribution shown in Fig. 7.5 (c), (2) resisting mantle basal drag acting in an anticlockwise direction, and either (3) locked northern and southern boundaries, or (4) unlocked northern and southern boundaries, fixed in the normal direction away from the rift tips. Nevertheless, none of the models presented so far predicts N-S compression in the western part of the southern boundary.

An approximately N-S direction of compression in the western part of the southern boundary may be produced by the mantle basal drag. The problem is that the mantle basal drag is expected to degrade the fit to the stress indicators in the north

of the microplate. This undesirable effect can be attenuated if the mantle basal drag is greater in the south of the microplate than in the north. If the microplate is not rotating about its centre but about a point closer to the northern boundary, as proposed by Schouten et al. (1993), an increase in the mantle basal drag magnitude from north to south is expected. This increase in the mantle basal drag magnitude towards the south could alone justify the dominance of the resisting mantle basal drag in the south of the microplate, and the dominance of the driving forces in the north.

To test this hypothesis I calculate a basal drag that is tangent to circles about the centre of rotation of the microplate proposed by Schouten et al. (1993)(a point in the NE part of the microplate). To include possible effects due to the geometry of the microplate another finite element grid is used. This grid, illustrated in Fig. 7.8, resembles more the shape of Easter microplate than the square grid used so far.

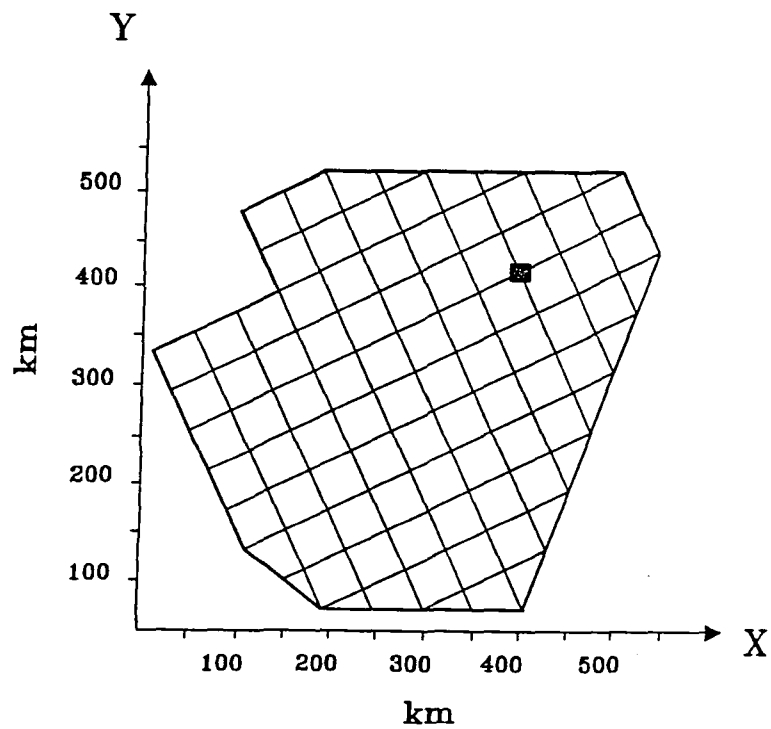

Fig. 7.8 Finite element grid used to represent Easter microplate. The filled square indicates the location of the microplate axis of rotation proposed by Schouten et al. (1993), and used as the centre of rotation of the anticlockwise mantle basal drag input to the models.

Two alternative sets of models are computed:

- Models E1D18 to E5D18 (Fig. 7.9) have northern and southern boundaries locked in both directions.
- Models H1D18 to H5D18 (Fig. 7.10) have northern and southern boundaries unlocked in the x direction, but fixed in the y direction in the half length away from rift tips.

The asthenosphere viscosity values, used in the mantle basal drag calculation, increase in steps of 1.0×10^{18} Pa s, from 1.0×10^{18} Pa s in models E1D18 and H1D18 to 5.0×10^{18} Pa s in models E5D18 and H5D18. The driving forces applied along the East and West Rifts vary between -15 MPa and +15 MPa.

The models in Fig. 7.9 and Fig. 7.10 are between two limiting situations. At one end the driving forces dominate the stress pattern, so that the mantle basal drag has only a minor effect (model E1D18 and H1D18). At the other end the resisting basal drag dominates the stress pattern, particularly in the southern part of the microplate (model E5D18 and H5D18).

In Fig. 7.9 there is a compromise between the driving forces (producing NE-SW compression along the northern boundary) and the resisting mantle drag (producing approximately N-S compression in the western part of the southern boundary) in models E2D18 and E3D18. They correspond to a situation in which the torque of the mantle basal drag is about half the torque of the driving forces along the East and West rifts. The forces along the northern and southern boundaries account for the other half of the total resisting torque. This situation is the one that best fits the earthquake focal mechanism evidence in the north of the microplate, and the elevation of the ridges in the western part of the southern boundary.

If only the earthquake focal mechanism evidence in the north of the microplate and adjacent Nazca plate is taken into account, then the 'best' model is E1D18 in Fig. 7.9. It corresponds to a situation in which 80% of the resistance to the driving forces comes from the northern and southern boundaries, and only 20% comes from the mantle basal drag.

Fig. 7.9 A dynamic model that aims to explain the earthquake focal mechanism evidence in Easter microplate. The boundary conditions are displayed at the bottom of the page. The force distribution applied along the East and West boundaries, indicated by arrows, varies between -15 MPa and +15 MPa. The + sign along the whole length of the northern and southern boundaries indicates fixing in both directions. The magnitude of the resisting mantle basal drag input to the models varies: in model E1D18 it has been computed for an asthenosphere viscosity of 1.0×10^{18} Pa s, in model E2D18 for 2.0×10^{18} Pa s, in model E3D18 for 3.0×10^{18} Pa s, in model E4D18 for 4.0×10^{18} Pa s, and in model E5D18 for 5.0×10^{18} Pa s.

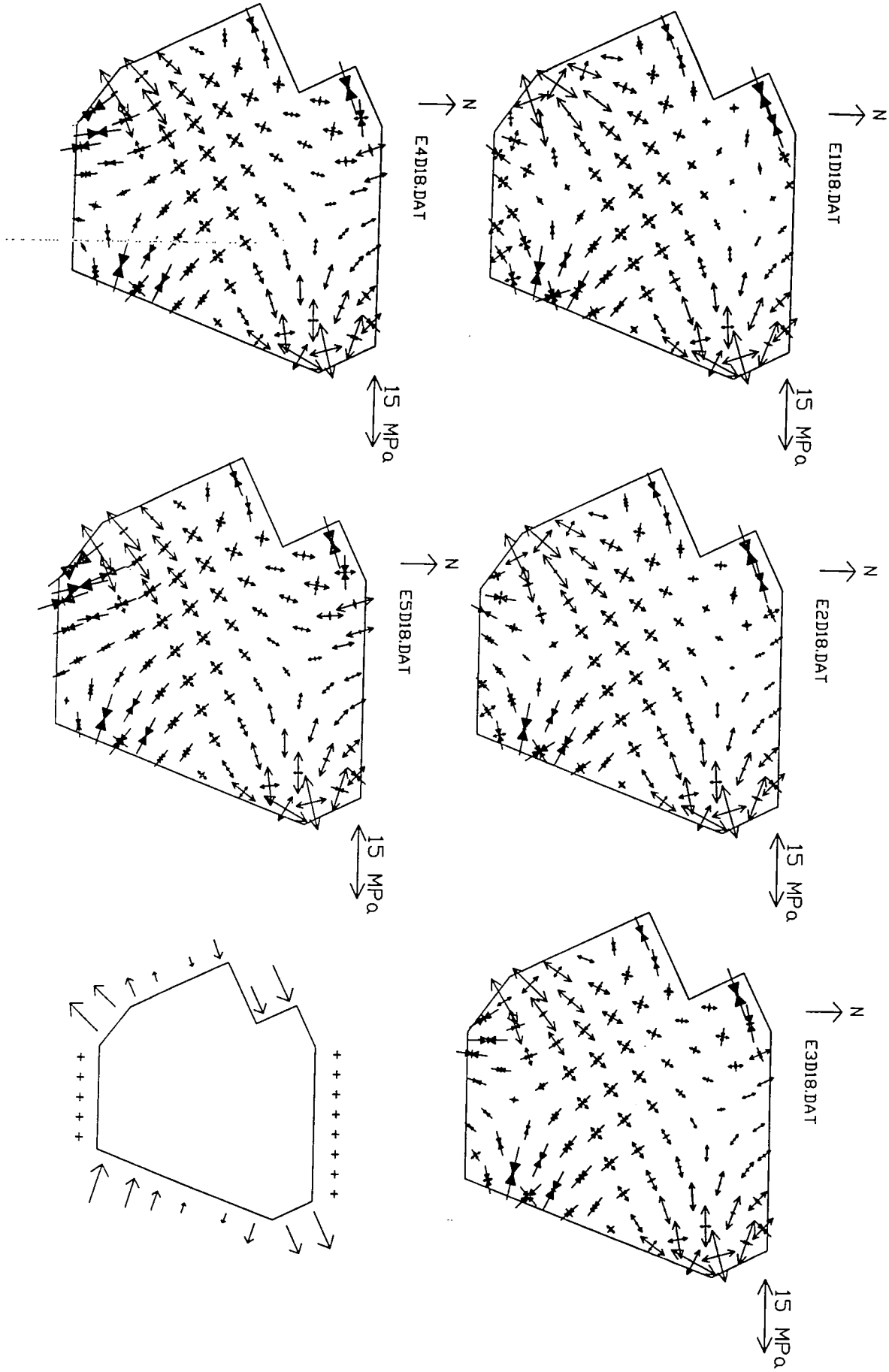
N
E1D18.DAT
15 MPa
N
E2D18.DAT
15 MPa
N
E3D18.DAT
15 MPa
N
E4D18.DAT
15 MPa
N
E5D18.DAT
15 MPa

Fig. 7.10 A dynamic model that aims to explain the compressional structures found in the Nazca plate to the north of Easter. The boundary conditions are displayed at the bottom of the page. The force distribution applied along the East and West boundaries, indicated by arrows, varies between -15 MPa and +15 MPa. The | sign in the half length of the northern and southern boundaries indicates fixing in the normal direction. The other haves of these boundaries are free. The magnitude of the resisting mantle basal drag input to the models varies: in model H1D18 it has been computed for an asthenosphere viscosity of 1.0×10^{18} Pa s, in model H2D18 for 2.0×10^{18} Pa s, in model H3D18 for 3.0×10^{18} Pa s, in model H4D18 for 4.0×10^{18} Pa s, and in model H5D18 for 5.0×10^{18} Pa s.

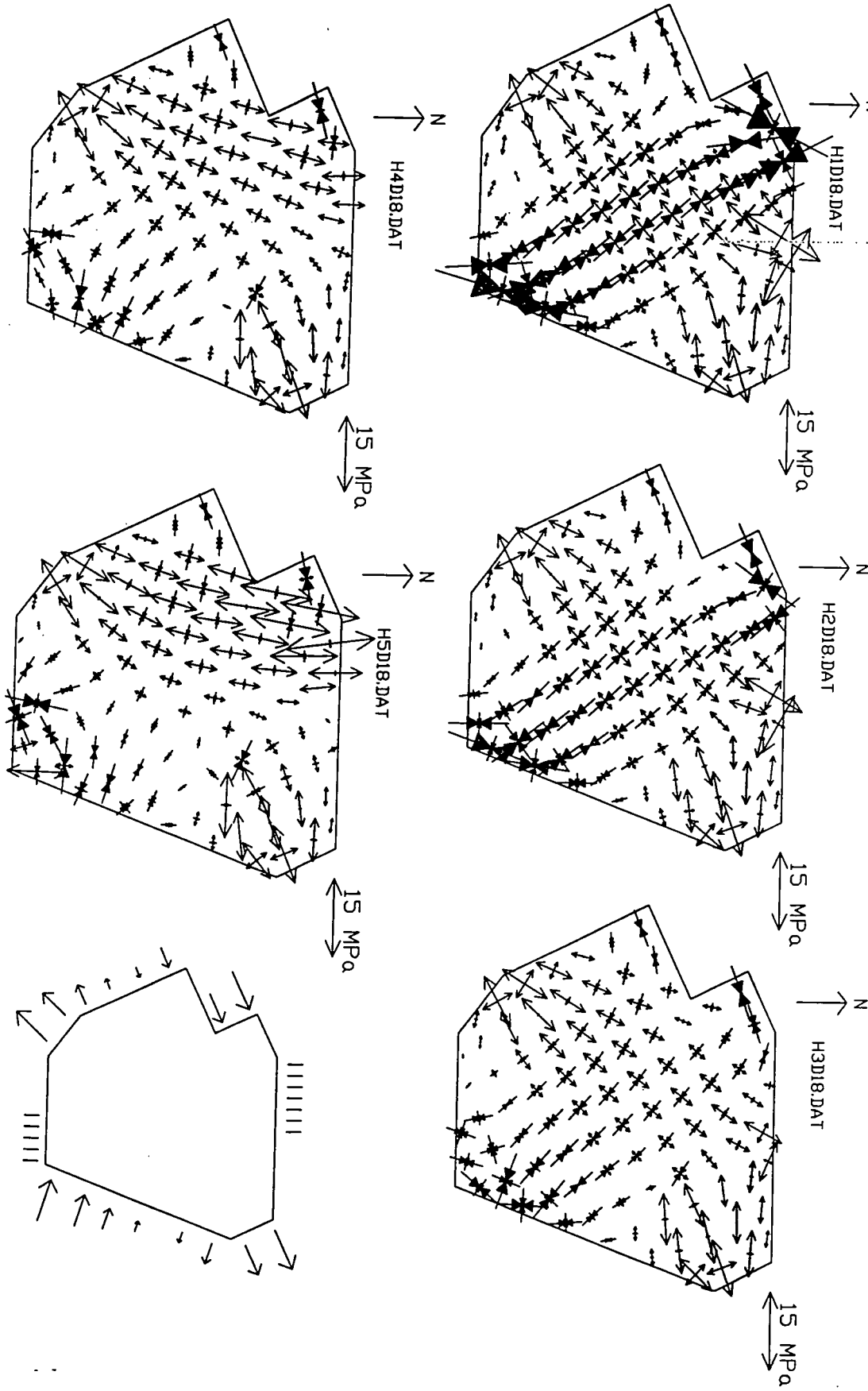
N
H1D18.DAT
15 MPa
N
H2D18.DAT
15 MPa
N
H3D18.DAT
15 MPa
N
H4D18.DAT
15 MPa
N
H5D18.DAT
15 MPa

In Fig. 7.10 the edge effects due to the geometry of the grid make the comparison with the stress indicators difficult. Nevertheless, a thrust faulting regime with a large component of N-S compression develops near the western end of the northern boundary. The largest compression occurs in model H1D18, suggesting that the best fit to the compressional features in the Nazca plate occurs when the mantle basal drag contributes to 20% (or less) of the total resisting torque.

The new dynamic model proposed for Easter involves time varying conditions along the northern boundary. When the boundary is locked (model E1D18, Fig. 7.9) shear stresses build up giving rise to earthquakes. When shear displacement along the boundary occurs, large normal resistances develop away from rift tips (model H1D18, Fig. 7.10), causing thrust faulting in the youngest region to the north.

7.9 Comparison with strength estimates

This section determines the magnitude of the driving forces along the East and West Rifts, needed to produce compressional failure in the Nazca plate. It is also intended to show that time varying boundary conditions are consistent with the strength estimates of section 7.3.

To simplify the analysis and avoid boundary effects, the following models are computed using the square grid, and assuming that the mantle basal drag rotates about a vertical axis located at the centre of the grid. Taking into account the results of the previous section, the asthenosphere viscosity is assumed to be 1.0×10^{18}Pa s.

Free boundary conditions in the half length of the northern boundary adjacent to the East Rift tip are likely to occur because the crust is weak in tension. This hypothesis is supported by bathymetry, gravity and magnetic data indicating that the broad zone (70-100 km) at the end of the East Rift, referred as the Pito Rift, is presently undergoing failure in extension (Martinez et al., 1991).

Let us assume that at a given time the boundary conditions in the microplate are those of model SEWRB4 (Fig. 7.11):

- Half length of the northern and southern boundaries near rift tips free. Other halves of these boundaries locked in both directions.
- Applied stresses along the East and West Rifts, having the distribution of Fig. 7.5 (c), and varying between -30 MPa and +30 MPa.
- Anticlockwise mantle basal drag computed for an asthenosphere viscosity of 1.0×10^{18}Pa s.

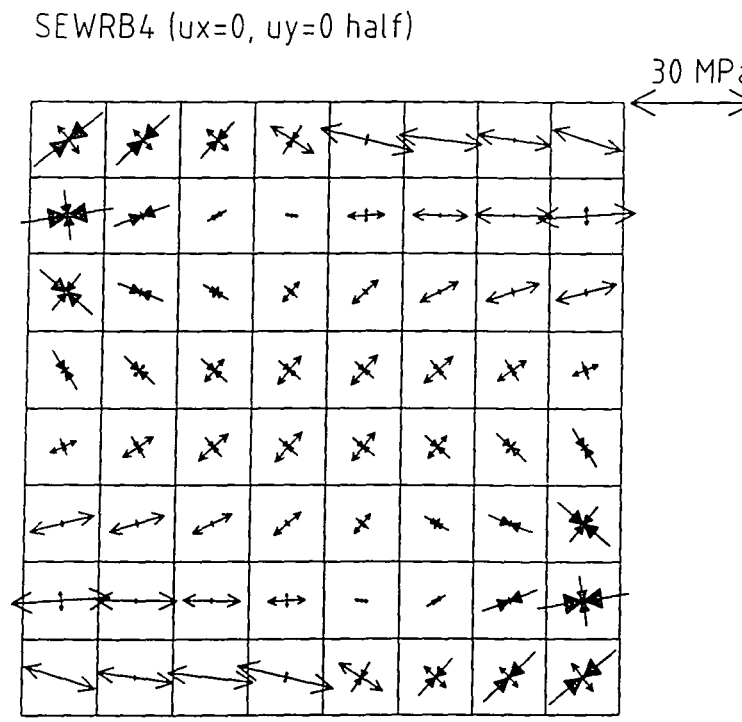

Fig. 7.11 Model SEWRB4 suggests that strike-slip may occur along the northern boundary (and a shear weakness may subsequently develop) after initial locked boundary conditions away from rift tips. The difference between the maximum and minimum principal stresses in the western end of the northern boundary exceeds 23 MPa, which is the mean strike-slip strength of a 2 km thick brittle plate.

The stress scale in Fig. 7.11 differs from that of previous figures, because the driving forces applied along the East and West Rifts have been increased by a factor of two.

The stress difference $\sigma_1 - \sigma_3$ in the western half of the northern boundary is in the range of 18-30 MPa. The mean strike-slip strength of a 2 km thick brittle plate (the tectonic force in table 7.1 divided by 2 km) is 23 MPa, but this is probably an upper bound for the strike-slip strength along the northern boundary of the microplate (section 7.3). Therefore, the modelling results are consistent with strike-slip failure and initiation of slip after locked boundary conditions.

The brittle thickness of the Nazca plate close to the East Pacific Rise is likely to be about 2 km. Compressional failure in the young Nazca plate may occur if the compressional stresses at the northern boundary of Easter exceed 56 MPa, which is the mean compressional strength of a brittle plate 2 km thick (Table 7.1). Compressional stresses of this size occur in model SEWRB5 (Fig. 7.12) which has the following boundary conditions:

- Northern and southern boundaries free in the x direction, but fixed in the normal direction in the half length away from the rift tips.
- Applied stresses along the East and West Rifts, having the distribution of Fig. 7.5 (c), and varying between -30 MPa and +30 MPa.
- Anticlockwise mantle basal drag computed for an asthenosphere viscosity of 1.0×10^{18}Pa s.

Testing has proved that minimum driving stresses of 30 MPa at the rift extremities are required to produce compressional stresses of 56 MPa in the NW region of the microplate. If a uniform average ridge resistance of 30 MPa is superimposed on the driving force distribution (so that no compressional stresses occur along the rifts), then the tensile stress at the rift tips becomes 60 MPa.

The models use the assumption of a 2 km thick elastic plate (the value used in the calculation of the mantle basal drag in section 7.4), so the tectonic force equivalent

to a stress of 30 or 60 MPa is respectively 60×10^9 or 120×10^9 N/m. To be able to withstand a tensile tectonic force in the range of 60×10^9 - 120×10^9 N/m the plate at the rift tips is required to have a brittle thickness in the range of approximately 3 – 4 km (Table 7.1). This result implies that the brittle thickness at the East and West rift tips must be about twice that characteristic of the East Pacific Rise. The generally observed dependence of the axial brittle thickness on the spreading rate and along-axis position, supports the idea that the brittle thickness increases towards the tips of the East and West Rifts.

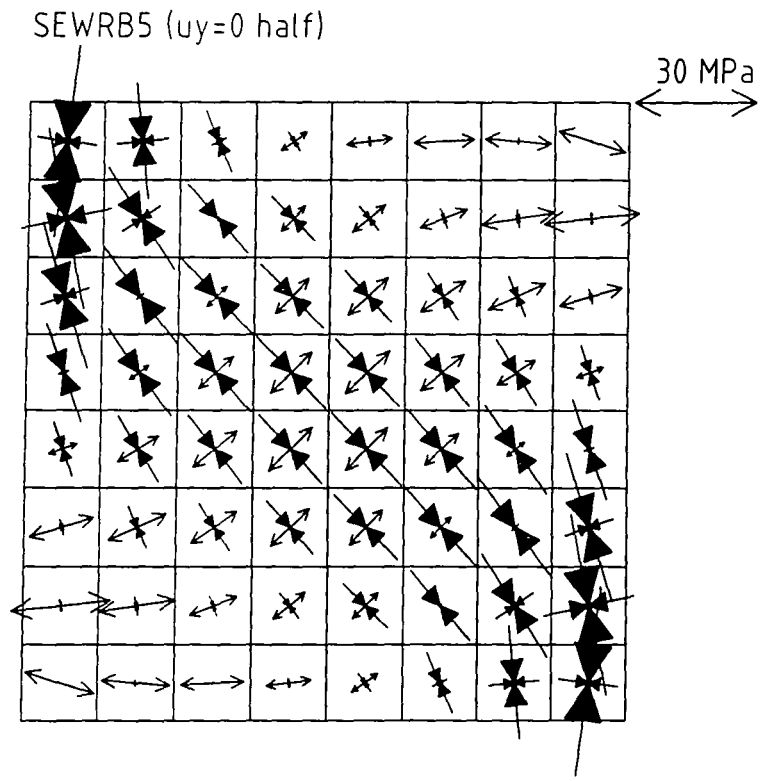

Fig. 7.12 Model SEWRB5 is the one that best explains the occurrence of compressional failure in the young Nazca plate to the north of Easter. The compressional stresses in the western end of the northern boundary exceed 56 MPa, which is the mean compressional strength of a brittle plate 2 km thick.

7.10 Discussion

The average ridge resistance, shown in Fig. 7.5b, would superimpose a uniform E- W tensile stress on the stress patterns that have been modelled. However, the modelling of the stress distribution associated with the East Pacific Rise (chapter 4) has shown that the average ridge resistance along a mid-ocean ridge has just a local effect. Thus, the tensile stresses decay with distance from the ridge axis, and in normal subsidence conditions a ridge resistance of 15 MPa along the EPR is associated with tensile deviatoric stresses of less than 1.5 MPa between 25 km and 75 km off-axis. Therefore, it would be artificial to superimpose on the models of Easter microplate a constant and uniform tensile stress caused by the ridge resistance.

To model the fading of the tensile stresses with increasing plate age we would have to include a weak rheology at the East and West Rifts of the microplate, to simulate not only the ridge resistance but also the ridge push. However, this would not be relevant to the analysis of the dynamics of Easter microplate rotation.

The fit between the modelling results and the stress indicators is not perfect, although it could be improved with small modifications in the geometry of the grid or in the specified forces. Nevertheless, that fit is more important in the northern than in the southern boundary for two two main reasons: (1) the stress indicators in the north of the microplate are more reliable regional stress indicators, and (2) the northern boundary approximately follows the 23°S latitude, and so its well represented by the E-W top boundary of the models.

The earthquake focal mechanisms in the north of the microplate have a broad distribution, extending into the adjacent Nazca plate. The only focal mechanism located on the northern boundary of the microplate is the strike-slip mechanism at 22.95°S, 112.58°W, within the Pito fracture zone (Fig. 2.9). Even this focal mechanism does not reflect the right-lateral strike-slip motion along the Pito fracture zone, as predicted by the Na-Ea instantaneous relative pole of rotation. Thus, the earthquake focal mechanisms in the north of the microplate reflect the regional stress rather than the deformation along any transform.

In contrast, the focal mechanisms in the south of the microplate gather along a relatively narrow region, along what is presumably the southern boundary. The southern boundary trends in a WNW-ESE direction in the west, but there is no structural information to constrain its direction in the east, so I opted to use the simplest configuration which is E-W. This is an oversimplification. The strike of the boundaries is extremely important in the modelling because the stress pattern is partially the result of fixing the boundaries.

If the modelling results in the southern part of the microplate are not taken into account, then it is concluded that the mantle basal drag contributes with a maximum of 20% to the total resisting torque. The remaining 80% are accounted by normal and shear resistances along the northern and southern boundaries (in locked conditions), or by just the normal resistances (in unlocked conditions).

In the previous section it has been argued that a brittle thickness of 4 km at the rift tips is consistent with a driving force distribution varying between -30 MPa and +30 MPa, which produces a driving torque equal to 8.8×10^{12}Nm. To produce a resisting torque that is less than or equal to 20% of 8.8×10^{12}Nm, the mantle basal drag has to be computed for an asthenosphere viscosity less than or equal to 2.0×10^{18}Pa s. Consequently, if there are no driving forces along the northern and southern boundaries, an asthenosphere viscosity larger than 2.0×10^{18}Pa s requires a brittle layer thickness at the rift tips larger than 4 km.

Chapter 8

Summary and conclusions

This chapter summarises the results obtained in the previous chapters. It brings into focus their common aspects and suggests further areas of research. At the end, an outline of the contribution of this study to the present knowledge of the mechanical behaviour of mid-ocean ridges and their offsets is presented.

8.1 Summary

8.1.1 Stress on the EPR flanks

The stress distribution associated with a mid-ocean ridge has been modelled for the particular case of the East Pacific Rise near 20°S. The models include both ridge flanks extending to approximately 1000 km off axis. Both the observed anomalous subsidence on the western flank of the East Pacific Rise and an idealised normal subsidence on both ridge flanks are modelled for comparative purposes. The density heterogeneities in the lithosphere associated with oceanic plate cooling are referenced to the depth-density structure of lithosphere 75 Ma old, and the mantle basal drag is neglected. The density anomalies in the asthenosphere are calculated in order to isostatically compensate the actual elevation of the seafloor relative to the normal depth of seafloor 75 Ma old. The main results of the modelling are:

- The weak rheology at the ridge crest is essential to the development of the ridge push. Deviatoric stress relaxation in the 2 km wide viscoelastic element at the ridge axis superimposes compressive stresses on the adjacent ridge flanks.

- Incomplete deviatoric stress relaxation in the viscoelastic element at the ridge axis simulates the ridge resistance.

- The magnitude of the ridge resistance determines the distance from the ridge axis at which the transition from near ridge tension to intraplate compression occurs.

- In normal subsidence conditions, the tensile stresses decay gradually from 15 MPa at the East Pacific Rise, become compressive at approximately 75 km off axis, and reach 40 MPa at 1000 km from the rise.

- Mantle basal shear stresses less than or equal to 0.1 MPa (consistent with asthenosphere viscosity values less or equal than 1.0×10^{19} Pa s) do not significantly affect the regional stress distribution associated with a mid- ocean ridge.

- Similarly to Cochran (1986), I have found that the anomalously shallow bathymetry in the western flank of the East Pacific Rise north of 20°S can be explained by an asthenospheric temperature gradient of 0.1°C/km, distributed between the base of the lithosphere and the 150 km compensation depth, starting at the ridge crest and increasing westwards.

- The effect of this asthenospheric thermal anomaly on the stress pattern is twofold: (1) it reduces the compressive stresses on the western flank of the rise, by up to 50% at 1000 km from the ridge axis, and (2) it imposes a compression of 5-10 MPa on the eastern flank of the East Pacific Rise, having therefore an across-axis impact. However, these stresses are small compared with those generated by seamount loading, which may dominate the area studied.

8.1.2 Normal faulting at mid-ocean ridges

The evolution of normal faults in the vicinity of mid-ocean ridges has been investigated considering both the effects of plastic yielding and loading by volcanic infill. The models are approximately 30 km long, corresponding to the maximum extent of active normal faulting at mid-ocean ridges, and include just one fault. The fault is planar and cuts the entire brittle thickness of the lithosphere, which is assumed to overlie an inviscid fluid. The evolution of the fault is analysed by applying successive increments of extension to the brittle layer. An oceanic strength envelope, derived by application of Byeerle's law to the oceanic lithosphere, is used to predict the occurrence of plastic failure. Models with a brittle layer thickness of 2 km represent a section of the lithosphere at a fast spreading ridge, or at the middle section of a slow spreading segment. Models with a brittle layer thickness of 8 km represent a section of the lithosphere at the end of a slow spreading segment centre. The effect of loading by volcanic infill is studied using the 2 km thick models. The effect of changing the fault dip angle is studied using the 8 km thick models. The essential results of the modelling are:

- In oceanic regions the strength increases linearly with depth, from zero at the seabed.
- Increasing the brittle thickness increases the maximum possible fault throw, the flexure of the plate, and the time period of fault activity.
- For a given applied extension and brittle layer thickness, increasing the fault dip angle increases the extent of plastic failure and the fault throw.
- Loading by volcanic infill widens the half-graben significantly, increases the subsidence of the hanging wall and reduces the uplift of the footwall.
- Plasticity reduces the equivalent elastic plate thickness and causes the narrowing of the half graben. It places a limit on the maximum fault throw that can be achieved.

- Plasticity prevents the achievement of large fault throws in thin brittle layers and reduces the ability of high-angle normal faults to withstand large amounts of extension.

- Fault throws of more than 1000 m can occur for a 8 km thick brittle plate, whereas a maximum footwall uplift of about 100 m is predicted for a 2 km thick brittle plate. These results compare well with observations at slow and fast spreading ridges respectively.

8.1.3 Ridge transform and non-transform offsets

The topographic loading created by the elevation of mid-ocean ridges relative to old ocean floor has been studied at ridge transform and non-transform offsets. The positive topography, assumed to be isostatically compensated by sublithospheric low densities, produces vertical stresses between the two opposite loads. The effect of the vertical loading on the horizontal non-lithostatic stresses is evaluated, so that it can be applied to 2D horizontal models under the plane stress assumption. A viscoplastic rheology is used at the ridge axis. The frictional resistance at transform faults and non-transform offsets is not specified. Instead either locked or unlocked offsets are modelled. A finite width ridge discontinuity with a viscoplastic rheology is also modelled, to simulate a transform with finite strength. The modelling has shown that:

- The stress pattern associated with a mid-ocean ridge does not strongly depend on the subsidence rate, but is essentially determined by the ridge resistance.

- Outside the ridge axial region the topographic loading created by the elevation of mid-ocean ridges can generate significant ridge parallel stresses, provided that transform faults are locked in the normal direction.

- Frictional resistance along a transform fault is essential to the development of extensional structures oblique to the ridge axis.

- The ridge parallel tensile stresses are observed to rotate in the vicinity of locked offsets. The highest stresses are developed at the inside corners of the ridge-offset intersections.

- At locked transforms, oblique normal faults trending up to 60° oblique to the ridge axis are predicted at the inside corners of ridge-transform intersections.

- Finite width offsets having the same strength as the adjacent ridge segments behave as locked transform faults. At ridge-transform intersections the angle of stress rotation relative to the ridge trend decreases with decreasing offset strength. Also, the weaker the offset the more ridge parallel the stresses within the offset become.

- Tensile stresses at locked non-transform offsets trend at 35° – 50° oblique to the ridge axis. Failure in extension along the offset may occur at an average trend of 45° oblique to the ridge axis.

8.1.4 Dynamics of Easter microplate

The dynamics of Easter microplate are investigated using the condition of mechanical equilibrium. The forces assumed in the torque balance are: (1) unknown boundary forces along the East and West Rifts, (2) a resisting mantle basal drag, acting about the centre of rotation of the microplate in an anticlockwise direction, and (3) unknown boundary forces along the northern and southern boundaries. To constrain the distribution of the driving and resisting boundary forces, the stress field resultant from the modelling is compared with the indicators of stress orientations at Easter microplate. To constrain the magnitude of the driving forces, the stress magnitudes in the models are compared with estimates of the strength of the lithosphere in the microplate and adjacent Nazca plate. The most important results of the modelling are:

- The Schouten et al. (1993) roller-bearing model is not compatible with the stress indicators at Easter microplate, unless the drag of the main plates pro-

duces simultaneously shear driving forces and normal resisting forces along the northern and southern boundaries of the microplate, which seems unlikely.

- An increasing ridge resistance towards the rift tips produces a clockwise torque on the microplate, and provides a driving mechanism alternative to the Schouten et al. hypothesis.

- The model that best fits the earthquake focal mechanism evidence in the northern part of the microplate and adjacent Nazca plate includes: (1) a driving force distribution along the East and West Rifts, with tensile stresses increasing towards the rift tips, (2) a mantle basal drag contributing with 20% (or less) to the total resisting torque, and (3) northern and southern boundaries locked in both directions, and contributing with 80% (or more) to the total resisting torque.

- The model that best fits the evidence of compressional failure in the Nazca plate to the north of Easter includes: (1) a driving force distribution along the East and West Rifts, with maximum tensile stresses of 60 MPa at rift tips, (2) a mantle basal drag computed for an asthenosphere viscosity of 1.0×10^{18}Pa s, and (3) northern and southern boundaries offering no resistance to shear displacement, but locked in the normal direction away from the rift tips.

- The minimum brittle thickness at the tips of the East and West Rifts must be in the range of 3-4 km (which is twice the brittle layer thickness characteristic of the East Pacific Rise), to be consistent with the occurrence of compressional failure in the north of Easter microplate and adjacent Nazca plate.

- The limit of 20% on the contribution of the mantle basal drag to the total resisting torque places constraints on the value of the asthenosphere viscosity. If the brittle thickness at the rift tips is 4 km, then the asthenosphere viscosity has an upper bound of 2.0×10^{18}Pa s.

8.2 The strength of the lithosphere

The rheology and the strength, which determine the mode of deformation in the lithosphere, are mainly controlled by the lithospheric temperature structure (e.g. Kusznir and Park, 1982). The temperature distribution at mid-ocean ridges depends fundamentally on the processes of crustal accretion, especially on the balance between the heat of crustal emplacement and the hydrothermal cooling resulting from the penetration of seawater through fissures and faults (Phipps Morgan and Chen, 1993).

The time averaged heat supply at fast spreading ridges is larger than at slow spreading ridges, because a larger volume of melt per unit of time is emplaced. This results in a higher thermal regime with shallower isotherms at fast than at slow spreading ridges. Furthermore, because the accretion process is relatively continuous at fast spreading rates (e.g. evidence of long-lived magma chambers continuous along the EPR), and both spatially and temporarily discontinuous at slow spreading rates (e.g. evidence of alternating periods of magmatic and amagmatic extension, and of three-dimensional mantle upwelling), variations in the thermal regime are expected to be larger at slow than at fast spreading ridges.

Variations in the thermal regime cause variations in the brittle thickness, and are the main cause of variations in the lithospheric strength at mid-ocean ridges. Because the ductile lower lithosphere withstands very small deviatoric stress, its contribution to the overall strength can be neglected.

Previous studies have shown that differences in the strength of the axial lithosphere, and in the rate of thickening of the plates, can explain the differences in axial morphology between fast and slow spreading ridges (e.g. Chen and Morgan, 1990; Eberle et al., 1998). In this study I have shown that variations in the brittle thickness and associated lithospheric strength can explain the differences in the fault throw observed between fast and slow spreading ridges, and between segment centres and segment ends of slow spreading ridges. No ductile lower crust is required to exist (Shaw and Lin, 1996) nor weakening effects of serpentinites on the frictional

strength of the fault are needed (Escartin et al., 1998). Instead, a single-layer elasto-plastic rheological model and a frictionless fault are able to predict the fault throw observations.

The lithospheric strength at the ridge axis can be identified with the ridge resistance (i.e. the tensile deviatoric stress resisting plate separation, integrated over the depth of the lithosphere). Previous studies at ridge-transform intersections and non-transform offsets, as well as my own, have shown that depending on the frictional strength along the offset, variations in the ridge resistance cause variations in the degree of obliquity of extensional structures relative to the ridge axis. The ratio between the ridge resistance and the transform resistance is also thought to control the geometry of non-transform offsets (Grindlay and Fox, 1993). Moreover, variations in the ridge resistance caused by variations in the magmatic input to ridges may determine the stability of such small offsets.

The unstable nature of non-transform offsets is inferred from their often observed evolving geometry and along-axis migration (e.g. Macdonald et al., 1988; Grindlay et al., 1991). Although several mechanisms have been proposed to explain rift propagation and along-axis migration of second-order ridge offsets (e.g. concentration of gravity spreading stresses at the rift tips (Phipps Morgan and Parmentier, 1985), relation between crack length and crack propagation driving force (Sempere and Macdonald, 1986), changes in the spreading direction (Searle and Hey, 1983), and the relative motion between mid-ocean ridges and the underlying, fixed asthenosphere (Schouten et al., 1987), the most robust hypothesis attributes the cause of rift propagation to sustained periods of high melt supply at mid-ocean ridges (Cormier et al., 1996). Long periods of high melt supply are expected to reduce the strength of the lithosphere and favour the overshooting of dykes beyond the rift tips. They are also expected to produce an inflated bathymetry, leading to gravity spreading stresses.

8.3 The origin of Easter microplate

The proximity of a hotspot to a mid-ocean ridge and the lateral migration of a spreading system over anomalously hot asthenosphere are two potential sources of increased melt supply. Fast propagating rifts in the region just north of Easter microplate (between 16°S and 19°S) have been attributed to the westward migration of the East Pacific Rise over the anomalously hot asthenosphere (Cormier et al., 1996). The modelling in chapter 4 suggests that this has not been the cause of the northward migration of the East Rift, which initiated the formation of Easter microplate (Rusby and Searle, 1995). Thus, if ridges propagate into the most stressed region, or away from the shallower segments, then rift propagation should first occur into the Pacific plate, and not into the Nazca plate as the northwards propagation of the East Rift implies.

So, at Easter microplate the influence of the nearby Easter hotspot is probably greater than the influence of the asthenospheric temperature gradient beneath the western flank of the rise. Geological, geochemical and geochronological data suggest that the Easter hotspot lies close to Easter island, just 350 km east of the microplate southern boundary (Haase et al., 1996). Isotopic data for lavas from the Easter seamount chain and geochemical data for basalts dredged from the East Rift provide evidence for a bi-directional mantle flow between the microplate spreading axis and the plume (e.g. Schilling et al., 1985; Haase et al., 1996).

At present, a high melt supply to the East Pacific Rise due to Easter hotspot, is indicated by the shallow and inflated bathymetry of the spreading segments south of Easter microplate. In this region, rift propagation since 1.5 Ma has resulted in a large Overlapping Spreading Centre (120 km × 120 km) at 29°S, which may be an incipient microplate (Hey et al., 1995).

The influence of Easter hotspot on the origin of Easter microplate is however not clear. Bird and Naar (1994) suggested that a change in plate motions at 5.6 Ma ago triggered the propagation of rifts from within large left-stepping transform faults, initiating the formation of both Easter and Juan Fernandez microplates. Changes

in the regional stress field may also explain the origin of other microplates and palaeoplates formed at mid-ocean ridge offsets away from hotspots.

Several microplates and palaeoplates occur or have formed at triple junctions (e.g. the Juan Fernandez microplate (Herron, 1972; Forsyth, 1972), and the Chinook palaeoplate (Mammerickx and Sharman, 1988)). A recent model of triple junction evolution, based mainly on observations at the Pacific-Antartic-Nazca triple junction, proposes that microplate formation and subsequent accretion to larger plates can be a stage of triple junction migration, which progresses by repeated episodes of rift propagation (Bird et al., 1999).

Independently of the microplate tectonic setting, microplates always form by rift propagation in regions of weakness and high melt supply (either due to the fast spreading rate environment, the proximity of a hotspot or the junction of spreading centres). Further investigation on the mechanics of rift propagation and mid-ocean ridge offset migration is needed to determine the origin of microplates. This is at present one of the most challenging problems on mid-ocean ridge dynamics.

8.4 Further work

8.4.1 The dynamics of other microplates

A project for further research directly following from this study is the investigation of the dynamics of other active microplates, such as the Galapagos and Juan Fernandez microplates. This investigation is needed to check if the principles underlying the new dynamic model proposed for Easter are valid for microplates in general. The project involves the compilation of the stress indicators at these other microplates, and the computation of the plate strength estimates compatible with the observations.

Although the Juan Fernandez microplate has a deforming SE boundary which Easter does not (Kleinrock and Bird, 1994), the Easter and the Juan Fernandez

microplates share many points in common, including a similar geometry, tectonic pattern, and history of evolution (Searle et al., 1993). So, the dynamic model for the Juan Fernandez microplate is expected to be analogous to that of Easter microplate. In contrast, the Galapagos microplate has few points of similarity with the Easter and Juan Fernandez microplates. It is younger (its age is 1 Ma), smaller (its dimensions are $13,000$ km^2), and apparently rotates at a much slower rate (its rotation rate has been estimated to be $6°$/Ma) (Lonsdale, 1988). Also, it is bounded by three spreading arms, instead of just two, and its geometry is rather complex (Fig. 8.1).

These differences imply substantial modifications to the dynamic model that has been proposed in this study. Nevertheless, the forces involved in the torque balance should be the same (driving forces along the bounding ridges, resisting mantle basal drag, and normal and shear forces along other boundaries). It is interesting to determine the torque ratios associated with these forces, and to investigate what constraints they can place on the asthenosphere viscosity and brittle layer thickness in the region of the Galapagos microplate.

If the attempt of producing a dynamic model consistent with the stress indicators fails, it may be that the assumption of internal rigidity is not verified at the Galapagos microplate. This possibility needs to be considered because observational data at the Galapagos microplate does not entirely support the roller-bearing kinematic model (Schouten et al., 1993).

The methodology used to study microplates can be applied at other locations of plate boundary reorganisations, such as triple junctions. Investigation of the dynamics of areas bounded by ridges and transforms, at the Bouvet (McKenzie and Morgan, 1969) and the Azores (Krause and Watkins, 1970) triple junctions for instance, can help to better constrain the local plate boundary forces. Particular attention should be given to possible variations of the ridge resistance along spreading centres, in order to further understand their role on the dynamics of the young oceanic lithosphere.

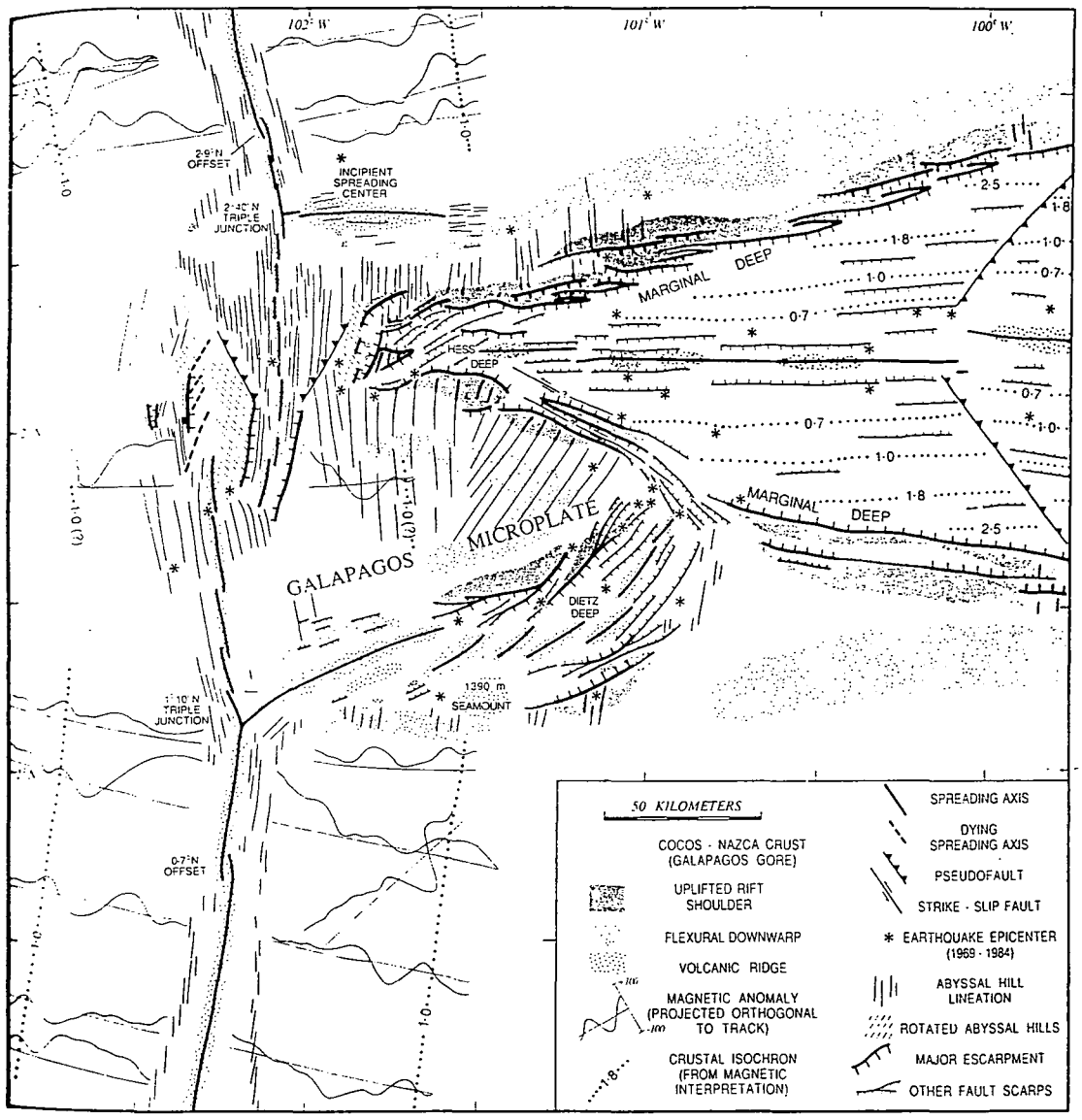

Fig. 8.1 Tectonic sketch map of the Galapagos microplate and surrounding region, based on interpretation of Sea Beam, GLORIA and other data. Earthquakes are teleseismically recorded events located by the International Seismological Center (after Lonsdale, 1988).

8.4.2 The origin of microplates

To investigate the origin of microplates we need first to develop a methodology capable of simulating rift propagation. Numerical models of rift propagation have first been developed by Pollard and Aydin (1984). Using a boundary element method and considering cracks as analogues to ridge segments, they calculated the shear stresses developed at ridge offsets in response to applied plate boundary forces (ridge push, and ridge resistance).

Since then considerable advances have been made in the understanding of the mechanisms of rift propagation. A recent study recognises that in addition to gravity spreading stresses at rift tips, asthenospheric along-axis flow can also provide a driving force for rift propagation (West et al., 1999). Furthermore, it indicates that the depression at the rift tip is isostatically balanced by crustal thinning, rather than maintained by the viscous resistance to asthenospheric flow. New numerical models of rift propagation should therefore include topographic loading, asthenospheric shear stresses at the base of the lithosphere, and a changing strength along the rift due to changes in lithospheric thickness.

Once these models are developed and tested against observed pattern of actual ridge propagation, they can be applied to study the origin of microplates. The local factors that determine the onset of microplate formation can be found by changing the variables of the model (the plate strength, the topographic loading and the mantle basal shear stresses) as a function of the tectonic setting. The importance of these local factors can then be compared with the effect of changes in the far field regional stress resulting from changes in the plate motions.

8.5 Conclusions

In this thesis a strong emphasis has been put on the role exerted by the ridge resistance on the stress field at mid-ocean ridges and their offsets. Estimates of the ridge resistance at mid- ocean ridges are often based on the conduit model of

Lachenbruch (1973), or on numerical modelling efforts that use morphological and structural observations at mid-ocean ridges to estimate the model parameters (e.g. Sleep and Rosendahl, 1979). Here the ridge resistance is regarded as the tensile strength of the lithosphere at the ridge axis. The derivation of an oceanic strength envelope leads to estimates of the ridge resistance as a function of the brittle plate thickness, and this is one of the main contributions of this work. Values of the brittle layer thickness at the ridge axis ranging from 1 to 8 km correspond to values of the ridge resistance, averaged over the layer thickness, ranging from 7.5 MPa to 60 MPa. From this range, lower bounds occur at segment centres of fast spreading ridges, and upper bounds occur at segment ends of slow spreading ridges.

The role of plasticity on the evolution of normal faulting at mid-ocean ridges has been investigated for the first time. Plastic failure reduces the equivalent elastic plate thickness, sharpens the plate curvature, and reduces the width of the half-graben. It does not significantly modify the fault throw, but places a limit on the maximum fault throw that can be achieved. As a consequence, plasticity prevents the achievement of large fault throws at fast spreading ridges. Variations in the strength caused entirely by variations in the brittle layer thickness can account for the variations in the observed character of mid- ocean ridge faulting.

Previous stress modelling efforts had already recognised that the ratio between the ridge resistance and the transform resistance determines the geometry and the structural pattern of mid-ocean ridge offsets (Phipps Morgan and Parmentier, 1984; Grindlay and Fox, 1993). This study has confirmed that the greater the resistance to shear displacement along the offset the greater the obliquity of normal faults relative to the ridge trend. Its new contribution is the demonstration that extensional structures at high angles ($> 35°$) to ridge trends, often observed at ridge-transform intersections and non-transform offsets, can be explained by the rotation of ridge parallel tensile stresses. Also, previous studies at mid-ocean ridge offsets have overlooked the importance of the topographic loading created by the elevation of mid-ocean ridges relative to old seafloor. In contrast, this thesis proposes that this topographic loading is a source of significant ridge parallel tensile stresses, and

shows how it can be incorporated into 2D horizontal models.

Finally and most importantly this thesis proposes the first dynamic model for Easter microplate. Variations in the brittle thickness, associated with variations in the spreading velocity, cause variations in the ridge resistance along the bounding rifts of the microplate. These variations in the ridge resistance produce a driving torque on the microplate, which is opposed by the mantle basal drag and by resisting forces along the northern and southern boundaries. The role of the mantle basal drag is small, so the asthenosphere viscosity beneath the microplate is estimated to be approximately 1×10^{18} Pa s. The boundary conditions along the northern boundary change with time, in order to fit both the earthquake focal mechanisms and the evidence of compressional failure to the north of the microplate. However, normal resistances in the direction perpendicular to the northern boundary, away from rift tips, are required at all times. These normal resistances are difficult to reconcile with the microplate driving mechanism proposed by Schouten et al. (1993), i.e. with shear driving forces along the northern and southern boundaries.

Naturally, it remains to be investigated whether the new model proposed for Easter microplate is applicable to other microplates. Nevertheless, it is clear that the contribution of the variations of the ridge resistance to the dynamics of ridge overlap systems needs to be considered from now on.

References

Anderson, E.M., 1951, The dynamics of faulting and dyke formation with applications to Britain. Oliver and Boyd, Edinburgh, pp.206

Anderson, R.N., D.W. Forsyth, P. Molnar and J. Mammerickx, 1974, Fault plane solutions of earthquakes on the Nazca plate boundaries and the Easter plate. *Earth Planet. Sci. Lett.*, vol. 24, p.188-202.

Appelgate, B. and A.N. Shor, 1994, The northern Mid-Atlantic and Reykjanes Ridges: spreading center morphology between 55°50′N and 63°00′N. *J. geophys. Res.*, vol. 99, no. B9, p.17935-17956.

Artyushkov, E.V., 1973, Stresses in the lithosphere caused by crustal thickness inhomogeneities. *J. geophys. Res.*, vol. 78, no. 32, p.7675-7708.

Bergman, E.A. and S.C. Solomon, 1984, Source mechanisms of earthquakes near mid-ocean ridges from body waveform inversion: Implications for the early evolution of oceanic lithosphere. *J. geophys. Res.*, vol. 89, no. B13, p.11415-11441.

Bicknell, J.D., J.-C. Sempere and K.C. Macdonald, 1987, Tectonics of a fast spreading center: A Deep-Tow and Sea Beam survey on the East Pacific Rise at 19°30′S. *Mar. geophys. Res.*, vol. 9, p.25-45.

Bird, R.T. and D.F. Naar, 1994, Intratransform origins of mid-ocean ridge microplates. *Geology*, vol. 22, p.987-990.

Bird, R.T., S.F. Tebbens, M.C. Kleinrock and D.F. Naar, 1999, Episodic triple-junction migration by rift propagation and microplates. *Geology*, vol. 27, p.911-914.

Blackman, D.K., 1997, Variation in lithospheric stress along ridge- transform plate boundaries. *Geophys. Res. Lett.*, vol. 24, no.4, p.461- 464.

Bodine, J.H. and A.B. Watts, 1979, On lithospheric flexure seaward of the Bonin and Mariana trenches. *Earth Planet. Sci. Lett.*, vol. 43, p.132-148.

Bodine, J.H., M.S. Steckler and A.B. Watts, 1981, Observations of flexure and the rheology of the oceanic lithosphere. *J. geophys. Res.*, vol. 86, no. B5, p.3695-3707.

Bott, M.H.P., 1982, The interior of the Earth: Its structure, constitution and evolution. Edward Arnold, London, pp.403.

Bott, M.H.P. and N.J. Kusznir, 1984, The origin of tectonic stress in the lithosphere. *Tectonophysics*, vol. 105, p.1-13.

Bott, M.H.P., 1991, Ridge push and associated plate interior stress in normal and hot spot regions. *Tectonophysics*, vol. 200, p.17-32.

Bott, M.H.P., 1996, Flexure associated with planar faulting. *Geophys. J. Int.*, vol. 126, P.F21-F24.

Bott, M.H.P., 1997, Modeling the formation of a half graben using realistic upper crustal rheology. *J. geophys. Res.*, vol. 102, no. B11, p.24605-24617.

Brace, W.F. and D.L. Kohlstedt, 1980, Limits on lithospheric stress imposed by laboratory experiments. *J. geophys. Res.*, vol. 85, no. B11, p.6248-6252.

Brune, J.N., T.L. Henyey and R.F. Roy, 1969, Heat flow, stress, and rate of slip along the San Andreas Fault. *J. geophys. Res.*, vol. 74, p.3821-3827.

Buck, W.R. and E.M. Parmentier, 1986, Convection beneath young oceanic lithopshere: Implications for thermal structure and gravity. *J. geophys. Res.*, vol. 91, no. B2,p.1961-1974.

Buck, W.R., 1988, Flexural rotation of normal faults. *Tectonics*, vol. 7, no. 5, p.959-973.

Byerlee, J., 1978, Friction of rocks. *Pure and applied geophys.*, vol. 116, p.615-626.

Carbotte, S.M. and K.C. Macdonald, 1994, Comparison of seafloor tectonic fabric at intermediate, fast, and super fast spreading ridges: Influence of spreading rate, plate motions, and ridge segmentation on fault patterns. *J. geophys. Res.*, vol. 99, no. B7, p.13609-13631.

Cessaro, R.K. and D.M. Hussong, 1986, Transform seismicity at the intersection of the Oceanographer fracture zone and the Mid-Atlantic Ridge. *J. geophys. Res.*, vol. 91, no. B5, p.4839-4853.

Chen, Y. and W.J. Morgan, 1990, A non-linear rheology model for mid-ocean ridge axis topography. *J. geophys. Res.*, vol. 95, no. B11, p.17583-17604.

Cloetingh, S. and R. Wortel, 1986, Stress in the Indo-Australian plate. *Tectonophysics*, vol. 132, p.49-67.

Cochran, J.R., 1986, Variations in subsidence rates along intermediate and fast spreading mid-ocean ridges. *Geophys. J. R. astr. Soc.*, vol. 87, p.421-454.

Collette, B.J., 1974, Thermal contraction joints in a spreading seafloor as origin of fracture zones. *Nature*, vol. 251, p.299-300.

Conte, S.D. and C. de Boor, 1981, Elementary numerical analysis. An algorithmic approach. McGraw-Hill, Int. Ser., pp.432.

Cormier, M.-H. and K.C. Macdonald, 1994, East Pacific Rise 18° – 19°S: Asymmetric spreading and ridge reorientation by ultrafast migration of axial discontinuities. *J. geophys. Res.*, vol. 99, no. B1, p.543-564.

Cormier, M.-H., K.C. Macdonald and D.S. Wilson, 1995, A three-dimensional gravity analysis of the East Pacific Rise from 18° to 21°30′S. *J. geophys. Res.*, vol. 100, no. B5, p.8063-8082.

Cormier, M.-H., D.S. Scheirer and K.C. Macdonald, 1996, Evolution of the East Pacific Rise at 16°-19° S since 5 Ma: Bisection of overlapping spreading centers by new, rapidly propagating ridge segments. *Mar. geophys. Res.*, vol. 18, p.53-84.

Courtillot, V., A. Galdeano and J.L. Le Mouel, 1980, Propagation of an accreting plate boundary: A discussion of new aeromagnetic data in the Gulf of Tadjurah and southern Afar. *Earth Planet. Sci. Lett.*, vol. 47, p.144-160.

Crane, K., 1976, The intersection of the Siqueiros transform fault and the East Pacific Rise. *Marine Geology*, vol. 21, p.25-46.

Cowie, P.A., C.H. Scholz, M. Edwards and A. Malinverno, 1993, Fault strain and seismic coupling on mid-ocean ridges. *J. geophys. Res.*, vol. 98, no. B10, p.17911-17920.

Dahlen, F.A., 1981, Isostasy and the ambient state of stress in the oceanic lithosphere. *J. geophys. Res.*, vol. 86, no. B9, p.7801-7807.

Davis, E.E. and C.R.B. Lister, 1974, Fundamentals of ridge crest topography. *Earth Planet. Sci. Lett.*, vol. 21, p.405-413.

Detrick, R.S., P. Buhl, E. Vera, J. Mutter, J. Orcutt, J. Madsen and T. Brocher, 1987, Multi-channel seismic imaging of a crustal magma chamber along the East Pacific Rise. *Nature*, vol. 326, p.35-41.

Dziewonski A.M. and D.L. Anderson, 1981, Preliminary reference Earth model. *Phys. Earth Planet. Inter.*, vol. 25, p.297-356.

Dziewonski A.M. and J.H. Woodhouse, 1983, An experiment in systematic study of global seismicity: Centroid-moment tensor solutions for 201 moderate and large earthquakes of 1981. *J. geophys. Res.*, vol. 88, no. B4, p.3247-3271.

Eberle, M.A., D.W. Forsyth and E.M. Parmentier, 1998, Constraints on a buoyant model for the formation of the axial topographic high on the East Pacific Rise. *J. geophys. Res.*, vol. 103, no. B6, p.12291-12307.

Eberle, M.A. and D.W. Forsyth, 1998, An alternative, dynamic model of the axial topographic high at fast spreading ridges. *J. geophys. Res.*, vol. 103, no. B6, p.12309-12320.

Engeln, J.F. and S. Stein, 1984, Tectonics of the Easter plate. *Earth Planet. Sci. Lett.*, vol. 68, p.259-270.

Engeln, J.F., S. Stein, J. Werner and R.G. Gordon, 1988, Microplate and shear zone models for oceanic spreading center reorganizations. *J. geophys. Res.*, vol. 93, no. B4, p.2839-2856.

Escartin, J., G. Hirth and B. Evans, 1997, Effects of serpentinization on the lithospheric strength and the style of normal faulting at slow-spreading ridges. *Earth Planet. Sci. Lett.*, vol. 151, p.181-189.

Escartin, J., P.A. Cowie, R.C. Searle, S. Allerton, N.C. Mitchell, C.J. MacLeod and A.P. Slootweg, 1999, Quantifying tectonic strain and magmatic accretion at a slow spreading ridge segment, Mid-Atlantic Ridge, 29°N. *J. geophys. Res.*, vol. 104, no. B5, p.10421-10437.

Fagan, M.J., 1992, Finite element analysis: Theory and practice. Harlow: Longman Scientific and Technical, New York.

Fleitout, L. and C. Froidevaux, 1982, Tectonics and topography for a lithosphere containing density heterogeneities. *Tectonics*, vol. 1, no. 1, p.21-56.

Fleitout, L. and C. Froidevaux, 1983, Tectonic stresses in the lithosphere. *Tectonics*, vol. 2, no. 3, p.315-324.

Fornari, D.J., D.G. Gallo, M.H. Edwards, J.A. Madsen, M.R. Perfit and A.N. Shor, 1989, Structure and topography of the Siqueiros transform fault system: Evidence for the development of intra-transform spreading centers. *Mar. geophys. Res.*, vol. 11, p.263-299.

Forsyth, D.W., 1972, Mechanisms of earthquakes and plate motions in the East Pacific. *Earth Planet. Sci. Lett.*, vol. 17, p.189-193.

Forsyth, D. and S. Uyeda, 1975, On the relative importance of the driving forces of plate motion. *Geophys. J. R. astr. Soc.*, vol. 43, p.163-200.

Forsyth, D.W., 1992, Finite extension and low-angle normal faulting. *Geology*, vol. 20, p.27-30.

Fowler, C.M.R., 1990, The solid Earth. An introduction to global geophysics. *Cambridge University Press*, pp.472.

Fox, P.J. and D.G. Gallo, 1984, A tectonic model for ridge-transform-ridge plate boundaries: Implications for the structure of oceanic lithosphere. *Tectonophysics*, vol. 104, p.205-242.

Fox, P.J. and D.G. Gallo, 1986, The geology of North Atlantic transform plate boundaries and their aseismic extensions. In: *The geology of North America*, vol. M., The western north Atlantic region, P.R. Vogt and B.E. Tucholke, eds., Geol. Soc. Am., p.157-172.

Francheteau, J., A. Yelles-Chaouche and H. Craig, 1987, The Juan Fernandez microplate north of the Pacific-Nazca-Antartic junction at 35° S. *Earth Planet. Sci. Lett.*, vol. 86, p.253-268.

Francheteau, J., P. Patriat, J. Segoufin, R. Armijo, M. Doucoure, A. Yelles-Chaouche, J. Zukin, S. Calmant, D.F. Naar and R.C. Searle, 1988, Pito and Orongo fracture zones: the northern and southern boundaries of the Easter microplate (southeast Pacific). *Earth Planet. Sci. Lett.*, vol. 89, p.363-374.

Fujita, K. and N.H. Sleep, 1978, Membrane stresses near mid-ocean ridge-transform intersections. *Tectonophysics*, vol. 50, p.207-221.

Gallo, D.G., P.J. Fox and K.C. Macdonald, 1986, A Sea Beam investigation of the Clipperton transform fault: The morphotectonic expression of a fast slipping transform boundary. *J. geophys. Res.*, vol. 91, no. B3, p.3455-3467.

Goetze, C. and B. Evans, 1979, Stress and temperature in the bending lithosphere as constrained by experimental rock mechanics. *Geophys. J. R. astr. Soc.*, vol. 59, p.463-478.

Goodman, R.E., R.L. Taylor and T.L. Brekke, 1968, A model for the mechanics of jointed rock. *J. Soil Mech. Found. Div. Am. Soc. Civ. Eng.*, vol. 94, p.637-658.

Grindlay, N.R., P.J. Fox and K.C. Macdonald, 1991, Second-order ridge axis discontinuities in the South Atlantic: Morphology, structure and evolution. *Mar. geophys. Res.*, vol. 13, p.21-49.

Grindlay, N.R. and P.J. Fox, 1993, Lithospheric stresses associated with nontransform offsets of the Mid-Atlantic Ridge: Implications from a finite element analysis. *Tectonics*, vol. 12, no. 4, p.982-1003.

Gudmundsson, A., 1995, Stress field associated with oceanic transform faults. *Earth Planet. Sci. Lett.*, vol. 136, p.603-614.

Haase, K.M., C.W. Devey and S.L. Goldstein, 1996, Two-way exchange between the Easter mantle plume and the Easter microplate spreading axis. *Nature*, vol. 382, p.344-346.

Hager, B.H., R.W. Clayton, M.A. Richards, R.P. Comer and A.M. Dziewonski, 1985, Lower mantle heterogeneity , dynamic topography and the geoid. *Nature*, vol. 313, p.541-546.

Hager, B.H., 1991, Mantle viscosity: a comparison of models from post-glacial rebound and from geoid, plate driving forces and advected heat flux. In: Glacial isostasy, sealevel and mantle rheology, Sabadini R., K. Lambeck and E. Boschi, eds., Kluwer, Dordrecht.

Handschumacher, D.W., R.H. Pilger, J.A. Foreman and J.F. Campbell, 1981, Structure and evolution of the Easter microplate. *Mem. Geol. Soc. Am.*, vol. 154, p.63-76.

Herron, E.M., 1972, Two small crustal plates in the South Pacific near Easter Island. *Nature Phys. Sci.*,Vol. 240, p.35-37.

Hey, R.N., F.K. Duennebier and W.J. Morgan, 1980, Propagating rifts on midocean ridges. *J. geophys. Res.*, vol. 85, no. B7, p.3647-3658.

Hey, R.N., D.F. Naar, M.C. Kleinrock, W.J. Phipps Morgan, E. Morales and J.-G. Schilling, 1985, Microplate tectonics along a superfast seafloor spreading system near Easter island. *Nature*, Vol. 317, p.320-325.

Hey, R.N., J.M. Sinton and F.K. Duennebier, 1989, Propagating rifts and spreading centers. In: *The geology of North America*, vol. N, The eastern Pacific ocean and Hawaii, E.L. Winterer, D.M. Hussong and R.W. Decker, eds., Geol. Soc. Am., p.161-176.

Hey, R.N., P.D. Johnson, F. Martinez, J. Korenaga, M.L. Somers, Q.J. Huggett, T.P. LeBas, R.I. Rusby and D.F. Naar, 1995, Plate boundary reorganization at a large-offset, rapidly propagating rift. *Nature*, Vol. 378, p.167-170.

Hickman, S.H., 1991, Stress in the lithosphere and the strength of active faults. *Reviews geophys.*, supplement, p.759-775.

Hirth, G. and D.L. Kohlstedt, 1996, Water in the oceanic upper mantle: implications for rheology, melt extraction and the evolution of the lithosphere. *Earth Planet. Sci. Lett.*, vol. 144, p.93- 108.

Hirth, G., J. Escartin and J. Lin, 1998, The rheology of the lower oceanic crust: Implications for lithospheric deformation at mid-ocean ridges. In: Faulting and magmatism at mid-ocean ridges, R. Buck et al., eds., *AGU Monogr.*, p.291-303.

Huang, P.Y. and S.C. Solomon, 1988, Centroid depths of mid-ocean ridge earthquakes: Dependence on spreading rate. *J. geophys. Res.*, vol. 93, no. B11, p.13445-13477.

Hubbert, M.K. and W.W. Rubey, 1959, Role of fluid pressure in mechanics of overthrust faulting I. Mechanics of fluid-filled porous solids and its application to overthrust faulting. *Bull. Geol. Soc. Am.*, vol. 70, p.115-166.

Jaeger, J.C., 1969, Elasticity, fracture and flow, with engineering and geological applications. Methuen & Co. Ltd, pp.268.

Karato, S., 1986, Does partial melting reduce the creep strength of the upper mantle? *Nature*, vol. 319, p.309-310.

Karson, J.A. and H.J.B. Dick, 1983, Tectonics of ridge-transform intersections at the Kane fracture-zone. *Mar. geophys. Res.*, vol. 6, p.51-98.

Karson, J.A., 1990, Seafloor spreading on the Mid-Atlantic Ridge: Implications for the structure of ophiolites and oceanic lithosphere produced in slow-spreading environments. In: Ophiolites oceanic crustal analogues, Malpas J., E. M. Moores, A. Panayiotou and C. Xenophontos, eds., *Proceedings of the symposium TROODOS 1987*, Geological Survey Department, Nicosia, Cyprus, p.547-555.

Kastens, K.A., W.B.F. Ryan and P.J. Fox, 1986, Structural and volcanic expression of a fast slipping ridge-transform-ridge-plate boundary: Sea MARC I and photographic surveys at the Clipperton transform fault. *J. geophys. Res.*, vol. 91, no. B3, p.3469-3488.

Kearey, P. and F.J. Vine, 1996, Global tectonics. Blackwell Science, pp.333.

Kent, G.M., A.J. Harding, J.A. Orcutt, R.S. Detrick, J.C. Mutter and P. Buhl, 1994, Uniform accretion of oceanic crust south of the Garret transform at 14°15′S on the East Pacific Rise. *J. geophys. Res.*, vol. 99, no. B5, p.9097-9116.

Kirby, S.H., 1980, Tectonic stresses in the lithosphere: Constraints provided by the experimental deformation of rocks. *J. geophys. Res.*, vol. 85, no. B11, p.6353-6363.

Kirby, S.H., 1983, Rheology of the lithosphere. *Rev. geophys. spac. phys.*, vol. 21, no. 6, p.1458-1487.

Kleinrock, M.C. and R.T. Bird, 1994, Southeastern boundary of the Juan Fernandez microplate: Braking microplate rotation and deforming the Antarctic plate. *J. geophys. Res.*, vol. 99, no. B5, p.9237-9261.

Kohlstedt, D.L., 1992, Structure, rheology and permeability of partially molten rock at low melt fractions. In: Mantle flow and melt generation at mid-ocean ridges, J. Phipps Morgan et al., eds., *AGU Monogr.*, no. 71, p.103-121.

Kong, L.S.L., S.C. Solomon and G.M. Purdy, 1992, Microearthquake characteristics of a mid-ocean ridge along-axis high. *J. geophys. Res.*, vol. 97, no. B2, p.1659-1685.

Krause, D.C. and N.D. Watkins, 1970, North Atlantic crustal genesis in the vicinity of Azores. *Geophys. J. R. astr. Soc.*, vol. 19, p.261-283.

Kuo, B.Y. and D.W. Forsyth, 1988, Gravity anomalies of the ridge-transform system in the South Atlantic between 31° and 34.5°S: Upwelling centers and variations in crustal thickness. *Mar. geophys. Res.*, vol. 10, p.205-232.

Kusznir, N.J. and M.H.P. Bott, 1977, Stress concentration in the upper lithosphere caused by underlying visco-elastic creep. *Tectonophysics*, vol. 43, p.247-256.

Kusznir, N.J. and R.G. Park, 1982, Intraplate lithosphere strength and heat flow. *Nature*, vol. 299, p.540-542.

Kusznir, N.J., G. Marsden and S.S. Egan, 1991, A flexural-cantilever simple-shear/pure-shear model of continental lithosphere extension: applications to the Jeanne d'Arc Basin, Grand Banks and Viking Graben, North Sea. In: The geometry of normal faults, Roberts, A.M., G. Yielding and B. Freeman, eds., *Geol. Soc. Spec. Publ.*, no. 56, p.41-60.

Kusznir, N.J., 1991, The distribution of stress with depth in the lithosphere: thermo-rheological and geodynamic constraints. *Phil. Trans. R. Soc. Lond. A*, vol. 337, p.95-110.

Lachenbruch, A.H. and G.A. Thompson, 1972, Oceanic ridges and transform faults: their intersection angles and resistance to plate motion. *Earth Planet. Sci. Lett.*, vol. 15, p.116-122.

Lachenbruch, A.H., 1973, A simple mechanical model for oceanic spreading centers. *J. geophys. Res.*, vol. 78, no. 17, p.3395-3417.

Lachenbruch, A.H. and J.H. Sass, 1981, Corrections to 'Heat flow and energetics of the San Andreas fault zone' and some additional comments on the relation between fault friction and observed heat flow. *J. geophys. Res.*, vol. 86, p.7171-7172.

Lanczos, 1970, The variational principles of mechanics. Dover Publications, New York, pp.418.

Larson, R.L., R.C. Searle, M.C. Kleinrock, H. Schouten, R.T. Bird, D.F. Naar, R.I. Rusby, E.E. Hooft and H. Lasthiotakis, 1992, Roller-bearing tectonic evolution of the Juan Fernandez microplate. *Nature*, vol. 356, 571-576.

Leeds, A.R., L. Knopoff and E.G. Kausel, 1974, Variations of upper mantle structure under the Pacific Ocean. *Science*, vol. 186, p.141-143.

Liggett, J.A., 1994, Fluid mechanics. McGraw-Hill, pp.495.

Lilwall, R.C. and R.E. Kirk, 1985, Ocean-bottom seismograph observations on the Charlie-Gibbs fracture zone. *Geophys. J. R. astr. Soc.*, vol. 80, p.195-208.

Lin, J. and E.M. Parmentier, 1989, Mechanisms of lithospheric extension at mid-ocean ridges. *Geophys. J.*, vol. 96, p.1-22.

Lin, J., G.M. Purdy, H. Schouten, J.-C. Sempere and C. Zervas, 1990, Evidence from gravity data for focused magmatic accretion along the Mid-Atlantic Ridge. *Nature*, vol. 344, p.627-632.

Lin, J. and J. Phipps Morgan, 1992, The spreading rate dependence of three-dimensional mid-ocean ridge gravity structure. *Geophys. Res. Lett.*, vol. 19, no.1, p.13-16.

Lister, C.R.B., 1975, Gravitational drive on oceanic plates caused by thermal contraction. *Nature*, vol. 257, p.663-665.

Lonsdale, P., 1978, Near-bottom reconnaissance of a fast-slipping transform fault zone at the Pacific-Nazca plate boundary. *Journal of Geology*, vol. 86, p.451-472.

Lonsdale, P., 1988, Structural pattern of the Galapagos microplate and evolution of the Galapagos triple junctions. *J. geophys. Res.*, vol. 93, no. B11, p.13551-13574.

Macdonald, K.C., K. Kastens, F.N. Spiess and S.P. Miller, 1979, Deep tow studies of the Tamayo transform fault. *Mar. geophys. Res.*, vol. 4, p.37-70.

Macdonald, K.C., 1982, Mid-ocean ridges: Fine scale tectonic, volcanic and hydrothermal processes within the plate boundary zone. *Ann. Rev. Earth Planet. Sci.*, vol. 10, p.155-190.

Macdonald, K.C., D.A. Castillo, S.P. Miller, P.J. Fox, K.A. Kastens and E. Bonatti, 1986, Deep-Tow studies of the Vema Fracture Zone: 1. Tectonics of a major slow slipping transform fault and its intersection with the Mid-Atlantic Ridge. *J. geophys. Res.*, vol. 91, no. B3, p.3334-3354.

Macdonald, K.C., P.J. Fox, L.J. Perram, M.F. Eisen, R.M. Haymon, S.P. Miller, S.M. Carbotte, M.-H. Cormier and A.N. Shor, 1988, A new view of the mid-ocean ridge from the behaviour of ridge-axis discontinuities. *Nature*, vol. 335, p.217-225.

Macdonald, K.C., D.S. Scheirer and S.M. Carbotte, 1991, Mid-ocean ridges: discontinuities, segments and giant cracks. *Science*, vol. 253, p.986-994.

Madsen, J.A., D.W. Forsyth and R.S. Detrick, 1984, A new isostatic model for the East Pacific Rise crest. *J. geophys. Res.*, vol. 89, no. B12, p.9997-10015.

Mammerickx, J., E. Herron and L. Dorman, 1980, Evidence for two fossil spreading ridges in the southeast Pacific. *Geol. Soc. Am. Bull.*, vol. 91, p.263-271.

Mammerickx, J. and G.F. Sharman, 1988, Tectonic evolution of the North Pacific during the Cretaceous quiet period. *J. geophys. Res.*, vol. 93, no. B4, p.3009-3024.

Mammerickx, J., D.F. Naar and R.L. Tyce, 1988, The Mathematician paleoplate. *J. geophys. Res.*, vol. 93, no. B4, p.3025-3040.

Martinez, F., D.F. Naar, T.B. Reed IV and R.N. Hey, 1991, Three-dimensional seaMARC II, gravity, and magnetics study of large-offset rift propagation at the Pito Rift, Easter microplate. *Mar. geophys. Res.*, vol. 13, p.255-285.

Mauduit, T. and O. Dauteuil, 1996, Small-scale models of oceanic transform zones. *J. geophys. Res.*, vol. 101, no. B9, p.20195-20209.

McAdoo, D.C., J.G. Caldwell and D.L. Turcotte, 1978, On the elastic-perfectly plastic bending of the lithosphere under generalized loading with application to the Kuril Trench. *Geophys. J. R. astr. Soc.*, vol. 54, p.11-26.

McGarr, A. and N.C. Gay, 1978, State of stress in the Earth's crust. *Ann. Rev. Earth Planet. Sci.*, vol. 6, p.405-436.

McKenzie, D.P., 1969, The relation between fault plane solutions for earthquakes and the directions of the principal stresses. *Bull. Seism. Soc. Am.*, vol. 59, no. 2, p591-601.

McKenzie, D.P. and W.J. Morgan, 1969, Evolution of triple junctions. *Nature*, vol. 224, p.125-133.

McKenzie, D. and J. Jackson, 1983, The relationship between strain rates, crustal thickening, palaeomagnetism, finite strain and fault movements within a deforming zone. *Earth Planet. Sci. Lett.*, vol. 65, p.182-202.

McNutt, M.K. and H.W. Menard, 1982, Constraints on yield strength in the oceanic lithosphere derived from observations of flexure. *Geophys. J. R. astr. Soc.*, vol. 71, p.363-394.

McNutt, M.K. and K.M. Fischer, 1987, The South Pacific superswell. In: Seamounts, islands, and atolls, B.H. Keating et al., eds., *AGU Monogr.*, no. 43, p.25-34.

McNutt, M.K. and A.V. Judge, 1990, The Superswell and mantle dynamics beneath the South Pacific. *Science*, vol. 248, p.969-975.

McNutt, M.K., 1998, Superswells. *Reviews geophys.*, vol. 36, p.211-244.

Meijer, P.TH. and M.J.R. Wortel, 1992, The dynamics of motion of the South American Plate. *J. geophys. Res.*, vol. 97, no. B8, p.11915-11931.

Michael, A.J., 1987, Use of focal mechanisms to determine stress: a control study. *J. geophys. Res.*, vol. 92, no. B1, p.357-368.

Mitchell, N.C. and L.M. Parson, 1993, The tectonic evolution of the Indian Ocean Triple junction, anomaly 6 to present. *J. geophys. Res.*, vol. 98, no. B2, p.1793-1812.

Mithen,D.P., 1980, Numerical investigations into the mechanism of graben formation. *PhD Thesis*, University of Durham.

Mount, V.S. and J. Suppe, 1992, Present-day stress orientations adjacent to active strike-slip faults: California and Sumatra. *J. geophys. Res.*, vol. 97, no. B8, p.11995-12013.

Mueller, B., V. Wehrle and K. Fuchs, 1997, The 1997 release of the World Stress Map. Available on-line at http:/www-wsm.physik.uni- Karlsruhe.de/pub/Rel97/wsm97.html.

Mutter, J.C. and J.A. Karson, 1992, Structural processes at slow-spreading ridges. *Science*, vol. 257, p.627-634.

Mutter, J.C., S.M. Carbotte, W. Su, L. Xu, P. Buhl, R.S. Detrick, G.M. Kent, J.A. Orcutt and A.J. Harding, 1995, Seismic images of active magma systems beneath the East Pacific Rise between 17°05′ and 17°35′S. *Science*, vol. 268, p.391-395.

Naar, D.F. and R.N. Hey, 1989, Recent Pacific-Easter-Nazca plate motions. In: Evolution of Mid Ocean Ridges, J.M. Sinton, ed., *AGU Monogr.*, no. 57, p.9-30.

Naar, D.F. and R.N. Hey, 1991, Tectonic evolution of the Easter microplate. *J. geophys. Res.*, vol. 96, no. B5, p.7961-7993.

Navin, D.A., C. Peirce and M.C. Sinha, 1998, The RAMESSES experiment-II. Evidence for accumulated melt beneath a slow spreading ridge from wide-angle refraction and multichannel reflection seismic profiles. *Geophys. J. Int.*, vol. 135, p.746-772.

Nishimura, C.E. and D.W. Forsyth, 1985, Anomalous Love-wave phase velocities in the Pacific - sequential pure-path and spherical harmonic inversion. *Geophys. J. R. astr. Soc.*, vol. 81, p.389-407.

Norrell, G.T., 1991, Lithospheric strength and rheological stratification at mid-ocean ridges. *J. Geol. Soc., Lond.*, vol. 148, p.521-525.

Okal, E.A., J. Talandier, K.A. Sverdrup and T.H. Jordan, 1980, Seismicity and tectonic stress in the South-Central Pacific. *J. geophys. Res.*, vol. 85, p.6479-6495.

Oldenburg, D.W. and J.N. Brune, 1972, Ridge transform fault spreading pattern in freezing wax. *Science*, vol. 178, p. 301-304.

Oldenburg, D.W. and J.N. Brune, 1975, An explanation for the orthogonality of ocean ridges and transform faults. *J. geophys. Res.*, vol. 80, no. 17, p.2575-2585.

Owen, D.R.J. and E. Hinton, 1980, Finite elements in plasticity: Theory and practice. Pineridge Press Ltd, pp.594.

Parsons, B. and J.G. Sclater, 1977, An analysis of the variation of ocean floor bathymetry and heat flow with age. *J. geophys. Res.*, vol. 82, no. 5, p.803-827.

Parsons, B. and F.M. Richter, 1980, A relation between the driving force and geoid anomaly associated with mid-ocean ridges. *Earth Planet. Sci. Lett.*, vol. 51, p.445-450.

Parmentier, E.M. and J. Phipps Morgan, 1990, Spreading rate dependence of three-dimensional structure in oceanic spreading centres. *Nature*, vol. 348, p.325-328.

Peltier, W.R., 1989, Mantle convection: plate tectonics and global tectonics. Gordon and Breach, New York.

Phipps Morgan, J. and E.M. Parmentier, 1984, Lithospheric stress near a ridge-transform intersection. *Geophys. Res. Lett.*, vol. 11, no.2, p.113-116.

Phipps Morgan, J. and E.M. Parmentier, 1985, Causes and rate-limiting mechanisms of ridge propagation: a fracture mechanics model. *J. geophys. Res.*, vol. 90, no. B10, p.8603-8612.

Phipps Morgan, J., E.M. Parmentier and J. Lin, 1987, Mechanisms for the origin of mid-ocean ridge axial topography: Implications for the thermal and mechanical structure of accreting plate boundaries. *J. geophys. Res.*, vol. 92, no. B12, p.12823-12836.

Phipps Morgan, J., 1991, Mid-ocean ridge dynamics: observations and theory. *Reviews geophys.*, supplement, p.807-822.

Phipps Morgan, J. and Y. Chen, 1993, Dependence of ridge-axis morphology on magma supply and spreading rate. *Nature*, vol. 364, p.706- 708.

Pockalny, R.A., 1997, Evidence of transpression along the Clipperton transform: Implications for processes of plate boundary reorganization. *Earth Planet. Sci. Lett.*, vol. 146, p.449-464.

Pollard, D.D. and A. Aydin, 1984, Propagation and linkage of oceanic ridge segments. *J. geophys. Res.*, vol. 89, no. B12, p.10017- 10028.

Purdy, G.M., L.S.L. Kong, G.L. Christeson and S.C. Solomon, 1992, Relationship between spreading rate and the seismic structure at mid-ocean ridges. *Nature*, vol. 355, p.815-817.

Ranalli, G., 1995, Rheology of the Earth. Chapman & Hall, pp.413.

Rea, D.K., 1978, Asymmetric sea-floor spreading and a non-transform axis offset: The East Pacific Rise 20°S survey area. *Bull. Geol. Soc. Am.*, vol. 89, p.836-844.

Ricard, Y., C. Vigny and C. Froidevaux, 1989, Mantle heterogeneities, geoid, and plate motion: A Monte Carlo inversion. *J. geophys. Res.*, vol. 94, no. B10, p.13739-13754.

Richardson, R.M., S.C. Solomon and N.H. Sleep, 1979, Tectonic stress in the plates. *Rev. Geophys. Space Phys.*, vol. 17, no. 5, p.981-1019.

Richardson, R.M. and L.M. Reding, 1991, North American plate dynamics. *J. geophys. Res.*, vol. 96, no. B7, p.12201-12223.

Robinson, E.M., B. Parsons and M. Driscoll, 1988, The effect of a shallow low-viscosity zone on the mantle flow, the geoid anomalies and the geoid and depth age relationships at fracture zones. *Geophys. J.*, vol. 93, p.25-43.

Rowlett, H., 1981, Seismicity at intersections of spreading centers and transform faults. *J. geophys. Res.*, vol. 86, no. B5, p.3815-3820.

Rusby, R.I., 1992, Tectonic pattern and history of the Easter microplate, based on GLORIA and other geophysical data. *PhD Thesis*, University of Durham.

Rusby, R.I. and R.C. Searle, 1993, Intraplate thrusting near the Easter microplate. *Geology*, vol. 21, p.311-314.

Rusby, R.I. and R.C. Searle, 1995, A history of the Easter microplate, 5.25 Ma to present. *J. geophys. Res.*, vol. 100, no. B7, p.12617-12640.

Schilling, J.-G., H. Sigurdsson, A.N. Davis and R.N. Hey, 1985, Easter microplate evolution. *Nature*, vol. 317, p.325-331.

Scholz, C.H., 2000, Evidence for a strong San Andreas fault. *Geology*, vol. 28, p.163-166.

Schouten, H., H.J.B. Dick and K.D. Klitgord, 1987, Migration of mid-ocean ridge volcanic segments. *Nature*, vol. 326, p.835-839.

Schouten, H., K.D. Klitgord and D.G. Gallo, 1993, Edge-driven microplate kinematics. *J. geophys. Res.*, vol. 98, no. B4, p.6689-6701.

Searle, R.C and A.S. Laughton, 1977, Sonar studies of the Mid- Atlantic Ridge and Kurchatov Fracture Zone. *J. geophys. Res.*, vol. 82, no. 33, p.15313-5328.

Searle, R.C., 1983, Multiple, closely spaced transform faults in fast-slipping fracture zones. *Geology*, vol. 11, p.607-610.

Searle, R.C. and R.N. Hey, 1983, GLORIA observations of the propagating rift at 95.5° W on the Cocos-Nazca spreading center. *J. geophys. Res.*, vol. 88, no. B8, p.6433-6447.

Searle, R.C., 1986, GLORIA investigations of oceanic fracture zones: comparative study of the transform fault zone. *J. Geol. Soc., Lond.*, vol. 143, p.743-756.

Searle; R.C., R.I. Rusby, J. Engeln, R.N. Hey, J. Zukin, P.M. Hunter, T.P. LeBas, H.-J. Hoffman and R. Livermore, 1989, Comprehensive sonar imaging of the Easter microplate. *Nature*, vol. 341, p.701-705.

Searle, R.C., 1992, The volcano-tectonic setting of oceanic lithosphere generation, in: Ophiolites and their modern oceanic analogues, L.M. Parson, B.Y. Murton and P. Browning, eds., *J. Geol. Soc. Lond. Spec. Publ.*, vol. 60, p.65-79.

Searle, R.C., R.T. Bird, R.I. Rusby and D.F. Naar, 1993, The development of two oceanic microplates: Easter and Juan Fernandez microplates, East Pacific Rise. *J. Geol. Soc. Lond.*, vol. 150, p.965-976.

Sempere, J.-C. and K.C. Macdonald, 1986, Overlapping spreading centers: Implications from crack-growth simulation by the displacement discontinuity method. *Tectonics*, vol. 5, p.151-163.

Sempere, J.-C., J. Lin, H.S. Brown, H. Schouten and G.M. Purdy, 1993, Segmentation and morphotectonic variations along a slow-spreading center: the Mid-Atlantic Ridge (24°00'N-30°40'N).*Mar. geophys. Res.*, vol. 15, p.153-200.

Shaw, P.R., 1992, Ridge segmentation, faulting and crustal thickness in the Atlantic Ocean. *Nature*, vol. 358, p.490-493.

Shaw, P.R. and J. Lin, 1993, Causes and consequences of variations in faulting style at the Mid-Atlantic Ridge. *J. geophys. Res.*, vol. 98, no. B12, p.21839-21851.

Shaw, W.J. and J. Lin, 1996, Models of ocean ridge lithospheric deformation: Dependence on crustal thickness, spreading rate, and segmentation. *J. geophys. Res.*, vol. 101, no. B8, p.17977-17993.

Sigmundsson, F., 1991, Post-glacial rebound and asthenosphere viscosity in Iceland, *Geophys. Res. Lett.*, vol. 18, p.1131-1134.

Sleep, N.H., 1969, Sensitivity of heat flow and gravity to the mechanism of sea-floor spreading. *J. geophys. Res.*, vol. 74, no. 2, p.542-549.

Sleep, N.H. and B.R. Rosendahl, 1979, Topography and tectonics of mid-oceanic ridge axes. *J. geophys. Res.*, vol. 84, no. B12, p.6831-6839.

Solomon, S.C., N.H. Sleep and R.M. Richardson, 1975, On the forces driving plate tectonics: Inferences from absolute plate velocities and intraplate stress. *Geophys. J. R. astr. Soc.*, vol. 42, p.769-801.

Stein, S., S. Cloetingh, D.A Weins and R. Wortel, 1987, Why does near ridge extensional seismicity occur primarily in the Indian Ocean?. *Earth Planet. Sci. Lett.*, vol. 82, p.107-113.

Stein, S. and A. Pelayo, 1991, Seismological constraints on stress in the oceanic lithosphere. *Phil. Trans. R. Soc. Lond. A*, vol. 337, p.53-72.

Stevenson, J.M., J.A. Hildebrand, M.A. Zumberge and C.G. Fox, 1994, An ocean bottom gravity study of the southern Juan de Fuca Ridge. *J. geophys. Res.*, vol. 99, no. B3, p.4875-4888.

Su, W., R.L. Woodward and A. M. Dziewonski, 1992, Deep origin of mid-ocean-ridge seismic velocity anomalies. *Nature*, vol. 360, p.149-152.

Sykes, L.R, 1967, Mechanism of earthquakes and nature of faulting on the mid-oceanic ridges. *J. geophys. Res.*, vol. 72, no. 8, p.2131-2153

Tapponnier, P. and J. Francheteau, 1978, Necking of the lithosphere and the mechanics of slowly accreting plate boundaries. *J. geophys. Res.*, vol. 83, no. B8, p.3955-3970.

Thatcher, W. and D.P. Hill, 1995, A simple model for the fault- generated morphology of slow-spreading mid-oceanic ridges. *J. geophys. Res.*, vol. 100, no. B1, p.561-570.

Tolstoy, M., A.J. Harding and J.A. Orcutt, 1993, Crustal thickness on the Mid-Atlantic Ridge: Bull's-eye gravity anomalies and focused accretion. *Science*, vol. 262, p.726-729.

Toomey, D.R., S.C. Solomon and G.M. Purdy, 1988, Microearthquakes beneath median valley of Mid-Atlantic Ridge near 23°N: Tomography and tectonics. *J. geophys. Res.*, vol. 93, no. B8, p.9093-9112.

Tucholke, B.E. and H. Schouten, 1988, Kane Fracture Zone. *Mar. geophys. Res.*, vol. 10, p.1-39.

Tucholke, B.E. and J. Lin, 1994, A geological model for the structure of ridge segments in slow spreading ocean crust. *J. geophys. Res.*, vol. 99, no. B6, p.11937-11958.

Tucholke, B.E., J. Lin, M.C. Kleinrock, M.A. Tivey, T.B. Reed, J. Goff and G.E. Jaroslow, 1997, Segmentation and crustal structure of the western Mid-Atlantic Ridge flank, $25°25' - 27°10'$ N and 0-29 m.y. *J. geophys. Res.*, vol. 102, no. B5, p.10203-10223.

Tucholke, B.E., J. Lin and M.C. Kleinrock, 1998, Megamullions and mullion structure defining oceanic metamorphic core complexes on the Mid- Atlantic Rige. *J. geophys. Res.*, vol. 103, no. B5, p.9857-9866.

Turcotte, D.L. and E.R. Oxburgh, 1973, Mid-plate tectonics. *Nature*, vol. 244, p.337-339.

Turcotte, D.L., 1974, Are transform faults thermal contraction cracks? *J. geophys. Res.*, vol. 79, no. 17, p.2573-2577.

Turcotte, D.L. and G. Schubert , 1982, Geodynamics: Applications of continuum physics to geological problems. John Wiley & Sons, pp.450.

Van der Hilst, R.D., S. Widiyantoro and E.R. Engdahl, 1997, Evidence for deep mantle circulation from global tomography. *Nature*, vol. 386, p.578-584.

Walcott, R.I., 1970, Flexural rigidity, thickness, and viscosity of the lithosphere. *J. geophys. Res.*, vol. 75, no. 20, p.3941- 3954.

Wang, X. and J.R. Cochran, 1993, Gravity anomalies, isostasy, and mantle flow at the East Pacific Rise crest. *J. geophys. Res.*, vol. 98, no. B11, p.19505-19531.

Wang, K., J. He and E.E. Davis, 1997, Transform push, oblique subduction resistance, and intraplate stress of the Juan de Fuca plate. *J. geophys. Res.*, vol. 102, no. B1, p.661-674.

Watts, A.B., J.H. Bodine and M.S. Steckler, 1980, Observations of flexure and the state of stress in the oceanic lithosphere. *J. geophys. Res.*, vol. 85, no. B11, p.6369-6376.

Weertman, J. and J.R. Weertman, 1975, High temperature creep of rock and mantle viscosity, *Ann. Rev. Earth Planet. Sci. Lett.*, vol. 3, p.293-315.

Weins, D.A. and S. Stein, 1984, Intraplate seismicity and stresses in young oceanic lithosphere. *J. geophys. Res.*, vol. 89, no. B13, p.11442-11464.

Weissel, J.K. and G.D. Karner, 1989, Flexural uplift of rift flanks due to mechanical unloading of the lithosphere during extension. *J. geophys. Res.*, vol. 94, no. B10, p.13919-13950.

West, B.P., J. Lin and D.M. Christie, 1999, Forces driving ridge propagation. *J. geophys. Res.*, vol. 104, no. B10, p.22845-22858.

Whitehead, J.A., H.J.B. Dick and H. Schouten, 1984, A mechanism for magmatic accretion under spreading centres. *Nature*, vol. 312, p.146-148.

Whitmarsh, R.B. and A.S. Laughton, 1975, The fault pattern of a slow-spreading ridge near a fracture zone. *Nature*, vol. 258, p.509-510.

Whittaker, A., M.H.P. Bott and G.D. Waghorn, 1992, Stresses and plate boundary forces associated with subduction plate margins. *J. geophys. Res.*, vol. 97, no. B8, p.11933-11944.

Wilcock, W.S.D., G.M. Purdy and S.C. Solomon, 1990, Microearthquake evidence for extension across the Kane transform fault. *J. geophys. Res.*, vol. 95, no. B10, p.15439-15462.

Wilson, D.S., 1992, Focused mantle upwelling beneath mid-ocean ridges: Evidence from seamount formation and isostatic compensation of topography. *Earth Planet. Sci. Lett.*, vol. 113, p.41-55.

Wolfe, C.J., G.M. Purdy, D.R. Toomey and S.C. Solomon, 1995, Microearthquake characteristics and crustal velocity structure at 29°N on the Mid-Atlantic Ridge: The architecture of a slow spreading segment. *J. geophys. Res.*, vol. 100, no. B12, p.24449-24472.

Wortel, M.J.R., M.J.N. Remkes, R. Govers, S.A.P.L. Cloetingh and P.T. Meijer, 1991, Dynamics of the lithosphere and the intraplate stress field. *Phil. Trans. R. Soc. Lond. A*, vol. 337, p.111-126.

Woodhouse, J.H. and A.M. Dziewonski, 1984, Mapping the upper mantle: Three-dimensional modeling of Earth structure by inversion of seismic waveforms. *J. geophys. Res.*, vol. 89, no. B7, p.5953-5986.

Wuming, B., C. Vigny, Y. Ricard and C. Froidevaux, 1992, On the origin of deviatoric stresses in the lithosphere. *J. geophys. Res.*, vol. 97, no. B8, p.11729-11737.

Zienkiewicz, O.C., 1977, The finite element method. McGraw-Hill, London.

Zoback, M.D., 1991, State of stress and crustal deformation along weak transform faults. *Phil. Trans. R. Soc. Lond.*, vol. 337, p.141-150.

Zoback, M.L., 1992, First- and second-order patterns of stress in the lithosphere: the World Stress Map Project. *J. geophys. Res.*, vol. 97, no. B8, p.11703-11728.